Dipl.-Ing. Markus Gößler BSc

In situ magnetometry of nanoporous metals during dealloying and charging

Doctoral Thesis

to achieve the university degree of

Doktor der technischen Wissenschaften

Doctoral Programme of Technical Sciences: Technical Physics

submitted to

Graz University of Technology

Supervisor

Univ.-Prof. Dr. Roland Würschum

Institute of Materials Physics

Graz, July 2021

Affidavit

I declare that I have authored this thesis independently, that I have not used other than the declared sources/resources, and that I have explicitly marked all material which has been quoted either literally or by content from the used sources.

_____   _____
          Date   Signature

Abstract

Voltage-control of magnetism has become a highly attractive research field as it offers the perspective of an energy-efficient switching of magnetisation, minimising heat dissipation losses. A promising subdivision of magneto-electric materials for that purpose are magneto-ionic material systems, which affect magnetic properties via voltage-controlled electrochemical reactions. High-surface area electrodes are beneficial for such an approach, as a large fraction of atoms is biased by chemical surface reactions, while also kinetics for intercalation reactions is enhanced.

Nanoporous metal electrodes prepared by electrochemical dealloying synthesis, a selective dissolution process of one component from an alloy, offer these advantages in combination with great versatility of the process itself. Composition, pore size, and specific surface area of the nanoporous electrodes can all be adjusted in the manufacturing process, while samples with macroscopic outer dimensions are obtained in a single step. In this thesis nanoporous, dealloyed metals are introduced in the field of magneto-ionics.

The material system of choice for this thesis was nanoporous Pd dealloyed from a Co-rich CoPd alloy for two main reasons: (i) the residual Co concentration in the nanoporous structure after dealloying can be used to tailor its intrinsic magnetic properties and (ii) the nanoporous Pd matrix provides an efficient host lattice for hydrogen atoms, which can be intercalated electrochemically from aqueous electrolytes providing the basis for a magneto-ionic tuning effect.

In a first step, the electrochemical dealloying process of a CoPd alloy itself is scrutinised with a focus on the evolution of magnetic properties using *in situ* SQUID magnetometry. Primary and secondary dealloying stages, as the formation of nanoporosity and further dissolution from the already porous structure, are identified in trends of magnetic moment in combination with supportive resistance and length changes during dealloying.

Nanometre-sized residues of the original CoPd alloy are found to evolve in buried clusters under the nanoporous structure, which exhibit superparamagnetic behaviour. The average size of those Co-rich clusters increases with increasing Co content and is sensitive to applied corrosion potential and heat treatment. Optimised magnetic nanoporous structures for magnetic tuning in electrochemical cells are created that way.

This magnetic tuning is first tested in non-aqueous electrolytes and aqueous electrolyte in a chemically inactive region, i.e. upon double-layer charging, where small changes of the magnetic moment are detected using *in situ* SQUID magnetometry. Lowering the potential in the aqueous electrolyte allows using hydrogen-charging as a stimulus for magneto-ionic switching, where relative switching amplitudes ΔM_{rel} up to 600% are achieved. A fully reversible magneto-ionic switching effect of ΔM_{rel}=100%, corresponding to an absolute value ΔM=0.15 emu g^{-1}, is obtained upon hydrogen-charging. As such a phenomenon has not been observed in the literature so far, all influences on the magnetic properties are carefully analysed, when finally a magneto-ionic switching mechanism based on the coupling of superparamagnetic clusters is devised. In that mechanism, hydrogen strengthens a Ruderman-Kittel-Kasuya-Yosida (RKKY)-type interaction between superparamagntic clusters, which makes their moments stable against thermal fluctuations and thus raises the net magnetic moment. The prediction of an enhanced magnetic anisotropy energy from this mechanism is confirmed in temperature-dependent magnetisation curves upon hydrogen-charging. Future perspectives of this magneto-ionic switching scheme are outlined.

Kurzfassung

Spannungskontrollierter Magnetismus hat sich zu einem attraktiven Forschungsfeld entwickelt, da ein energieeffizientes Schalten von Magneten ermöglicht werden kann, welches ohmsche Wärmeverluste durch Ströme in Elektromagneten vermeidet. Aus einer Vielzahl von magneto-elektrischen Ansätzen, welche sich diesem Thema widmen, ist der magneto-ionische Effekt besonders vielversprechend. Dabei werden die magnetischen Eigenschaften indirekt durch elektrochemische Reaktionen, welche wiederum durch eine äußere Spannung ausgelöst werden, kontrolliert. Materialien mit einem großen Verhältnis von Oberfläche-zu-Volumen sind dafür von Vorteil, da einerseits ein größerer Anteil von Oberflächenatomen chemisch beeinflussbar wird und andererseits auch der kinetische Ablauf von Interkalationsreationen, wie der Einbau von Wasserstoffatomen ins Kristallgitter, beschleunigt wird.

Nanoporöse Metallelektroden, hergestellt durch elektrochemische Entlegierung, einem selektiven Auflöseprozess einer Komponente aus einer Legierung, vereinen die oben genannten Vorteile mit den vielseitigen Möglichkeiten bei der Herstellung selbst. Chemische Zusammensetzung, Porengröße und spezifische Oberfläche der nanoporösen Metallelektroden können bei der Produktion adaptiert werden, wobei stets Proben mit makroskopischen äußeren Dimensionen in einem einzigen Schritt entstehen. In dieser Arbeit werden nanoporöse Metallelektroden, welche durch Entlegieren hergestellt werden, erstmals in das Forschungsfeld der Magneto-Ionik eingeführt.

Das Materialsystem der Wahl für diese Arbeit war nanoporöses Palladium entlegiert aus einer Kobalt-reichen Kobalt-Palladium Legierung, welches aus den folgenden Gründen gewählt wurde: (i) Der Restgehalt an Kobalt nach dem Entlegierungsschritt kann zur Anpassung der magnetischen Eigenschaften direkt genutzt werden und (ii) die nanoporöse Palladiummatrix ist ein effizientes Wirtsgitter für Wasserstoffatome, welche elektrochemisch in das Gitter eingebaut werden können. Elektrochemischer Wasserstoffeinbau bildet zugleich die Grundlage für den magneto-ionischen Effekt in nanoporösem Palladium.

In einem ersten Schritt wird der elektrochemische Entlegierungsprozess an sich untersucht, wobei die Entwickung der magnetischen Eigenschaften mittels *in situ* SQUID Magnetometrie in den Fokus gerückt wird. Primäres und sekundäres Entlegieren, als die Umwandlung von Legierung in eine porösen Struktur, sowie die weitere Auflösung vom bereits porösen Material, spiegeln sich sowohl in den Änderungen des magnetischen Moments, als auch in Änderungen des Widerstands und der Länge wider. Nanometer-große Reste der Kobalt-Palladium Ausgangslegierung, welche sich superparamagnetisch verhalten, finden sich unter der nanoporösen Palladium-Oberfläche in Clustern begraben. Die Größe dieser Kobalt-reichen Cluster nimmt mit steigendem Gesamtgehalt an Kobalt zu und lässt sich durch das Korrosionspotential beim Entlegieren sowie eine Temperaturbehandlung steuern. Optimierte magnetische nanoporöse Strukturen für das magnetische Schalten werden auf diese Weise hergestellt.

Das Schalten magnetischer Eigenschaften wird zuerst im chemisch inaktiven Bereich, also bei Doppelschichtbeladung, sowohl in nicht-wässrigen Elektrolyten als auch in wässrigem Elektrolyt untersucht. Kleine Änderungen der Magnetisierung wurden in diesem Bereich bei Anlegen einer äußeren Spannung mittels *in situ* SQUID Magnetometrie detektiert. Durch eine Verringerung des Potentials im wässrigen Elektrolyten kann die Wasserstoffbeladung als Stimulus für das magneto-ionische Schalten verwendet werden, wobei dabei wesentlich größere Schalteffekte von ΔM_{rel} bis zu 600% erzielt werden können. Ein völlig reversibles Schalten über den magneto-ionischen Effekt mit einer Amplitude von ΔM_{rel}=100%, was einer absoluten Änderung von ΔM=0.15 emu g^{-1} entspricht, wird durch Wasserstoffbeladung in nanoporösem Palladium-Kobalt ermöglicht. Da dieses Phänomen in der Literatur bisher nicht bekannt ist, werden alle Einflüsse auf die magnetischen Eigenschaften gründlich diskutiert, um schließlich einen neuartigen magneto-ionischen Mechanismus, der auf der Kopplung zwischen superparamagnetischen Clustern basiert, zu präsentieren. In diesem Mechanismus wird eine Wechselwirkung vom Ruderman-Kittel-Kasuya-Yosida-Typ zwischen den Clustern durch Wasserstoff verstärkt, was zu einer erhöhten Stabilität gegenüber thermischen Fluktuationen und somit zu einer größeren Magnetisierung führt. Die Vorhersage einer Erhöhung der magnetischen Anisotropieenergie bei Wasserstoffbeladung in diesem Mechanismus wird durch temperaturabhängige Magnetisierungskurven bestätigt. Zukunftsperspektiven dieses magneto-ionischen Schaltkonzepts werden erläutert.

Contents

CHAPTER 1

Introduction

"When boiling eggs, you are free to decide - depending on the cooking time, the egg becomes hard or it remains soft. However, some decisions are irrevocable - a hard-boiled egg will never become soft-boiled again. There would be less trouble at the breakfast table if you could simply switch between the different properties of the egg."

The above quotation, translated from German, is a metaphor used by Prof. Jörg Weissmüller to motivate his research on tunable properties and make it accessible to a greater non-scientific public[1]. While certainly not entirely serious, it illustrates an important technological challenge: Present-day methods allow adjusting properties of complex materials to one's needs almost without restrictions in the manufacturing process ('property tailoring'). For increasingly complex applications, however, flexible and controllable properties for materials in use are demanded ('property tuning'). The development of such 'smart materials' is a cornerstone of 21st-century research. While the term 'smart materials' is not precisely defined, they generally involve the reliable tuning of intrinsic materials properties (such as magnetisation, polarisation, strain, or resistance) by external stimuli (such as magnetic fields, electric fields, stress, current, or temperature). Electric-field or voltage bias of those properties is of special importance as it promises a fast implementation in today's electronic components and devices.

A prominent example of such a smart material can be found in modern memory devices. Hard disk drives (HDD), where information is stored in magnetic bits, are arguably one of the most important device inventions of the 20th century. Despite increasing competition from solid-state drives (SSD), the technology is still heavily used and steadily developed. A stable magnetisation over time is required for long-term data storage, whereas small bit sizes are demanded for large information densities. When reducing the magnetic bit sizes, one ultimately faces the limitation of superparamagnetism (see Sec. 2.3), i.e. thermally unstable magnetisation. The usage of materials with high effective anisotropy constant K_{eff} allows for smaller sizes, but the generation of strong enough magnetic fields for writing becomes challenging[2]. Heat-assisted magnetic recording (HAMR), is a comparably new idea to bypass this limitation, where one switches between a soft-magnetic 'write' state and a hard-magnetic 'store' state by laser-induced heating of the magnetic bits[2].

The introductory quotation seems particularly fitting for the tuning of magnetic properties, where the switching between a magnetic soft and magnetic hard state is envisaged. A contemporary subject of research is the switching between magnetic states by means of electric fields, rather than thermal heating or magnetic fields, which promises an energy-efficient switching, minimising heat dissipation losses[3–5]. Besides multiferroic materials[6] or dilute magnetic semiconductors,[7] electrochemical setups are highly topical for that purpose[8–24]. One can distinguish three fundamentally different processes at the electrode-electrolyte interface, which can be exploited for the electrochemical control of magnetism: (I) capacitive or pseudo-capacitive double-layer charging,[8–12] (II) redox surface reactions,[13–19] or (III) bulk intercalation triggered by chemical reactions[20–27]. For the approaches (II) and (III) based on electrochemical reactions[28] the term 'magneto-ionics' was coined.

Compared to conventional magneto-electric materials, magneto-ionic approaches have a direct advantage that the electric-field screening in metals can be overcome by the use of chemical reactions. As chemical reactions are typically limited by available surface area, recent research in this field has directed special attention to geometries with high surface-to-volume ratios, such as thin films[22,29–32] or nanostructured systems[18,19,33–37]. Ion intercalation reactions can lead to even larger active interaction volumes of ions with magnetic materials, offering the possibility to change bulk- instead of surface-magnetic properties of magnetic materials.

Alteration of magnetic properties has been observed upon electrochemical intercalation of various smaller ionic species, such as Li^{+} [21,23,38,39], Na^{+} [40], F^{-} [25], or H^{+} [26,27,32,41,42].

Magneto-ionic systems can potentially enable a non-volatile control of bulk magnetic properties, with the speed being in principle only limited by ionic diffusion. The state of the art timescale for the ionic control in analogous memristive devices, where resistance is controlled via charge, is well down in the subnanosecond range [43,44], while the fastest magneto-ionic switching to date is in the 1 ms range [45] for a hydrogen-based system. Hydrogen ions or atoms are particularly promising for magneto-ionic devices, as they promise fast ion diffusion and thus rapid switching of magnetic properties.

In this thesis, the main focus is put on hydrogen-charging of various Pd/Co-based nanoporous systems for magneto-ionic applications. Palladium not only has the ability to take up hydrogen in its crystal lattice, but shows interesting magnetic properties itself (Sec. 2.2), which can be modified by the addition of Co. Here, the top-down preparation process of electrochemical dealloying is used to prepare nanoporous Pd(Co) from a CoPd alloy. Nanoporous Pd(Co) obtained by the dealloying route is characterised using a variety of physical and (electro-)chemical methods (Sec. 4.2), with a special focus on its magnetic properties (Sec. 4.3). Various subroutines of this dealloying preparation route are presented in this section, which allow a targeted tailoring of the overall Co-content and the intrinsic magnetic properties of nanoporous Pd(Co). As a highlight, the evolution of magnetic properties (magnetisation and coercivity) in the dealloying process itself could be monitored *in situ* in a SQUID (superconducting quantum interference device) magnetometer [46] in Sec. 4.1, while the corresponding discussion can be found in Sec. 5.1. The tailoring of magnetic properties in nanoporous Pd(Co) is then put to use for magnetic tuning applications in Sec. 4.4. Using a custom-made electrochemical cell in a SQUID magnetometer allows tracking the magnetic properties directly as a function of applied potential. While the attention was directed onto hydrogen-charging as the most promising stimulus for magneto-ionic effects, measurements on the (pseudo-)capacitive double-layer of nanoporous Pd(Co) are also presented in Sec. 4.4.1, with the majority stemming from the Master's thesis of Alexander Steiner [47]. Capacitive effects are analysed and interpreted in Sec. 5.2.1. The core part of this thesis in Sec. 4.4.2 elaborates the hydrogen magneto-ionic tuning of (saturation) magnetisation, field-dependent magnetisation and temperature-dependent magnetisation

curves for nanoporous Pd(Co) electrodes. In the discussion (Sec. 5) the magneto-electric performance of nanoporous Pd(Co) is assessed on the basis of magneto-electric coupling coefficients in Sec. 5.2.3. A thorough analysis of hydrogen-based magneto-ionic effects in nanoporous Pd(Co), the switching performance in terms of speed and reversibility as well as other competing influences on the magnetic properties are all included in the discussion chapter of this thesis in Sec. 5.2.2. Finally, compositional changes of nanoporous Pd(Co) electrodes during electrochemical cycling are elaborated in Sec. 5.2.4.

A list of publications arising from this thesis is enclosed in the following.

- **Hydrogen-induced plasticity in nanoporous palladium** [Ref. 48]

  <u>M. Gößler</u>, E.-M. Steyskal, M. Stütz, N. Enzinger, and R. Würschum

  Beilstein J. Nanotechnol. **9** (2018) 3013-3024

  > <u>Author contributions:</u> M.G. performed all measurements and drafted the manuscript. E.-M.S. conceptualised the work and assisted dilatometry experiments. M.S. and N.E. produced the base alloy. M.G., E.-M.S and R.W. analysed and interpreted the data. R.W. supervised the overall project.

- **Magneto-Ionic Switching of Superparamagnetism** [Ref. 41]

  M. Gößler, M. Albu, E.-M. Steyskal, G. Klinser, H. Krenn, and R. Würschum

  Small **8** (2019) 1904523

  > <u>Author contributions:</u> M.G. designed the electrochemical cells, carried out the measurements and prepared the manuscript. E.-M.S. supported electrochemical cell design and electrochemical data analysis. H.K. supervised the SQUID-measurements. M.G., G.K, R.W. and H.K. analysed and interpreted SQUID-data. M.A. conducted TEM and EDS experiments. R.W. supervised the project as a whole.

- **Evolution of superparamagnetism in the electrochemical dealloying process** [Ref. 46]

  M. Gößler, M. Nachtnebel, H. Schöttner, H. Krenn, E.-M. Steyskal, and R. Würschum

  J. Appl. Phys. **128** (2020) 093904

  > <u>Author contributions:</u> M.G. devised and built the electrochemical cell, performed the magnetic measurements and wrote the manuscript. M.N. performed EDS measurements, which were interpreted by M.N. and H.S. E.-M.S. was involved in resistometry data analysis and discussion. H.K. supervised the SQUID-measurements, which were discussed and interpreted by M.G., R.W. and H.K. R.W. conceived the project idea.

- **Nanoporous Pd$_{1-x}$Co$_x$ for hydrogen-intercalation magneto-ionics** [Ref. 42]

  M. Gößler, S. Topolovec, H. Krenn, and R. Würschum

  APL Mater. **9** (2021) 041101

  <u>Author contributions:</u> M.G. conceptualised the work, performed all the measurements and drafted the manuscript. All authors discussed and interpreted magnetic data. M.G., S.T. and R.W. finalised the manuscript. The project was supervised by R.W.

1.1 List of Symbols and Abbreviations

np	Nanoporous
PCD	Potentiostatically controlled dealloying
PCD+T	PCD followed by an annealing treatment
GCD	Galvanodynamically controlled dealloying
QCD	Charge-controlled dealloying
U_D	Dealloying potential, used for charge- and potential-controlled dealloying
I_R	Residual dealloying current in potentiostatically controlled dealloying
H_C	Coercive field
M_S	Saturation magnetisation
npPd(Co)	Nanoporous Palladium-Cobalt prepared via PCD
$npPd_{(1-x)}Co_x$	Nanoporous Palladium-Cobalt with adjustable Cobalt content prepared via GCD
SQUID	Superconducting quantum interference device
RKKY	Ruderman Kittel Kasuya Yosida
SEM	Scanning electron microscopy
STEM	Scanning transmission electron microscopy
EDS	Energy-dispersive X-ray spectroscopy
EELS	Electron energy loss spectroscopy
KMC	Kinetic Monte Carlo
XRF	X-ray fluorescence
XPS	X-ray photoelectron spectroscopy
EIS	Electrochemical impedance spectroscopy

CHAPTER 2

Fundamentals

2.1   Dealloying

High surface-to-volume ratios are beneficial for all chemical reactions, as reaction kinetics (which scales with surface area between the reactants) is enhanced for a given material expense (which scales with volume). Catalysis, as a particularly strong research field close to industry, benefits greatly from such materials. Nanoparticles are the most prominent example from the class of materials with high surface-to-volume ratios, which are extensively studied. A major drawback of nanoparticles is the difficulty to establish electrical contact for electrochemical reaction control. First high surface area electrodes were produced from compacted nanoparticles. Small pellets of nanoparticulate materials could be produced, with macroscopic outer dimensions, while retaining the high internal surface area in a nanoporous structure[49]. The contacting issue is solved at the cost of a slightly reduced surface area that way. Since then, more elaborate ways of producing nanoporous network structures have been developed, with dealloying being a particularly elegant example.

Dealloying is a one-step fabrication method for the preparation of nanoporous metals, based on the selective removal of one element from a (mostly binary) alloy. Originally conceptualised as a corrosion process based on the different electrochemical standard potentials of the constituents[50,51], nowadays other subvariations of dealloying exists, such as liquid-metal

11

dealloying[52,53] (based on differences in miscibility) and vapour-phase dealloying[54,55] (based on differences in vapour pressure).

During electrochemical dealloying, a bicontinuous network of nanometre-sized pores and solid struts, called ligaments, evolves gradually with time. A schematic of the dealloying process is presented in Fig. 2.1. The dealloying process relies on two basic atomistic processes, (i) the dissolution of the less noble component, and (ii) the surface diffusion of both constituents in a binary alloy[56]. Dissolution of the less noble component leads to an initial surface roughening of the alloy (Fig. 2.1a-b). Surface diffusion of the more noble component first leads to passivation on the surface (Fig. 2.1b) and a subsequent undercutting of the ligaments and the exposure of new alloy regions to the electrolyte (Fig. 2.1c-d). Surface diffusion of noble metal atoms at the metal-electrolyte interface is known to be an extremely fast process, i.e. orders of magnitude faster compared to the metal-vacuum interface[57]. The characteristic size for both pores and ligaments in electrochemical dealloying is controlled by this surface diffusion process (Fig. 2.1c-e) and scales inversely with melting temperature of the more noble element[58,59], as does surface mobility. The smallest ligaments sizes attained via electrochemical dealloying have been achieved for the high-melting-point metals Pt and Pd[59].

As a prerequisite for the production of nanoporous metals via dealloying, the dissolving alloy component needs to be percolating the initial alloy. For a continuous etching process, electrolyte penetration and solvation of dissolved ions must be warranted, which shifts the actual limiting concentrations to higher values[60,61]. The 'parting' limit represents the lower composition limit for successful dealloying and lies at ~ 55 at% Ag for the textbook dealloying system of AgAu, which is higher than the purely geometric percolation limit ($\sim$19 at% for an fcc lattice[62]). Similar parting limits are expected for other fcc binary alloy systems, which are limited by purely geometric thresholds. Simultaneous oxidation of the more noble component can hinder the formation of nanoporosity and lead to a substantially higher parting limit up to 75 at%[63]. In practice, typical alloys for dealloying contain 70 at% to 85 at% of the less noble component[64–71], as higher concentration might lead to the disintegration of the alloy upon selective dissolution rather than the formation of nanoporosity.

From an electrochemical standpoint, a minimum potential for dealloying exists, often termed 'critical' dealloying potential[50,56,72]. Below that critical potential only the low-coordinated

surface sites are depleted from the less noble component, which ultimately leads to surface passivation by a noble element layer[50,56,61]. Above the critical potential dissolution occurs also from sites with high coordination, enabling complete dealloying above the parting limit.

Literature often divides the dealloying step into two subprocesses, namely primary and secondary dealloying[69,73,74]. Primary dealloying, on the one hand, is associated with dissolution from the alloy and the accompanied progression of the etching front. Secondary dealloying, on the other hand, involves the dissolution of residual atoms from the already porous structure behind the etching front. Primary dealloying consumes the major part of the charge in the overall process, however, it has been impossible to distinguish between primary and secondary dealloying on the basis of charge or current data solely. In this thesis *in situ* magnetometry data during dealloying[46] are presented in order to differentiate between primary and secondary dealloying contributions.

When using nanoporous electrodes in aqueous electrolytes, a hybrid nanomaterial with solid metal ligaments and electrolyte-filled pores with nanoscale intermixing is created[61]. Electrical charge stored on the metal-electrolyte interface, as originally proposed by Gleiter et al.[75], or electrical charge transfer through the metal-electrolyte interface is the basis for the tunable properties by voltage in a plethora of literature examples[49,76–80] and also, as magneto-ionic effect, the foundation of this thesis.
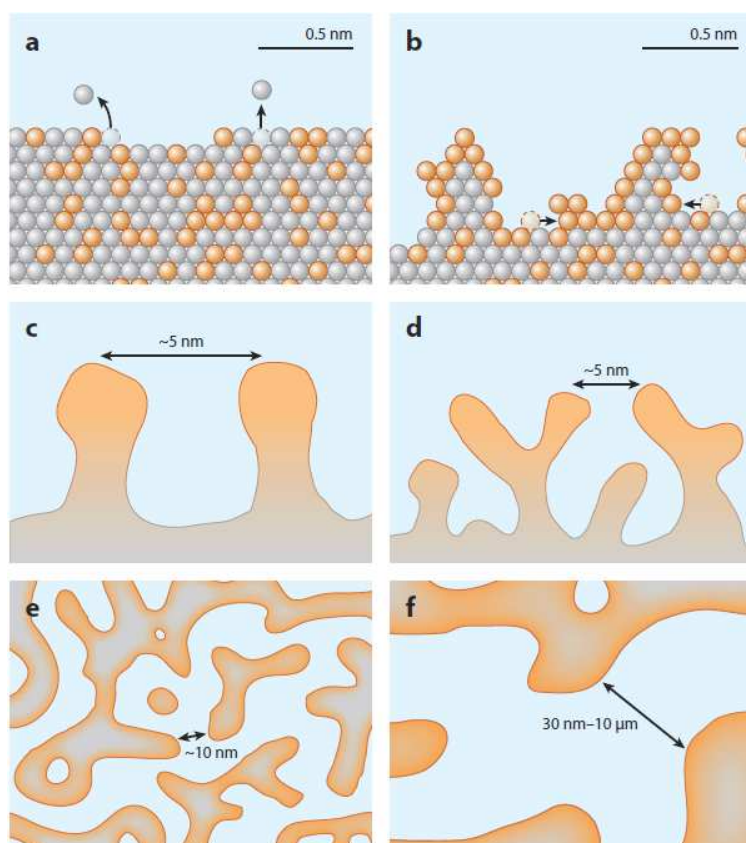
Figure 2.1: Porosity evolution in the dealloying process (less noble component - grey; more noble component - orange). (a) Less noble atoms are dissolved from the topmost layers. (b) Surface diffusion leads to a surface roughening and passivation with the more noble alloy component. (c,d) Above the critical dealloying potential and below the parting limit, dealloying then proceeds as the more noble atoms are insufficient to cover the full surface. Ligaments start to bifurcate at this point, creating a characteristic ligament and pore size in the nanometre regime. (e) A bicontinuous nanoporous structure is formed, with the surfaces fully covered with more noble alloy atoms. (f) Temperature-treatment or prolonged exposure to the electrolyte coarsens the nanoporous structure via a surface diffusion mechanism. Reprinted with permission from McCue et al. (Ref. 53).

2.2 Magnetism of palladium

The electronic band structure of the high-susceptibility Pauli paramagnet palladium, schematically depicted in Fig. 2.2(a), almost fulfils the Stoner criterion for ferromagnetism[81]. In the Stoner model a metal will become ferromagnetic if the density of states at the Fermi level $D(E_F)$ is large enough. For Pd, the Fermi energy resides just above a narrow peak in the density of states, which would favour ferromagnetic band splitting. Subtracting electrons from the outermost bands of Pd would therefore shift the Fermi level towards this peak in the density of states, which might induce spontaneous band splitting and the occurrence of ferromagnetism. One way to achieve band splitting is the alloying of small quantities of ferromagnetic 3d atoms to Pd, which turn the whole alloy ferromagnetic. For PdCo alloy the critical Co concentration is around 10 at% at room temperature[82], although dilute concentrations of 0.1% Co still lead to ferromagnetism with a Curie temperature of T_C=7 K[82]. Giant moments up to 10 μ_B per Co atom are obtained in such alloys, while pure Co atoms in a hcp crystal only exhibit a moment of 1.72 μ_B per atom[83]. It was found that not only Co atoms carry a magnetic moment in the PdCo alloy, but Pd atoms get magnetically polarised in the vicinity of Co and carry a magnetic moment themselves, which is indicated in Fig. 2.2(b). Exchange coupling of Co 3d electrons and Pd 4d electrons is thought to be responsible for this mechanism[82].

Magnetic impurities in d-band metals are also known to transmit the indirect RKKY (Ruderman-Kittel-Kasuya-Yosida) interaction via the conduction electrons[84–86], which has an oscillating sign (i.e. switches between ferromagnetic and antiferromagnetic coupling) over long distances. For high-susceptibility paramagnets as Pd the large polarisability of the d-band electrons leads to a pronounced ferromagnetic maximum at short distances, a suppressed first antiferromagnetic minimum and an extended interaction range of the RKKY interaction in general[87,88] (exchange-enhanced RKKY interaction), a scenario which is exemplified in Fig. 2.2(b) for a single Co atom impurity in Pd. This type of interaction plays an essential role for the changes of magnetic moment induced by hydrogen-charging in this thesis (see Sec. 5.2.2).

The platinum-group metals Ni, Pd, and Pt all have a great affinity to hydrogen, which is only one reason why they all are excellent catalyst materials in chemistry. A central feature which
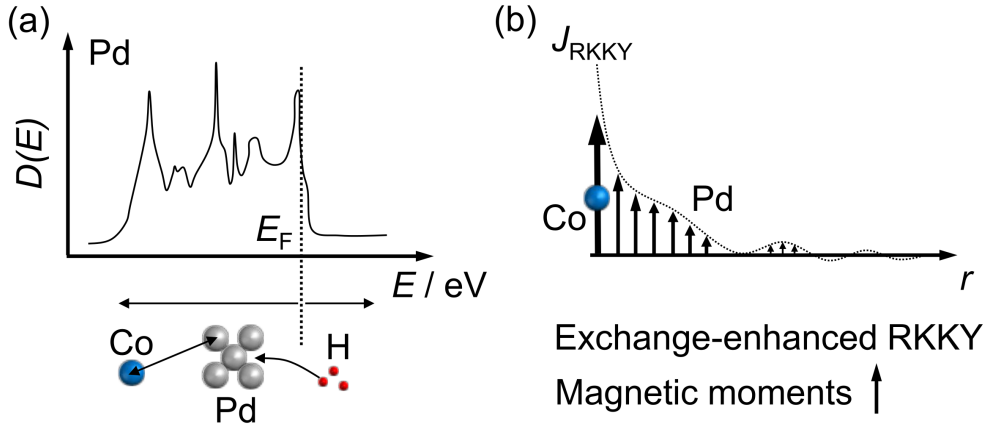
Figure 2.2: Origin of magnetism in Pd and PdCo. (a) Electronic band structure of Pd (schematic). While alloying with Co shifts the Fermi energy to lower energies and turns the alloy ferromagnetic, hydrogen-charging has the converse effect and shifts the Fermi energy to higher values, reducing the magnetic susceptibility. (b) Exchange-enhanced RKKY-interaction originating from a single Co atom impurity (schematic). The interaction is transmitted via the Pd conduction electrons, which get polarised and carry a magnetic moment themselves.

distinguishes palladium from other noble metals such as platinum is its ability to absorb hydrogen into its bulk, which has been known since the mid-nineteenth century[89]. Palladium hosts solute hydrogen atoms on octahedral sites in its face-centered-cubic crystal lattice. Thus, the limiting stoichiometry would be a sodium chloride crystal structure, when the hydrogen and palladium ratio H:Pd would be one. Typically hydrogen-charging is facilitated by pressurisation of the Pd metal with hydrogen gas, which allows controlling the hydrogen concentration via the applied gas pressure. In this thesis electrochemical absorption of H-atoms into a palladium electrode is utilised, where hydrogen concentration can be controlled via charge and potential. A comparison of both charging methods can be found in Ref. 90.

Hydrogen atoms in the Pd lattice act as electron donors in the rigid band model and thus shift the Fermi energy to higher values compared to pure Pd, as sketched in Fig. 2.2(a). The density of states at the Fermi level $D(E_F)$ is decreased, which in hand reduces the magnetic susceptibility[76]. This simplistic picture of hydrogen filling rigid bands with electrons holds up well not only for Pd but also its alloys with Co[91–93].

Hitherto research groups investigated the tuning of magnetism in PdCo structures via (pseudo-)capacitive double-layer charging in electrolytic environments[10,94,95] and upon gas-phase hydrogenation[91,93,96–101]. Besides, PdCo structures were proposed as hydrogen sensors based upon the strong effect of hydrogen on the magnetic properties[102,103]. In this thesis the
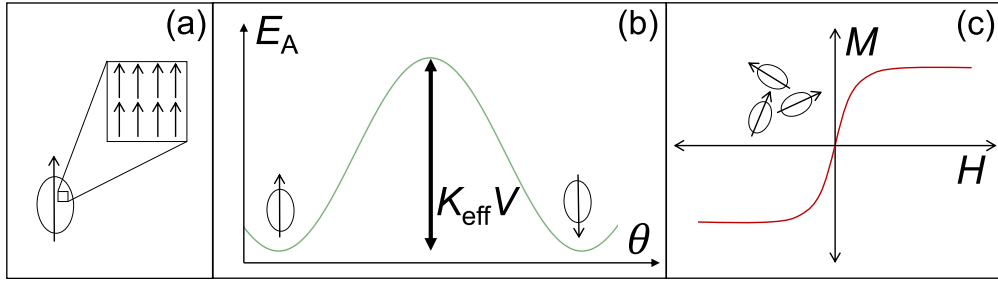
Figure 2.3: Schematic explanation of superparamagnetism. (a) Superparamagnetic particles retain ferromagnetic ordering of elementary magnetic moments in a single domain, which is only destroyed above the Curie temperature T_C. (b) Anisotropy energy E_A of a superparamagnetic single-domain particle dependent on the angle between external field and easy axis θ. The energy barrier to flip the magnetisation direction is $K_{eff}V$, which can be overcome by thermal energy for superparamagnetic particles. (c) Typical magnetisation (M) curve for assemblies of superparamagnetic particles with external field H, following the Langevin function, i.e. the classical limit for paramagnetism.

preparation and application of Pd/Co-based systems is investigated for the magneto-ionic tuning of magnetism.

2.3 Superparamagnetism

As a fundamental principle of physics resulting from the second thermodynamic law, any physical system will always strive to minimise its Gibbs free energy G. For any given system this minimisation of G will be responsible for its overall physical behaviour and properties. Physical properties on the nanoscale can differ vastly from the well-known and expected bulk behaviour, as competing energy contributions to G scale differently with decreasing size. The properties of ferromagnets are governed by the interplay of four main energy contributions: stray field energy E_S, magnetostatic (or Zeeman) energy E_H, anisotropy energy E_A, and exchange energy E_{ex}. Trying to predict physical properties using these energy contributions often yields complex energy minimisation problems, resulting in Brown's equations of micromagnetism[104]. The energy balance in magnetism does not only account for the manifestation of magnetic domains and their cunning patterns, but is also responsible for superparamagnetism.

Below a certain critical size a ferromagnetic nanoparticle will only consist of a single magnetic domain with all spins aligned in parallel, reducing its exchange energy E_{ex} to zero, as

schematically shown in Fig. 2.3(a). Without an external applied field H, which implies E_H is also zero, the direction of magnetisation within the particle is then given solely by the anisotropy energy E_A. Anisotropy energy can be written as a product of anisotropy constant K and particle volume V,

$$E_A = KV, \tag{2.1}$$

with K showing a directional dependence as

$$K = K_{\text{eff}} \sin^2(\theta), \tag{2.2}$$

where K_{eff} is the material's effective anisotropy constant and θ is the angle between magnetisation direction and the magnetic easy axis. In order to reverse the magnetisation of a single-domain particle, Eq. 2.1 gives the energy cost for that process, which is also depicted schematically in Fig. 2.3(b). When shrinking single-domain particles further, thermal energy $k_B T$ becomes comparable to anisotropy energy, which is strongly dependent on the particle diameter d ($V \propto d^3$). Particles start to randomly flip their magnetisation direction excited by thermal fluctuations, retaining no average net magnetisation in a particle assembly. The term superparamagnetism was coined for such particles, as they behave as paramagnetic substances with a giant magnetic moment. A transition between stable (or 'blocked') ferromagnetism and superparamagnetism can be observed in experiments, when measuring magnetisation as a function of temperature (see also Sec. 4.3). When superparamagnetic moments in an assembly are frozen in random directions at a low temperature, an unblocking of moments can be observed at a size-dependent blocking temperature T_B upon heating in a low magnetic field. For a complete unblocking of all randomly oriented particles in the assembly, the full energy barrier $K_{\text{eff}}V$ needs to be overcome. This reflects itself in the well-known blocking criterion, which can be written as[228]

$$25 \, k_B T_B = K_{\text{eff}} V, \tag{2.3}$$

where the factor of 25 is a typical value for the natural logarithm of measurement frequency $(1/100 \text{ s}^{-1})$ divided by the attempt frequency for magnetisation reversal (10^9 s^{-1}).

The blocking temperature can be considered a transition temperature between ferromagnetism and superparamagnetism, which is necessarily always smaller than the Curie temperature of the material ($T_\mathrm{B} < T_\mathrm{C}$). Note that the ordering of spins within a single-domain particle remains ferromagnetic above T_B and is only destroyed at T_C, as shown in Fig. 2.3(a).

In contrast to typical paramagnetic materials, magnetisation directions for superparamagnetic particles can be considered continuous, rather than quantised, while the magnetic moment μ is considerably larger. Magnetisation M as a function of magnetic field H for monodisperse superparamagnetic particles therefore follows the classical limit for paramagnetism, which can be written using a Langevin function as

$$M = n\mu \coth(x) - \frac{1}{x},\tag{2.4}$$

where n is the number of superparamagnetic particles per unit volume and

$$x = \frac{\mu H}{k_\mathrm{B} T}.\tag{2.5}$$

While paramagnetic moments for electron spins are in the order of $1\mu_\mathrm{B}$, single-domain particles can have much larger magnetic moments in the order of $\mu{=}10^3$ to $10^5\mu_\mathrm{B}$[105]. A schematic magnetisation curve for superparamagnetic particle assemblies, following the Langevin function, is shown in Fig. 2.3(c).

An interesting aspect for magneto-electric applications is that superparamagnetic materials per se contain ferromagnetic units with a large 'hidden' magnetic moment. Promoting one of the energy contributions for nanoscale magnetism electrically is a promising concept to pin the magnetisation direction of superparamagnetic particles, making the large moment and ferromagnetic behaviour reappear. First studies have proved the viability of this concept by inducing a magneto-elastic energy contribution[106,107]. Magneto-elastic coupling of superparamagnetic particles to the strain in a matrix, which is piezoelectric and thus controllable by electric fields, allowed the magneto-electric switching between superparamagnetism and ferromagnetism[106,107].

CHAPTER 3

Materials and Methods

This chapter introduces both the preparation of the most relevant materials and the main experimental methods used in this thesis. The first section. 3.1 defines conventions and abbreviations, which are used throughout this thesis. Electrochemical methods are summarised in Sec. 3.2, with subsections devoted to the electrochemical cell setup (Sec. 3.2.1) and the geometries used for *in situ* magnetometry, resistometry and dilatometry (Sec. 3.2.2 and Sec. 3.2.3), as well as dedicated subsections for the most important electrochemical procedures used in this work, i.e. cyclic voltammetry in Sec. 3.2.4, chronoamperometry in Sec. 3.2.5, chronopotentiometry in Sec. 3.2.6 and electrochemical impedance spectroscopy in Sec. 3.2.8. Alloy preparation is described in Sec. 3.3, while the SQUID magnetometry method in general is covered in Sec. 3.4. Methods for electron microscopy and compositional analysis are presented in Sec. 3.5. The last section Sec. 3.6 introduces the computational method used for Kinetic Monte Carlo (KMC) simulations in this thesis.

3.1   Conventions and abbreviations used in this thesis

The abbreviation npPd specifies nanoporous palladium prepared via potentiostatically-controlled dealloying (**PCD**), which is the standard production method for nanoporous metals via electrochemical dealloying. The two important parameters for this dealloying synthesis route, namely the applied dealloying potential U_D, and the current at which the

procedure was stopped I_R are stated explicitly in brackets for such samples. For temperature-treated PCD samples the abbreviation PCD+T is used, with both annealing temperature T_A and duration stated additionally. The expression $npPd_{(1-x)}Co_x$ is used for nanoporous palladium-cobalt prepared via galvanodynamically-controlled dealloying (**GCD**), where the final the Co concentration x, as fixed in the measurement, is used to specify the samples. For charge-controlled dealloying (**QCD**) samples are not fully nanoporous in nature, but contain a residual backbone of the initial alloy. These types of samples are named via the relative charge consumed during dealloying Q/Q_{tot}, where the total, nominal charge Q_{tot} can be calculated from sample mass using Faraday's law:

$$Q = \frac{m \; N_A \; z \; e}{M}. \tag{3.1}$$

Herein, Q represents the nominal charge, m is the mass of the dissolved component (typically Co), z is the valency of the dissolved species ($z=2$ for Co^{2+}), M is the molar mass of the dissolved component (Co: $M=58.9$ g Mol^{-1}), while N_A and e are the usual physical constants. Charge Q is always determined via trapezoidal integration of corresponding current curves over time. If not explicitly stated otherwise, potentials in this thesis refer to a commercial Ag/AgCl(3M KCl) reference electrode.

3.2 Electrochemical Methods

3.2.1 Electrochemical cell setup

Alloy platelets for dealloying experiments were contacted with a gold wire (Mateck/Chempur, 99.9%[a], $\varnothing= 0.25$ mm). For samples processed for magnetic *ex situ* characterisation, i.e. measurements outside the electrochemical cells, the gold wire was folded around the sample once and mechanically attached using a screw press. This procedure enables good electrical contact during dealloying, but also allows a straightforward detachment from the wire afterwards by unfolding the wire. For *in situ* samples a longer piece of gold wire ($\sim$15 cm) was wrapped around the sample both length- and crosswise and fixed with the screw press

---

[a]Concentrations of all metal precursors are given in at% on the basis of metals content only, as declared by the manufacturers.

afterwards to ensure enduring electrical contact for all following electrochemical treatments. A three-electrode electrochemical cell setup was generally used, where the gold-connected sample was placed as the working electrode. A commercial Ag/AgCl (3M KCl - Metrohm) with a standard potential $U=+0.21$ V vs. NHE served as the reference electrode, while a coiled palladium wire (Chempur, 99.95%, $\varnothing= 0.25$ mm) was placed as the counter electrode in a 30mL beaker as electrolyte compartment. The dealloying electrolyte for CoPd was 0.1 M H_2SO_4 prepared from 2N sulfuric acid (Roth) and high-purity water (Roth, ROTIPURAN®, p.a.). All dealloying experiments were controlled using a potentiostat (Metrohm Autolab, PGSTAT128N). Potentials for dealloying (U_D) and residual etching currents, at the point where the dealloying was stopped (I_R), are directly stated in the text. After dealloying, samples were carefully rinsed in distilled water for several hours and subsequently dried at room temperature.

3.2.2 *In situ* magnetometry

The electrochemical cell setup used for *in situ* SQUID magnetometry in this thesis builds upon cell geometries developed earlier in our group for magnetic tuning[108], electrodeposition[109,110], and battery charging[111–113]. Such specialised *in situ* cells are subject to several restrictions and constraints, which need to be taken into account when designing experiments[114]. Besides the obvious size limitation in the MPMS-XL-7 measurement chamber (diameter~8 mm), the cell needs to be sealed, as it is exposed to vacuum in the airlock and to lower He pressures in the measurement chamber of the magnetometer. Furthermore, the measured magnetic signal of the working electrode should not be influenced by any other cell component. General requirements for electrochemical cells, as stable potentials for reference electrodes, high-surface counter electrodes and electrolytic stability of all compounds also need to be fulfilled. A three-electrode configuration, consisting of working electrode, reference electrode, and counter electrode, was used for all electrochemical cells in this thesis. A schematic of a typical electrochemical cell used for hydrogen-charging of npPd electrodes is depicted in Fig. 3.1, which is reprinted from Ref. 42.

Cells were assembled in Pyrex® borosilicate NMR glass tubes (Wilmad, $\varnothing= 5$ mm) as electrolyte compartment. This elongated type of electrolyte container extends over the whole
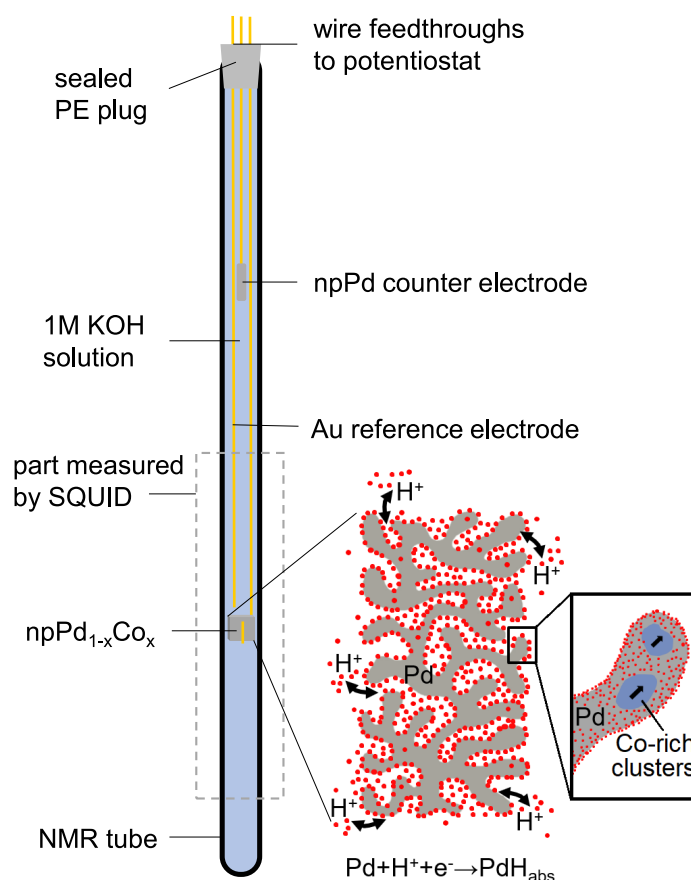
Figure 3.1: Schematic depiction of the electrochemical cell used for *in situ* hydrogen charging in the SQUID magnetometer: The hydrogen-charging process in npPd(Co) is shown schematically (bottom right). Reprinted from Ref. 42

length of the magnetic pick-up coils, which guarantees an unchanging magnetic background from electrolyte and compartment during a single SQUID scan. The working electrodes were placed in the lower third of the NMR tube about 5-6 cm above the bottom end. For tuning experiments in KOH solution, a gold wire was installed as quasi reference electrode, while for *in situ* dealloying (Sec.4.1) a homemade AgCl-coated silver wire was used. For coating the AgCl layer, silver wires (0.25 mm, Mateck, 99.995%) were immersed 1 cm in 3 M KCl solution, when a current density of $+0.25$ mA cm^{-2} was applied for 3 minutes. A platinum wire was used as both counter and reference electrode. After every 30 s current was reversed for 5 s to obtain a smooth coating.

Other electrolyte systems used in this thesis for *in situ* SQUID characterisation comprised LiPF$_6$ in ethylene carbonate/ethyl methyl carbonate 1:1 (EC/EMC) and Na$^+$-ions in propylene carbonate solution. While the sample contacting remained unchanged for the alternative

electrolytes, counter and reference electrodes were adapted. In the $LiPF_6$-based electrolyte, metallic Li wrapped onto Cu-wires was used for both counter and reference electrodes. In the Na^+-based electrolyte, Pt wires were used instead also for both counter and reference electrodes. The cell compartment for non-aqueous electrolytes was a PE tube, which was fused on the lower end with comparable dimensions to the NMR glass tube.

In the electrochemical cells for the use in the SQUID magnetometer, the reference electrode and the gold contact wire for the working electrode were insulated using a fine polyethylene tubing (0.4 mm ID, Smiths Medical) to avoid short-circuits. About 2 mm of the reference electrode were left uncovered on the lower end close to the working electrode to enable sufficient contact with the electrolyte solution. The total distance between the working and the reference electrode was 1-2 cm. The diamagnetic nature of the reference electrode materials (Au, Ag and AgCl) ensures that there is no noticeable contribution of the reference electrodes to the magnetic dipole fits of the working electrode sample. The counter electrode was placed about 4-5 cm off the top of the NMR tube, well out of the detection range of the pick-up coils. Dealloyed npPd platelets contacted with gold wires were used as counter electrodes for *in situ* dealloying and hydrogen-charging experiments in the SQUID magnetometer, as they have similarly high surface areas as the working electrodes. This is a key requirement for counter electrodes in order to keep the current densities at the counter electrode low, preventing a potential drop on the counter electrode side. In contrast to carbon cloth electrodes contacted with Au-wires, npPd proved to have a better long-term electrochemical stability even at higher currents.[b] For hydrogen-charging tests, aqueous potassium hydroxide solution (1 Mol/L) prepared from KOH pellets (Roth, ≥85%, p.a.) and high-purity water (Roth, ROTIPURAN®, p.a.) served as the electrolyte. NMR tubes were filled with the electrolyte solutions up to 2-3 cm from the top and closed with a PE plug with three drilled holes as wire feedthroughs. All electrodes wires were first passed through the holes, colour-coded at their ends and fixed in the plug with epoxy resin (Uhu Schnellfest), securing the positions of the electrodes relative to each other. The whole plug with electrodes connected was also glued in the NMR tube with a different type of resin (Uhu Endfest) to

---

[b]The strong magnetic switching effect upon hydrogen charging of npPd(Co) working electrodes was reproduced using such a carbon cloth counter electrode, ensuring that an eventual dissolution/redeposition of magnetic Co atoms from the counter electrode can be excluded as the source of the magneto-ionic effect.

close the cell completely. For an ideal sealing of the cell, a third layer of epoxy resin (Loctite Hysol®) was applied, which cured overnight.

The prepared cells were attached to the transfer rod of the SQUID magnetometer using a plastic straw, with the external parts of the wires connected to electrical feedthroughs available on the bottom side transfer rod. Electrical contact to the transfer rod was carefully checked for all cells. Only afterwards the sample was fixed on the rod for the magnetic measurements with adhesive tape. As sample positions within the electrochemical cells differed slightly, the distance to the fixed part of the transfer rod had to be adjusted to 125.5 cm to allow automatic sample centering with respect to the pickup coils via the MultiVu software.

3.2.3 *In situ* resistometry and dilatometry

Electrochemical resistometry and dilatometry *in situ* experiments were used as complementary methods to *in situ* magnetometry for the study of the dealloying process of a $Co_{75}Pd_{25}$ alloy. In the resistometry setup, a $Co_{75}Pd_{25}$ alloy platelet (3×10 mm^2) was contacted in a four-point geometry using Au wires (0.25 mm, Mateck, 99.9%) to a Keithley 2400 Source Meter, which monitored the electrical resistance. A separate fifth supporting contact wire was used for electrochemical process control via a potentiostat (Metrohm Autolab, PGSTAT128N). Wires were folded over the long edge of the sample and glued onto the alloy (Crystalbond 509 glue - Aremco) to assure electrical contact during the entire dealloying measurement. Details regarding the resistometry setup are available in Ref. 80.

For *in situ* dilatometry the sample was placed under the pushrod of a Linseis L75 vertical dilatometer, which applied a constant force of 100mN. Electrical contact to an Autolab PGSTAT204 potentiostat was established using an Au wire (0.25 mm, Mateck, 99.9%).

PCD experiments in both the resistometry and the dilatometry setup were conducted in H_2SO_4 (0.1 Mol/L) electrolyte solution at a constant potential of U_D=0.55 V vs. a commercial Ag/AgCl (sat. KCl) reference electrode (Metrohm Autolab). Both experiments used a coiled Pd-wire and an Ag/AgCl (sat. KCl) electrode (Metrohm) as counter and reference electrodes, respectively.
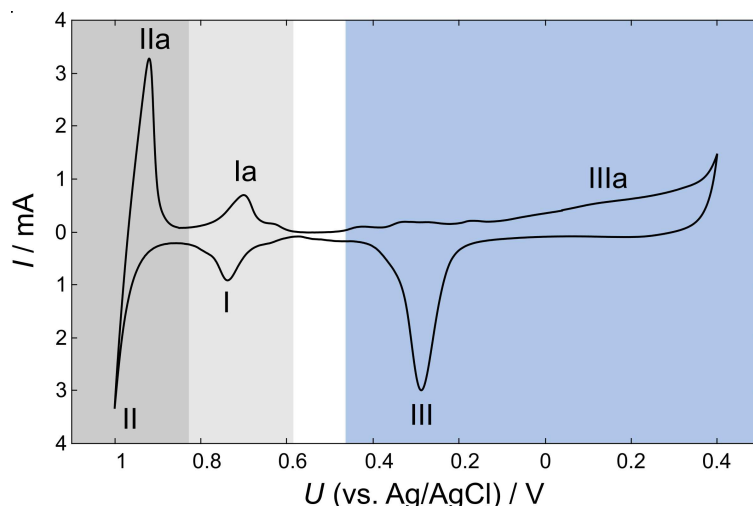
Figure 3.2: Typical cyclic voltammogram for a npPd(Co) electrode in 1 M KOH recorded at a scan rate of 0.1 mVs^{-1} in the potential range between -1 V and 0.4 V. The region of hydrogen ad-/desorption is shaded light grey, the hydrogen ab-/desorption region is shaded in darker grey. Oxygen-related ad-/desorption reactions occur in the bluish-grey area. The white region indicates double-layer charging. Numbered peaks are discussed in the text.

3.2.4   Cyclic Voltammetry

Cyclic voltammetry is not only the most widely employed method for studying electrode kinetics[115], but its application is also documented in various publications in the field of magneto-ionics[9–11,18,32,33,41,42,116,117], as it allows a continuous switching between magnetic states and the simultaneous gain of electrochemical information about the interface reactions. By applying a triangular AC voltage profile between working and reference electrode, the electrode is driven into different chemical regimes in a specified voltage window. This voltage window is limited by the potentials for electrolyte decomposition. In the case of aqueous electrolytes the potentials for water electrolysis, i.e. cathodic hydrogen gas evolution and anodic oxygen gas formation, leave a maximum voltage window in the order of 1.5 V to study chemical reactions. The slope of the triangular voltage signal is referred to as scan rate (in units of Vs^{-1} or mVs^{-1}), which specifies the speed of cycling between the lower and upper voltage limit. The resulting curve of current as a function voltage is the cyclic voltammogram (CV), with a typical single cycle for a npPd(Co) electrode in 1 M KOH recorded with a scan rate of 0.1 mVs^{-1} being depicted in Fig. 3.2.

According to IUPAC specifications, positive currents refer to anodic reactions, while negative currents imply cathodic reactions[118]. All peaks in Fig. 3.2 can be attributed to electrochemical

reactions on the nanoporous Pd electrode[119]. Cyclic voltammograms are run through in clockwise direction. The cathodic peak I is characteristic for hydrogen adsorption on the Pd surface. At more negative potentials adsorbed hydrogen atoms migrate into the bulk and become absorbed in the Pd metal, while simultaneously adsorbed hydrogen atoms on the surface recombine to form H_2 gas. The corresponding hydrogen reduction reactions overlap in cathodic peak II in the cyclic voltammogram. On the anodic side, peak IIa is the reoxidation of absorbed hydrogen species, i.e. desorption of absorbed hydrogen. Current associated with H_2 gas cannot be recovered in the anodic half-cycle due to the volatility of gaseous H_2[c]. This hydrogen desorption peak grows in height and width if the lower potential limit is extended to more negative values, as for higher hydrogen concentrations diffusion of hydrogen atoms in the Pd lattice becomes a limiting factor[119]. Peak Ia, corresponding to the desorption of adsorbed hydrogen, might be overshadowed by the strong diffusive hydrogen reoxidation peak IIa, as observed later e.g. in Fig. 4.37. The white central region with characteristically low currents comprises the double-layer regime, where no charge-transfer through the electrode-electrolyte interface occurs. The specific surface area of npPd(Co) electrodes was calculated from the double-layer capacitance in that region (see Sec. 4.2.2.1). The broad anodic peak IIIa corresponds to the formation of surface palladium oxide, while the distinct cathodic peak III is the corresponding counter-reaction, namely oxide reduction. Oxide formation and reduction on the npPd(Co) electrode are irreversible processes, as peaks on the anodic and cathodic side do not appear within 57 mV at room temperature as would be characteristic for reversible processes[115].

For larger scan rates, peaks ascribed to certain reactions tend to 'smear', i.e. they are less distinct and spread over a certain voltage range instead of appearing as a sharp peak. Peak currents increase with the square root of the scan rate[115]. The attributes 'large' or 'small' when referring to scan rates depend on the surface area of the electrodes used. Potential-controlled reactions imply certain current densities through the electrode-electrolyte interface. For cyclic voltammetry and small deviations from the equilibrium potential, this current density can be described by the Butler-Volmer equation[120]. Higher total electrode surface area therefore entails higher total currents measured in a CV. For nanoporous electrodes, as used in this work, peaks in the CV broaden additionally due to a potential-drop from

---

[c]For that reason cathodic hydrogen charge is always larger than anodic hydrogen charge. This holds also for the CV in Fig. 3.2 and becomes apparent in peak area when plotted over time (not shown).

macroscopic surface to inner pore regions, where electrolytic diffusion is also slower. Typical scan rates to obtain well-separated, distinct current peaks for dealloyed, nanoporous metal electrodes are in the order of 0.1-1 mV s^{-1}.

In this work cyclic voltammetry was the standard procedure for magneto-ionic tuning measurements on npPd(Co) electrodes in the *in situ* electrochemical cells, i.e. cyclic hydrogen-charging whilst recording magnetic data using the SQUID magnetometer.

3.2.5 Chronoamperometry - Potential-controlled dealloying

Chronoamperometry (CA) involves the application of one or multiple potential-steps to the working electrode, while current is recorded as a function of time. The current density induced by such a potential step decays to zero with a time dependence of $t^{-\frac{1}{2}}$ for diffusion-controlled simple redox reaction, as predicted by the Cottrell equation[115]. In contrast to cyclic voltammetry, chronoamperometry allows studying a single, specific chemical reaction from a kinetic point of view. In this thesis chronoamperometry is used for two different purposes: On the one hand, a CA procedure is used for the standard potentiostatically-controlled dealloying (PCD) synthesis of npPd(Co), while, on the other hand, it is used to charge npPd(Co) samples with hydrogen to a fixed concentration for magnetic measurements. A typical PCD procedure for dealloying a $Co_{75}Pd_{25}$ alloy in 0.1 M H_2SO_4 at room temperature using a dealloying voltage U_D=0.55 V is shown in Fig.3.3. Dealloying was stopped at a residual current I_R=100 μA. Gradually decaying currents with time are typical for the dealloying process, where current density is related to the less noble atom fraction on the surface. The total magnitude of the current depends on the sample size. For the preparation of PCD+T samples, an annealing treatment was performed in a vacuum furnace after the dealloying process.

3.2.6 Chronopotentiometry - Current-controlled dealloying

In analogy to the chronoamperometry procedure in the previous section, a chronopotentiometry (CP) measurement is the application of one or multiple current steps to the working electrode, while recording the applied potential necessary to sustain this constant current flow.
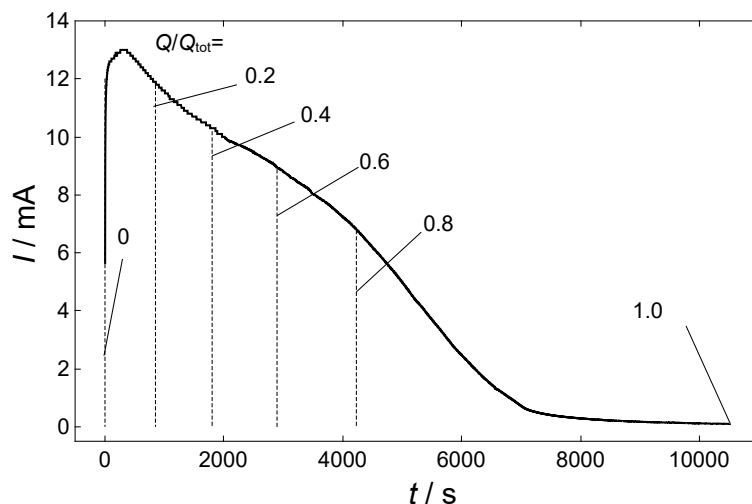
Figure 3.3: Current as a function of time for a typical potential-controlled electrochemical dealloying experiment of $Co_{75}Pd_{25}$, which is referred to as PCD in this thesis. Dealloying was conducted in 0.1 M H_2SO_4 at a potential U_D=0.55 V at room temperature. Charge-controlled dealloying samples were prepared at relative charges values Q/Q_{tot} as indicated in the plot.

In this thesis, a CP procedure was utilised for the galvanodynamically-controlled dealloying (GCD) variation[121], which allows controlling the residual Co-content x in $npPd_{1-x}Co_x$. Thereby, a typical PCD dealloying curve is discretised into four steps of constant current (see Fig. 4.20). The nominal Co dissolution charge Q_{tot}, calculated via Faraday's law (see Eq. 3.1), was distributed on the four steps as follows: 0.32 Q_{tot} at I=2 mA, 0.43 Q_{tot} at I=1 mA, 0.22 Q_{tot} at I=0.5 mA, and 0.03 Q_{tot} at I=0.1 mA. This distribution of charge over the four steps is empirically selected to resemble the typical decay in PCD. To gain control over the residual Co content in the dealloyed nanoporous sample, the duration of the second etching step (1 mA) was lowered by a fixed time to retain a certain amount of Co $x_{Co,nom}$ corresponding to a certain residual Co charge.

3.2.7 Coulometry - Charge-controlled dealloying

Coulometry is the direct measurement of charge in an electrochemical measurement, either via the continuous integration of current flow or the electronic equivalent using the built-in integrator circuit in the potentiostat. This method is particularly attractive for studying the dealloying progress, as charge relates directly to the mass of dissolved Co via Faraday's law (Eq. 3.1). In this thesis potentiostatic coulometry was used to study dealloying progress at certain amounts of relative charge Q/Q_{tot} consumed. Relative charge values used for

dealloying studies in this thesis are indicated in the typical PCD dealloying current curve for $Co_{75}Pd_{25}$ dealloying in Fig. 3.3. Values of Q/Q_{tot} correspond to the nominally removed Co fraction. As direct comparability with *in situ* dealloying measurements in the SQUID magnetometer is intended, an analogous Ag/AgCl wire quasi-reference electrode was used for QCD dealloying. Preparation of homemade Ag/AgCl wires is described in Sec.3.2.2.

3.2.8 Electrochemical impedance spectroscopy

Electrochemical impedance spectroscopy (EIS) allows studying processes at the electrode-electrolyte interface in a broad frequency range. In the case of nanoporous metals, such experiments yield information about pore size and geometry, as well as specific surface area, which is related to the measured capacitance.

The EIS setup used here builds upon the basic three-electrode setup for electrochemical measurements. A npPd(Co) sample (U_D=0.55 V; I_R=100μA) served as working electrode, while a coiled Pt wire was used as counter electrode. A 1 μF capacitance was placed in parallel to the commercial Ag/AgCl (3M KCl - Metrohm) reference electrode in the electrolyte, to avoid a high-frequency contribution stemming from the reference electrode. A 0.01 M concentration solution of perchloric acid $HClO_4$ diluted from 1 M $HClO_4$ (Honeywell/Fluka, 1.0N) and high-purity water (Roth, ROTIPURAN®, p.a.) was the preferred electrolyte. Three scans of cyclic voltammetry (0.1 mVs^{-1} between -0.3 V and 1.1 V) were applied as a pre-treatment prior to recording the EIS spectra to remove eventual oxides emerging in the dealloying process. For analysis, the obtained impedance spectrum is fitted with an equivalent circuit by the impedance data analysis tool implemented in the NOVA software.

3.3 Alloy preparation

The precursor alloys for dealloying were melted from Pd granules (AlfaAesar, 99.95%), Co slugs (AlfaAesar, 99.95%) to obtain $Co_{75}Pd_{25}$ using an arc melter (Edmund Bühler MAM1). The arc plasma is ignited between a water-cooled copper ground plate and a tungsten tip. After several steps of evacuating the sample chamber and purging it with Ar gas, a titanium getter was melted first to bind residual oxygen gas. $Co_{75}Pd_{25}$ alloys obtained by

arc-melting were heat-treated at 900°C for 12 hours in a vacuum furnace at 10^{-6} mbar for homogenisation. After further heat treatment for 1 hour at 900°C in Ar atmosphere, the alloy was quenched in water. Natural oxide on the surface after quenching was abraded mechanically. The CoPd phase diagram shows complete miscibility at elevated temperatures, but at high Co concentrations a hcp Co phase can form[122]. The rapid quenching step stabilises the homogeneous single-phase fcc alloy at room temperature, which is a requirement for dealloying precursors. For further processing, the alloy was rolled to a thickness of 250-270 μm, ground and polished. Homogeneity of the alloy foil was confirmed via XRD measurements. Specimen were directly cut from the alloy foil and contacted with Au wires for electrochemical dealloying. Typical sample sizes for measurements in the SQUID magnetometer were 2×2 mm² for *in situ* dealloying and 3×4 mm² for nanoporous samples for *in situ* tuning tests.

3.4   SQUID magnetometry

This thesis is focused on the variation of magnetic properties of Pd-based systems upon electrochemical bias, which requires a method to detect these variations accurately. SQUID (Superconducting Quantum Interference Device) magnetometry is an ideal method to study the magnetic properties of various magnetic materials, due to the possibility to measure a wide range of magnetic moments (about 10^{-8} to 2 emu[123], or 10^{12} to 2·10^{20} μ_{B}, equivalently). In contrast to other techniques based on MOKE (magneto-optical Kerr effect) or AHE (anomalous Hall effect) measurements, SQUID magnetometry suffers the disadvantage of comparably low speed ($\sim$20 s for single-point measurements), while it allows the determination of absolute – instead of relative – changes in the magnetisation. As electrochemical reactions also suffer intrinsic limitations in speed (typically by ion diffusion in the electrolyte or reaction rates on the electrode surface), the SQUID magnetometry timescale is sufficient for a great variety of electrochemical reactions. Absolute values of magnetic moments (in emu or A m²) from SQUID magnetometry have an additional benefit for magneto-ionic systems: In combination with electrochemical charge they allow the calculation of magnetisation changes on the scale of μ_{B}/atom, which contains valuable information about the chemical reactions involved in the magnetism changes and the underlying magneto-ionic mechanism.

Magnetic measurements in this work were performed using a MPMS-XL-7 (Quantum Design) SQUID magnetometer at the Institute of Physics (University of Graz) in close collaboration with Prof. Heinz Krenn. This specific instrument is equipped with a superconducting pick-up coil arranged in a second-order gradiometer configuration, which is inductively coupled to the SQUID sensor, as illustrated in Fig. 3.4.
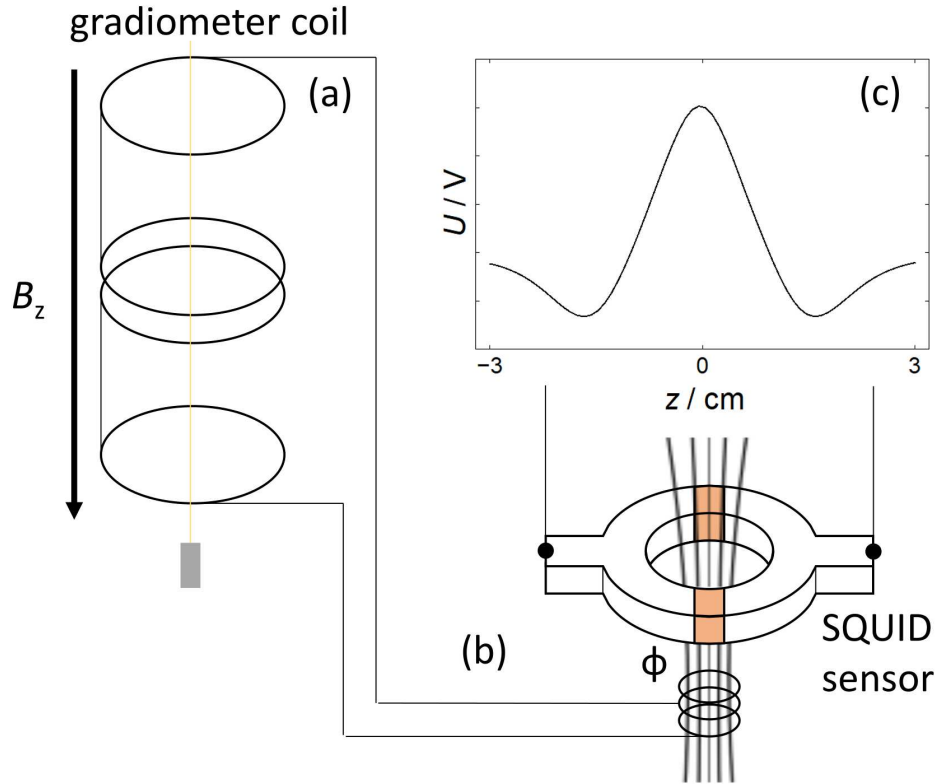

Figure 3.4: Working principle of a SQUID magnetometer: (a) The sample is moved through the superconducting gradiometer coil in the sample chamber, where an external field B_z can be applied in the direction of movement. (b) The flux change ϕ through the gradiometer coils is inductively transferred to the SQUID sensor, which consists of two Josephson junctions in a superconducting ring. (c) The SQUID sensor converts flux changes into a voltage output U, from which the absolute magnetic moment is obtained via a fitting procedure.

A superconducting magnet encompasses the gradiometer coil allowing the applications of a field in the range between -7 T and 7 T. All superconducting components are cooled in a liquid helium dewar. The sample chamber was operated in a He atmosphere of a few mbar at temperatures between T=4.2 K and T=300 K, the precise value of T is stated explicitly for all samples in the text. Once a (magnetised) sample is pulled through the pick-up coils, the magnetic flux through the superconducting detection loop changes, as does the flux through the SQUID sensor (Fig. 3.4(b)). For increased sensitivity, the SQUID detector is shielded in a

superconducting housing. The SQUID output electronics produces a voltage, which is strictly proportional to the current flow induced in the SQUID sensor[123] and also the magnetic moment of the sample. By fitting the voltage output as a function of distance (Fig. 3.4(c)) with the analytical solution of magnetic flux of a point dipole moved through the gradiometer coil[124], absolute values of magnetic moment m can be obtained. For sample sizes below 2 cm the SQUID response is qualitatively of the same form as a magnetic dipole[125]. For typical sample lengths < 4mm, the error of the moment calculated from the standardised dipole fits calculated in the MultiVu software is smaller than 3%[125]. Absolute magnetic moments m in this thesis are given in emu (1 emu=10^{-3}A m^2), emu g^{-1} (total sample mass), or μ_B/atom (1 μ_B=9.27$\cdot 10^{-21}$ emu). Relative changes in magnetisation are always given as the percentual increase in M from a baseline magnetisation M_0, which is the minimum magnetisation in the cycling experiment.

3.5   Compositional analysis

3.5.1   Scanning electron microscopy

Scanning electron micrographs for nanoporous samples were recorded by Dr. Manfred Nacht-nebel at the Institute of Electron Microscopy and Nanoanalysis at TU Graz. A Zeiss Sigma 300 VP (Variable Pressure) scanning electron microscope (SEM) was used for the determination of Co concentrations via EDS. This device is equipped with an Oxford X-max 80 energy-dispersive X-ray (EDS) spectrometer system. Reliable quantification of EDS spectra is assured via regular calibration of the EDS system. Data analysis was performed using the Aztec software (Oxford). All EDS spectra from SEM images presented in this work were recorded using the same measurement parameters (electron energy, acquisition time, etc.) to enable optimal comparability. To determine an estimation of the electron beam penetration depth and the EDS signal origin in the specimen, the simulation tool CASINO (Monte Carlo simulation of electron trajectory in solids) was used[126].

3.5.2   Transmission electron microscopy

Transmission electron micrographs were acquired by Dr. Mihaela Albu at the Institute of Electron Microscopy and Nanoanalysis at TU Graz. For scanning transmission electron microscopy TEM (STEM) a probe corrected FEI Titan G2 60–300 (S/TEM) microscope with an X-FEG Schottky field-emission electron source operated at 300 kV (150 pA current, beam diameter of 1Å) was used. Specimen for chemical analysis were pulverised mechanically to a powder, which was investigated on a Cu grid. For high-resolution images of dealloyed structures, the sample was embedded in resin and thinned via ion milling to TEM lamellas, which were cut in depth from the sample surface.

The microscope was equipped with a FEI Super-X detector (Chemi-STEM technology), consisting of four individual silicon drift detectors[127] and a Dual EELS - Gatan Imaging Filter (GIF) Quantum[128]. High Angular Annular Dark Field (HAADF) and Annular Dark Field (ADF) detectors were used for imaging. Chemical analysis via X-ray spectroscopy (EDS) used the spectrum image technique, quantification was based on the k-factor method[129]. Oxygen was detected via EDS analysis, which has not been included in the quantitative analysis of the ligament composition, but characterised separately via Raman spectroscopy.

3.5.3   Raman spectroscopy

Raman spectroscopy can be used to detect vibrational modes in matter via the inelastic scattering of light. Vibrational modes can be associated with certain types of chemical bonds, thus enabling chemical analysis. Pure metals cannot be detected in Raman spectroscopy, but metal oxides and hydroxides do typically show Raman spectra. For dealloyed metals surface oxides evolving in the dealloying process or during chemical post-treatment can be characterised in such experiments.

Raman spectroscopy was carried out by Dr. Harald Fitzek at the Institute of Electron Microscopy and Nanoanalysis at TU Graz. A LabRAM HR 800 spectrometer combined with an Olympus BX41 microscope and a 50x Olympus LMPlanFLN (NA=0.5) objective lens were used. With the given grating/slit setup (300 lines/mm; 200 μm) the spectral (pixel) resolution is about 4.2 cm^{-1}. In addition, the DuoScan System was applied to continuously

scan the laser spot over a 25×25 μm area. For *ex situ* measurements on as-dealloyed npPd(Co) (U_D=0.7 V; I_R=100μA) a laser wavelength of 473 nm (6 mW) with an acquisition time of 30 s (2-fold accumulations) was used.

For Co-rich GCD-prepared npPd$_{85}$Co$_{15}$ we performed Raman spectroscopy measurements using an *in situ* electrochemical cell setup to find eventual oxide-related changes on the surface, which could be relevant for magneto-ionics. A specimen with the highest Co-content was selected for *in situ* Raman spectroscopy, as eventual effects related to Co oxides were expected to be the most prominent. A Petri dish with a 3 cm circular opening on the top side was used as electrolyte compartment for *in situ* Raman measurements, with side feedthroughs for the typical three-electrode setup. The objective lens was passed through the top opening and placed at a working distance of $\sim$5 mm from the electrolyte surface ($\sim$10 mm from the sample in total). The sample was fixed on a microscopy slide with electrolyte-resistant epoxy, contacted with an Au-wire and centred under the objective lens. A high surface area carbon cloth served as counter electrode, while an Au-wire was used as reference electrode, adapting a similar electrode configuration as for *in situ* SQUID magnetometry (Sec. 3.2.2) to directly compare experimental findings. 1 M KOH aqueous solution was used as the electrolyte, electrochemistry was controlled using an Autolab PGSTAT204 potentiostat. For the *in situ* measurements a laser wavelength of 473 nm (25 mW) with an acquisition time of 20 s (2-fold accumulations) was used.

3.5.4   X-ray photoelectron spectroscopy

X-ray photoelectron spectroscopy (XPS) measures binding energies of near-core electrons, which are emitted via photoelectric X-ray excitation. These binding energies are fingerprints for the elements included in the specimen, while small shifts (in the order of eV) of the binding energies give information about atomic oxidation states and thus chemical environment. Even more than EDS, XPS is an extremely surface-sensitive technique typically probing only a few nanometres in depth. Similar to the Raman spectroscopy method described above, XPS measurements were used to identify eventual oxides on the surface of Co-rich GCD-prepared npPd$_{85}$Co$_{15}$. XPS was measured by Prof. Martin Sterrer at the Institute of Physics, University of Graz. To avoid oxidation effects arising from contact with air, sample preparation for XPS

was conducted in an Ar inert gas chamber. Electrochemical preparation otherwise followed the same routine as for *in situ* Raman spectroscopy using an analogous cell setup. XPS measurements were conducted in a vacuum chamber operated at~10^{-8} mbar, which was equipped with an X-ray gun (XR 50, SPECS) with an aluminium anode and a hemispherical analyser (PHOIBOS 150, SPECS).

3.5.5   X-ray fluorescence

X-ray fluorescence (XRF) measurements detect characteristic fluorescent photons upon X-ray excitation. In contrast to XPS measurements, XRF probes a larger fraction of the specimen in depth. An advantage of the XRF technique is the possibility to measure under ambient air conditions. All XRF-measurements in this thesis were conducted with a Panalytical Epsilon 1 XRF analyser equipped with an Ag anode at the Institute of Solid State Physics at TU Graz. A standardless analysis approach was selected for the calculation of the sample composition from the fluorescence intensities. Only Pd and Co peaks were included in the analysis, while peaks associated with elements originating from the Mylar® foil sample holder were explicitly excluded. The limited sample sizes, which did not cover the whole sample holder, might lead to minor deviations from the actual composition.

3.6   Kinetic Monte Carlo simulations

Kinetic Monte Carlo (KMC) simulations allow the computational mimicking of systems on mesoscopic time and length scales[130]. As KMC works on the basis of rate equations, it is possible to relate simulation results to real timescales, in contrast to, e.g., conventional Monte Carlo techniques. KMC simulations have found application for vacancy diffusion[131], dislocation mobility[132], or surface catalytic processes[133]. Since Erlebacher[56] managed to model the dealloying process on the basis of two simple rate equations for surface diffusion and dissolution of the less noble component, KMC has become a standard simulation tool for dealloyed systems[69,134–139]. Here, the implementation of this algorithm by Krekeler et al.[69] was followed, who shifted focus on the less noble residues in the nanoporous structure. A lattice

with periodic boundary conditions in two directions was created to simulate unidirectional dealloying in a $50 \times 50 \times 50$ atoms cube with a fcc lattice. The rate equations can be written as

$$k_{\text{diff}} = \nu_{\text{D}} \exp\left(\frac{nE_{\text{b}}}{k_{\text{b}}T}\right) \tag{3.2}$$

and

$$k_{\text{diss}} = \nu_{\text{E}} \exp\left(\frac{nE_{\text{b}} + e\Phi}{k_{\text{b}}T}\right), \tag{3.3}$$

where k_{diff} is the diffusion rate in s^{-1}, ν_{D} is the Debye frequency for lattice vibrations (set as 10^{13} s^{-1}), n is the coordination number of the respective atom site, E_{b} is the single-bond binding energy, k_{diss} is the dissolution rate in s^{-1}, ν_{E} is the attempt frequency for dissolution (set as 10^{4} s^{-1}), Φ is the parametrised electrode potential, T is the temperature in K, while e and k_{b} are the usual physical constants. While diffusion is permitted for both types of atoms in the alloy, dissolution is limited to the less noble component. In order to apply the simulation to the $\text{Co}_{75}\text{Pd}_{25}$ alloy system, the homogeneous binding energy between all alloy atoms was scaled on the basis of melting point data (E_{b}=-0.15 eV for $\text{Ag}_{75}\text{Au}_{25}$[69], E_{b}=-0.18 eV for $\text{Co}_{75}\text{Pd}_{25}$). Rate parameters were adopted from Krekeler et al.[69]. The number of simulation steps and the dealloying potential Φ are stated in the text for each simulation specifically. Our KMC simulation of the dealloying process was implemented in MATLAB, while the open-source software OVITO[140] was used for the visualisation of the generated structures.

A single step for the overall algorithm of the KMC simulation for the dealloying process is sketched in Fig. 3.5. Diffusion and dissolution rates are calculated using Eq. 3.2 and 3.3 for all atoms at the start. Note that both types of rates, k_{diff} and k_{diss}, decrease with increasing coordination number, i.e., diffusion and dissolution of atoms with more neighbouring atoms becomes less likely. In the simulation, a random number q is generated in the following to select an event (either diffusion or dissolution) from the sum of all rates k_{tot}, as illustrated by the boxes in Fig. 3.5. The probability for an event to be selected scales with the rate k_{i} and the total number of atoms accessible for this event N_{i}. After an event has been chosen, a single atom eligible for that event is again randomly picked and the corresponding event is executed for that single atom on the lattice, as illustrated in Fig. 3.5 using red and golden spheres. As coordination numbers change in the local environment of that atom,

rate constants of the surrounding are updated after every event. Typically, $x=10^5$ to 10^8 consecutive steps are performed in a loop, with the rate constants being updated after each step.

1) define rate constants k_i

2) calculate sum of all rates $k_{tot} = \sum_i k_i N_i$

3) Generate random number $q \in [0,1]$

4) pick process corresponding to $q \cdot k_{tot}$

$$k_{tot}$$

| $k_1 N_1$ | $k_2 N_2$ | $k_3 N_3$ | | ... | $k_i N_i$ |

5) execute correct event on lattice

dissolution   diffusion
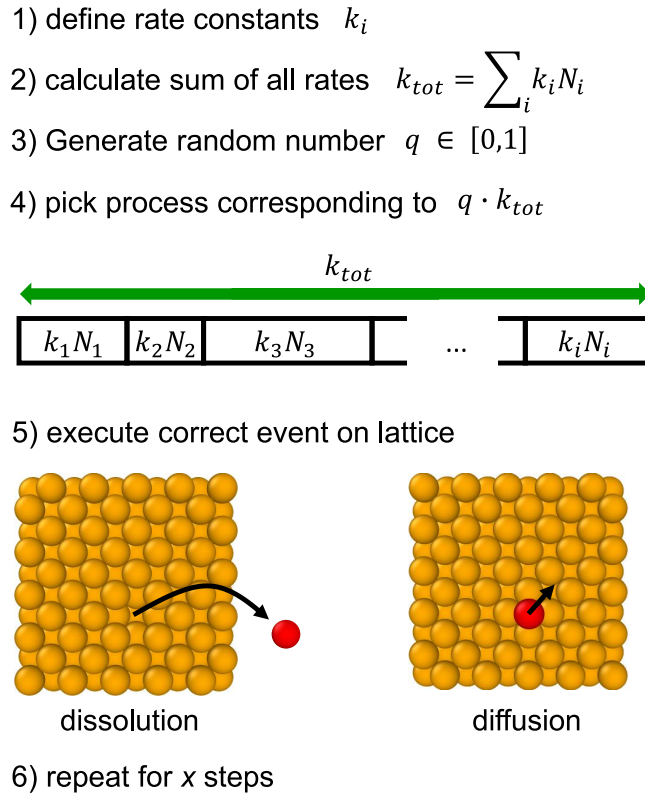
6) repeat for *x* steps

Figure 3.5: Schematic of a single step in the KMC algorithm for the dealloying simulation: 1) Rate constants are calculated according to Eq. 3.2 and 3.3. 2), 3) and 4) A random number q selects the process to be executed from the total sum of all rates k_{tot}, with the probability being proportional to both rate k_i and the number of eligible atoms for the respective process N_i. 5) The correct event is executed on the virtual lattice. Dissolution is limited to surface atoms of the less noble element, while surface diffusion is possible for all surface atoms. 6) The whole process is repeated for x steps.

CHAPTER 4

Results

4.1 From CoPd alloy to nanoporous Pd(Co) - *in situ* and *ex situ* dealloying techniques

In this chapter the dealloying process from a $Co_{75}Pd_{25}$ alloy to fully nanoporous Pd(Co) is investigated using *in situ* and *ex situ* techniques. Major parts of this chapter have been previously published in Ref. 46. Section 4.1.1 presents *ex situ* X-ray diffraction (XRD) measurements for npPdCo for discrete steps of relative charge Q/Q_{tot} upon charge-controlled dealloying (QCD). Novel *in situ* dealloying magnetometry experiments developed as part of this thesis constitute the core part of this chapter in Sec. 4.1.2. An *in situ* dealloying resistometry measurement during potential-controlled dealloying (PCD) is introduced in Sec.4.1.3, while a previously unpublished *in situ* dilatometry measurement is shown in Sec. 4.1.4. Changes in concentrations of surface-near Co upon dealloying were measured via energy-dispersive X-ray spectroscopy (EDS) from large scale scanning electron microscopy (SEM) images, which are both presented in Sec.4.1.5, in combination with transmission electron micrographs (TEM) of the nanoporous structure at two different points of the dealloying. As a complementary computational technique kinetic Monte Carlo (KMC) simulations of the dealloying process for $Co_{75}Pd_{25}$ are included in Sec. 4.1.6.
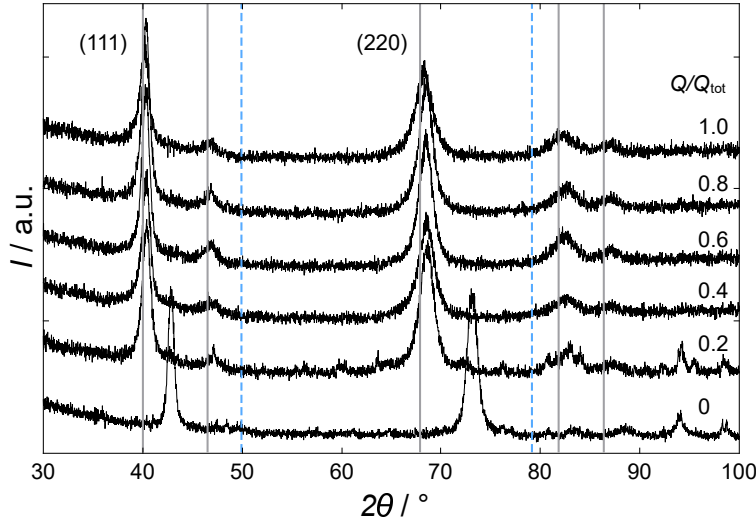
Figure 4.1: X-ray diffraction patterns upon QCD dealloying of a $Co_{75}Pd_{25}$ alloy at U_D=0.55 V (vs. Ag/AgCl sat.KCl) in the range between 2θ=30° and 2θ=100°. Relative charge flow for QCD dealloying is given on the right of the respective pattern. $Q/Q_{tot} = 0$ represents the initial alloy, while $Q/Q_{tot} = 1$ corresponds to the completely dealloyed nanoporous structure. Diffractions patterns are vertically shifted to enable comparison. Reference lines for fcc Pd (PDF88-2335) and fcc Co (PDF-88-2325) are added in grey and dashed blue, respectively. Crystal orientations for the main peaks are labelled with their corresponding Miller indices. Reprinted from Ref. 46.

For the sake of comparability, all *in situ* dealloying techniques are depicted in a common plot (Fig.4.3). As a measure for dealloying progress, relative charge values were used on the abscissa for this graph. Relative charge flow Q/Q_{tot} uses the total nominal charge Q_{tot}, which is calculated from the nominal Co content in the sample via Faraday's law (Eq. 3.1). In contrast to dealloying time, which depends on the alloy fraction exposed to the electrolyte and sample mass, Q/Q_{tot} provides a more objective measure, as the same stages of dealloying are monitored qualitatively.

4.1.1 X-ray diffraction

X-ray diffraction (XRD) during dealloying does not only give information about lattice constants, but also contains information about grain size and lattice stress during dealloying. Here, XRD-pattern were recorded after QCD stopped at different relative charge values, $Q/Q_{tot} = 0, 0.2, 0.4, 0.6, 0.8, 1.0$. The resulting XRD patterns are shown in Fig. 4.1. Grey vertical lines represent reference data for Pd (PDF88-2335) and blue vertical dashed lines give reference peak positions of Co (PDF88-2325).

Diffraction peaks are markedly shifted to lower angles 2θ in the early stage of the dealloying process (from $Q/Q_{tot} = 0$ to 0.2), corresponding to an increasing lattice constant. This is in accordance with the removal of Co from the lattice during dealloying. Interestingly, in the intermediate stages (from $Q/Q_{tot} = 0.2$ to 0.8) no further peak shift was observed. This points towards the formation of a single crystallographic phase with a constant composition already in the beginning of the dealloying process. At any dealloying stage, only peaks associated with either alloy or nanoporous Pd are observed, indicating that the underlying alloy backbone remains undetected in XRD for all dealloyed samples ($Q/Q_{tot} = 0.2$ to 1.0). In the last dealloying step from $Q/Q_{tot} = 0.8$ to 1.0 a slight shift towards the Pd reference lines occurs again, which indicates further removal of Co from the lattice at this point, i.e. Co dissolution from the already nanoporous lattice.

4.1.2 *In situ* magnetometry

Magnetic properties of dealloyed materials have already been studied in the literature for nanoporous Ni prepared from MnNi[65,141] and CuNi[142] alloys. In these systems, the ferromagnetic component Ni is the more noble element of the alloy, which rearranges into a nanoporous Ni structure upon removal of the less noble compound. For a CoPd alloy, as studied in this thesis, the situation is different as the ferromagnetic component Co is the less noble element, which is removed during dealloying. While the referenced nanoporous Ni structures are ferromagnetic in their final state, the $Co_{75}Pd_{25}$ alloy is ferromagnetic[82] prior dealloying. In this section, it is demonstrated how magnetic properties of a ferromagnetic base alloy change during dealloying, which is investigated *in situ* for the first time using SQUID magnetometry.

Using the electrochemical cell setup described in Sec. 3.2.2, the magnetic moment and coercivity were tracked during the entire transition from alloy to fully nanoporous structure. Changes in coercivity H_C and hysteresis squareness M_r/M_S during dealloying of a $Co_{75}Pd_{25}$ alloy are shown in Fig. 4.2 (a) as a function of relative charge Q/Q_{tot}. As expected, the $Co_{75}Pd_{25}$ base alloy exhibited soft ferromagnetic behaviour with a coercivity of H_C=38.5 Oe. This is also demonstrated by the *m-H* curve from -3 kOe to 3 kOe in Fig. 4.2 (b), where a small hysteresis becomes apparent in the inset. During dealloying it was found that both

H_C and M_r/M_S increased slightly for relative charge values Q/Q_{tot} <0.6. The maximum in coercivity is reached at Q/Q_{tot}=0.6 when H_C=44.5 Oe, while the maximum in hysteresis squareness of $M_r/M_S \approx$0.14 is reached at a higher relative charge of Q/Q_{tot}=0.7. Both H_C and M_r/M_S decrease sharply at higher relative charge values Q/Q_{tot} >0.7 until they almost vanish in the final nanoporous state at Q/Q_{tot}=1. The full m-H curve between -3 kOe and 3 kOe for the final npPd(Co) structure is shown in Fig. 4.2 (c). A small residual coercivity of H_C=5.5 Oe and a residual squareness of $M_r/M_S \approx$0.02 were detected.

It has been shown in the scientific literature that magnetic fields can alter the nanoporous structure obtained by the dealloying process. Surface rearrangement of Ni atoms during dealloying of an AlNi alloy was shown to be influenced by external fields[143], leading to field-dependent structural sizes. Even dealloying of non-magnetic base alloys such as AlAu in external magnetic fields[144], leads to different nanoporous morphologies, as a result of magnetic-field dependent corrosion rates[145]. Here, the dealloying step was always conducted without an applied external field.

As an additional magnetic key quantity, the total magnetic moment m was also recorded during dealloying of $Co_{75}Pd_{25}$ at a constant field of 5000 Oe. A graph depicting m as a function of relative charge Q/Q_{tot} is shown in Fig. 4.3 (a). For the sake of comparability, complementary *in situ* resistance and strain measurements, which will be introduced in the next section, are plotted in the same graph in (b) and (c). Magnetic moment m, as an extensive thermodynamic property, scales with the total amount of alloy. For the initial alloy mass of m=4.28 mg a moment m=0.505 emu was detected corresponding to a moment value of 1.95μ_B per Co atom as calculated from alloy mass.[d] Upon dealloying m decreases linearly almost over the full range of Q/Q_{tot}, with only a reduced slope at Q/Q_{tot} >0.95. This is confirmed by the linear fit up to Q/Q_{tot}=0.95 as shown in Fig. 4.3 (a) in red, which yielded excellent agreement with the data points. From the total electrical charge Q an average magnetic moment $\bar{m}$ per dissolved Co atom can be calculated using a variation of Faraday's law (Eq. 3.1) as:

$$\bar{m} = \frac{m}{N_{Co}} = \frac{mze}{Q} = 0.0589 \text{ emu/As} = 2.03 \ \mu_B/\text{atom}, \qquad (4.1)$$

---

[d]For a comparison of magnetic moments with literature data the reader is referred to the discussion (Sec. 5.1).
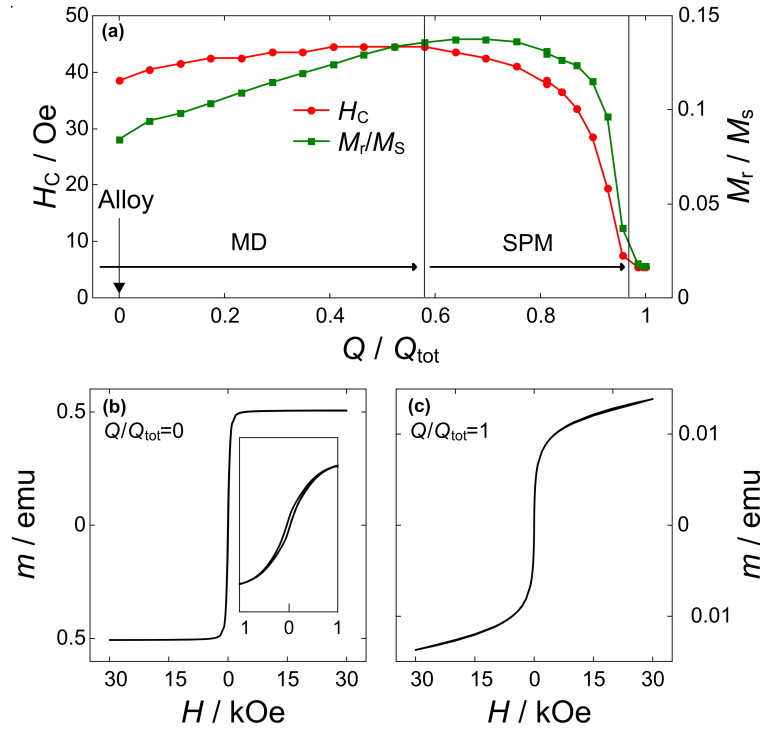
Figure 4.2: Evolution of coercivity H_C and hysteresis squareness M_r/M_S upon $Co_{75}Pd_{25}$ PCD dealloying monitored using *in situ* SQUID magnetometry: (a) Coercivity H_C (red) and hysteresis squareness M_r/M_S (green) plotted as a function of relative charge Q/Q_{tot}. Coercivity H_C, remanence M_r and saturation M_S were obtained from individual M-H curves measured after each dealloying step. Uncertainty values of 1.5 Oe for the coercivity are not represented in the plot. A transition from predominantly multi-domain (MD) behaviour to emergent superparamagnetism (SPM) is indicated by the arrows. (b) M-H curve for the ferromagnetic $Co_{75}Pd_{25}$ alloy ($Q/Q_{tot}=0$). The hysteretic nature of the magnetisation curve becomes apparent in the inset. M-H curve for superparamagnetic npPd(Co) ($Q/Q_{tot}=1$). Note the about 50 times large y-axis scaling in (b) compared to (c). Reprinted from Ref. 46.

where N_{Co} is the number of dissolved Co atoms (corresponding to the number of Co ions in solution), m is the magnetic moment from Fig. 4.3 (a), z is the valency of Co ions which equals 2, e is the elementary charge, and Q is the total charge during dealloying (see Sec. 3.1). This calculation of the magnetic moment per dissolved Co atoms neglects a contribution of dissolved Co^{2+}-ions in aqueous solutions to the magnetic moment. The total susceptibility of ions in solution can be estimated by the concentration-weighed solvent and ionic susceptibilities according to Wiedemann's law[146]. For Co^{2+} in aqueous solution, a transition from diamagnetic behaviour of pure water to paramagnetic behaviour is expected at a concentration between 0.01 M and 0.1 M[146]. Estimating the local Co^{2+} concentration from charge and electrolyte volume close to the sample in our electrochemical cells ($V \sim 0.5$ mL), yields a concentration of 0.09 M/L. Although one cannot define precisely whether the solutions

contributes with a diamagnetic or paramagnetic signal to the measured magnetic moment, the low absolute concentrations indicate low susceptibility in either case. Furthermore, once diffusion has homogenised the Co^{2+} across the whole cell volume, the electrolyte can no longer be detected in the SQUID due to the elongated nature of the cells and the unchanging electrolyte susceptibility when moving through the SQUID pickup coils.
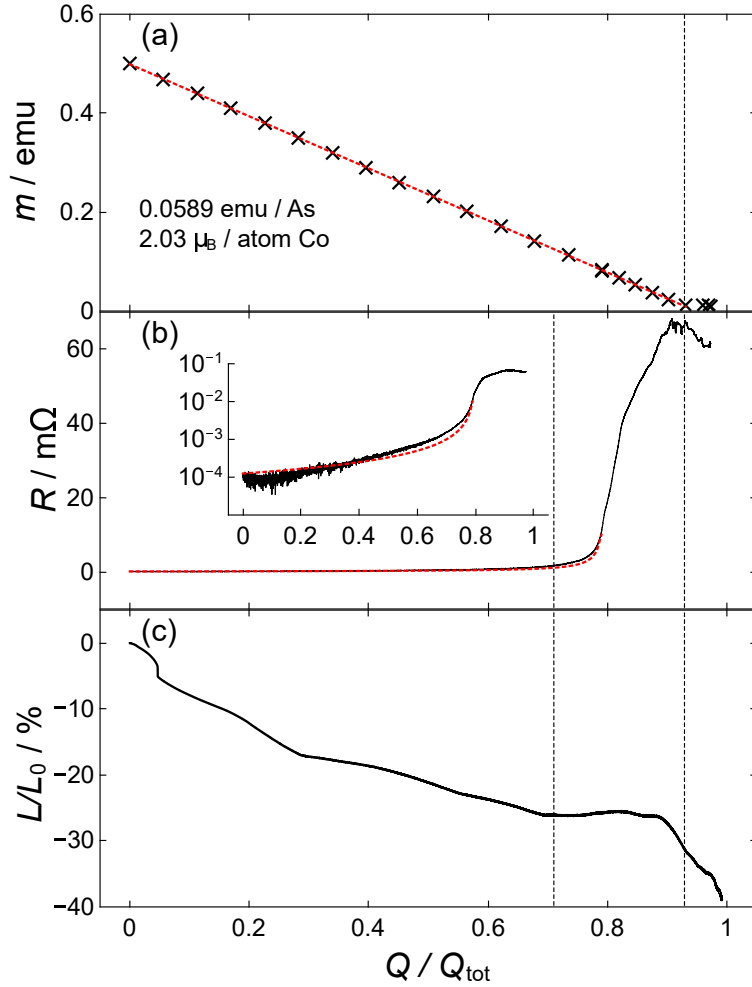

Figure 4.3: Property evolution during dealloying $Co_{75}Pd_{25}$ monitored using *in situ* techniques: (a) Magnetic moment m at a field of 0.5 T plotted as a function of relative charge Q/Q_{tot}. Data points were fitted with the line in dashed red between Q/Q_{tot}=0 and Q/Q_{tot}=0.95. The slope of the fitted line in the m-Q-curve yields 0.0589 emu As^{-1}, out of which the corresponding moment per dissolved atom was calculated using Eq. 3.1 amounting 2.03 μ_B per atom. (b) Resistance R as a function of relative charge. The inset shows the same curve with a logarithmic scale. The red dashed curve is a fit to the data following equation 5.1. (c) Relative length changes $\Delta L/L_0$ as a function of relative charge Q/Q_{tot}. Vertical dashed lines serve as guides to the eye. Recreated from Ref. 46.

4.1.3 *In situ* resistometry

In the past, resistometry was already utilised successfully to investigate the dealloying process of AgAu and CuPt alloys *in situ* [74], when it was possible to discern different stages of the dealloying process ('primary' and 'secondary' dealloying) on the basis of resistance data. Here, simultaneous resistance measurements during dealloying of $Co_{75}Pd_{25}$ are presented, which have previously been included in Ref. 46.

Electrical resistance R for a $Co_{75}Pd_{25}$ dealloying experiment as a function of relative charge Q/Q_{tot} is shown in Fig. 4.3 (b). Large changes in the electrical resistance by three orders of magnitude from alloy ($Q/Q_{tot}=0$) to nanoporous structure ($Q/Q_{tot}=1$) are observed, which is similar to observations for AgAu and CuPt [74]. This effect has been attributed to a combination of porosity formation and surface oxidation [74]. In Fig. 4.3 (b) resistance increases drastically at $Q/Q_{tot} \approx 0.8$ by a factor of ≈ 10 followed by a levelling of the curve around $Q/Q_{tot} \approx 0.85$ and a subsequent decay for values of $Q/Q_{tot} > 0.9$.

4.1.4 *In situ* dilatometry

Volumetric shrinkage inevitably accompanies electrochemical dealloying, as the major fraction of atoms in the alloy is dissolved in the process. Dilatometry during dealloying of the AgAu alloy system has likely been the first *in situ* method used to study dealloying [147] after its discovery for the production of nanoporous metals [50]. Since then it has been adopted to other material systems, such as Au(Pt)Ag [73] or PdCu [70]. Here, we apply the *in situ* dilatometry method to the $Co_{75}Pd_{25}$ alloy system. Fig. 4.3 (c) shows the relative length changes $\Delta L/L_0$ upon *in situ* dilatometry during dealloying as a function of relative charge Q/Q_{tot}. Length decreases by $\sim$40% from alloy $Q/Q_{tot} = 0$ to fully nanoporous structure $Q/Q_{tot} = 1$, which is much larger compared to length changes below 10% in the literature for AgAu or CuPd. The decrease in length is non-monotonic with the steepest slope at $Q/Q_{tot} > 0.9$. A plateau is visible between $Q/Q_{tot} = 0.7$ and $Q/Q_{tot} = 0.9$, where length does not change at all. Relative changes in length of $\sim$40% were reproducible in several experiments, but it should be mentioned that the general behaviour of the curve could be quite different with samples showing partial increases in length at intermediate dealloying stages.
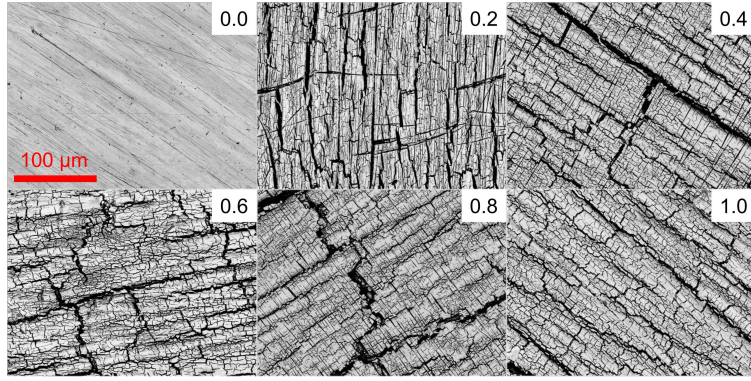
Figure 4.4: Large-scale electron micrographs of $Co_{75}Pd_{25}$ at different stages of dealloying. Relative charge values Q/Q_{tot} for all images are given in the top right corners, the scale bar in red corresponds to all images. Microcracks on the surface are visible for all stages of dealloying with $Q/Q_{tot} \geq 0.2$.

4.1.5 Microstructure and Co concentration

Cobalt concentration is of utmost importance for the magnetic properties of CoPd alloys. In homogeneous alloys already a small Co concentration of x_{Co}=0.1 at% is sufficient to turn the entire alloy ferromagnetic at low temperatures below T_C=7 K[82]. At room temperature, the alloy is ferromagnetic for Co concentrations larger than x_{Co}=10 at%[82]. During dealloying Co content from a $Co_{75}Pd_{25}$ alloy is gradually reduced until only a small residual Co fraction remains in the npPd(Co) structure. In order to track Co concentrations during dealloying, EDS elemental concentrations of Co were measured at different points of relative charge Q/Q_{tot}, averaging over areas from large scale SEM images with sizes of $\sim 200{\times}250$ μm^2. SEM micrographs are depicted in Fig. 4.4. Relative charge values are indicated in the top rights corners for all micrographs. Microcracks appear during dealloying for $Q/Q_{tot} \geq 0.2$. For the early dealloying stages, $Q/Q_{tot} = 0.2$ cracks seem to form primarily along scratches and grooves on the initial alloy surface $Q/Q_{tot} \geq 0.2$, which result from the grinding procedure. For later dealloying steps $Q/Q_{tot} > 0.2$ these initial microcracks branch out, leading to finer cracks on the surface.

Co concentrations x_{Co} measured via EDS for the different values of relative charge (dealloyed at U_D=0.55 V) are stated in Tab. 4.1. Only Pd and Co were used for quantification, uncertainties for concentration account for different local compositions at different sampling spots on the surface, but not the intrinsic uncertainty from EDS spectral deconvolution. Due to the limited penetration depth of electrons in SEM analysis, the concentrations from EDS
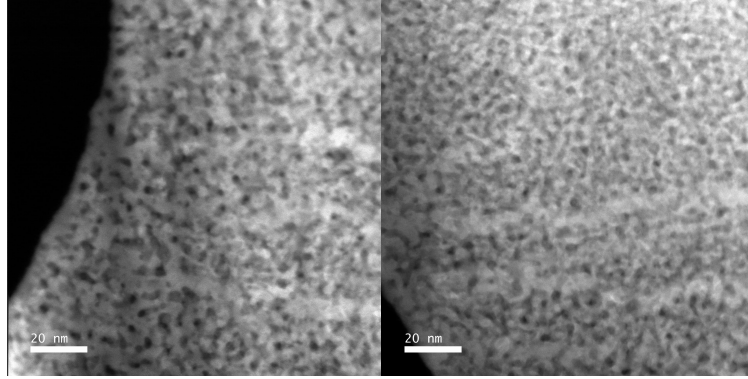
Figure 4.5: Transmission electron micrographs of npPd(Co) at two different stages of dealloying. Left: 600 s dealloying corresponding to $Q/Q_{tot} = 0.07$. Right: 4500 s dealloying corresponding to $Q/Q_{tot} = 0.55$.

analysis is also only representative for a limited depth. Electron trajectory simulations for solid $Co_{10}Pd_{90}$ alloys in this work yielded penetration depths up to 400 nm. The highest X-ray intensity for EDS arises from a depth of $\sim$100 nm, which might be slightly larger in reality due to the nanoporous nature of dealloyed samples. In Tab. 4.1 the detected Co concentration of $x_{Co} = 73.0 \pm 0.3\%$ for the alloy ($Q/Q_{tot} = 0$) is slightly lower than the nominal Co content of the alloy $x_{Co,nom}$=75%.

Table 4.1: Surface cobalt concentration during $Co_{75}Pd_{25}$ dealloying: Relative charge Q/Q_{tot} for different dealloying stages and corresponding cobalt concentrations x_{Co} determined from EDS spectra averaged over the areas shown in Fig. 4.4. The sampled depth is about 100 nm.

Q/Q_{tot}	x_{Co} / at%
0	73.0 ± 0.3
0.2	14.4 ± 0.5
0.4	13.7 ± 0.5
0.6	9.4 ± 0.4
0.8	10.4 ± 0.4
1.0	5.1 ± 0.1

To obtain information about nanoporosity during dealloying, two different dealloying states for a $Co_{75}Pd_{25}$ alloy (t=600 s and t=4500 s corresponding to $Q/Q_{tot} = 0.07$ and $Q/Q_{tot} = 0.55$) were investigated via TEM. Micrographs obtained in the TEM are shown in Fig.4.5. The nanoporous structure reached a depth of several μm from the surface after 600 s of dealloying. Pore sizes in the range between 3-5 nm were observed for $Q/Q_{tot} = 0.07$ (left image), which did not change significantly when dealloying was stopped after 4500 s at $Q/Q_{tot} = 0.55$ (right image). For this type of experiment an effectively higher corrosion potential than the
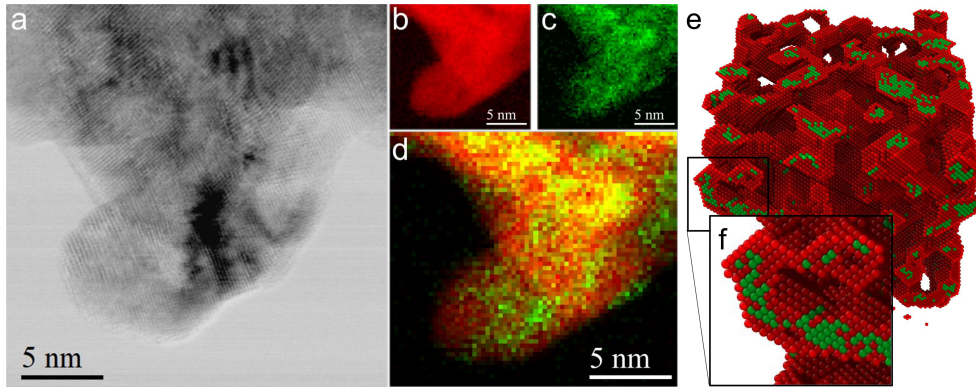
Figure 4.6: Nanostructure of npPd(Co): STEM/EDS micrographs of a npPd(Co) (U_D=0.7 V; I_R=0.1 mA) single ligament with an annular dark field (ADF) image at 300 kV in (a), elemental maps from EDS for Pd (red) and Co (green) in (b) and (c), and an enlarged, combined EDS elemental map in (d). The related KMC simulation for npPd(Co) (E_b=-0.18 eV, Φ=1.14 eV) is shown in (e), using the same color coding. Co-rich clusters in the simulation are enlarged in (f), which are also visible in the EDS maps in (d). (a) to (d) were adapted from Ref. 41.

nominally applied U_D=0.55 V is present, caused by the electrolyte exchange in a flow cell setup used for these dealloying experiments.

High-resolution STEM/EDS images of single ligaments of as-dealloyed npPd(Co) (U_D=0.7 V; I_R=0.1 mA) were recorded to determine Co-content and distribution on a smaller length scale in Fig. 4.6. Elemental maps reconstructed from EDS data for Pd and Co in a single npPd(Co) ligament in Fig. 4.6(a) are shown in Fig. 4.6b-c, with an enlarged superposition depicted in 4.6d. The most important finding from these STEM images is the inhomogeneous Co distribution on the ligament level. Co shows aggregations in discrete regions (Fig. 4.6d), which will be referred to as Co-rich clusters throughout this thesis. Pd atoms, on the contrary, are homogeneously distributed over the whole ligament volume. For npPd(Co) (U_D=0.7 V; I_R=0.1 mA) cluster sizes of 1.5 to 2.0 nm and a Co content between 14 and 20 at% were determined via STEM and EDS. EDS measurements might underestimate the Co-concentration in the clusters, as they are expected to lie well below layers of Pd atoms, indicated by the KMC simulation data in Fig. 4.6e and f. Details on the KMC simulation are stated in the next section. Simulations indicate the cluster composition to be closer to the composition of the original alloy, which is $Co_{75}Pd_{25}$ in the present case. The observed clustering of the residual element is a direct result of surface diffusion of both elemental components during dealloying, which has been studied in nanoporous Au(Ag) recently[69,148].
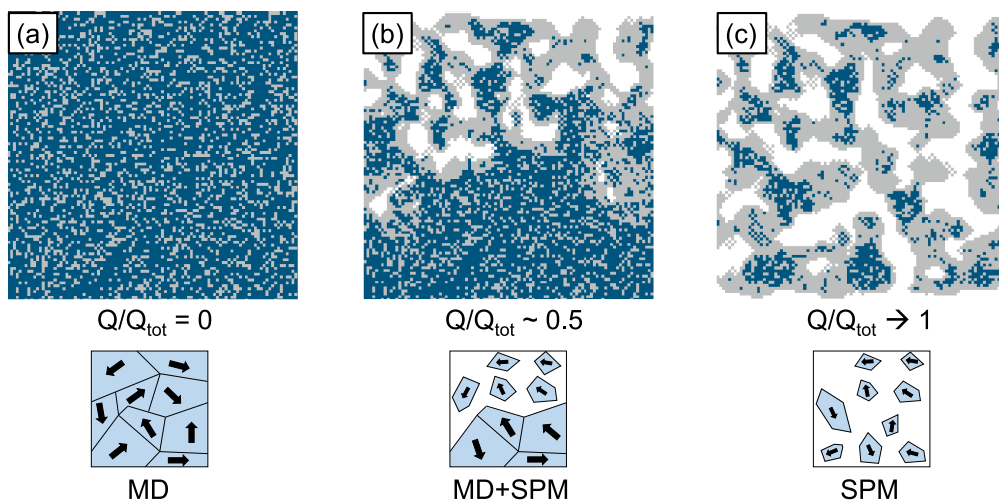
Figure 4.7: Two-dimensional cross-sectional snapshots from a KMC simulation of the CoPd dealloying process at different stages Q/Q_{tot}. Blue squares indicate Co, grey squares indicate Pd. Snapshots are shown for 0 (a), 1.8×10^6 (b), and 5.0×10^6 (c) dealloying simulation steps. Only etching from the top was allowed in the simulation, while the other faces of the simulated cube were connected via periodic boundary conditions. Note the presence of alloy residues close to the original alloy composition in the nanoporous structure (c). Sketches below the simulation snapshots relate to the magnetic property evolution during dealloying: The proposed transition from a multi-domain state (MD) to superparamagnetic behaviour (SPM) is discussed in Sec. 5.1. Reprinted from Ref. 46.

Note that ligament sizes ranging from 10 to 15 nm, as deduced from the annular dark field (ADF) images, e.g. in Fig. 4.6(a), are systematically larger than the values summarised in Sec. 4.2.4. This discrepancy arises most likely from the different dealloying parameters used (U_D=0.7 V here, compared to U_D=0.55 V in Sec. 4.2.4).

4.1.6 Kinetic Monte Carlo simulation

For the Kinetic Monte Carlo (KMC) simulation of the dealloying process a temperature of T=300 K, a parametrised electrode potential of Φ=1.14 eV, and a single-bond binding energy E_b=-0.18 eV were used to model dealloying for a $Co_{75}Pd_{25}$ alloy, which is the same composition as used in the experiments. Binding energy was scaled up from E_b=-0.15 eV for AgAu to E_b=-0.18 eV for CoPd on the basis of melting point data. Two-dimensional snapshots at different stages of the dealloying process (related to relative charge Q/Q_{tot}) are presented in Fig. 4.7.

The snapshots from the KMC simulation in Fig. 4.7 capture all the essential features of

the CoPd dealloying process qualitatively: A bicontinuous, nanoporous network with a characteristic pore and ligament size is generated directly behind the etch front in Fig. 4.7(b). A significant amount of Co is found in the final nanoporous structure (Fig. 4.7(c)) in clusters with a composition close to the original alloy. These clusters are crucial for the superparamagnetic properties of nanoporous Pd(Co) as elaborated in Sec. 4.3 and the magnetic property evolution during dealloying, which is discussed in Sec. 5.1.

4.2 Characterisation of nanoporous Pd

Here important intrinsic properties of nanoporous Pd prepared by dealloying will be presented. To gain information about the surface chemical composition, Raman spectroscopy measurements are shown in Sec. 4.2.1. Two different techniques were employed to measure the specific surface area of npPd(Co), namely double-layer capacitance measurements and nitrogen sorption isotherms, which are both shown in Sec. 4.2.2. Electrochemical impedance spectroscopy (EIS) for npPd(Co) also allow insights into pore structure and geometry, which is demonstrated in Sec. 4.2.3. EIS spectra were measured and interpreted by Philipp Brunner in his Master's project[149], which I had the pleasure to guide experimentally. Finally, the hydrogen storage capacity of npPd(Co) is explored by electrochemical methods, which is important regarding the hydrogen-driven magneto-ionic application of npPd(Co) in a later section (Sec. 4.4.2). The hydrogen storage measurements have already been part of Ref. 48.

4.2.1 Raman spectroscopy

A Raman spectrum of as dealloyed npPd(Co) (U_D=0.7 V; I_R=0.1 mA) recorded in ambient air is presented in Fig. 4.8. The most prominent lines were associated with fcc CoO (540 cm^{-1} [150]) and C (1350 cm^{-1} and 1600 cm^{-1} [151]). The two broad carbon lines stem from a poorly ordered[151] carbon species. The origin of carbon in the dealloying process remains unclear, as no obvious source of carbon can be determined in our setup. Contamination from a carbon cloth counter electrode, which is used for voltammetric cycling rather than dealloying experiments, might be one conceivable explanation. Interestingly, CoO was found on the surface of the as-dealloyed sample. The broad Raman peak at 540 cm^{-1} matches reference data for fcc CoO nanostructures[150] or fcc CoO nanocrystals[152] with a Raman shift of 530 cm^{-1}. Palladium oxides, which one might anticipate on the surface of npPd(Co) in analogy to oxidised gold on the surface of dealloyed AuAg[153], were not found in Raman spectroscopy experiments (a PdO peak would be expected at ∼640 cm^{-1} [154]). A partial oxygen adsorbate layer has been reported to form in the dealloying process of AuAg and PtCu alloys.
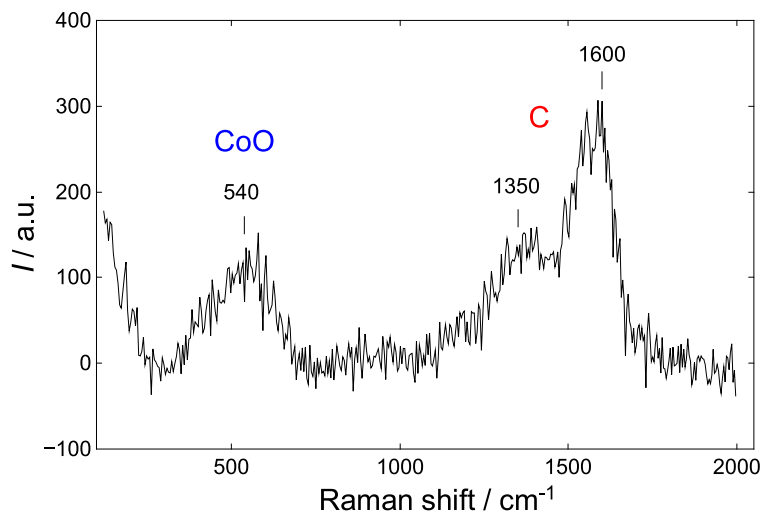
Figure 4.8: Raman spectrum for npPd(Co) (U_D=0.7 V; I_R=0.1 mA) in the as-dealloyed state. Reference lines for CoO at 540 cm^{-1} and C at 1350 cm^{-1} and 1600 cm^{-1} were obtained from literature data[150,151].

The Pourbaix diagram for Co in aqueous environments in Fig. 4.9, however, does not predict the formation of Co oxides in acidic (dealloying) solutions. One possible origin of this surface oxide could be the rinsing step with distilled water after dealloying, which is described in the experimental section (Sec. 3.2.1). The pH-value upon replacement of the electrolyte is shifted from acidic to neutral, which corresponds to a shifting chemical equilibrium from left to right in Fig. 4.9. Residing Co-ions in the pores might precipitate locally on the nanoporous ligaments and form the observed Co oxides in the Raman spectra. A similar precipitation mechanism upon rinsing has been previously suggested to be responsible for Cu-oxides on the surface of nanoporous gold, after dealloying from an AuCu alloy[66].

4.2.2 Specific surface area

4.2.2.1 Double-layer capacitance

The surface area of metal electrodes can be determined using the capacitance of the double-layer forming at the electrode-electrolyte interface, provided a reference value for the capacitance per unit area is known (for smooth Pd: 23.1 μF/cm^2 [156] in 0.5 M H_2SO_4). The total surface capacitance was calculated by measuring a series of CV cycles with increasing scan rate (s=0.1, 0.2, 0.5, 1.0, 2.0, 5.0, 10.0 mVs^{-1}) in the chemically inactive double-layer region (U=0.2 V-0.3 V vs. Ag/AgCl) in 0.5 M H_2SO_4. Data for these experiments have already
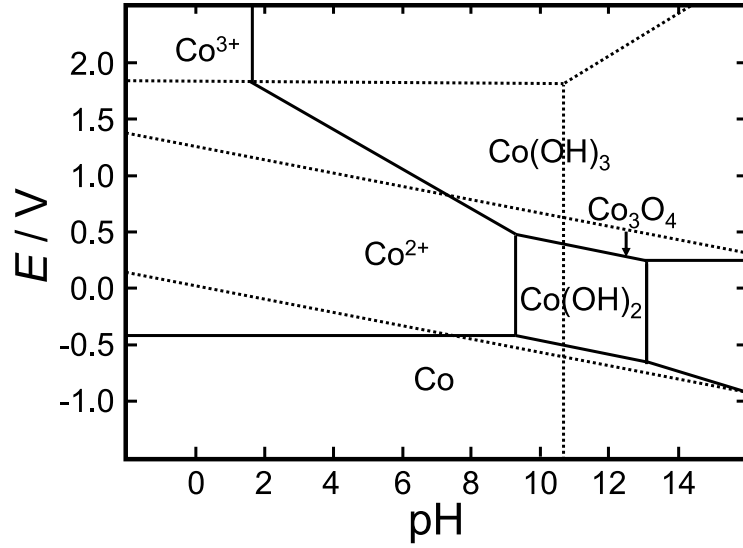
Figure 4.9: Pourbaix diagram for Co in aqueous solution. Electrochemical potential E as a function of pH. Chemical equilibrium species are stated in the diagram. Adapted from Ref. 155

partly been presented in Ref. 157. All CV cycles, as well a plot of double-layer current I_{DL} as a function of scan rate s are depicted in Fig. 4.10.

For an ideal capacitor, I_{DL} is constant over the whole voltage range, whereas for real systems ohmic contributions alter the shape of the CV. Values for the double-layer current were extracted from the CV curves at 0.25 V after centering around 0 current, which accounts for leakage currents. Fitting the I_{DL}-s data with a straight line directly yields the capacitance C of the double-layer as the slope following

$$C = \frac{\mathrm{d}Q}{\mathrm{d}U} = \frac{I_{\mathrm{DL}}\mathrm{d}t}{\mathrm{d}U} = \frac{I_{\mathrm{DL}}}{s}. \tag{4.2}$$

For npPd(Co) (U_D=0.55 V; I_R=0.1 mA) C was found to be 0.09 mAsV^{-1}, which was converted into a specific surface of S_A=13.3 m^{2}g^{-1} using a reference value of 23.1 μF/cm^2 [156] for a smooth Pd electrode, where the mass reference was the total mass of the nanoporous samples. Taking advantage of structural information about dealloyed nanoporous metals, i.e., the identical length scales and geometries of pore and ligament space as well as the arbitrary nature of the overall porosity, a simple relation between specific surface area and ligament size [158] could be deduced.

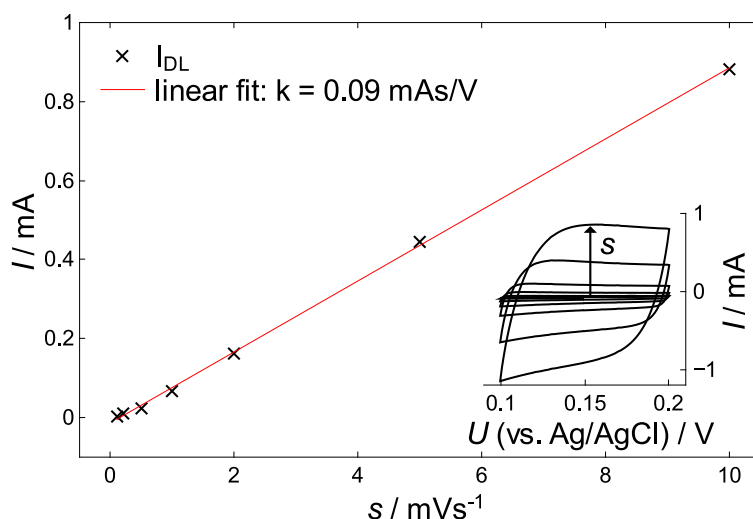$$d = \frac{3.7}{\rho S_{\mathrm{A}}}, \tag{4.3}$$

Figure 4.10: Surface area determination via cyclic voltammetry for npPd(Co) (U_D=0.55 V; I_R=0.1 mA) in the double-layer regime: Double-layer current I_D as a function of scan rate s for CVs between U=0.1 V and 0.2 V in 0.5 M H_2SO_4. Individual CV cycles are shown in the inset, the arrow indicates the trend with increasing scan rate. The red line represents a linear fit to the data, the slope corresponds to the double-layer capacitance according to Eq. 4.2.

where d is the ligament diameter and ρ is the bulk density of the pure metal. The factor of 3.7 is a dimensionless constant related to the geometry of the structure. Using this formula and the bulk density of Pd (ρ=11.99 g cm^{-3}) one obtains an estimate for the ligament size of d=23 nm.

4.2.2.2 Nitrogen adsorption isotherms - BET surface area

In analogy to electrochemical adsorption, adsorption of atoms/molecules from the gas phase is commonly utilised to determine the surface area of nanoporous materials. An IUPAC recommendation[159], concerned with the use of gas adsorption experiments to measure specific surface areas and porosity, specifies nomenclature for nanoporous materials as follows: Pores with widths <2 nm are called *micropores*, pores in the range between 2-50 nm are called *mesopores*, and pores with sizes >50 nm are called *macropores*[159]. The more generic term *nanopores*, which is almost exclusively used in the dealloying research community, comprises pores widths <100 nm and therefore includes all three pore categories by IUPAC, micro-, meso- and macropores[160]. Especially for gas adsorption experiments, the finer division is useful, as the shape of the sorption isotherms is characteristic for each micro-, meso- and macropores.
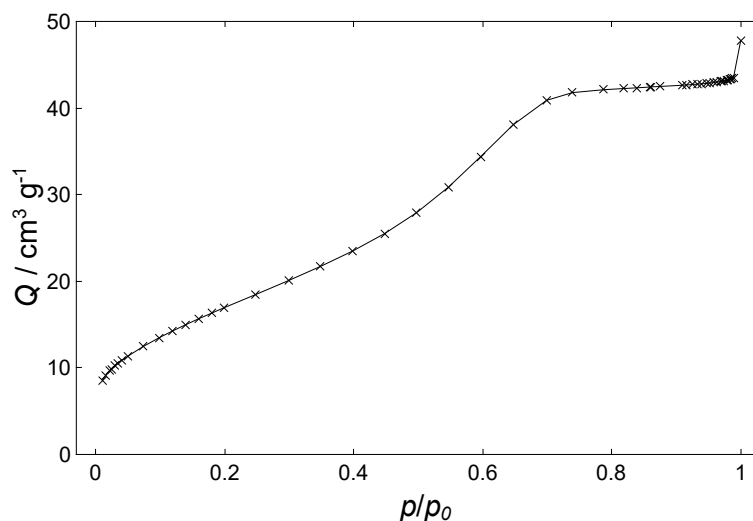
Figure 4.11: Adsorbed quantity of nitrogen Q as a function of relative pressure p/p_0 for npPd(Co) (U_D=0.55 V, I_R=0.1 mA) at 77 K upon adsorption. Values upon desorption were not recorded. Specific surface area according to the BET method was calculated from this sorption isotherm using the linear approximation for $p/p_0 < 0.2$.

Nitrogen sorption isotherms for npPd(Co) were recorded by Christoph Neubauer at the Institute of Particle and Process Engineering at TU Graz. A typical nitrogen gas sorption isotherm at liquid nitrogen temperature (77 K) was recorded for as-dealloyed npPd (U_D=0.55 V; I_R=0.1 mA), which is presented in Fig. 4.11. The adsorbed quantity of nitrogen Q is plotted as a function of relative pressure p/p_0, where p_0 is the equilibrium vapour pressure at the measurement temperature. IUPAC groups physisorption isotherms into 6 categories, distinguished by the shape of the isotherms[160]. The adsorption curve in Fig. 4.11 for npPd can be classified as a type IV isotherm, typical for mesoporous materials (pore widths between 2-50 nm). Typical features of type IV isotherms include a plateau at high relative pressures p/p_0 and a characteristic step in the quantity absorbed at lower values of p/p_0. For BET surface area evaluation the region of lower relative pressures $p/p_0 < 0.2$ in the isotherm in Fig. 4.11 was used, which yielded a specific surface area of S_A=(63.7±0.6) m^{2}g^{-1}. This is similar to values of S_A=50-70 m^{2}g^{-1} for hierarchical npPd dealloyed from PdAl base alloys[68]. However, a considerable discrepancy with surface area from double-layer capacitance (S_A=(13.3) m^{2}g^{-1}) exists, which might be explained by a coarsening effect during electrochemical pretreatment before the surface area determination in the double-layer regime. This is addressed in greater detail when discussing pore sizes from different techniques below.
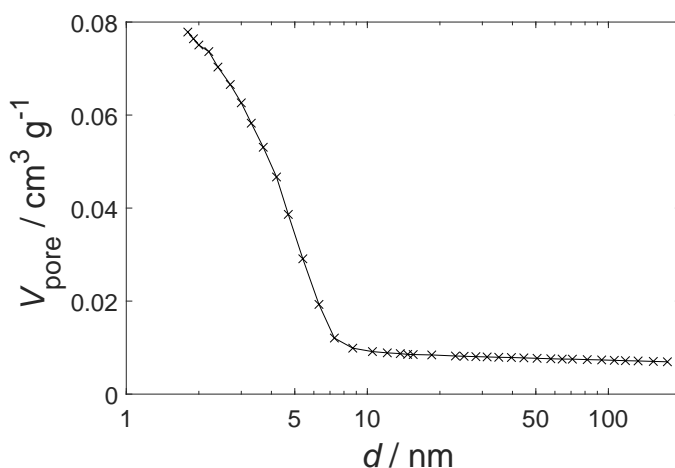
Figure 4.12: Cumulative pore volume V_{pore} as a function of pore diameter d_{pore} for npPd(Co) (U_D=0.55 V, I_R=0.1 mA) according to the BJH method, calculated from the nitrogen sorption isotherms in Fig. 4.11.

Simultaneously to BET surface area, the cumulative pore size distribution was calculated from the sorption isotherm using the Barrett-Joyner-Halenda method[161], which is shown in Fig.4.12. An average pore diameter of $\bar{d}$ =4.1 nm was obtained from Fig. 4.12, with a considerable fraction of smaller pores in the distribution. Almost no pores with diameters >10 nm were found, which goes in hand with pore sizes from the complementary methods using transmission electron microscopy in Sec.4.5.

The Barrett-Joyner-Halenda method[161] allows the calculation of a pore size distribution from sorption isotherm based on the Kelvin equation. This is nowadays a standard procedure to gain information about pore sizes, although for smaller mesopores (pore diameters $<\sim$ 10 nm) it is known to underestimate pore sizes by 20-30 %[160]. For smaller (mesoporous) pore sizes, capillary condensation occurs, which is not included in the theory of either the BET or the BJH method. A more reliable analysis of pore size distributions, also taking capillary condensation into account, would be afforded by methods based on DFT or molecular simulations[160].

Another disadvantage of gas adsorption experiments for the surface area determination of nanoporous metals is the comparably large quantity of material needed for the measurements ($\approx$1 m^2 in total, dealloyed from a $\sim$300 mg piece of alloy), which makes them more expensive compared to electrochemical methods, which require smaller quantities of material (typically $\sim$20-50 mg of alloy).
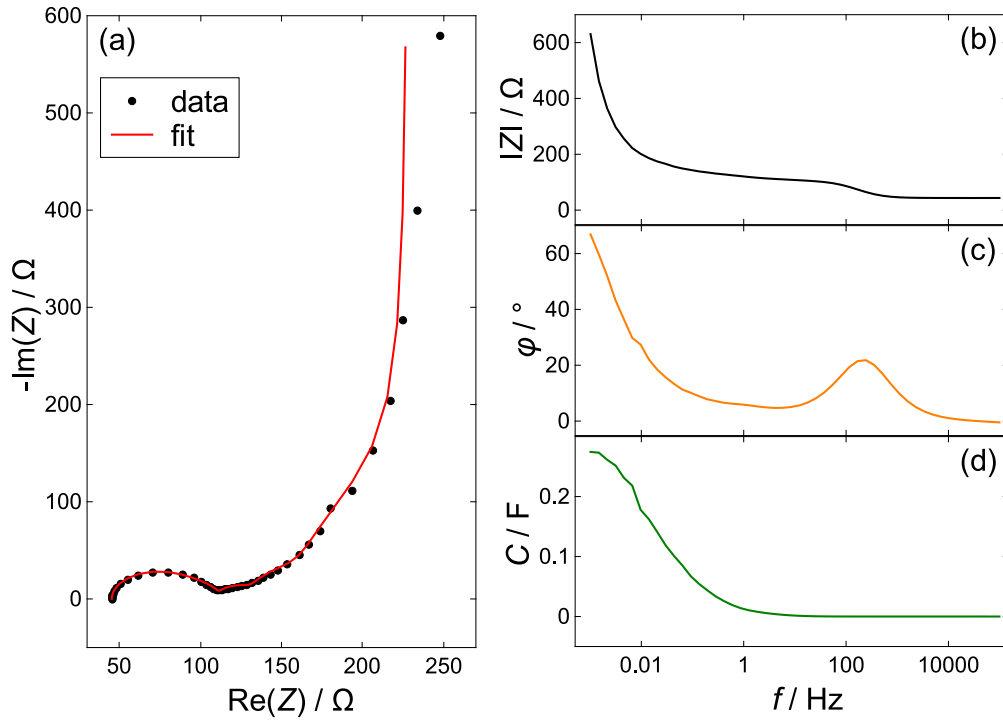
Figure 4.13: Electrochemical impedance spectra for npPd(Co) (U_D=0.55 V; I_R=0.1 mA): (a) Nyquist representation of -Im(Z) as a function of Re(Z). Data points were fit using an equivalent circuit containing a transmission line model, which is shown in red. Frequency decreases from left to right. Bode representation of $|Z|$ (b) and ϕ (c) as a function of frequency f for the same measurement. (c) shows the variation of capacitance C with frequency f, which was calculated from Im(Z) using $C = 1/(2\pi \text{Im}(Z)f)$.

4.2.3   Electrochemical impedance spectroscopy

In contrast to classical electrochemical experiments, electrochemical impedance spectroscopy (EIS) additionally uncovers information about pore size and geometry, exploiting the variation of pore resistance with frequency. An EIS spectrum for npPd(Co) (U_D=0.55 V; I_R=0.1 mA) recorded in 0.01 M HClO$_4$ at a constant potential of 0.125 V in the frequency range between 0.01 Hz and 100000 Hz is shown in Fig. 4.13.

Graphs of complex resistance Z are shown in Nyquist (a) and Bode representation (b and c). The Nyquist plot shows a semicircular feature at high frequencies between 50 Ω and 100 Ω of Re(Z), which is attributed to contact impedance. The slope in the mid-part between 100 Ω and 150 Ω of $\sim$22.5° yields information about the pore geometry. In EIS theory pores are most commonly modelled as cylindrical pores with an infinite length on an otherwise planar surface. Deviations from this cylindrical model have been considered [162,163], but pores remained infinitely long in either case. For arbitrary nanoporous networks structures

produced by dealloying, such theoretical consideration can only give a rough estimation of pore shape. Comparing the shape of Fig. 4.13(a) with calculated spectra for different pore geometries[163], a deltoid-like pore shape comes closest to the measured spectrum for npPd(Co)[149]. For an ideal uniform pore size -Im(Z) diverges with an angle of $\phi=90°$ at high values of Re(Z). A deviation from this ideal slope of 90° in Fig. 4.13(a) reflects itself in the discrepancy between fit and data, which can also be seen at low frequencies f in Fig. 4.13(c). Deviations of the ideal 90° are indications for a distribution of pore sizes in npPd(Co)[149]. The Bode plot of EIS measurements on npPd(Co) in Fig.4.13(b) and (c) contains the frequency information, which is missing in the Nyquist representation of Fig. 4.13(a). Both the step in $|Z|$ in Fig. 4.13(b) and the peak in ϕ in Fig. 4.13(c) at $f \sim 100$ Hz correspond to the semicircle region in the Nyquist plot, which is indicative of a contact resistance contribution. The increase of $|Z|$ and ϕ at low frequencies f is caused by the porous structure, which is also seen in the plot of capacitance C as a function of f in Fig. 4.13(d). Low frequencies are able to penetrate the pores more deeply, enhancing the measured capacitance[149]. The low frequency limit of C can be used to estimate the total area of the nanoporous specimen. As no specific capacitance values exist for Pd in $HClO_4$ as a reference, a specific capacitance of 23.1 $\mu F/cm^2$[156] for smooth Pd in 0.5 M H_2SO_4, was approximated for the conversion to $A=1.2$ m^2 ($S_A=103$ m^{2}g^{-1}). This value of A is used further for an estimation of the pore size. In the picture of infinite cylindrical pores, one can calculate a pore radius r and a pore length l using data from impedance spectra following

$$r = 2\frac{V_{\text{pore}}}{A} \tag{4.4}$$

and

$$l = \sqrt{\frac{3V_{\text{pore}}R_\Omega}{\rho}}, \tag{4.5}$$

where V_{pore} is the pore volume, A is the total surface area of the pores, R_Ω is one-third of the pore resistance, and ρ is the resistivity of the electrolyte solution. V_{pore} was estimated from the alloy volume, its shrinkage during dealloying and a porosity value of 0.5, which is typical for dealloyed structures. The area A was determined from the double-layer capacitance as in Sec. 4.2.2.1, while ρ was directly measured using an EC meter. The value for R_Ω was obtained graphically as indicated in Fig. 4.13(a), as the point where the diverging slope at Re(Z)$\sim$250 Ω

intersects the x-axis, subtracting the contact and solution resistance contributions[149,164]. Using this method, a pore radius of r=2-4 nm and a pore length of l=510±90 μm have been calculated[149]. This pore size from the purely geometrical estimation according to Eq. 4.4 is in agreement with pore sizes from TEM (d <5 nm) and BET ($\bar{d}$ =4.1 nm). The pore length l exceeded the macroscopic thickness of the sample platelet, which has been interpreted as an indication for tortuous pores[149]. Tortuosity is not a commonly assessed parameter in relevant dealloying literature, as it is not easy to access experimentally. A value of tortuosity τ=2.3 has been calculated from pore length and macroscopic dimension[149]. Considering the simplifications in our estimations, the value of τ is still plausible, as expected values for nanoporous network structures generated via dealloying are below τ=3[165].

Although pore models in EIS theory are only crude approximations for real nanoporous structures generated by dealloying, valuable information regarding pore geometry, pore size and tortuosity could be extracted from EIS measurements. The electrochemical impedance spectra of npPd(Co) are elaborated in much greater depth in the master's thesis of Philipp Brunner[149].

4.2.4 Comparison of experimental pore sizes in npPd

Ligament and pore sizes for dealloyed structures have been shown to be highly sensitive to process parameters as temperature[166], electrolyte[64,167], alloy composition[71], or applied potential[71,73,158], as well as electrolytic post-treatment[57]. When comparing pore and ligament size values from the different techniques here, one therefore has to consider the different corrosion potentials used. Pore sizes determined from BET ($\bar{d}$ =4.1 nm), TEM (d <5 nm) and EIS (d=2-4 nm) all determined for npPd(Co) (U_D=0.55 V, I_R=0.1 mA) are in decent agreement with each other. The value obtained from the electrochemical double-layer capacitance (d=23 nm) represents a clear overestimation of this pore size, although the same etching parameters were used. A conceivable reason for this finding is the pre-treatment in H_2SO_4, where the double-layer CVs were recorded. Prolonged storage in an acidic environment alone has been reported to coarsen the structure for npAu[57] due to the high surface diffusivity of Au in acids. Coarsening of npAu upon voltammetric cycling in H_2SO_4 has also been reported[168,169], although latest results point only towards a faceting of

the ligament structure without a concomitant coarsening upon cycling for npAu[170]. This issue has not been covered for dealloyed npPd in the scientific literature so far. The higher melting point of Pd compared to Au, suggests a less significant coarsening to be expected, but the mechanism is still viable for Pd. In Sec. 5.2.4 structural and compositional changes upon cycling of npPd in KOH are addressed, which hints towards a surface restructuring also for npPd.

4.2.5   Hydrogen storage capacity

The most common method to evaluate the hydrogen storage capacity of any material is the measurement of pressure-composition isotherms using various hydrogen pressures applied. Here, npPd(Co) was charged and discharged with hydrogen electrochemically at constant potentials, which is thermodynamically equivalent to the measurement of pressure-composition isotherms[174]. The hydrogen concentration was calculated from the total charge flow during desorption using Faraday's law (Eq. 3.1). Charging during hydrogen ad- and absorption might be accompanied by hydrogen gas evolution, especially at more negative sorption potentials, which makes a concentration determination from charge infeasible during ad- and absorption. A set of hydrogen charging and discharging experiments with successively more negative sorption potentials was recorded for a npPd(Co) sample (U_D=0.55 V, I_R=0.1 mA). Hydrogen discharging was conducted at a constant potential of −0.4 V. Potentials during charging and discharging were held for 1 h, when a constant equilibrium current was reached. The hydrogen concentrations, represented as the fraction of hydrogen per metal atom x_H (explicitly including Co atoms), is plotted as a function of applied charging potential in Fig. 4.14. Representative charging and discharging curves for the highest hydrogen concentration are shown in (b) and (c), respectively.

Hydrogen concentration x_H increases with more negative sorption potentials throughout all points in Fig. 4.14. As the two different phases of PdH are defined by concentration, one can immediately identify regions of different phase constitutions in the graph. In the region down to U=−0.96 V, where concentration increases only slightly with more negative potential, the PdH$_\alpha$ phase is present exclusively with a concentration of x_H <0.07. At intermediate sorption potentials between U=−0.96 V and U=−0.99 V both solid solution phase PdH$_\alpha$
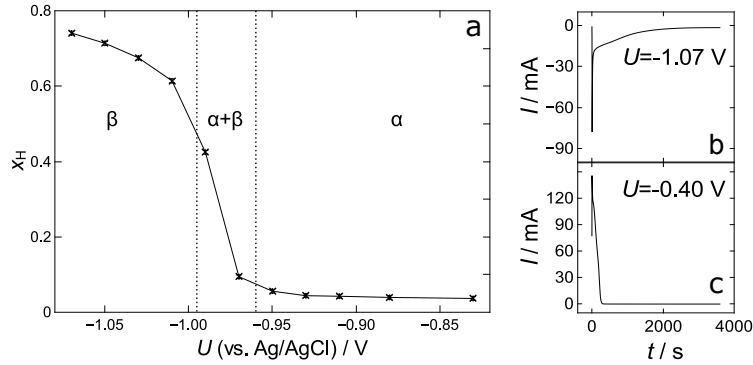
Figure 4.14: (a) Hydrogen to metal atom fraction x_H as a function of hydrogen charging potential U for npPd(Co) in 1 M KOH. Vertical dashed lines indicated regions of different hydride phases in hydrogen-charged npPd(Co). PdH_α represents the solid solution phase, while PdH_β is the hydride phase. A typical charging and discharging experiment for the determination of a single data point in the phase diagram in (a) are shown in (b) and (c).

and hydride phase PdH_β coexist. For even more negative sorption potentials $U < -0.99$ V pure hydride phase PdH_β commences, which reaches a maximum x_H value of 0.7.

Charging and discharging curves in Fig. 4.14(b) and (c) used for the evaluation of x_H, show decaying behaviour, typical for such experiments. Larger peak currents for desorption indicate a faster reaction rate compared to hydrogen absorption, while the larger area under the current curve for charging shows a larger charge consumption in that process. For hydrogen charging at -1.07 V a stable current of 1.5 mA emerged after 2400 s, which is related to hydrogen gas evolution. In contrast, the current after discharging at -0.4 V dropped to almost 0 after 400 s. This indicates that eventual side reactions, such as the potential oxidation of surface Co, do not contribute to the charge balance after 400 s and an equilibrium state has been reached. A small systematic error due to a charge fraction consumed by side reactions, however, cannot be excluded. Another source of error is a possible coarsening of the npPd(Co) electrode upon cyclic hydrogen charging and discharging, which could in turn change the hydrogen absorption capacity after each charging cycle. The possibility of such a coarsening effect is discussed in Sec. 5.2.4. Although these error sources certainly need to be taken into account, desorption charge is considered a suitable measure for hydrogen concentration in the literature for nanoporous Pd electrodes[175].

Alloying of Co to Pd has been known to decrease the hydrogen-storage capacity compared to pure Pd[91], when only 10 at% of Co are sufficient to diminish the maximum capacity to x_H=0.3[91]. As small residual amounts of Co remain in the nanoporous Pd structure after

dealloying, it was unclear a priori how the hydrogen storage capacity would be affected by the residual Co fraction in npPd. From the large maximum x_H value of about 0.7 in Fig. 4.14, which is comparable to the experimental value of x_H=0.72 for bulk Pd at a hydrogen pressure of ∼1 bar[171], it becomes apparent that residual Co has no significant influence on the hydrogen storage capacity of npPd(Co). Slightly lower values in the order of x_H ∼0.5-0.6 have previously been reported for npPd(Co)[172,173], hierarchical npPd(Cu)[175], and npPd(Al)[176] prepared via dealloying. A part of the high hydrogen sorption capacity in npPd structures is attributed to a stronger contribution of hydrogen surface adsorption compared to bulk Pd[175], which is naturally understood in terms of the larger specific surface area. Another possible factor influencing the hydrogen storage capacity in nanoporous Pd is surface stress[175], although its influence on the present system is not investigated.

The large hydrogen storage capacity and intriguing magnetic properties have made nanoporous Pd(Co) an attractive material system for hydrogen magneto-ionics, which is explored in Sec. 4.4.2.3.

4.3 Tailoring Co content and distribution in nanoporous Pd

As this chapter is mainly about the magnetic properties of npPd(Co), it might be seen as an extension to the previous chapter on physical properties. However, as magnetic properties of npPd(Co) are of utmost importance for the entire thesis, an individual chapter is devoted to this crucial topic. Here, methods for the adjustment of Co content and distribution in npPd(Co) via various dealloying techniques are presented. While Co content is directly measured via EDS or XRF elemental analysis, temperature-dependent magnetisation measurements give information about the Co distribution. As the magnetic properties of npPd(Co) are sensitive to the dealloying method, magnetisation measurements are presented in conjunction with the Co content for the respective dealloying technique. In Sec. 4.3.1 the influence of static dealloying potential in the PCD process on Co content and magnetic properties is presented. Furthermore, the influence of temperature-treatment in PCD+T preparation on the Co distribution and the closely related magnetic properties is addressed in Sec. 4.3.2. In the third section (Sec. 4.3.3), current-controlled GCD dealloying is presented as a new method for the tailoring of Co content and distribution in $npPd_{1-x}Co_x$. Lastly, a summary and comparison of magnetic key quantities is provided in Sec. 4.3.4. Parts of this chapter are reprinted from Ref. 41 with permission.

4.3.1 Magnetic properties of npPd(Co) by PCD

Dealloying potential U_D in PCD experiments is probably the parameter in electrochemical dealloying that is the easiest to control. Its effect on the residual content of the secondary dealloying component[73,177] and the ligament size[71,73,158] has been extensively studied in the dealloying literature. While the magnetic properties of dealloyed materials have previously been explored[65,141,142,178], the influence of U_D on these magnetic properties has not been covered in publications unrelated to this thesis. Magnetisation curves for npPd(Co) prepared via PCD dealloying at different potentials U_D from 0.4 V to 0.8 V are presented in Fig. 4.15.
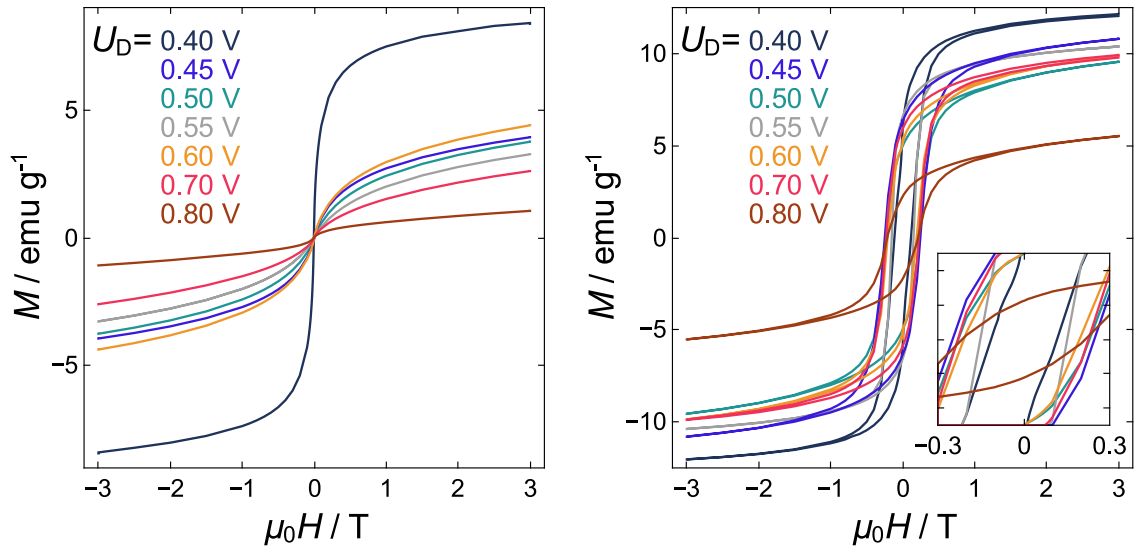
Figure 4.15: Magnetisation curves for PCD npPd(Co) at 300 K (left) and 4.2 K (right) prepared at different dealloying potentials U_D. Dealloying potential varies from U_D=0.4 V (blue) to U_D=0.8 V (brown). Magnetisation M is plotted as a function of magnetic field $\mu_0 H$ in the range from -3 T to 3 T. Initial magnetisation curves are not depicted. The inset in the right graph shows the low field region for improved comparability of coercive fields.

Magnetisation curves at room temperature in Fig. 4.15 on the left, show superparamagnetic characteristics for all dealloying potentials U_D. The origin of superparamagnetism in npPd(Co) is attributed to small residual Co-rich clusters, which emerge during dealloying (Fig. 4.6). All curves in Fig. 4.15 on the left exhibit the generic shape of a typical Langevin function. An uncommon feature for superparamagnetic magnetisation curves, however, is the absence of saturation at large fields, where all curves still show a slope up to 3 T, which indicates extremely small superparamagnetic units. The magnetisation at $\mu_0 H$=3 T at room temperature $M_{3T,RT}$, which is the rightmost point for the magnetisation curves on the left, is clearly affected by the choice of dealloying potential. The highest magnetisation at U_D=0.4 V reaches a value of $M_{3T,RT}$=8.40 emu g^{-1}, while the lowest value for U_D=0.8 V equals $M_{3T,RT}$=1.05 emu g^{-1}, eight times less. Numerical values of $M_{3T,RT}$ are included in an overview table (Tab. 4.2) at the end of this chapter in Sec. 4.3.4. A rough trend suggests a decrease of $M_{3T,RT}$ with increasing dealloying potential from blue to brown, with one exception being the curve for U_D=0.6 V. Low-temperature magnetisation curves at T=4.2 K in Fig. 4.15 on the right show clearly different behaviour. A hysteresis loop is observed for all dealloying potentials, which is a distinctive feature for ferromagnetism. The high-field magnetisation at 3 T $M_{3T,4K}$ still does not show saturation and ranges from $M_{3T,4K}$=5.52 emu g^{-1} for U_D=0.8 V to $M_{3T,4K}$=12.04 emu g^{-1} for U_D=0.4 V, which are markedly higher compared to the room

temperature curves on the left (note the different axis scaling). The rough trend of higher magnetisation at large fields for lower dealloying potentials is still valid. Coercivity is rather similar for all dealloying potentials U_D in the order of $\mu_0 H \sim 0.2$ T, with no clear observable trend. Numerical values of coercivity and large-field magnetisation can again be found in the overview table Tab. 4.2 in Sec. 4.3.4.

While magnetisation curves can in principle give qualitative information about the Co content via the saturation magnetisation, temperature-dependent magnetisation curves yield information about the size of Co aggregates and their size distribution. Zero-field cooling/field cooling (ZFC/FC) experiments are conducted for that purpose, as shown in Fig. 4.16. For a ZFC curve the (demagnetised) sample is cooled to $T{=}4.2$ K, when only then a small magnetic field ($\mu_0 H{=}0.005$ T) is applied and the magnetisation M_ZFC is measured upon heating. The field-cooling experiment is the direct application of the same field at room temperature, when the magnetisation M_FC is measured upon cooling. Differences in M_ZFC and M_FC indicate dynamic effects contributing to the magnetic properties, i.e., superparamagnetism or spin-glass behaviour. Typically both M_ZFC and M_FC are shown in common plots, whereas in this chapter they are shown in separate subplots next to each other to keep the depiction lucid when showing multiple samples at once.

Fig. 4.16 presents both FC and ZFC magnetisation curves for npPd(Co) with different dealloying potentials U_D in PCD dealloying. Results are presented using the analogous colour-coding as in Fig.4.15.

Field-cooling curves show an increase in magnetisation M_FC for all dealloying potentials U_D upon cooling in Fig. 4.16 on the left. This is unsurprising as any para- or ferromagnetic substance would show such behaviour. Room-temperature magnetisation values at a low field of $\mu_0 H{=}0.005$ T appear similar for all samples, with the curve for $U_\mathrm{D}{=}0.8$ V being an exception with a higher value there. The most interesting part is the levelling-off of magnetisation at lower temperatures of $T < 20$ K for all curves, which is indicative of an additional magnetic interaction between the magnetic units[179] (likely dipolar or Ruderman–Kittel–Kasuya–Yosida - RKKY-type, see discussion). All zero-field-cooling curves on the right exhibit a peak typical for blocked superparamagnetism. Starting from a negative value of M_ZFC for most curves, a peak is observed upon heating between $T{=}46$ K for $U_\mathrm{D}{=}0.8$ V and $T{=}117$ K for $U_\mathrm{D}{=}0.6$ V and $U_\mathrm{D}{=}0.4$ V, followed by a decrease back to the same high-temperature value as for M_FC
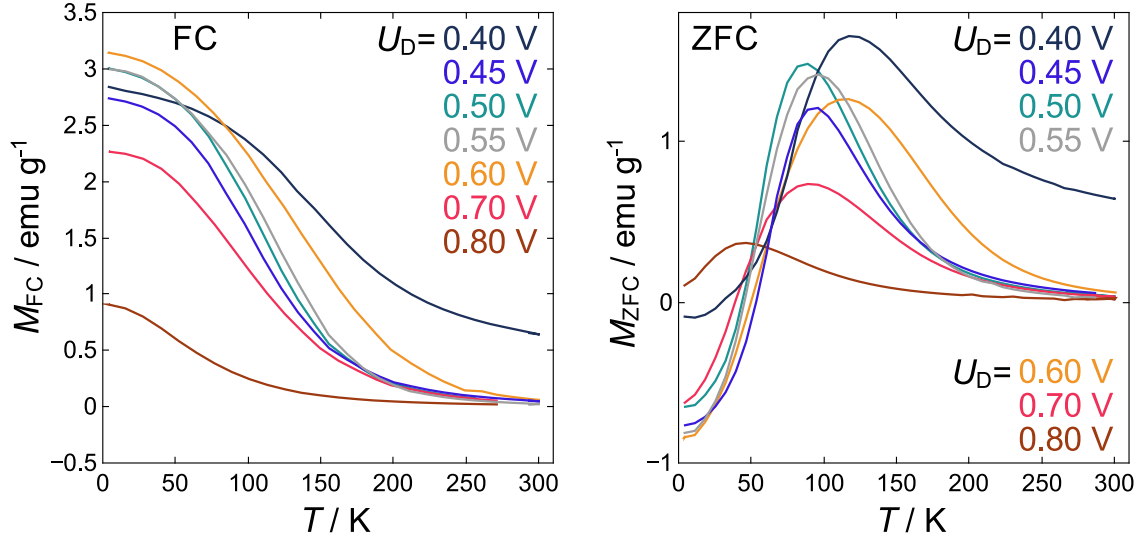
Figure 4.16: Field-cooled (FC - left) and zero-field-cooled (ZFC - right) magnetisation for PCD npPd(Co) prepared at different dealloying potentials U_D at a field of $\mu_0 H = 0.005$ T. Dealloying potential varies from $U_D = 0.4$ V (blue) to $U_D = 0.8$ V (brown). Both magnetisations M_{FC} and M_{ZFC} are plotted as a function of temperature T in the range from 4.2 K to 300 K. The plot uses the same colour coding as field-dependent magnetisation curves in Fig. 4.15. Zero-field cooling curves on the right have previously been published in Ref. 41.

in the left plot (note the difference in y-axis scaling). The temperature at which the peak occurs is a decent approximation for the blocking temperature T_B of superparamagnetic entities, which yields information about the magnetic size. Larger blocking temperatures and broader peaks in the ZFC curves indicate larger superparamagnetic units and a broader size distribution of those units. Blocking temperature as the most important parameter regarding magnetic size is also included in Tab. 4.2 in Sec. 4.3.4 for all dealloying potentials U_D.

The behaviour of blocking temperature T_B and magnetisation at 3 T and 300 K $M_{3T,RT}$ with dealloying potential U_D and their correlation with the absolute residual Co content x_{Co} in npPd(Co) measured via EDS is also depicted in a separate figure (Fig. 4.17).

All three curves show a similar trend with increasing dealloying potential. A minimum in T_B, $M_{3T,RT}$, and x_{Co} between $U_D = 0.5$ V and 0.55 V is followed by a peak between $U_D = 0.6$ V and 0.7 V. At higher dealloying potentials both the blocking temperature T_B, magnetisation at 3 T $M_{3T,RT}$ and the residual Co content x_{Co} decrease again. The minimum Co content was determined for a dealloying potential of 0.55 V, which was also used as the fixed potential for the charge-dependent study of the magnetic properties presented in Sec. 4.1. The correlation of total Co content x_{Co} and blocking temperature T_B is in line with the notion that Co
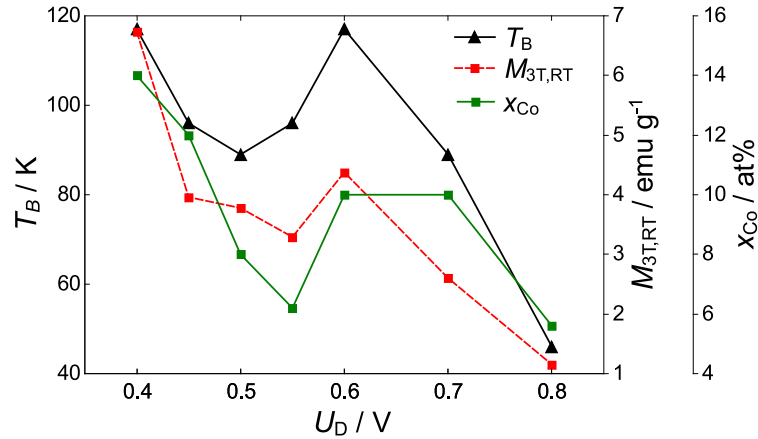
Figure 4.17: Blocking temperature T_B (black triangles), magnetisation at 3 T and 300 K $M_{3T,RT}$ (red squares), and residual Co concentration x_{Co} (green squares) determined via EDS for different dealloying potentials U_D. Blocking temperatures represent the peak positions in the ZFC curves in Fig. 4.16 and are a measure for the average cluster size. Reprinted from Ref. 41.

residues are located in Co-rich alloy clusters after dealloying. The key finding in this section is that dealloying potential U_D can control the size of those alloy clusters and their magnetic behaviour.

4.3.2 Magnetic properties of npPd(Co) by PCD+T

The influence of post-annealing on the ligament size of dealloyed materials has been extensively studied in the dealloying literature[67,166,180–184]. Only recently, the influence of temperature treatment on the residual element distribution has been recognised by Krekeler et al.[69]. In their work, a clustering of residual Ag in npAu is observed as a natural by-product of the dealloying process from AgAu alloys. Furthermore, it is demonstrated that the Ag distribution in npAu can be homogenised via a thermal annealing treatment. This work motivated the present study on the magnetic properties of thermally annealed npPd(Co), which are expected to be strongly dependent not only on the residual Co content, but also on its distribution in the Pd matrix. Measurements presented here have already been part of the Master's project of Alexander Steiner[47].

Magnetisation measurements for (PCD+T) npPd(Co) (U_D=0.55 V, I_R=0.01 mA) annealed at different temperatures from T_A=373 K (yellow) to T_A=973 K (dark red) are shown in Fig. 4.18 in comparison to an untreated, as-dealloyed reference sample (green).
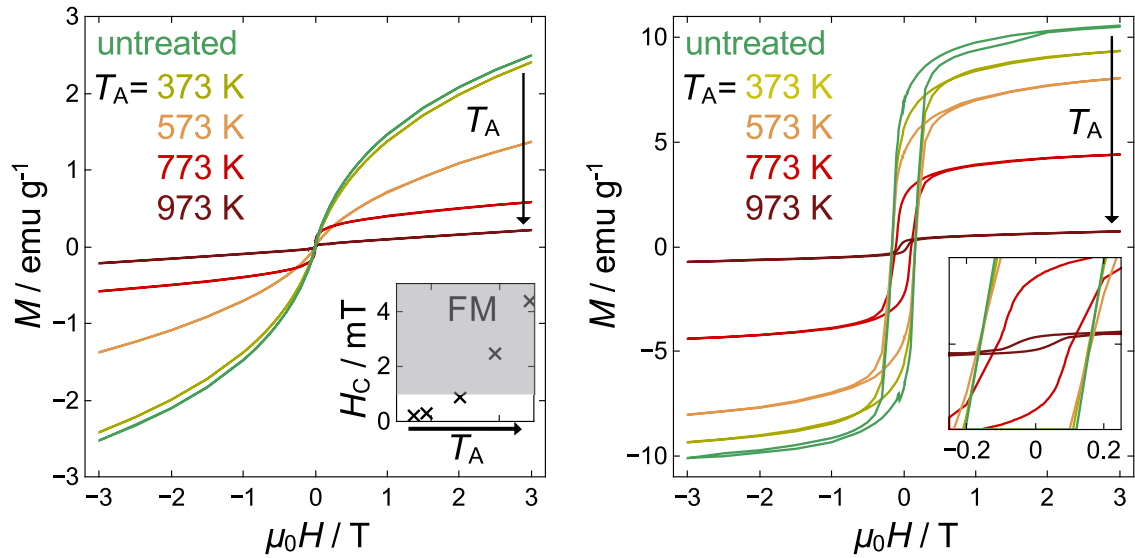
Figure 4.18: Magnetisation curves for temperature-treated (PCD+T) npPd(Co) measured at 300 K (left) and 4.2 K (right). Dealloying conditions were the same for all samples (U_D=0.55 V, I_R=0.01 mA). The annealing temperature T_A for each curve is given in the plot and ranges from 373 K (yellow) to 973 K (dark red), with a not annealed PCD sample shown as a reference (green). The holding time was 10 min for all annealing treatments (heating and cooling times excluded). Magnetisation M is plotted as a function of magnetic field $\mu_0 H$ in the range from -3 T to 3 T. For better comparability initial magnetisation curves are not depicted. The inset in the left graph shows coercivities H_C for increasing T_A extracted from the magnetisation curve. Weak ferromagnetism is indicated by the grey shading. The inset in the right graph shows the low field region for improved comparability of coercive fields. Arrows in both plots indicate the trend with increasing annealing temperature T_A.

Magnetisation curves at 300 K on the left in Fig. 4.18 show mostly superparamagnetic behaviour, similar to the magnetisation curves for npPd(Co) dealloyed at different potentials U_D in Fig. 4.15. With increasing annealing temperature T_A magnetisation decreases steadily from the untreated sample (green) to T_A=973 K (dark red), as indicated by the arrow. This reflects itself also in the high field value $M_{3T,RT}$, which decreases from 2.52 emu g^{-1} for the reference sample to 0.22 emu g^{-1} for an annealing temperature of T_A=973 K. Magnetisation curves transform from an s-shape without saturation for low annealing temperatures to a shape resembling a step function with a much flatter slope at high fields. In contrast to as-dealloyed samples in Fig. 4.15, upon closer inspection one finds small coercivities H_C even in the magnetisation curves at 300 K, which is demonstrated in the inset to the left plot. A value of $\mu_0 H_{C,RT}$=0.005 T was found for T_A=773 K, while $\mu_0 H_{C,RT}$=0.009 T was extracted from the curve with T_A=973 K. While these two samples can be considered weakly ferromagnetic at room temperature, insignificant coercivities for the other annealing temperatures lie within the experimental error. Therefore, samples with T_A <773 K are still considered purely superparamagnetic. Values for high-temperature magnetisation $M_{3T,RT}$ and room-temperature coercivity $\mu_0 H_{C,RT}$ are included in the overview table of magnetic properties in Tab. 4.2 in Sec. 4.3.4.

The magnetisation measurements for (PCD+T) npPd(Co) at 4.2 K are shown in Fig. 4.18 on the right. All curves exhibit clearly ferromagnetic hysteresis, while a small slope at large fields is still apparent instead of full saturation. The same trend of a decreasing overall magnetisation with annealing temperature T_A (from green to dark red) as for room temperature magnetisation on the left is valid for the magnetisation curves at 4.2 K on the right, also indicated by the arrow. However, it is clearly evident that all hysteresis loops have larger magnetisation compared to the room-temperature measurement on the left. High-field magnetisation increased to $M_{3T,4K}$=10.57 emu g^{-1} for the untreated as-dealloyed sample and to $M_{3T,4K}$=0.73 emu g^{-1} for an annealing temperature of T_A=973 K. Coercivities ranged between $\mu_0 H_{C,4K}$=0.05 T for the highest annealing temperature and $\mu_0 H_{C,4K}$=0.16 T for the as-dealloyed sample as extracted from the inset on the right. Numerical values are again summarised in Tab. 4.2.

Temperature-dependent magnetisation curves for annealed PCD+T samples were also recorded in analogy to the potential-dependent dealloying study in Fig. 4.16. Results are presented
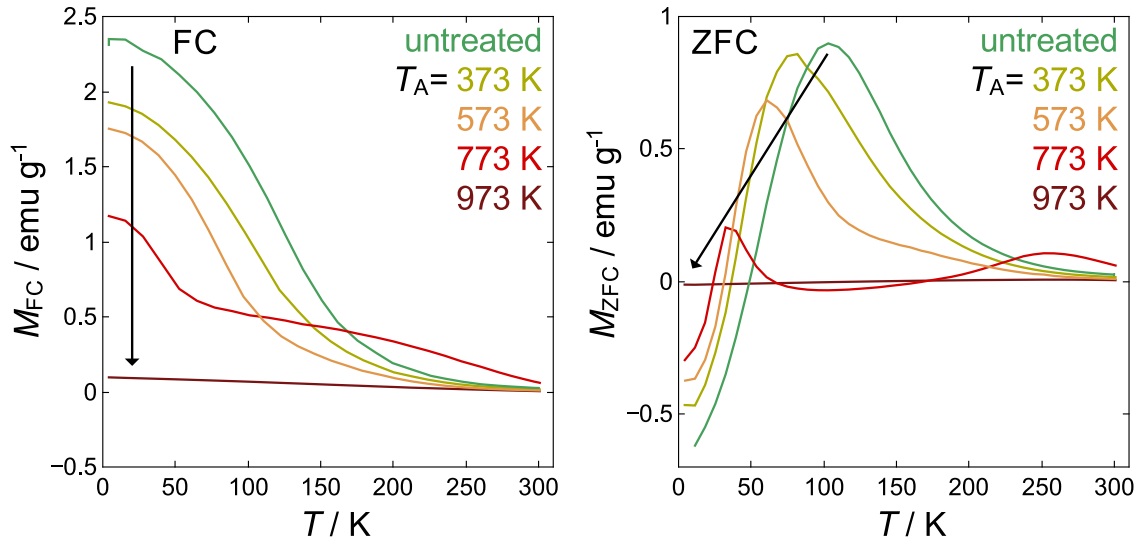
Figure 4.19: Field-cooled (FC - left) and zero-field-cooled (ZFC - right) magnetisation for temperature-treated (PCD+T) npPd(Co) at a field of $\mu_0 H$=0.005 T: Dealloying conditions were the same for all samples (U_D=0.55 V, I_R=0.01 mA). The annealing temperature T_A for each curve is given in the plot and ranges from 373 K (yellow) to 973 K (dark red), with a not annealed PCD sample shown as a reference (green). The holding time was 10 min for all annealing treatments (heating and cooling times excluded). Both magnetisations M_{FC} and M_{ZFC} are plotted as a function of temperature T in the range from 4.2 K to 300 K. Arrows in both plots indicate the trend with increasing annealing temperature T_A. The plot uses the same colour coding as field-dependent magnetisation curves in Fig. 4.18.

in Fig. 4.19 for the FC magnetisation M_{FC} on the left and for the corresponding ZFC magnetisation M_{ZFC} on the right. The same colour scheme as in Fig. 4.18 for the field-dependent magnetisation was also used here.

FC and ZFC magnetisation in Fig. 4.19 were measured in the range from 4.2 K to 300 K at a constant field of $\mu_0 H$=0.005 T. The same overall trends as observed for the field-dependent magnetisation in Fig. 4.18 hold also for the temperature-dependent experiments shown here: FC magnetisation M_{FC} on the left increases with decreasing temperature for all samples, with the as-dealloyed sample exhibiting the largest overall magnetisation. Magnetisation M_{FC} successively decreases with increasing annealing temperature T_A (from green to dark red) as indicated by the arrow. The overall shape of the FC curves with a steep increase at intermediate temperatures and a flattening at low temperature values is similar to the FC-curves for the PCD dealloying presented in Fig. 4.16. The FC curve for the sample annealed at T_A=773 K, however, appears different, with two distinct regions of rising magnetisation. Starting with a flatter, almost constant slope upon cooling down to $T \sim$60 K, the curve rises steeply at $T \sim$60 K until it eventually bends towards the ordinate for low temperatures

$T < 20$ K. For an even higher annealing temperature of $T_A=973$ K, a linear increase to lower measurement temperatures with a diminished slope was observed over the full temperature range.

ZFC magnetisation M_{ZFC} on the right in Fig. 4.19 shows a pronounced superparamagnetic blocking peak for all samples $T_A < 773$ K. Taking the peak position again as a good approximation for the bocking temperature T_B, one can see a lowering of both peak height and T_B with increasing annealing temperature T_A (from green to dark red) as indicated by the arrow. Comparing with the FC magnetisation M_{FC} on the left one can also tell that the bifurcation temperature, i.e., the temperature where the FC and ZFC curves split, shifts to higher values with higher annealing temperatures, which is indicative of a broader superparamagnetic size distribution for higher annealing temperatures. Interestingly, for the sample annealed at $T_A=773$ K, two different blocking peaks at $T_B=33$ K and $T_B=260$ K are observed, in line with the two different slopes observed in the FC curve on the left. This might well be an indication of two different characteristic superparamagnetic sizes present in this annealed npPd(Co) specimen. For the highest annealing temperature $T_A=973$ K again no characteristic features appear in the ZFC magnetisation M_{ZFC} on the right, which increases from a small negative value at $T=4.2$ K to a near-zero value at 300 K. All other curves with $T_A < 973$ K have more negative starting values at $T=4.2$ K, which is discussed below. Blocking temperatures for all samples are summarised in the overview table Tab. 4.2 in Sec. 4.3.4.

The decreasing saturation magnetisation and blocking temperature at higher annealing temperatures might seem counter-intuitive at first sight. As all samples underwent the same dealloying procedure, the Co content is expected to be roughly the same, which was confirmed by XRF measurements of the Co content in Tab. 4.2. The different magnetic properties are therefore solely connected to the Co distribution in PCD+T npPd(Co).

For low Co concentrations in homogeneous CoPd alloys, a spin disalignment and breakdown of the ferromagnetic state has previously been observed[185]. This was attributed to a magnetic interaction between spins with random sign at large distances[185], which could be RKKY-type in nature. Such a disaligned magnetic phase is expected to coexist with the superparamagnetic Co-rich phase in npPd(Co). Although the global Co concentration remains constant during temperature-treatment of dealloyed samples, Co concentration can fluctuate locally due to a

redistribution of atoms induced by annealing, which also affects the phase fractions of the magnetic phases.

Alloy clusters, which retain a composition close to the base alloy[69] ($Co_{75}Pd_{25}$ in the present case), gradually transform into a more dilute Co-phase when they mix with the nanoporous Pd matrix upon thermal treatment. Precisely this Co redistribution can explain both the changes in saturation magnetisation and blocking temperature: Co-rich clusters, responsible for superparamagnetic behaviour, shrink at the expense of a magnetically dilute Co-phase with disaligned magnetic spins during temperature treatment. The blocking temperature, as a measure for cluster size, therefore shifts to lower temperatures with increasing annealing temperature T_A. At the same time, the saturation moment decreases due to the growing dilute Co phase with disaligned spins. For the highest annealing temperature, clusters have almost completely dissolved in the Pd matrix, leaving no observable blocking peak and a vanishing overall magnetisation characteristic for the disaligned spin state in dilute CoPd alloys[185]. This transformation of alloy clusters into dilute phase can be considered a homogenisation of the total Co concentration. As a side-effect, the surface of npPd(Co) is repopulated with Co atoms during this homogenisation, which can be beneficial for its magneto-ionic application. Thermal annealing therefore is another technique for the effective tailoring of the magnetic properties of npPd(Co), which is utilised for electrochemical charging experiments in Sec. 4.4.1.

4.3.3   Magnetic properties of npPd$_{1-x}$Co$_x$ by GCD

Although the influence of the dealloying parameters on the residual element content has been frequently studied[73,167,186–189], direct control of residual element content independent from pore size in the dealloying process has been demonstrated for an AgAu alloy only recently by Lackmann et al.[121]. The GCD process used here is adapted from that reference for the direct control of Co content during dealloying of a CoPd alloy. Here, the variations of the magnetic properties of GCD npPd$_{1-x}$Co$_x$ with different nominal Co concentrations $x_{Co,nom}$ (0%, 3%, 6%, and 9%) are presented. These measurements were part of the Bachelor's thesis of Benedikt Huemer (unpublished).
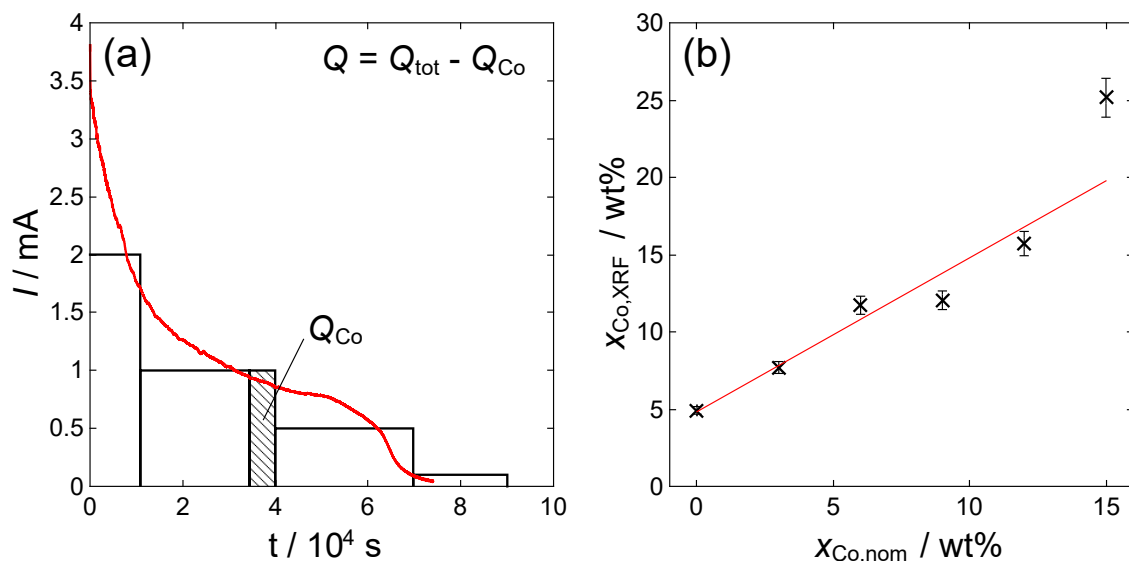
Figure 4.20: Galvanodynamically controlled dealloying (GCD) of a $Co_{75}Pd_{25}$ alloy to obtain $npPd_{(1-x)}Co_x$ with variable Co content x: (a) Schematic discretisation of a typical dealloying curve at constant potential (red) into static current steps of 2 mA, 1 mA, 0.5 mA, and 0.1 mA. Residual Co content is controlled via adjustment of charge Q, or more specifically, the duration of the second etching step. (b) Co content after dealloying measured by XRF, $x_{Co,XRF}$, as a function of nominal Co content $x_{Co,nom}$, which can be chosen freely for the GCD preparation. Error bars are given for the concentration measured in the XRF $x_{Co,XRF}$. The red line represents a linear fit to the data points. Reprinted from Ref. 42.

The GCD procedure used in this work has already been described in Sec. 3.2.6, with its characteristic current steps being depicted in Fig. 4.20(a). Co concentrations $x_{Co,XRF}$ obtained for $npPd_{(1-x)}Co_x$ prepared via the GCD procedure were experimentally determined using XRF spectrometry, with the results plotted in Fig. 4.20(b) as a function of nominal Co content $x_{Co,nom}$, which is related to a fixed charge value subtracted from the total dealloying charge in the GCD process (see Sec.3.2.6). Numerical values can be found in Tab. 4.2 below.

It should be noted that the Co concentrations of $npPd_{(1-x)}Co_x$ obtained from the GCD procedure are expected to be higher than nominal values, as minor side reactions (e.g. Pd oxidation) are consuming parts of the total charge. Indeed, the concentration detected in the XRF, $x_{Co,XRF}$, is about 5 wt% higher than the nominal Co content $x_{Co,nom}$ chosen for GCD. Considering these experimental results in Fig. 4.20(b), it can be clearly stated that GCD dealloying is able to tailor the total Co concentration in $npPd_{(1-x)}Co_x$. Porosity in the GCD process is expected to remain almost unaltered, which was confirmed by evaluating electrochemical double layer currents for $npPd_{(1-x)}Co_x$, which indicate similar surface areas (not shown). As demonstrated by KMC simulations and TEM imaging in previous works[41,46]
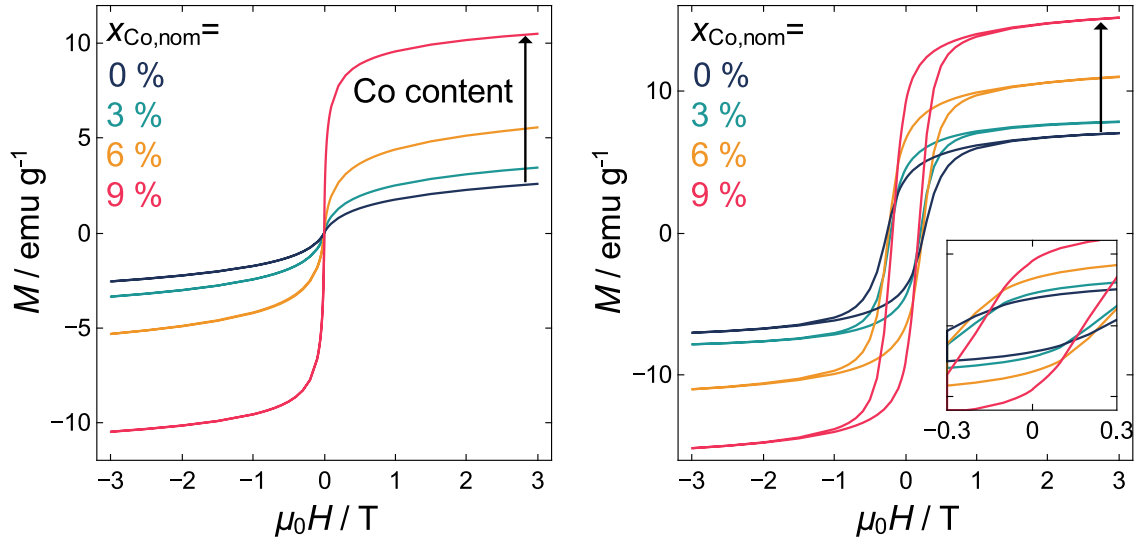
Figure 4.21: Magnetisation curves for GCD $npPd_{1-x}Co_x$ at 300 K (left) and 4.2 K (right) with different nominal Co concentrations $x_{Co,nom}$. Concentrations increased from $x_{Co,nom}=0$ wt% (dark blue) to $x_{Co,nom}=9$ wt% (red). Magnetisation M is plotted as a function of magnetic field $\mu_0 H$ in the range from -3 T to 3 T. For better comparability initial magnetisation curves are not depicted. The inset in the right graph shows the low field region for improved comparability of coercive fields. Arrows in both plots indicate the trend with increasing Co content $x_{Co,nom}$.

and shown in Fig. 4.6, Co atoms are not homogeneously distributed in the npPd matrix, but reside in Co-rich clusters, as relics of the base alloy retaining the original alloy composition. Those clusters are responsible for the superparamagnetic properties, as already indicated in the previous sections.

Field-dependent magnetisation measurements for $npPd_{1-x}Co_x$ at two different temperatures $T=300$ K and $T=4.2$ K are shown in Fig. 4.21. Magnetisation curves at 300 K on the left again show typical Langevin-shape, characteristic for superparamagnetism. Overall magnetisation increases with nominal Co concentrations $x_{Co,nom}$ (from blue to red) as indicated in the graph. High-field magnetisation for $x_{Co,nom}=0\%$ is $M_{3T,RT}=2.57$ emu g^{-1}, which increases to a value of $M_{3T,RT}=10.50$ emu g^{-1} for $x_{Co,nom}=9\%$. Values for all concentrations are presented in Tab. 4.2 in Sec. 4.3.4. Low-temperature magnetisation for $npPd_{1-x}Co_x$ is depicted in Fig. 4.21 on the right. Even the sample with the lowest nominal Co concentration $x_{Co,x}=0\%$ exhibits ferromagnetic hysteresis, indicating a minor fraction of Co still included in the Pd matrix. Saturation for all curves is still superimposed by a linearly increasing part, as for all samples characterised in this chapter. The trend of higher values of magnetisation for larger Co concentrations as in Fig. 4.21 on the left is also valid for the right plot, as shown
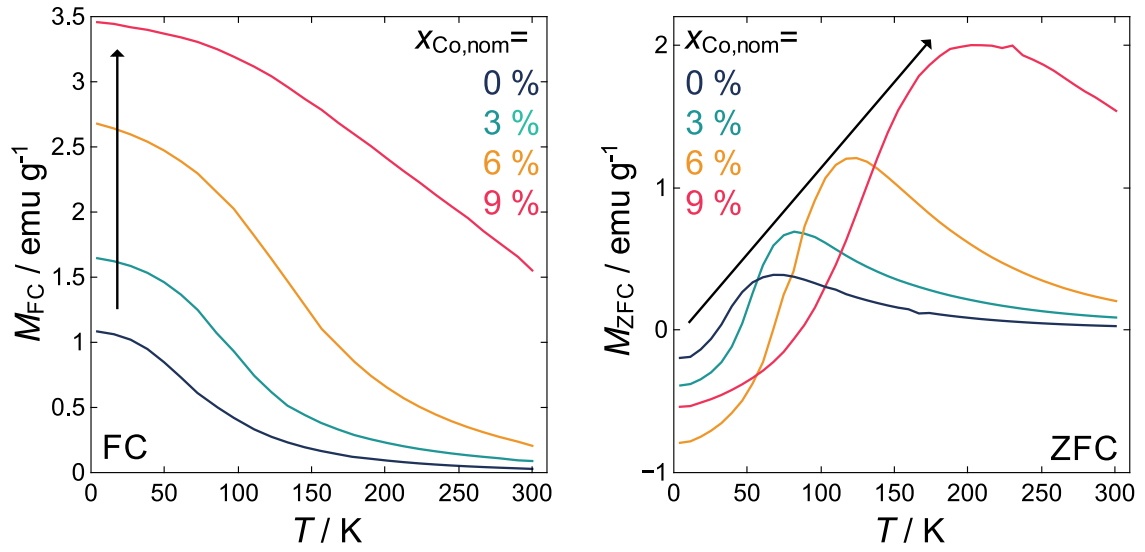
Figure 4.22: Field-cooled (FC - left) and zero-field-cooled (ZFC - right) magnetisation for GCD npPd(Co) with different nominal Co concentrations $x_{Co,nom}$ at a field of $\mu_0 H = 0.005$ T. Concentrations increased from $x_{Co,nom} = 0$ wt% (dark blue) to $x_{Co,nom} = 9$ wt% (red). Both magnetisations M_{FC} and M_{ZFC} are plotted as a function of temperature T in the range from 4.2 K to 300 K. Arrows in both plots indicate the trend with increasing Co content $x_{Co,nom}$. The plot uses the same colour coding as field-dependent magnetisation curves in Fig. 4.15.

by the arrow. Coercivities range between $\mu_0 H_{C,4K} = 0.18$ T for the highest Co concentration $x_{Co,nom} = 9$ % and $\mu_0 H_{C,4K} = 0.26$ T for the lowest Co concentration $x_{Co,nom} = 0$ %. However, coercivities as seen in the inset and in Tab. 4.2 in Sec. 4.3.4 do not follow a clear trend with Co concentration.

The magnetic *ex situ* characterisation for GCD npPd$_{1-x}$Co$_x$ is completed with FC/ZFC curves measured at a field of $\mu_0 H = 0.005$ T in Fig. 4.22. FC curves on the left show the typical increase with decreasing temperature and the bend towards the ordinate for low temperatures, which is a characteristic feature for all npPd(Co) samples regardless of preparation. The trend of an increase in M_{FC} with increasing Co concentration, in line with field-dependent magnetisation measurements in Fig. 4.21, is indicated by the arrow. Room-temperature magnetisation for the different Co concentrations on the right end of the curves is already markedly different at a small field of $\mu_0 H = 0.005$ T. Zero-field-cooled magnetisation M_{ZFC} exhibits pronounced superparamagnetic blocking peaks, which strongly shifts to higher M_{ZFC}- and larger T_B-values for higher nominal Co concentrations $x_{Co,nom}$ (from green to blue). While a value of $T_B = 68$ K is obtained for $x_{Co,nom} = 0$%, T_B is 202 K for $x_{Co,nom} = 9$%, indicating larger superparamagnetic sizes for larger total Co concentration $x_{Co,nom}$. Values for the blocking temperature are added to the data in the overview table Tab. 4.2 in sec. 4.3.4. Negative

initial magnetisations at T=4.2 K are observed again as in Fig. 4.16 and Fig. 4.19, which are a common theme for all the ZFC measurements in this chapter. A conceivable reason for the negative initial magnetisation is residual flux trapped in the magnet after the measurement of magnetisation curves, which might be prevented by using a full demagnetisation procedure in future experiments. GCD dealloying offers the great advantage that Co content can be fixed manually in a broad range and not only indirectly via potential (PCD) as in Sec. 4.3.1. As a consequence, the superparamagnetic size of Co-rich clusters, where residual Co is located, can also be adjusted directly. Using this technique, magnetisation tuning measurements in dependence of superparamagnetic cluster sizes are presented in Sec. 4.4.2.3.

4.3.4 Summary of magnetic properties

Magnetic key quantities for all presented dealloying procedures (PCD, PCD+T, GCD) in this chapter are summarised in an overview table in Tab. 4.2 for easy comparability. Dealloying method and the relevant dealloying parameters are given in the first two columns. Co content determined via XRF and blocking temperature T_{B} as a measure for the superparamagnetic cluster size follow in columns 3 and 4. High-field magnetisation ($M_{\mathrm{3T,RT}}$ and $M_{\mathrm{3T,4K}}$) and coercivity ($\mu_0 H_{\mathrm{C,RT}}$ and $\mu_0 H_{\mathrm{C,4K}}$) at 300 K and 4.2 K are collected in the remaining four columns.

Table 4.2: Magnetic properties of npPd(Co) from different preparation routes: Dealloying method and relevant dealloying parameters are stated in the first two columns. $x_{\text{Co,XRF}}$ is the Co concentration measured via XRF, T_{B} the blocking temperature, $M_{\text{3T,RT}}$ the magnetisation at $\mu_0 H=3$ T at room temperature, $M_{\text{3T,4K}}$ the magnetisation at $\mu_0 H=3$ T at 4.2 K, $\mu_0 H_{\text{C,4K}}$ the coercive field at 4.2 K and $\mu_0 H_{\text{C,RT}}$ the coercive field at room temperature. The figures with the corresponding magnetisation curves and ZFC/FC curves for PCD, PCD+T, GCD, and QCD are referenced in the last column.

method	parameters	$x_{\text{Co,XRF}}$ / wt%	T_{B} / K	$M_{\text{3T,RT}}$ / emu g^{-1}	$M_{\text{3T,4K}}$ / emu g^{-1}	$\mu_0\,H_{\text{C,4K}}$ / T	$\mu_0\,H_{\text{C,RT}}$ / T	figure
PCD	U_{D}=0.40 V, I_{R}=0.1 mA	26.3	117	8.40	12.04	0.12	-	4.15 / 4.16
PCD	U_{D}=0.45 V, I_{R}=0.1 mA	9.3	96	3.96	10.80	0.25	-	4.15 / 4.16
PCD	U_{D}=0.50 V, I_{R}=0.1 mA	6.5	89	3.78	9.56	0.23	-	4.15 / 4.16
PCD	U_{D}=0.55 V, I_{R}=0.1 mA	5.0	96	3.29	10.39	0.15	-	4.15 / 4.16
PCD	U_{D}=0.60 V, I_{R}=0.1 mA	7.2	117	4.38	9.89	0.20	-	4.15 / 4.16
PCD	U_{D}=0.70 V, I_{R}=0.1 mA	7.3	89	2.60	9.78	0.23	-	4.15 / 4.16
PCD	U_{D}=0.80 V, I_{R}=0.1 mA	5.6	46	1.05	5.52	0.21	-	4.15 / 4.16
PCD	U_{D}=0.55 V, I_{R}=0.01~mA	5.7	103	2.52	10.57	0.16	-	4.18 / 4.19
PCD+T	T_{A}=373 K, U_{D}=0.55 V, I_{R}=0.01 mA	6.0	82	2.42	9.35	0.16	0.001	4.18 / 4.19
PCD+T	T_{A}=573 K, U_{D}=0.55 V, I_{R}=0.01 mA	5.3	61	1.38	8.05	0.16	0.002	4.18 / 4.19
PCD+T	T_{A}=773 K, U_{D}=0.55 V, I_{R}=0.01 mA	5.5	33	0.58	4.40	0.11	0.005	4.18 / 4.19
PCD+T	T_{A}=973 K, U_{D}=0.55 V, I_{R}=0.01 mA	5.1	-	0.22	0.73	0.05	0.009	4.18 / 4.19
GCD	$x_{\text{Co,nom}}$=0%	3.8	68	2.57	7.03	0.26	-	4.21 / 4.22
GCD	$x_{\text{Co,nom}}$=3%	6.7	82	3.40	7.84	0.21	-	4.21 / 4.22
GCD	$x_{\text{Co,nom}}$=6%	8.3	124	5.45	11.00	0.24	-	4.21 / 4.22
GCD	$x_{\text{Co,nom}}$=9%	13.4	202	10.50	15.15	0.18	-	4.21 / 4.22
QCD	Q/Q_{tot}=0.0 (alloy)	69.9	-	115.42	-	-	0.004	4.2(b)

All different dealloying methods allow an efficient tailoring of the Co-content in npPd, where measured values between $x_{\mathrm{Co,XRF}}$=3.8 and 26.3% were achieved as seen in Tab. 4.2. Cobalt content from XRF $x_{\mathrm{Co,XRF}}$ and EDS, which is plotted in Fig. 4.17 in at%, show the same trends, although numerical values are systematically higher by about 2 wt% for $x_{\mathrm{Co,XRF}}$. This systematic offset might be explained by a larger interaction volume of X-rays with the sample in XRF, compared to electrons in EDS. The surprisingly large deviation for the lowest dealloying potential U_{D}=0.40 V ($x_{\mathrm{Co,XRF}}$=26.3 wt% and $x_{\mathrm{Co,EDS}}$=8.2 wt%, which corresponds to 14 at%), might be related to a residual alloy part captured in the XRF analysis, but not in the EDS analysis, although this remains to be clarified. The blocking temperature T_{B} generally follows the trend in Co content for the PCD (see also Fig. 4.17) and GCD dealloying, while independent control over the blocking temperature was facilitated using a temperature-treatment in PCD+T dealloying. This is in line with the picture that Co is mainly located in Co-rich clusters under the Pd surface, which grow with total Co-concentration. Upon thermal treatment, the Co-concentration is considered to be homogenised, by Co-rich clusters shrinking at the expense of Co-content in the surrounding Pd-matrix. Importantly, the ligament surface, which is depleted of Co-atoms in the dealloying process, is also repopulated with Co-atoms during thermal treatment as described in Sec. 4.3.2. A homogenisation of Ag in npAu(Ag) has been demonstrated by KMC simulations at elevated temperatures[69], where analogous effects were observed. Ligament and pore growth upon thermal treatment are well-documented in literature for dealloyed materials[138,181,184,190], including npPd[67,71]. As ligament size effects are considered to be of minor importance for the magnetic properties of npPd(Co) here, the reader is referred to the Master's thesis of Alexander Steiner (Ref. 47) for an assessment of ligament sizes during coarsening of PCD+T npPd(Co).

4.4 Magnetic property tuning using nanoporous Pd

Here the magnetoelectric effects in dealloyed nanoporous materials are introduced. Annealing strategies to tailor the Co content and distribution presented in Sec. 4.3 are applied to maximise magnetoelectric effects. Firstly, in Sec. 4.4.1 (pseudo-)capacitive charging of the electrochemical double-layer is investigated as external bias in different electrolytes for PCD+T npPd(Co) electrodes. These measurements were a core part of the Masters's project of Alexander Steiner[47], which I assisted in conceptualisation and experiment. Furthermore, hydrogen adsorption is investigated as a stimulus for magnetisation tuning for PCD+T npPd(Co) in Sec. 4.4.2.1. The core part of this thesis in Sec. 4.4.2 is devoted to the application of various nanoporous PdCo electrodes in hydrogen magneto-ionics. For that purpose hydrogen-charging, i.e. absorption of hydrogen, was used as an electrochemical bias reaction to influence magnetic properties in a variety of nanoporous Pd materials.

4.4.1 (Pseudo-)capacitive charging of npPdCo electrodes

4.4.1.1 Na-based electrolyte

A common electrolyte system used for double-layer charging are Na^+-ions in propylene carbonate (PC)[35,191–193]. The simplest way to prepare this electrolyte is to immerse small pieces of metallic Na into a PC solution, which will react with trace water and provide the necessary Na^+- and OH^--ions. The anhydrous nature of this electrolyte enables the application of large voltages without facing the limitation of water electrolysis. Here, npPd(Co) (U_D=0.7 V; I_R=0.1 mA) was capacitively charged, while the magnetic response upon voltage application was monitored as shown in Fig. 4.23.

The most prominent feature in Fig. 4.23 is a drifting baseline to higher values of magnetic moment, while no noticeable direct effect of capacitive charging (i.e. voltage application) on the magnetic properties of npPd(Co) was observed. The overall current was low in the order of μA, as to be expected for purely capacitive double-layer charging. This experiment suggests a negligible influence of purely capacitive double-layer charging on the magnetic properties of npPd(Co), which is further investigated in the following sections.
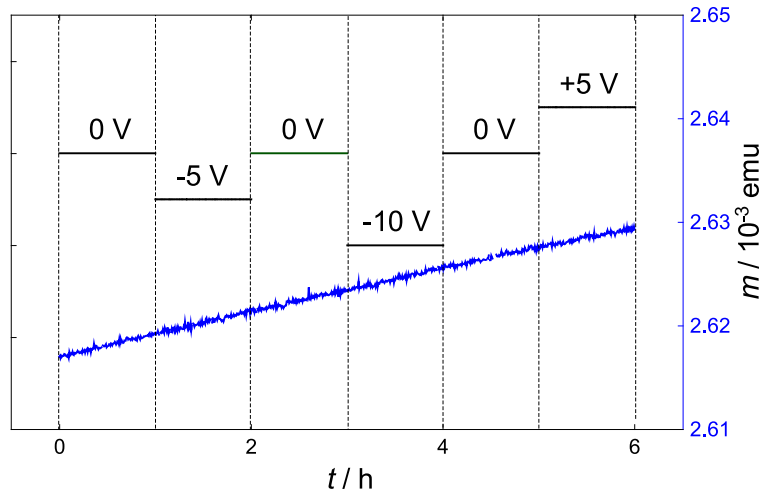
Figure 4.23: Variation of magnetic moment m as a function of time t under application of potentials for capacitive charging of npPd(Co) (U_D=0.7 V; I_R=0.1 mA) in PC containing Na$^+$-ions. The applied potentials are shown as black lines, points of switching are indicated by the dashed vertical lines.

4.4.1.2 Li-based electrolyte

Inspired by battery research, Li$^+$-ion-containing electrolytes have also received attention for magnetic tuning applications in the electrochemical double-layer[8,10,13]. Here, the charge response upon (pseudo-)capacitive double-layer charging in 1 M LiPF$_6$ dissolved in a 1:1 mixture of ethylene carbonate and ethyl methyl carbonate (EC/EMC) is presented for npPd(Co) with different Co distributions. For that purpose, the thermal annealing method presented in Sec. 4.3.2 is utilised to prepare samples with varying Co-distributions. For measurements in this section, the higher Co-content on the surface and the lower total surface area with higher annealing temperatures are considered to be the most important factors for the magnetic response upon double-layer charging. In contrast to the Na$^+$/PC system presented in the previous section, chemical reactions dominate the current upon application of larger voltages for LiPF$_6$ in alkyl carbonates[8]. The presence of HF, which forms via the reaction of PF$_6^-$ with trace water, leads to a limiting cathodic potential, where HF reduction sets in. Electrolyte oxidation limits the upper vertex potential. Due to the higher amount of Co on the surface, pseudo-capacitive charging, i.e. reversible chemical surface reactions involving the oxidation/reduction of Co, can contribute to the actual charging current in the double-layer regime.
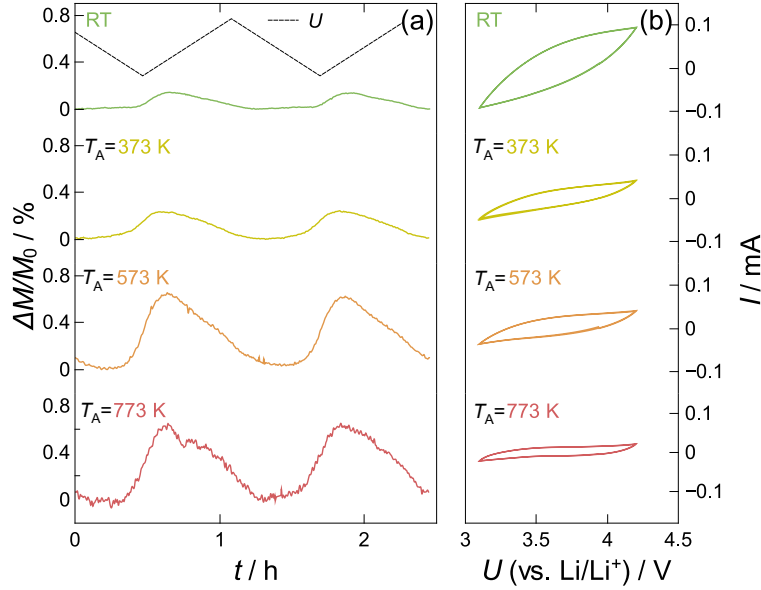
Figure 4.24: Charging response of annealed npPd(Co) in an LiPF$_6$-based electrolyte: (a) Relative variation of magnetisation $\Delta M/M_0$ at 0.5 T as a function of time t for two voltage cycles with a scan rate of 0.5 mVs^{-1} between U=3.1 and 4.2 V. The voltage variation between U=3.1 and 4.2 V is indicated as black dashed line. (b) Corresponding cyclic voltammograms as representation of current I over voltage U. Annealing temperatures are given in the respective subplots. With increasing annealing temperature from top to bottom, the Co concentration on the surface increases. A small drift in magnetisation was subtracted from all curves for improved comparability.

The magnetic response of annealed npPd(Co) (U_D=0.55 V; I_R=0.01 mA, T_A=373 K, 573 K, 773 K and RT) upon (pseudo-)capacitive charging in LiPF$_6$ in a voltage window between 3.1 and 4.2 V is presented in Fig. 4.24 and Fig. 4.25. The annealing temperature was held 10 min for each sample, ramp time for heating and cooling are not included.

In Fig. 4.24(a) small cyclic changes in relative magnetisation $\Delta M/M_0$ well below 1% are observed for all annealing temperatures. The maximum in magnetisation roughly corresponds to the point of the largest negative charge, i.e lies close to the point where current reverses its sign in Fig. 4.24(b). All CVs in 4.24(b) exhibit no characteristic features, typical for (pseudo-)capacitive charging. The shape of the curve changes from a lentil-shape with higher current magnitude for the room temperature sample to a more rectangular characteristics with lower currents for higher annealing temperatures. This behaviour can qualitatively be understood in terms of the lower total surface areas for nanoporous Pd(Co) with higher annealing temperatures (see Sec. 4.3.2). As all measurements shown in Fig. 4.24 featured a constant voltage scan rate of 0.5 mVs^{-1}, both higher currents and the lentil-shape distortion of the CV in the double-layer regime are expected for larger surface area samples.
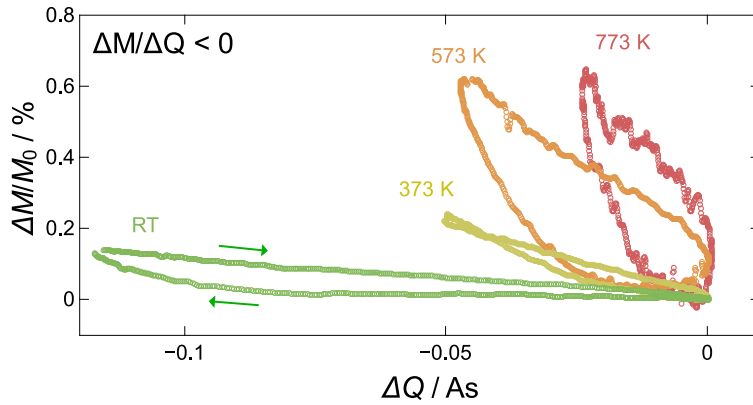
Figure 4.25: Alternative representation of the magnetic response of annealed npPd(Co) upon double-layer charging in a LiPF$_6$-based electrolyte (cf. Fig 4.24): Relative variation of magnetisation $\Delta M/M_0$ at 0.5 T as a function of charge Q upon voltage cycling with a scan rate of 0.5 mVs^{-1} between U=3.1 and 4.2 V. Annealing temperatures are given in the plot. The cycling direction is indicated by the arrows, which is the same for all curves. All samples exhibit a negative magneto-electric charge coefficient ($\Delta M/Q < 0$).

For a better understanding of the underlying magnetic mechanism upon (pseudo-)capacitive double-layer charging in LiPF$_6$ in EC/EMC, the relative changes in magnetisation $\Delta M/M_0$ are shown in Fig. 4.25 as a function of applied charge Q.

In Fig. 4.25 hysteretic behaviour of the relative magnetisation variation with charge is revealed. Hysteresis is visible for all annealing temperatures, with the higher temperatures exhibiting both a steeper slope (a higher magneto-electric charge coefficient $\Delta M/Q < 0$) and a larger hysteresis. The steeper slopes are a direct result of the limited amount of transferred charge and the slightly larger magnetisation changes for higher-temperature samples. Hysteretic charge behaviour in electrochemistry is generally attributed to irreversible chemical reactions, i.e. reaction and backward reaction being separated by more than $\Delta U > 0.06$ V in voltage. Here, hysteresis in the relative magnetisation $\Delta M/M_0$ as a function of charge Q might well be related to pseudocapacitive reactions which take place in the double-layer regime. For a quantitative assessment of the magneto-electric performance in LiPF$_6$ in EC/EMC, magneto-electric voltage coefficients $\alpha_{C,V}$ for the results presented in this section were calculated according to Ref. 4 and are presented in Tab. 5.1 in Sec. 5.2.3.
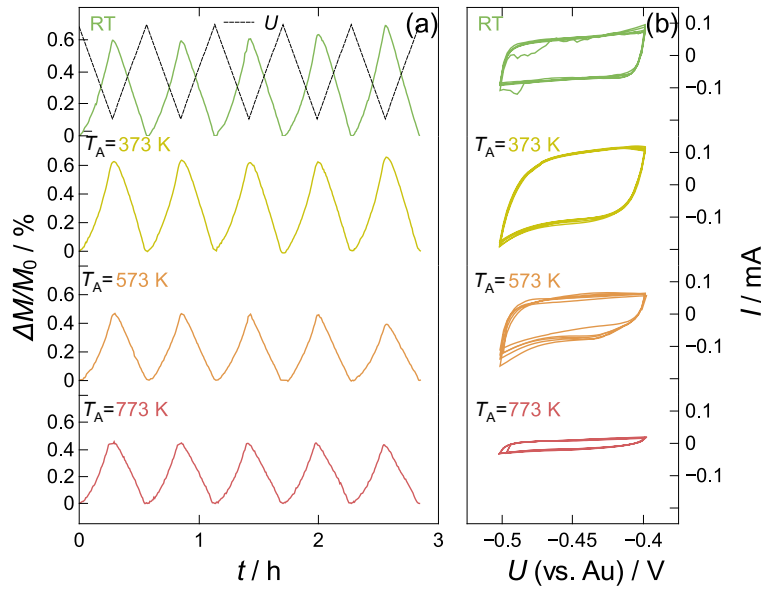
Figure 4.26: Charging response of annealed npPd(Co) in an aqueous KOH-based electrolyte: (a) Relative variation of magnetisation $\Delta M/M_0$ at 0.5 T as a function of time t for five voltage cycles with a scan rate of 0.5 mVs^{-1} between U=-0.5 and -0.4 V. The voltage variation between U=-0.5 and -0.4 V is indicated as black dashed line. (b) Corresponding cyclic voltammograms as representation of current I over voltage U. Annealing temperatures are given in the respective subplots. With increasing annealing temperature from top to bottom, the Co concentration on the surface increases. A small drift in magnetisation was subtracted from all curves for improved comparability.

4.4.1.3 Aqueous electrolyte

For hydrogen-charging, the electrolyte of choice throughout this thesis was 1 M aqueous potassium hydroxide solution, as npPd electrodes were found to have a reliable performance in KOH solution upon repetitive cycling, which was not the case for H_2SO_4 or KCl based aqueous electrolytes. Here (pseudo-)capacitive charging of npPd(Co) electrodes is studied in the same electrolyte solution in the double-layer regime. In analogy to measurements presented in the previous section, samples with varying Co-distributions produced by thermal annealing of dealloyed npPd(Co) (see Sec. 4.3) are investigated in the aqueous KOH electrolyte. Due to the aforementioned limitation of water electrolysis, the accessible voltage window for double-layer charging (ΔU=0.1 V) is smaller than in the non-aqueous electrolytes discussed before. Results for the (pseudo-)capacitive double-layer charging of temperature-treated npPd(Co) (U_D=0.55 V; I_R=0.01 mA, T_A=373 K, 573 K, 773 K and RT) in aqueous electrolyte are shown in Fig. 4.26 and Fig. 4.27, which are represented analogously to the results for charging in the LiPF$_6$-based electrolyte (Sec. 4.4.1.2 - Fig. 4.24 and Fig. 4.25).
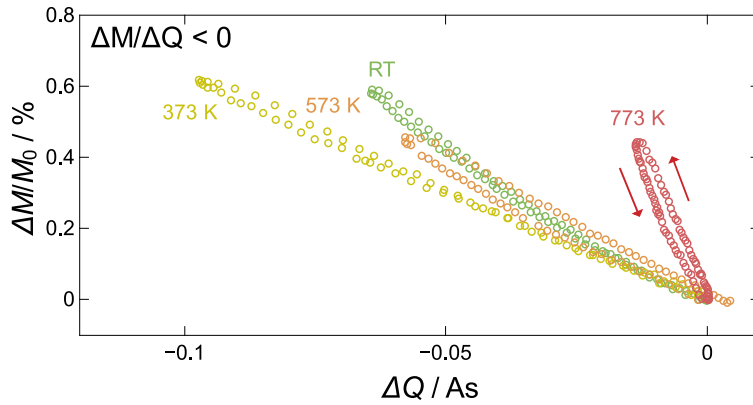
Figure 4.27: Alternative representation of the magnetic response of annealed npPd(Co) upon double-layer charging in the aqueous KOH-based electrolyte (cf. Fig 4.26): Relative variation of magnetisation $\Delta M/M_0$ at 0.5 T as a function of charge Q upon voltage cycling with a scan rate of 0.5 mVs^{-1} between U=-0.5 and 0.4 V. Annealing temperatures are given in the plot. Cycling direction is given by the arrows. All samples exhibit a negative magneto-electric charge coefficient ($\Delta M/Q < 0$).

A periodically changing relative magnetisation $\Delta M/M_0$ over time t is also noticed in Fig. 4.26(a). The maximum relative change is again well below 1% for samples irrespective of their temperature-treatment. In general, the tuning magnitude is similar for all annealing temperatures, with only a slight decrease from $\Delta M/M_0$=0.6% to 0.4% for 573 K and 773 K. Note that this trend is reversed compared to measurements in the Li-based electrolyte in Fig. 4.24(a), where the relative tuning magnitude increases with annealing temperature. Magnetisation peaks again close to the point in the CV, where current changes from negative to positive sign. In Fig. 4.26(b) CVs again show the almost rectangular shape typical for the double-layer regime, with the rough overall trend of decreasing current amplitudes with increasing annealing temperature due to lower total surface areas for high-temperature specimen.

The alternative representation of relative changes of magnetisation as a function of charge Q is shown in Fig. 4.27 for the same set of measurements plotted over time t in Fig. 4.26. Regardless of annealing temperature npPd(Co) shows almost linear behaviour of relative change in magnetisation $\Delta M/M_0$ as a function of charge Q. What stands out in contrast to the analogous measurements in the Li-based electrolyte in Fig. 4.25, is the absence of hysteresis. The slope of the curves, representing the magneto-electric charge coefficient ($\Delta M/Q < 0$), is negative for all samples, as for the case in LiPF$_6$ in EC/EMC. The sample annealed at 773 K displays the steepest slope, while slopes for the other annealing temperatures are similar.

4.4.2 Hydrogen-charging of npPdCo for magneto-ionics

In this section, the magnetic effects in nanoporous PdCo upon hydrogen-charging are introduced. This part largely builds upon material published in Ref. 41 and Ref. 42, but also includes previously unpublished new material. At first measurements in the H-adsorption regime are presented for annealed npPd(Co) samples in Sec. 4.4.2.1, only extending the measurement range to lower potential limits compared to the measurements presented in the previous in Sec. 4.4.1. In Sec. 4.4.2.2 the influence of hydrogen on the magnetic hysteresis loops of different npPd(Co) sample types is investigated. Lastly, the direct tuning of magnetisation in npPd(Co) via hydrogen-charging is presented in Sec. 4.4.2.3

4.4.2.1 Hydrogen adsorption for magnetisation tuning

Hydrogen adsorption on metal surfaces is a phenomenon which occurs for the majority of d-band metals[194], with Ni, Pt, and Pd being the most prominent examples. Appreciable hydrogen absorption into the bulk of metals at relatively low temperatures and pressures is limited to fewer materials such as Ti or Pd[195]. While reports on the effect of hydrogen absorption on the magnetic properties of metals are plentiful, the surface-limited hydrogen adsorption process has only been rarely studied with respect to changing magnetic properties[196–199]. Connecting to the double-layer charging measurements in aqueous electrolyte presented in Fig. 4.26 in the previous section, the potential limit for CV measurements of annealed npPd(Co) in the same electrolyte is lowered to more negative values, where hydrogen adsorption takes place. The nanoporous nature of npPd(Co) samples make hydrogen adsorption as a surface reaction also an interesting playground within the field of magneto-ionics.

Changes in magnetisation in the hydrogen-adsorption regime for annealed npPd(Co) (U_D=0.55 V; I_R=0.01 mA, T_A=373 K, 573 K, 773 K and RT) are presented in Fig. 4.28 and Fig. 4.29 in similar plots as for the double-layer measurements above.

A periodic variation of relative change in magnetisation $\Delta M/M_0$ is again observed as a function of time t for all annealing temperatures in Fig. 4.28(a). The magnitude of the variation increased to 3-5% compared to double-layer measurements (Fig. 4.26) with no clear
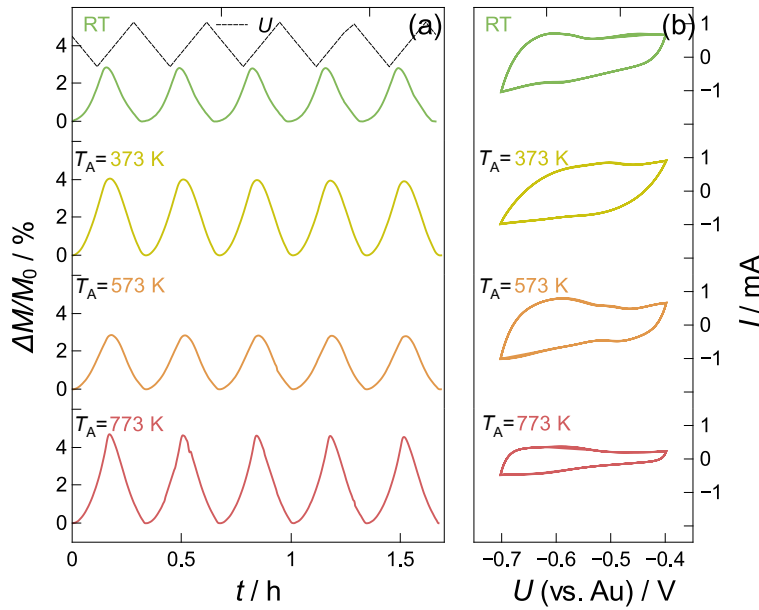
Figure 4.28: Hydrogen adsorption on annealed npPd(Co) in an aqueous KOH-based electrolyte: (a) Relative variation of magnetisation $\Delta M/M_0$ at 0.5 T as a function of time t for five voltage cycles with a scan rate of 0.5 mVs^{-1} between U=-0.7 and -0.4 V. The voltage variation between U=-0.7 and -0.4 V is indicated as black dashed line. (b) Corresponding cyclic voltammograms as representation of current I over voltage U. Annealing temperatures are given in the respective subplots. A small drift in magnetisation was subtracted from all curves for improved comparability.

trend with increasing annealing temperature. In the CV plots of current I as a function of U naturally higher currents up to 1 mA were observed in a larger potential window extending to U=-0.7 V as the lower limit. A distortion of the more rectangular characteristics at lower potentials compared to the double-layer (Fig. 4.26) is found, indicating the onset of hydrogen adsorption.

In the alternative representation of the same measurements as relative changes in magnetisation $\Delta M/M_0$ over charge Q in Fig. 4.29 for all samples a negative magneto-electric charge coefficient ($\Delta M/Q < 0$) is found. For low absolute values of charge ΔQ >-0.1 As, the curves coincide with the measured lines in the double-layer regime in Fig. 4.27, while for larger absolute values of charge ΔQ <-0.1 As a small loop is observed, hinting towards the hydrogen adsorption reaction. Interestingly, the direction of the loop in charge is reversed compared to the (minor) loop in the double-layer. Slopes are similar for all curves beside the npPd(Co) sample treated at 773 K, where a steeper slope was observed. The reason for this is the lower amount of charge needed to obtain a comparable magnetisation variation. This can be qualitatively understood in terms of the larger surface Co-content for higher-temperature
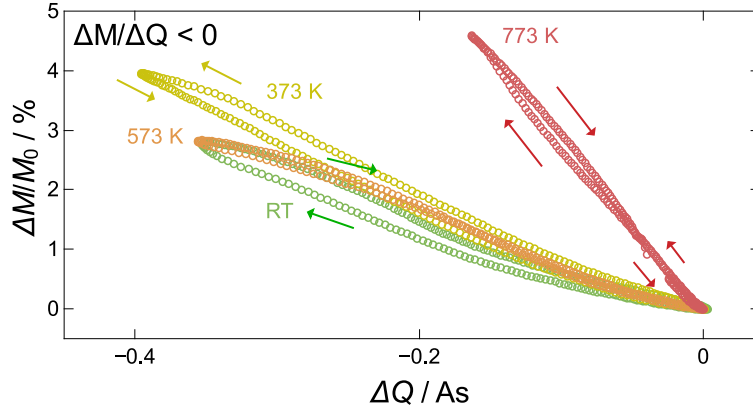
Figure 4.29: Alternative representation of the magnetic response of annealed npPd(Co) upon hydrogen adsorption in an aqueous KOH-based electrolyte (cf. Fig 4.28): Relative variation of magnetisation $\Delta M/M_0$ at 0.5 T as a function of charge Q upon voltage cycling with a scan rate of 0.5 mVs^{-1} between U=-0.7 and -0.4 V. Annealing temperatures are given in the plot. Cycling direction is given by the arrows. All samples exhibit a negative magneto-electric charge coefficient ($\Delta M/Q < 0$).

samples. The mechanism behind the magnetisation changes upon hydrogen adsorption is addressed in the discussion in Sec. 5.2.2

As a complementary measurement, a npPd(Co) sample which underwent a longer homogenisation treatment (T_A =773 K for 1h) was investigated in the hydrogen adsorption regime in 1 M KOH in a similar setup in Fig. 4.30. Nine CV cycles were recorded in a voltage range between U=0 and 0.2 V corresponding to hydrogen adsorption with a scan rate of 0.1 mVs^{-1}. The voltage range appears shifted compared to measurements above due to the use of a quasi-reference electrode and the different surface compositions of the samples. Both charge Q in (b) and magnetisation $\Delta M/M_0$ in (c) vary in phase and are only slightly shifted with respect to voltage U in (a). The CV representation of current I as a function of U shows a stronger hydrogen discharging peak compared to the previous measurements, with also a stronger total variation of relative magnetisation of up to 20 %, which drifts to lower values of magnetisation. An intriguing finding compared to the measurements for annealed npPd(Co) presented in Fig. 4.28 and Fig. 4.29 is the changed sign of the magneto-electric charge coefficient $\Delta M/Q > 0$, which is now positive. The positive coefficient can be interpreted in terms of simple hydrogen-related band filling with electrons.
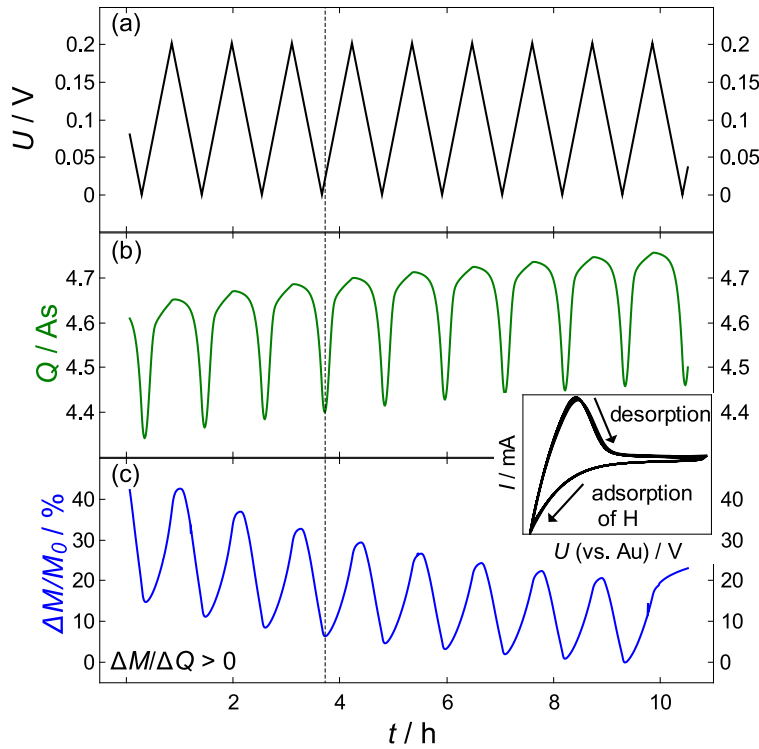
Figure 4.30: Hydrogen adsorption effect on the magnetic properties of homogenised npPd(Co) (1h annealing time, T_A=773 K): voltage U (a), charge Q (b) and relative change in magnetisation $\Delta M/M_0$ at 0.5 T (c) all as a function of time t. The CV representation of current I versus U is shown in the inset. The scan rate was 0.1 mVs^{-1}, the electrolyte was 1 M KOH.

4.4.2.2 Hydrogen-charging for hysteresis loop tuning

Tuning complete magnetisation curves rather than only changing the saturation magnetisation of a material constitutes a large part of research in magneto-ionics, pursuing the idea of switching between soft- and hard-magnetic states for magnetic memory devices. Thermal switching between soft- and hard-magnetic states for writing and data storage, known as heat-assisted magnetic recording[2], is a technology already used commercially. An all-electrical switching of magnetisation curves for memory application is a strong driving force for the magneto-electric research field in general.

Here such possibilities are investigated for npPd(Co). As presented in Sec.4.3, as-dealloyed npPd(Co) typically shows superparamagnetic behaviour at room temperature. As a stimulus for magnetisation switching a constant voltage of -1 V (vs. Au) is applied to npPd(Co) for hydrogen-charging in a 1 M aqueous KOH solution. This voltage resides in the hydrogen absorption regime, as shown later in the CV in Fig. 4.34. Changes in the magnetisation curve
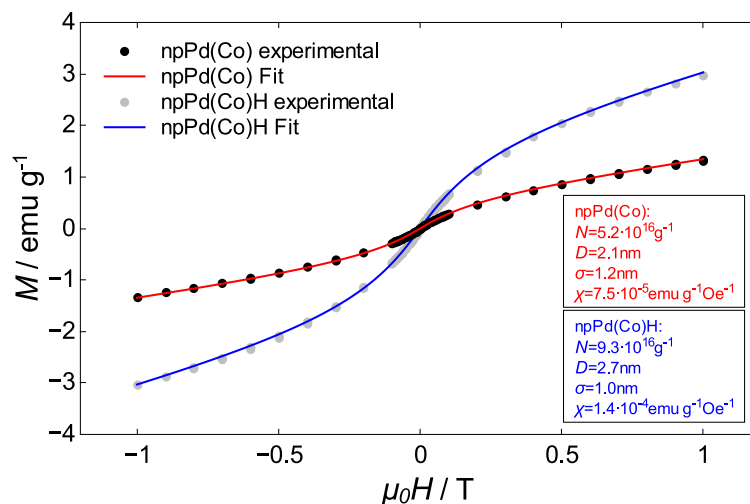
Figure 4.31: Hydrogen-charging effect on magnetisation curves of npPd(Co): magnetisation M as a function of applied field $\mu_0 H$ between -1 T and 1 T at 300 K for pristine npPd(Co) (black dots) after hydrogen-charging at U=-1.0 V vs. Au (grey dots). The charging potential was held constant during recording of the full hysteresis curve and for 2 h for equilibration before. Curves were fitted according to Eq. 5.4, with the fits for the pristine npPd(Co) and hydrogen-charged sample npPd(Co)H drawn in red and blue, respectively. Reprinted from the supporting material of Ref. 41.

for npPd(Co) (U_D=0.7 V; I_R=0.1 mA) between $\mu_0 H$=-1 T to 1 T upon hydrogen-charging at -1 V (vs. Au) are presented in Fig. 4.31.

Magnetisation curves as magnetisation M as a function of applied field $\mu_0 H$ in Fig. 4.31 exhibit superparamagnetic behaviour for both hydrogen-charged (grey) and pristine state (black). Nonetheless, a clearly steeper slope of the entire curve is observed for the hydrogen-charged sample. The model for superparamagnetic magnetisation curves presented in Sec. 5.2.2 was used to fit both curves, as shown in blue for the hydrogen-charged state and red for the pristine state. The resulting fit parameters are given directly in Fig. 4.31. An increase of the mean diameter of superparamagnetic entities from 2.1 nm to 2.7 nm is obtained from the fit, while also the total number of magnetic entities N and the paramagnetic background χ increase as seen in the fit parameters. Increasing cluster size in the fit accounts mostly for the increasing steepness at low fields <0.1 T, while N and χ become more relevant at higher fields. An increase in the effective magnetic cluster size is also postulated as the core mechanism behind the hydrogen-induced changes in the magnetic properties of npPd(Co) in Sec. 5.2.2. While a complete crossover to a ferromagnetic state could not be achieved in npPd(Co) (U_D=0.7 V; I_R=0.1 mA), hydrogen-charging leads to stronger superparamagnetic behaviour with larger susceptibility and moment. However, the effect observed here was not fully reversible, likely due to the strongly negative charging potential of U=-1.0 V, where hydrogen gas evolution accompanies the charging effect. One may speculate that hydrogen-induced defects in the Pd lattice[200] can lead to an irreversible contribution of hydrogen-charging on the magnetisation curves, although this peculiarity was not further investigated within this thesis.

Switching in magnetisation curves was also attempted for npPd(Co) (U_D=0.7 V; I_R=0.1 mA) at lower overall potentials. While the overall procedure remained similar to the experiment described above, the hydrogen-charging potential was chosen to be less negative as U=-0.6 V and two magnetisation curves at U=-0.3 V, close to the OCP, were measured prior to and after hydrogen-charging to test the reversibility of the mechanism. Magnetisation curves in the range from $\mu_0 H$=-1 T to 1 T for npPd(Co) in 1 M KOH at two different potentials are shown in Fig. 4.32.

Magnetisation curves indicated a minor ferromagnetic superposition to the otherwise superparamagnetic behaviour of npPd(Co) already at U=-0.3 V prior to the hydrogen-charging treatment in Fig. 4.32(a). The ferromagnetic part likely stems from an alloy residual covered during etching by the contact wires. At a low hydrogen-sorption potential of U=-0.6 V
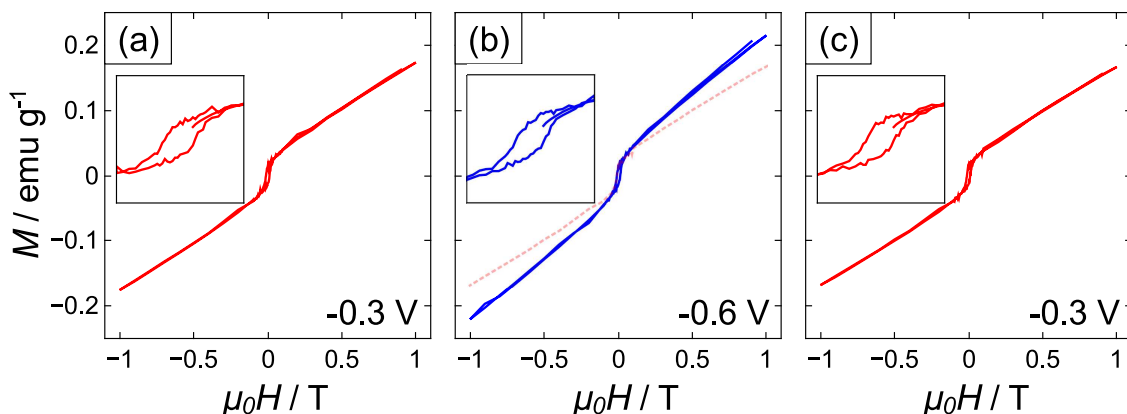
Figure 4.32: Hydrogen-charging effect on magnetisation curves of partly ferromagnetic npPd(Co): magnetisation M as a function of applied field $\mu_0 H$ at 300 K between -1 T and 1 T for a sample prior to hydrogen-charging at U=-0.3 V (a), after hydrogen-charging at U=-0.6 V (b) and after hydrogen-discharging again at U=-0.3 V (c). The small ferromagnetic hysteresis is shown enlarged in the insets. For comparison the curve from (a) is also given as grey dashed line in (b).

the slope of the magnetisation curve changes again in (b). After hydrogen desorption in Fig. 4.32(c) the magnetisation curve returns to its state before hydrogen-sorption. Thus, reversibility of the tuning effect on the magnetisation curves is achieved under mild hydrogen-sorption conditions. The potential used here U=-0.6 V lies close to the border of hydrogen ad- and absorption in the CV (not shown). As the effect is clearly similar compared to the results for strong hydrogen absorption at U=-1.0 V in Fig. 4.31, the effect here is attributed to absorbed hydrogen rather than adsorbed hydrogen, which was shown to have only a slight effect on the magnetic properties in Sec. 4.4.2.1.

As a hydrogen-induced transition from superparamagnetism to collective ferromagnetism was not observed in the magnetisation curves for npPd(Co) (U_D=0.7 V; I_R=0.1 mA), a homogenised npPd(Co) sample (1 h, T_A=773 K) was tested for that purpose. Magnetisation curves between $\mu_0 H$=-1 T and 1 T in 1 M KOH solution recorded at OCP, and after hydrogen absorption at U=-0.8 V and U=-1.0 V are presented in Fig. 4.33.

While the homogenised sample retained the typical superparamagnetic magnetisation characteristics at OCP in Fig. 4.33(a), in the hydrogen-charged state at U=-0.8 V in (b) a small ferromagnetic contribution to the superparamagnetic magnetisation curve becomes visible. A coercive field of $\mu_0 H_C$=0.012 T (9550 Am^{-1}) was extracted from Fig. 4.33(b). As for magnetisation curves of npPd(Co) without temperature-treatment in Fig. 4.31, hydrogen-charging produces a clearly enhanced slope of the (super-)paramagnetic background in the
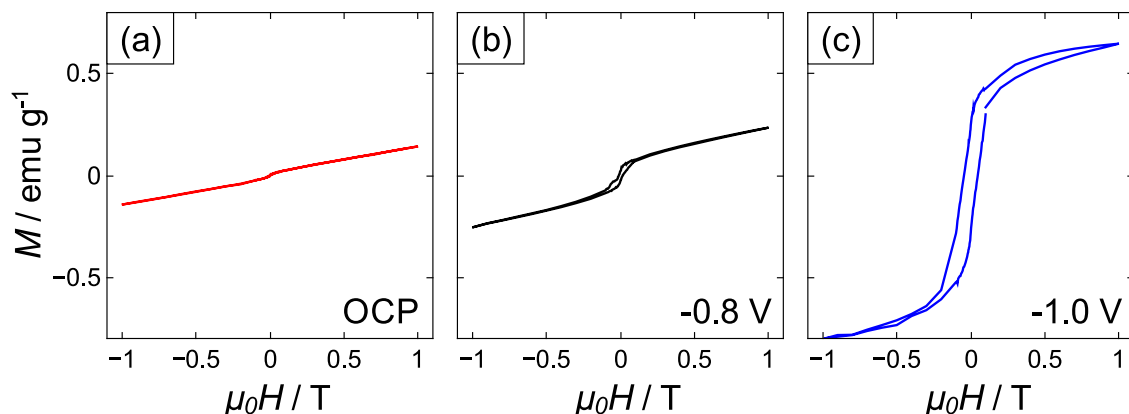
Figure 4.33: Hydrogen-charging effect on magnetisation curves for homogenised npPd(Co) (1h annealing time, T_A=773 K): magnetisation M as a function of applied field $\mu_0 H$ at 300 K between -1 T and 1 T for a sample prior to hydrogen-charging at the open circuit potential (OCP) (a), after hydrogen-charging at U=-0.8 V (b) and after hydrogen-charging at U=-1.0 V (c). Potentials were held during the entire measurement and 30 min before for chemical equilibration.

hysteresis. Magnetisation at 1 T increased by a factor of 1.8 in Fig. 4.33(b) compared to the uncharged state in (a), while both curves show the typical non-saturating magnetisation for superparamagnetic npPd(Co). A much more pronounced ferromagnetic hysteresis is observed for hydrogen charged samples at U=-1.0 V in (c). Magnetisation changed by a factor of 4 from OCP in (a) to the hydrogen-charged hysteresis in (c), where a coercive field $\mu_0 H_C$=0.045 T (35810 Am^{-1}) is apparent. It has to be noted that the magnetisation measurement in (c) did not produce a fully closed loop. The second sweep to positive magnetic fields H (not shown) yielded even higher values of magnetisation than the initial curve, which could not be reversed even after complete hydrogen desorption. A conceivable reason for this finding is the formation of hydrogen-induced lattice defects, which might lead to an irreversibly increasing magnetisation[200]. Open hysteresis loops can likely be prevented by prolonging the equilibration time for hydrogen absorption before the magnetisation measurement, although a permanent current associated with hydrogen gas evolution during the magnetisation measurement can hardly be prevented. Well-defined, unchanging electrochemical states over long measurement intervals for magnetisation curves ($\sim$5 h) are a challenging aspect of *in situ* SQUID magnetometry in general, especially at potentials close to the hydrogen evolution onset. A faster acquisition of magnetisation curves for tailor-made npPd(Co) samples by complementary techniques such as VSM or MOKE experiments, definitely has the potential to

enable a fully reversible transition from superparamagnetism to ferromagnetism by hydrogen absorption in future experiments.

4.4.2.3 Hydrogen-charging for magnetisation tuning

The most direct method to characterise the performance of magneto-ionic systems is the measurement of changes in the (saturation) magnetisation upon electrochemical treatment, as already presented for pseudo-capacitive charging measurements in Sec. 4.4.1.2. In contrast to Sec. 4.4.1.2, changes in saturation magnetisation upon hydrogen-charging are investigated for npPd(Co) with different Co-content and distribution in this section. A schematic depiction of the hydrogen-charging process is shown in Fig. 3.1. Parts of this section are reprinted from Ref. 41 and Ref. 42, which were both published under a CC-BY license.

Magnetisation variation for as-dealloyed npPd(Co)

At first, the variation of magnetisation for as-dealloyed npPd(Co) (U_D=0.7 V; I_R=0.1 mA) upon hydrogen-charging is presented in Fig. 4.34.

A combined plot of voltage U, charge Q, relative changes in magnetisation $\Delta M/M_0$, and absolute changes in magnetisation ΔM for npPd(Co) (U_D=0.7 V; I_R=0.1 mA) during voltammetric cycling between -0.9 V and 0.3 V at a rate of 0.5 mVs^{-1} in 1 M KOH is shown in Fig. 4.34a. The value M_0 was 0.15 emu g^{-1} and refers to the minimum magnetisation in the cycling range, which is used as the reference point for the relative changes. The charge (green curve in Fig. 4.34a) was set to zero in the chemically inactive double-layer regime, allowing an easy distinction of chemical regimes: Positive charges are attributed to oxygen-related reactions on the sample surface, while negative charges correspond to hydrogen-related processes, i.e. ad- and absorption. The drift to more negative charges towards the end of the measurement might be caused by a slightly shifting standard potential of the gold pseudo-reference electrode, relative to which the applied potential (black in Fig. 4.34a) is measured as well as by structural changes on the npPd(Co) surface after cyclic hydrogenation, which affects the electrochemically active area.

The relative magnetisation $\Delta M/M_0$ (blue in Fig. 4.34a) shows a giant increase coinciding with negative charge values upon electrochemical hydrogen-charging. The magnetisation can be altered by 100% (corresponding to 0.3 emu g^{-1}) with respect to an entirely constant
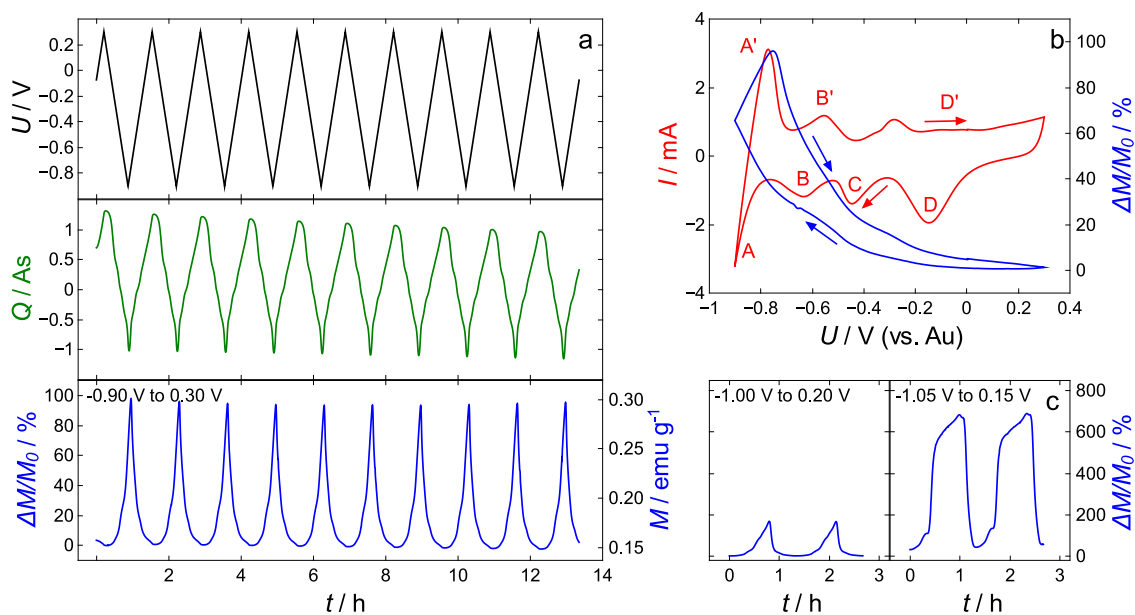
Figure 4.34: Hydrogen-charging induced magneto-ionic switching of magnetisation in npPd(Co) (U_D=0.7 V; I_R=0.1 mA): a) potential U, charge Q, relative changes in magnetisation $\Delta M/M_0$ and absolute magnetisation M of npPd(Co) as a function of time t upon voltammetric cycling between U=-0.9 V and 0.3 V with a scan rate of 0.5 mVs^{-1}. Magnetic field and temperature were held constant ($\mu_0 H$=0.5 T, T=300 K) during the entire measurement. An alternative representation of the same measurement is shown in b): current I and magnetisation $\Delta M/M_0$ as a function of potential U for a single electrochemical cycle. Arrows indicate the cycling direction. c) shows relative changes in magnetisation upon voltammetric cycling with a scan rate of 0.5 mVs^{-1} in potential ranges shifted to more negative values. $\Delta M/M_0$ reached peak values of more than 150% (0.4 emu g^{-1}) upon cycling to a lower potential limit of -1.0 V (left) and 600% (1.1 emu g^{-1}) upon cycling to a lower potential limit of -1.05 V (right). Note the change in y-axis scaling compared to a). Reprinted from Ref. 41.

baseline, indicating excellent reversibility. Fig. 4.34b shows the same measurement in the CV representation, depicting current I as a function of voltage U. Relative changes in magnetisation $\Delta M/M_0$ are added as a second y-axis on the right. This plot allows attributing changes in magnetisation directly to chemical reactions: At negative (cathodic) currents magnetisation starts to increase significantly below a voltage of -0.3 V. Three distinct peaks (A,B and C) can be identified in this potential region: Peak A corresponds to hydrogen absorption, while peaks B and C can be attributed to hydrogen adsorption on the surface. The relative increase in magnetisation of 100% in this region is equivalent to an additional magnetic moment of 0.017 μ_B per hydrogen atom compared to the initial state. Interestingly, the magnetisation reaches its maximum at positive currents (in the anodic regime), when hydrogen desorption is already the dominant process. The larger anodic peak A' in Fig. 4.34b can be attributed to desorption from bulk and surface, while the smaller peak B' is associated

with hydrogen desorption from both surface and palladium hydride α-phase[201]. The delayed decrease of the magnetisation with respect to charge is related to the volatility of the hydrogen-induced effect on magnetism and discussed below. A small contribution ($\Delta M/M_0$ <10%) to the overall magnetisation changes can be attributed to oxygen ad- and desorption processes on the npPd(Co) surface, occurring at potentials more positive than -0.3 V. The broad cathodic plateau D' corresponds to oxygen adsorption on the Pd surface, while the oxygen desorption occurs at peak D.

Measurements were extended to more negative potentials at which sustained absorption to larger hydrogen fractions in the palladium lattice occurs. As shown in Fig. 4.34c, the amplitude of magnetisation $\Delta M/M_0$ rises to 150% (0.4 emu g^{-1}) and to even more than 600% (1.1 emu g^{-1}) upon cycling when scanning to -1.00 V (left) or -1.05 V (right), respectively. The two successive voltammetric cycles, plotted for each voltage limit, indicate good reversibility of the magneto-ionic switching. However, bias to more negative voltages is accompanied by a considerable amount of hydrogen gas evolution, which distorts charge balance and requires a specialised *in situ* cell geometry.

Reduction of switching time

An additional experiment, exploring to what extent a faster switching of magnetisation is possible for npPd(Co), is presented in Fig. 4.35.

In Fig. 4.35 the effective time scale of the magnetic switching was investigated in the hydrogen regime using a faster scan rate of 15 mVs^{-1}. Voltage (black) was cycled between -0.3 V and -0.6 V in a time of 20 s, while recording the response of charge (green) and magnetisation (blue). Note that the total time scale changed from several hours in Fig. 4.34a to below one hour here. Magnetisation still closely follows the variation of charge, with both M and Q showing the same period as bias voltage U of 40 s. Magnetisation changes are much smaller in the order of 1%. As a time scale to record single magnetisation data points in a SQUID magnetometer is typically 10-20 s, faster switching cannot be resolved using our setup without aliasing effects.
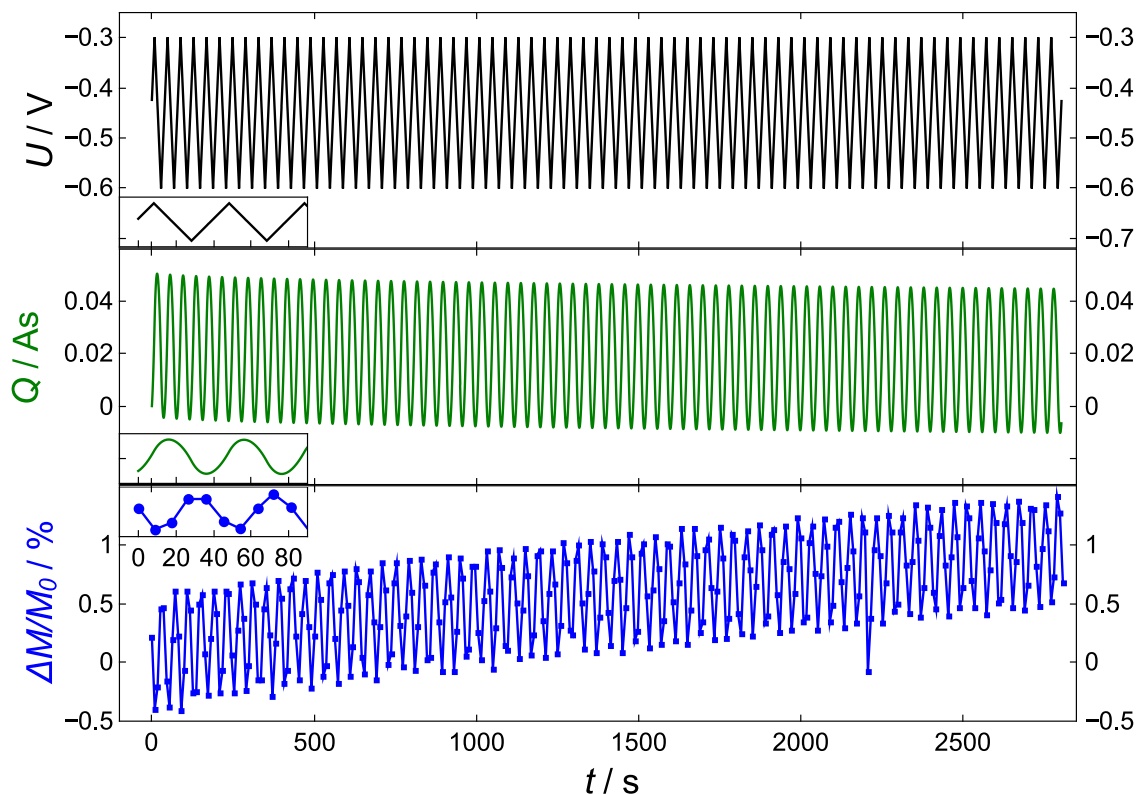
Figure 4.35: Investigation of magnetic switching speed in npPd(Co) (U_D=0.7 V; I_R=0.1 mA): Voltage U (black), charge Q (green), and relative changes in magnetisation $\Delta M/M_0$ (blue) as a function of time t for npPd(Co) upon fast hydrogen-charging. The voltage U was swept at a constant rate of 15 mVs^{-1} in the range between -0.6 V and -0.3 V, associated with the onset of hydrogen ab-/desorption. Magnetic field and temperature were held constant (H=0.5 T, T=300 K) during the entire measurement. The insets on the left show two successive cycles of U, Q, and $\Delta M/M_0$ for improved comparability. The switching time between hydrogen-charged and hydrogen-discharged states was 20s, which also reflects itself in magnetisation, as seen in the insets. Adapted from the supporting material of Ref. 41.

Volatility

Furthermore, the volatility of the hydrogen-induced magnetisation was probed. For that purpose npPd(Co) (U_D=0.7 V; I_R=0.1 mA) was charged with hydrogen using a linear sweep of voltage from OCP to -0.9 V with a scan rate of 0.5 mVs^{-1}. After reaching this potential, external electrochemical control was stopped and the sample equilibrated in a self-acting manner, in analogy to hydrogen outgassing experiments. The recorded magnetic moment is depicted in Fig.4.36. As expected from prior experiments, magnetic moment m increases in the region of electrochemical hydrogen sorption (hatched in green). After turning off the potential control, magnetic moment m astonishingly keeps increasing for more than 2400 s (40 min). At later stages m decreases following an exponential decay, as indicated by the fitted curve in red.
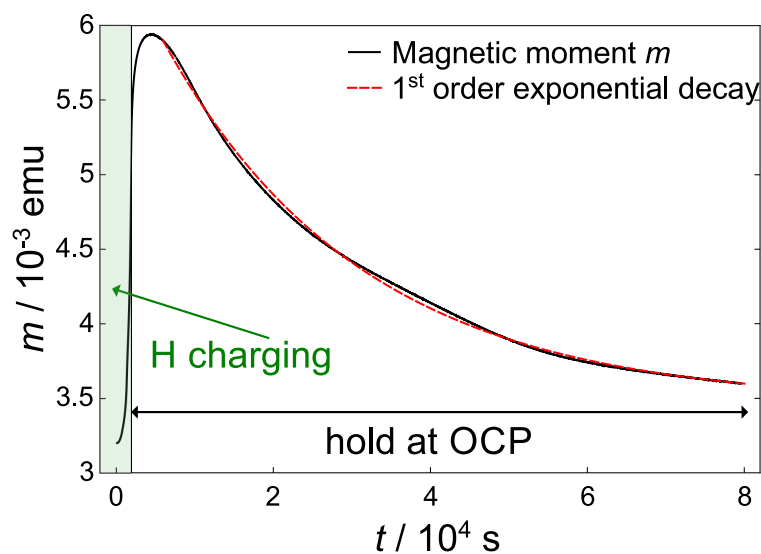
Figure 4.36: Magnetic moment m versus time t for npPd(Co) (U_D=0.7 V; I_R=0.1 mA) in a hydrogen-charging/discharging experiment. Hydrogen discharging was not enforced electrochemically, but is the result of the slow equilibration of adsorbed hydrogen atoms with hydrogen ions in solution at the open circuit potential (OCP). A fit to the discharging curve using a first-order exponential decay is shown in red.

The latency in magnetic response upon hydrogen desorption has already been observed in Fig. 4.34, where magnetic moment keeps increasing upon initial desorption. This effect is interpreted in terms of the hydrogen diffusion and superparamagnetic relaxation processes in Sec. 5.2.2.2 in the frame of the proposed superparamagnetic coupling mechanism.

Varying degree of charging

Besides switching speed and volatility, also the absolute magnitude of the changes in magnetisation upon hydrogen-charging was tested further in Fig. 4.37. Relative changes in magnetisation $\Delta M/M_0$ in the CV representation of current I as a function of voltage U enable insights into chemical reactions responsible for the magneto-ionic effects. While the larger variation $\Delta M/M_0$ upon lowering the voltage limit to U=-1.0 V became apparent already in Fig. 4.34c, a marked increase in magnetisation coinciding with the hydrogen desorption peak A' is revealed in Fig. 4.37. Magnetisation in blue clearly follows the hydrogen desorption peak A' of the current curve (black), which both shift to higher/lower potentials when the voltage limit of the CV scan is decreased/increased. This is a strong indication that hydrogen is indeed the driving force of the magneto-ionic effects in npPd(Co), rather than e.g. the oxidation of surface Co. The onset of the Co oxidation reaction is expected to occur at a constant anodic voltage, regardless of the lower potential limit, which stands in contrast to
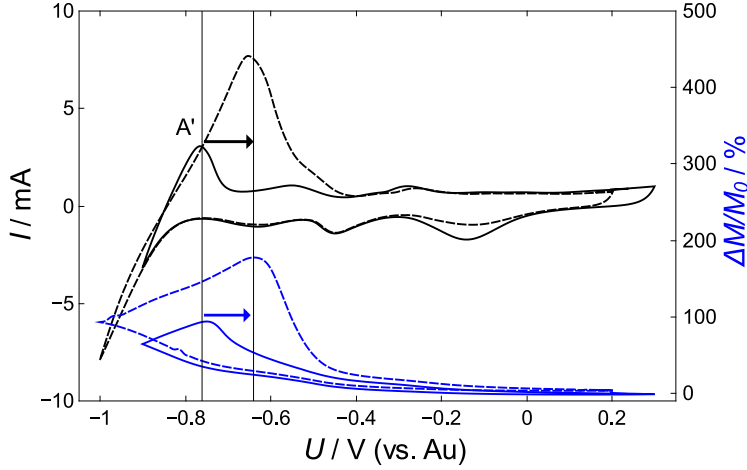
Figure 4.37: Relative changes in magnetisation $\Delta M/M_0$ upon hydrogen charging of npPd(Co) to different lower potential limits in the CV representation of current I as a function of voltage U. Full lines show a cycle between U=-0.9 V and 0.3 V, dashed lines show a cycle to lower voltage limits of U=-1.0 V and 0.2 V. A shifting peak position of the hydrogen desorption peak A' is indicated by the vertical lines. Reprinted from the supporting material of Ref. 41.

our observation in Fig. 4.37. A comprehensive discussion of alternative tuning mechanisms for the magnetisation changes in npPd(Co) is presented in 5.2.2.3.

Charging npPd$_{(1-x)}$Co$_x$ from the GCD method

As promising results regarding switchable magnetism were attained using hydrogen-charging in as-dealloyed npPd(Co), the GCD method to change Co content and distribution in npPd$_{(1-x)}$Co$_x$ described in Sec. 4.3 is applied here to test its influence on the magneto-ionic effect. Changes in magnetisation upon voltammetric cycling for npPd$_{(1-x)}$Co$_x$ with nominal Co concentrations $x_{Co,nom}$=0, 0.03, 0.06, 0.09, 0.12, and 0.15 are presented in Fig. 4.38.

For npPd$_{(1-x)}$Co$_x$ with six different Co concentrations $x_{Co,nom}$, relative variations of magnetisation $\Delta M/M_{min}$ upon hydrogen-charging and discharging are presented as a function of time t in Fig. 4.38(a)-(f) and as a function of charge ΔQ in parts (g)-(l). Numerical values of relative changes ($\Delta M/M_{min}$) and absolute changes in magnetisation (ΔM) are summarised in Tab. 4.3. Absolute magnetic moments were normalised to the sample weight to enable comparability. In Fig. 4.38(a)-(f) one observes a periodic variation of the magnetic moment for all compositions, with the minima/maxima occurring at the same points in time delayed with respect to the maxima/minima in applied voltage, as indicated by the grey line. However, the amplitude of the relative changes in magnetisation $\Delta M/M_{min}$ is clearly different
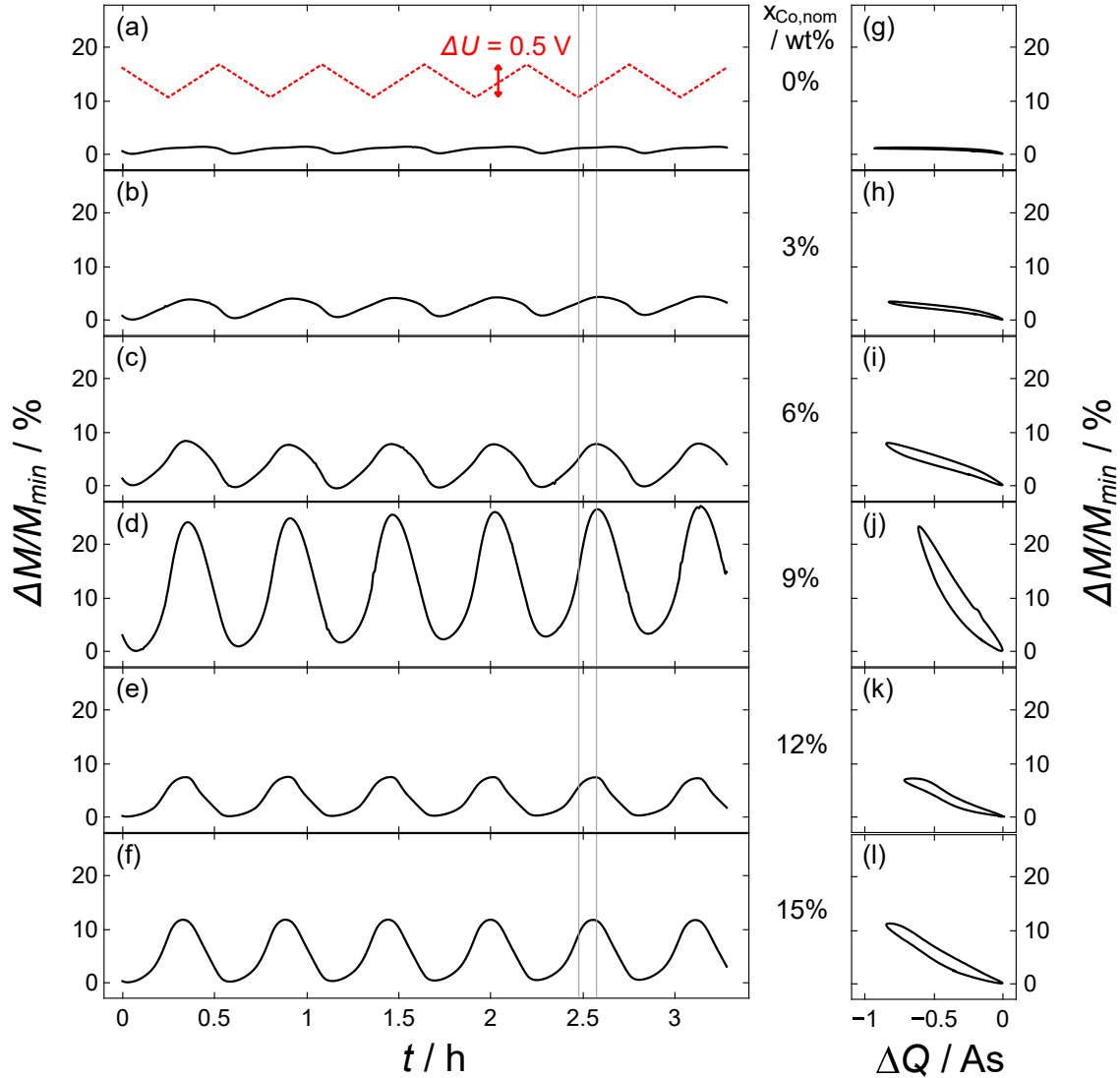
Figure 4.38: Variation of magnetisation $M/M_{\min}$ as a function of cycling time t (a)-(f) and of charge variation ΔQ (g)-(l) upon voltammetric hydrogen charging and discharging for npPd$_{1-x}$Co$_x$ with different Co content $x_{Co,nom}$. Nominal Co concentration $x_{Co,nom}$ increases from top (a)/(g) to bottom (f)/(l). The variation of hydrogen sorption potential U is depicted in dashed red, where a voltage scan rate of 0.5 mVs^{-1} was used in a voltage range between -0.4 V and -0.9 V. For better comprehensibility only a single voltammetric cycle is plotted for the variation of magnetisation $M/M_{\min}$ with charge ΔQ (g)-(l). The cycle is run clockwise with time for all compositions. Curves were measured at a magnetic field of 5000 Oe and a temperature of 300 K. Grey vertical lines at a minimum of hydrogen-charging voltage and a maximum of magnetisation are drawn through subplots (a)-(f) as a guide to the eye. Reprinted from Ref. 42.

for samples with different Co content $x_{Co,nom}$. One observes increasing relative variations in magnetisation from ∼1% to ∼24% for increasing Co content up to $x_{Co,nom}$=9 wt%. Samples at higher Co concentrations of $x_{Co,nom}$=12 wt% and $x_{Co,nom}$=15 wt% exhibit smaller tuning amplitudes of ∼7% and ∼12%. Absolute changes in magnetisation ΔM show a similar tendency of increasing changes for higher Co content up to $x_{Co,nom}$=9 wt%. At higher nominal Co concentrations absolute change first decreases slightly for $x_{Co,nom}$=12 wt% and then reaches with ΔM=1.5 emu g^{-1} the highest magnetisation modulation obtained for npPd$_{(1-x)}$Co$_x$ at $x_{Co,nom}$=15 wt%.

The loop forming in the ΔQ-$\Delta M/M_{min}$ plots in Fig. 4.38(g)-(l) reveals a slightly retarded change of M with respect to Q, i.e. there is no instantaneous linear response, which would be expected for M changes induced by reversible chemical reactions. This is related to the behaviour of magnetisation for hydrogen-charged npPd(Co) upon holding at OCP in Fig. 4.36, where magnetisation keeps increasing without further hydrogen uptake caused by the diffusion of hydrogen in Pd.
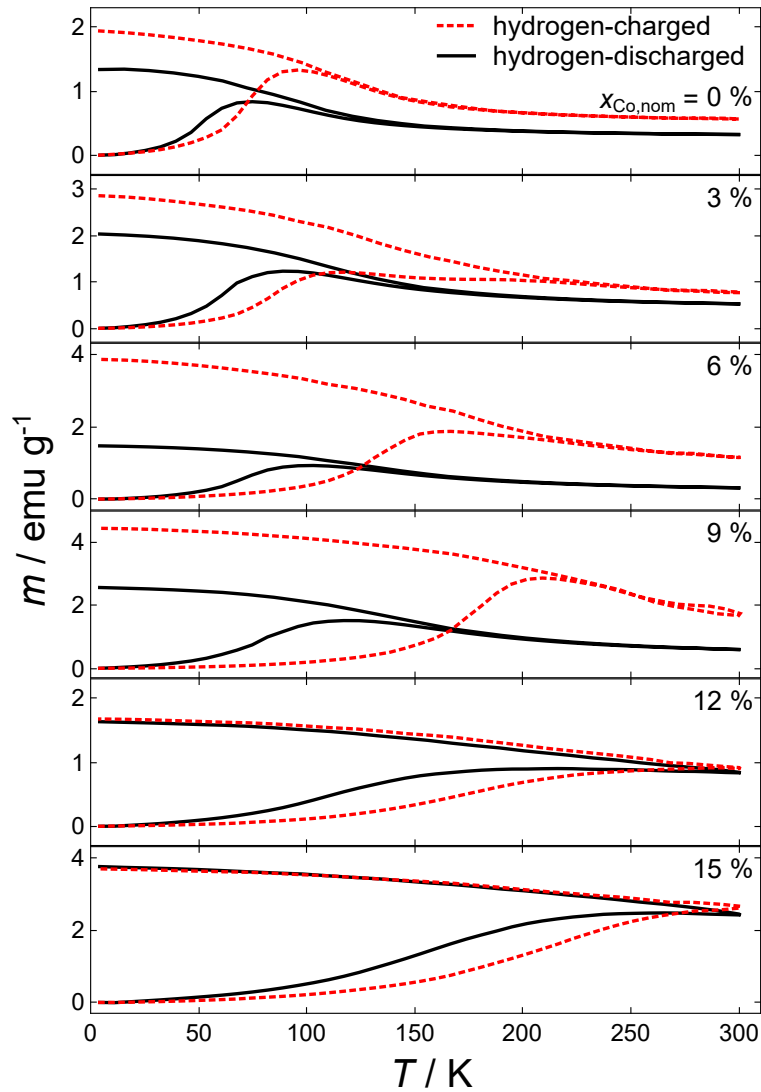
Figure 4.39: Zero-field cooled (ZFC) and field cooled (FC) magnetisation for $npPd_{(1-x)}Co_x$ with varying Co content $x_{Co,nom}$ charged with hydrogen (red, dashed lines) and after hydrogen desorption (black, solid lines). Magnetisation was recorded in a field of 50 Oe. For the sake of comparability low-temperature ZFC magnetisation at $T=0$ was set to 0 for all curves.

ZFC/FC-measurements during charging

Zero-field cooling (ZFC) curves for GCD $npPd_{(1-x)}Co_x$ with different Co content in Fig. 4.39 (black curves, solid lines) were already discussed in Sec. 4.3. Here, changes in the zero-field cooling/field cooling (ZFC/FC) magnetisation curves upon *in situ* hydrogen-charging are presented. These measurements require a specialised cell design to allow for electrolyte freezing during temperature-dependent measurements. The corresponding results are depicted in Fig. 4.39 (a)-(f) in red, together with the curves for $npPd_{(1-x)}Co_x$ after hydrogen discharging.

Hydrogen-charging has a strong effect on the shape of ZFC curves (see dashed red curves): For nominal Co concentrations from $x_{Co,nom}=0\%$ to $x_{Co,nom}=12\%$ the blocking temperature T_B as well as the absolute values of both FC (upper branch) and ZFC (lower branch) magnetisation increase considerably upon hydrogen-charging. For example, T_B in the hydrogen-charged state (listed as $T_{B,H}$ in Tab.4.3) is shifted from 75 K to 96 K for $x_{Co,nom}=0\%$ and from 117 K to 209 K for a concentration $x_{Co,nom}=9\%$. For samples with higher $x_{Co,nom}$ in (e) and (f), a shift in blocking temperature is still apparent, while changes in magnetisation are less pronounced.

The most striking difference in ZFC/FC curves in the hydrogen-charged and hydrogen-discharged state occurs at a Co concentration of $x_{Co,nom}=9\%$ in Fig. 4.39, which coincides with the largest relative changes in magnetisation in cyclic hydrogen-charging experiments (Fig. 4.38). For higher Co concentrations $>9\%$ (Fig. 4.39), variations of both T_B and $\Delta M/M_{min}$ are less prominent (compare Tab. 4.3). Higher values of T_B and the broad size distribution for Co concentrations $>9\%$ indicate larger magnetic clusters and suggest that a certain fraction of those clusters already in the ferromagnetic state. Magnetic properties of npPd$_{(1-x)}$Co$_x$ for all concentrations Co, nom are condensed in Tab. 4.3 at the end of this chapter.

Table 4.3: Overview of magnetic properties and magnetisation changes upon hydrogen loading for various chemical compositions of npPd$_{1-x}$Co$_x$. $x_{Co,nom}$ denotes the nominal Co content as expected from GCD, $x_{Co,XRF}$ is the measured Co content via XRF, M_{min} is the minimum magnetisation, ΔM is the absolute variation of magnetisation, $\Delta M/M_{min}$ is the relative change in magnetisation, $\alpha_{C,V}$ is the magnetoelectric-voltage coefficient as defined in Ref. 4 ($4\pi\Delta M/\Delta U$), T_B is the blocking temperature in the uncharged state, $T_{B,H}$ is the blocking temperature in the hydrogen-charged state. The arrow indicates the increasing cluster size from top to bottom. Data are extracted from Fig. 4.20 ($x_{Co,XRF}$), Fig. 4.38 ($\Delta M/M_{min}$), and Fig. 4.39 (T_B & $T_{B,H}$). Reprinted from Ref. 42.

$x_{Co,nom}$ / wt%	$x_{Co,XRF}$ / wt%	M_{min} / emu g^{-1}	ΔM / emu g^{-1}	$\Delta M/M_{min}$ / %	$\alpha_{C,V}$ / Oe V^{-1}	T_B / K	$T_{B,H}$ / K
0	4.9	1.22	0.02	1.3	5	75	96
3	7.7	1.86	0.07	3.8	19	89	117
6	11.7	2.87	0.22	8.4	65	103	167
9	12.0	3.67	0.88	24.2	255	117	209
12	15.7	8.42	0.61	7.4	177	216	286
15	25.2	13.08	1.50	11.8	422	265	≥300

cluster size

<div align="right">

CHAPTER 5

</div>

Discussion

In the following, results from the previous chapter will be discussed. This section is split in two major parts: Section 5.1 addresses results from *ex situ* and *in situ* dealloying techniques, while section 5.2 elaborates magnetism tuning measurements in nanoporous Pd.

5.1 Insights into CoPd dealloying

In this chapter the evolution of physical properties in the electrochemical dealloying process of a $Co_{75}Pd_{25}$ is discussed, which has been presented in Sec. 4.1. The gained understanding of CoPd dealloying is summarised using the input from all *ex* and *in situ* techniques, where comparisons are drawn to the paragon dealloying system of nanoporous Au prepared via etching from $Au_{75}Ag_{25}$ alloys. *In situ* characterisation of Pd dealloying itself is only scarcely represented in the dealloying literature[46,70], a gap which is attempted to be filled with this section. Parts of this chapter are reprinted with permission from Ref. 46.

5.1.1 Co-rich clusters in the dealloying process

The retention of the less noble alloy component in clusters during dealloying is of central importance for the magnetic properties of dealloyed nanoporous Pd(Co). Here, the mechanism behind this cluster formation is briefly summarised.

Dealloying is generally understood as a combination of two basic processes: dissolution of the less noble component and surface diffusion of atoms of the more noble component[56,62]. Considering dissolution only, an early passivation of the alloy surface with nobler atoms would bring the dealloying process to a halt. However, a high surface diffusivity of the more noble component at the electrode-electrolyte interface prevents complete passivation. Superficial noble atoms tend to maximise their coordination number by agglomeration, exposing previously covered alloy portions to the electrolyte for dissolution. At first, this leads to the formation of mounds on the alloy surface, which are eventually undercut, increasing the surface area and allowing a complete dealloying of a bulk alloy material[62]. Naturally, small parts of the alloy remain covered by layers of more noble atoms, leading to the occurrence of alloy clusters buried under the ligament surfaces. This peculiarity has only lately been discussed in the framework of the dealloying model[69]. Two-dimensional cross sections from a KMC simulation presented in Fig. 4.7 illustrate both pore formation and alloy clustering during the dealloying process. While the base alloy appears as a homogeneous solid solution of Co and Pd in our case (a), primary dealloying successively converts the alloy into porous regions containing small clusters of the base alloy (b). Note that the Co concentration within the alloy and the porous phase remain mostly constant, with the porous phase only growing at the expense of the alloy. Behind the corrosion front in the already porous state, Co concentration changes slightly as buried Co atoms are exposed to the electrolyte after sustained surface diffusion of the more noble component (secondary dealloying). Accordingly, cluster sizes decrease during secondary dealloying, which is also reflected in Fig 4.7 (c).

Co-rich clusters for dealloyed npPd(Co) detected via STEM/EDS are compared with predictions from KMC simulations in Fig. 4.6. Co-rich clusters are buried under the Pd surface with sizes in the nm-range, which confirms the viability of the KMC simulation adapted to the CoPd system. Cluster sizes in the KMC simulation crucially depend on the simulation parameters, which makes it difficult to capture the precise cluster sizes.

5.1.2 Variation of H_C upon dealloying-induced structural evolution

The trend of H_C with Q/Q_{tot} in the course of the dealloying process in Fig. 4.2 bears resemblance to Kneller's observation of coercivity in dependence of particle size[202]. Larger particles were found to exhibit a reduced coercivity due to the appearance of multiple magnetic domains within the particle, reducing the stray field energy. The transition to single-domain particles is characterised by a maximum in coercivity. For smaller particles coercivity drops rapidly and eventually vanishes, as particles become superparamagnetic. Furthermore, Kneller also reported that squareness M_r/M_S peaks at smaller particle sizes compared to coercivity, while the maximum of the squareness curve appears broader. A similar trend in coercivity was also observed for assemblies of non-isolated magnetic particles (granules) as a function of volume fraction, rather than particle size[203], although ambiguous results exist in literature.

In Kneller's work the correlation between coercivity and particle size is easily understood in terms of different domain states. The interpretation is similar for the particle assembly: For small packing fractions coercivity is reduced to zero as particles behave as isolated superparamagnetic entities, which is also the case for residual alloy clusters in the nanoporous samples after completed primary dealloying. Higher packing fractions lead to interactions between the particles and an eventual formation of magnetic domains, which increases the coercivity compared to the superparamagnetic state. Increasing the packing fraction further gives rise to the formation of a multi-domain state and a region where coercivity is smaller again, which is similar to the situation present in the initial alloy before dealloying. Coercivity behaviour as a function of packing fraction in general strongly depends on the interplay between interaction strength, particle size and temperature[204,205].

In the following, this notion of magnetic particle packing fraction being responsible for the coercivity is applied to the dealloying process in particular (see sketches in Fig. 4.7). As the linear decay of magnetic moment with charge flow in Fig. 4.3(a) suggests a continuous removal of Co atoms with charge from the CoPd alloy, the dealloying process is interpreted as the inverse of the magnetic percolation problem[206]. This implies the transition from percolating magnetic units, i.e. ferromagnetic behaviour, to non-percolating magnetic units,

i.e. superparamagnetic behaviour. Cobalt-rich, superparamagnetic clusters retaining the initial alloy composition have been reported to be present in npPd(Co)[41]. The CoPd precursor alloy platelet, as a soft ferromagnet, exhibits a magnetic domain structure consisting of multiple domains (Fig. 4.7, (a)), in accordance with the hysteresis curve in Fig. 4.2 (b). In the course of the dealloying process, the multi-domain alloy is successively converted into the nanoporous structure containing non-interacting superparamagnetic clusters of the alloy (Fig. 4.7, (b)). Initially, the multi-domain part in the sample is reduced as the alloy is dissolved, which can account for the slightly increasing coercivity up to the peak at $Q/Q_{\mathrm{tot}} \approx$0.6 in Fig. 4.2(a). Only at this point the contribution of the nanoporous superparamagnetic part becomes visible: Lowering the Co concentration further below this critical point at $Q/Q_{\mathrm{tot}} \approx$0.6 by pursued dealloying leads to a transition to predominant superparamagnetic cluster behaviour (Fig. 4.7, (3)), eventually resulting in a sharp drop in coercivity at $Q/Q_{\mathrm{tot}} >$0.8 in Fig. 4.2. Furthermore, in line with the interpretation of Kneller, hysteresis squareness $M_{\mathrm{r}}/M_{\mathrm{S}}$ peaks in a broader maximum at a larger Q/Q_{tot} of 0.7 corresponding to smaller cluster sizes.

In non-interacting magnetic two-phase systems the magnetic moments of the two individual phases add up linearly, while the coercivities add up weighted by the susceptibilities of the individual phases[202]. Thus, the exact point when coercivity starts to drop in Fig. 4.2 is determined by the individual susceptibilities of both ferromagnetic and nanoporous super-paramagnetic phase and their respective volume fractions. The fact that coercivity did not vanish in the present case after completed dealloying (Q/Q_{tot}=1.0) indicates that a fraction of magnetic clusters is still above the superparamagnetic size threshold, with the effective magnetic size being determined by interactions and individual Co cluster sizes. As residual alloy clusters in nanoporous metals follow a certain size distribution, a fraction of larger clusters accounting for the residual coercivity is expected.

Role of magnetocrystalline anisotropy

Magneto-crystalline anisotropy links the easy magnetisation direction in a crystal directly to its crystal structure. Therefore, a changing crystal structure during electrochemical dealloying might play a role for the measured variations in coercivity (Fig. 4.2). However, changes in the magneto-crystalline anisotropy can be ruled out as an explanation for the trends in coercivity based on XRD-patterns presented in Fig. 4.1. A single crystallographic phase is formed

already in the early stages of the dealloying process ($Q/Q_{\text{tot}} < 0.2$), while also no observable shift in diffraction lines occurred in the region, where the drop in coercivity becomes apparent. This supports the picture of the dealloying process as the growth of the nanoporous phase with an unchanging composition at the expense of the starting alloy. Furthermore, it strengthens the interpretation of the dealloying process as an 'inverse' magnetic percolation process, where a reduced Co concentration and changing intercluster coupling can fully explain the observed changes in coercivity.

Comparison with FePd

Only recently magnetic properties during dealloying have also been studied for FePd alloy thin films[207,208]. A similar peak in coercivity as in Fig. 4.2 for CoPd was observed for FePd in an intermediate dealloying step. The interpretation of the changes in coercivity for FePd involves changes of crystallite grain sizes and shape during dealloying[207], in analogy to the classical grain-size dependence of coercivity by Herzer[209] moving from large to small crystallite sizes. Such an interpretation is considered less likely in the case for CoPd alloy, as for conventional dealloying the grain structure of the parent alloy is typically preserved[62]. In general, the two dealloying systems of CoPd and FePd are surprisingly dissimilar from a mechanistic standpoint: Dealloying of FePd takes place below the critical dealloying potential, where Pd passivates the surface in the dealloying model of Erlebacher[56]. In contrast to the conventional dealloying picture, which applies for CoPd, grain boundary corrosion is heavily favoured in the FePd system. Grain boundaries are reported to have a higher Fe concentration[207], which facilitates porosity formation in FePd. Furthermore, for FePd a change in the crystal structure is reported upon dealloying[207]. CoPd on the other hand does not change its crystal structure in the dealloying process, as evidenced in the XRD patterns in Fig. 4.1. The magnetic moment during dealloying of CoPd in Fig. 4.3(a) decreases linearly with decreasing Co content (or increasing dissolution charge) as discussed in the following chapter, while in the case of FePt also grain boundary corrosion, the phase transformation and a loss of the film during dealloying have to be considered to account for the reduction of the magnetic moment during dealloying.

5.1.3 Variation of m and dealloying as a two-step process

In this section changes in magnetic moment upon electrochemical dealloying are discussed, which allows insights into the dealloying mechanism. The linear behaviour of magnetic moment with charge in Fig. 4.3(a) might be expected at first sight, as dealloying charge is in a good approximation directly proportional to the number of Co-atoms removed. This behaviour would be straightforward for samples consisting of Co solely, as the magnetic moment is an extensive quantity of a magnetic material. However, as the high magnetic polarisability of Pd is known to be dependent on the Co dilution in the alloy[82], a strictly linear decay of magnetisation with charge cannot be expected for CoPd dealloying a priori. The slope of the measured m-Q-curve allows the determination of a magnetic moment per dissolved Co atoms using Eq. 4.1. The obtained effective moment of 2.03 μ_{B}/atom clearly indicates that the measured moment cannot be attributed solely to the Co atoms, as a value of 1.7 μ_{B}/atom would be expected for bulk hcp Co. Directly calculating the moment per Co atom from nominal Co content and initial saturation moment yields a value of 1.95 μ_{B}/atom, which is also enhanced. Albeit this value is slightly lower compared to the moment calculated from the slope of the m-Q-curve, it is still significantly enhanced compared to the pure Co moment of 1.7 μ_{B}/atom.

This higher effective moment per Co atom results from the magnetic polarisation of Pd atoms in the vicinity of ferromagnetic Co. An increased Co moment due to the size effects in the present case, as reported for pure Co clusters below 400 atoms[210] cannot explain the enhanced moment for the plain alloy, in which Co and Pd are homogeneously distributed. As clusters in the present nanoporous structures always consist of master alloy residues rather than pure Co, the Pd polarisation mechanism is likely dominant also for smaller clusters, though size effects cannot be definitively ruled out for magnetic clusters on the basis of present data. For dilute CoPd alloys ($x_{\mathrm{Co}} < 0.1$ at%) magnetic moment values up to 10 μ_{B} per Co atom were reported[82]. An effective moment of $2\mu_{\mathrm{B}}$/atom corresponds to an alloy of 70at% Co[82], which is close to the composition of the dealloying precursor used here for magnetometry. The constant, enhanced moment corresponding to Co in the initial alloy suggests that the major part of the dealloying process (Q/Q_{tot} up to 0.95) is governed by alloy decomposition, i.e. Co dissolution from a locally unchanged alloy surrounding. This observation is in

accordance with the notion of dealloying as a two-step process[73]: Primary dealloying, as a fast removal of Co atoms from the alloy, and a subsequent secondary dealloying, as the removal of residual Co from the ligament in the nanoporous structure, which commences right behind the etching front. Changes in moment during purely secondary dealloying (i.e. after the completion of primary dealloying at $Q/Q_{tot} > 0.95$) are weaker compared to the situation where primary dealloying is still active ($Q/Q_{tot} < 0.95$ - compare Fig. 4.3). The magnetic moment at 5000 Oe could be considered the saturation moment for the major part of the dealloying process. However, when superparamagnetic clusters become the dominant contribution to magnetisation, saturation only occurs at much larger fields. Fig. 4.2 (c) shows that the sample is not fully saturated even at a field of 30000 Oe. The much smaller decrease of average magnetic moment in the late stages of the dealloying process can be explained by the sample moving out of saturation at 5000 Oe. This moving out of saturation of the superparamagnetic clusters becomes relevant to the overall magnetisation at a point where the ferromagnetic alloy backbone has been completely removed, i.e. after completed primary dealloying. The flatting of m at relative charge values of about Q/Q_{tot}=0.95 in Fig. 4.3 (a) is therefore indicative of the prevalence of secondary dealloying.

Variation of R with Q/Q_{tot}

Next, the supportive resistance measurements in Fig. 4.3(b) will be discussed. The behaviour of resistance upon dealloying of CoPd for $Q/Q_{tot} < 0.8$ can be compared to reference data for the dealloying of AgAu and CuPt alloys[74]. While dealloying for CuPt gives a steep increase only at very high values of $Q/Q_{tot} \approx 0.9$, the resistance of the AgAu alloy increases much earlier at $Q/Q_{tot} \approx 0.6$ and shows a pronounced flattening at $Q/Q_{tot} > 0.7$. Considering the resistometry measurement for CoPd in Fig. 4.3(b), resistance for CoPd resides between the two curves for AgAu and CuPt. Resistance of the CoPd alloy rises at $Q/Q_{tot} \approx 0.8$ in a narrow window and starts to flatten at $Q/Q_{tot} \approx 0.85$.

These different onset points for the sharp resistance increase of the three curves can be interpreted using the differences of surface diffusivity for the three metals Au, Pd and Pt. As Au has the lowest melting point of the three, surface diffusivity is highest. Likewise for Pt, surface diffusivity is lowest due to the largest melting point. The progression of the etching front in primary dealloying is fastest for the element with the highest surface mobility, namely Au. This implies that an all-porous structure is created comparably fast, leading to

the earliest strong increase in resistance at comparably low values of Q/Q_{tot}. Accordingly, the resistance curves for Pd and Pt rise at higher values of Q/Q_{tot}, as primary dealloying takes a larger share of the overall process, due to slower progression of the etching front. A high surface diffusivity also promotes surface atom rearrangement on the existing porous structure, which exposes less noble atoms to the electrolyte to be dissolved during secondary dealloying. Therefore, a high surface diffusivity causes a more pronounced period of purely secondary dealloying.

The above reasoning enables the qualitative distinction of primary and secondary dealloying contributions as the completion of the steep resistance increase for AgAu and CuPt, which has also been supported using a theoretical model[74]. Based on the reasonable assumption that the resistance of the alloy R_m is significantly smaller than that of the nanoporous structure R_p, one can use a simplified equation for the resistance R in analogy Ref. 74 to reproduce R up to $Q/Q_{\text{tot}} = 0.8$:

$$R = \frac{R_0}{0.8 - Q/Q_{\text{tot}}}, \tag{5.1}$$

where R is the monitored resistance and R_0 is the resistance of the sample before the etching process at $Q/Q_{\text{tot}} = 0$. In this simple model, primary dealloying is considered the only charge consuming process, which makes it applicable up to a maximum value of Q/Q_{tot}. Here, this maximum value for the model was chosen to be $Q/Q_{\text{tot}} = 0.8$, up to which a fit to the experimental data for in Fig. 4.3(b) following Eq. 5.1 ($R_0 = 100\mu\Omega$) yielded good agreement. For higher Q/Q_{tot} values secondary dealloying starts to influence resistance noticeably, leading to the failure of this simple model. A direct application of the theoretical model by Steyskal et al.[74] in the full measurement range, which would also take secondary dealloying into account, is impossible due to the decreasing R at high Q/Q_{tot}. The fit in Fig. 4.3(b) according to the simple model of Eq. 5.1 allows the conclusion that primary dealloying is the dominant dealloying process up to $Q/Q_{\text{tot}} = 0.8$. However, a precise threshold, where primary dealloying does no longer contribute to charge, cannot be determined from resistometry data solely. This threshold is expected at $Q/Q_{\text{tot}} > 0.95$ on the basis of magnetometry data discussed earlier in this section, but cannot be detected in resistometry data due to the decrease of R at high Q/Q_{tot} for the CoPd alloy, which is discussed next.

In contrast to the monotonously increasing resistances for AgAu and CuPt alloys, CoPd exhibits a marked decrease at $Q/Q_{\text{tot}} > 0.9$. This decreasing resistance at higher Q/Q_{tot}

might be connected to the ferromagnetic nature of the sample. Resistivity in a ferromagnet is determined by separate conduction pathways for spin up and spin down electrons. For ferromagnetic PdCo alloy a sharp drop in resistivity has been observed at small Co concentrations, which was attributed to an altered filling of both majority and minority spin bands with decreasing Co concentration[211]. Taking this concentration-dependent resistivity into account allows a coherent interpretation of primary and secondary dealloying using both magnetic moment and resistance data: Primary dealloying can be viewed as the conversion of alloy into porous structure, where Co concentrations in both alloy (75 at%) and porous structure ($\approx$ 6 at% from EDS) are almost constant. This is in accordance with the linear decrease in magnetic moment in Fig. 4.3 (a) up to $Q/Q_{tot} = 0.95$. Purely secondary dealloying, conversely, changes the composition of the porous structure which could lead to the decrease in resistance at high Q/Q_{tot}. This is in good agreement with the observation from magnetic moment data, indicating that secondary dealloying takes over at $Q/Q_{tot} > 0.95$.

The observed shift in the XRD-patterns in Fig. 4.1 closer to the Pd reference lines from $Q/Q_{tot} = 0.8$ to $Q/Q_{tot} = 1.0$ is in accordance with the prevalence of secondary dealloying in that range: As Co is removed in the secondary dealloying, lattice constants of the porous structure get closer to a pure Pd lattice. The unchanged peak position prior $Q/Q_{tot} = 0.8$ also indicates that purely secondary dealloying becomes dominant only at higher Q/Q_{tot} values, which is also deduced from magnetic moment and resistance measurements.

Variation of $\Delta L/L_0$ with Q/Q_{tot}

As a third quantity, relative length changes in Fig. 4.3(c) during dealloying can give additional information about the separate dealloying stages. Shrinkage during dealloying has previously been interpreted in the picture of primary and secondary dealloying for npAu(Pt)[73]: While primary dealloying is thought to have only a small contribution to overall length changes, secondary dealloying was assigned the dominant role governing the shrinkage. Right behind the dealloying front secondary dealloying commences, leading to the immediate onset of shrinkage. The precise course of relative length change as a function of dealloying time is known to be highly potential-dependent[70,73], with larger potentials leading to a faster decay at earlier times due to the promotion of secondary dealloying in that stage. In general higher dealloying potentials are known to lead to larger total shrinkage[70,73] and the appearance of microscopic cracks in the dealloyed material[71]. Cracking was observed

in electron micrographs after different dealloying stages of CoPd (see Fig. 4.4), indicating a fast secondary dealloying already in the early dealloying stages. The observed relative length changes as a function of dealloying charge in Fig. 4.3(c) can be generally interpreted consistently with the observations from magnetic moment and resistance in (a) and (b): Secondary dealloying behind the etch front leads to a strong decrease in length from the start of dealloying, which is likely enhanced in the very early stages ($Q/Q_{tot} <0.1$) by crack formation. With ongoing primary dealloying, i.e. when more alloy converted into nanoporous structure, length decreases with a successively smaller gradient. The final steep decrease at $Q/Q_{tot} >0.9$ again, roughly correlates with the point of completed primary dealloying from magnetometry data. One possible hypothesis for that decay in length is a ligament yielding starting at this point due to the absence of an alloy backbone, although further test are certainly required to clarify the origin of this observation. The overall shrinkage in the order of $\sim$40% is much larger compared to the references for npAu[73,147] or npPd[70], where length changes were in the order of several percent. Crack formation during dealloying in the present case does likely contribute to this divergence, as in the references mostly crack-free samples were obtained at milder corrosion potentials. In order to obtain crack-free npPd(Co), a reduction of the dealloying potential as in Ref. 71 is certainly advisable for future experiments.

5.2 Magnetic tuning mechanisms and tuning performance of nanoporous Pd

Here, results from magnetic property tuning in nanoporous Pd from Sec. 4.4 will be discussed. While Sec. 5.2.1 addresses the tuning mechanism in the electrochemical double-layer, Sec. 5.2.2 is devoted to tunable magnetism arising from hydrogen-related reactions. Section 5.2.3 evaluates the tuning performance on the basis of magneto-electric voltage coefficients and compares findings with literature in the field of magneto-ionics. The last section (Sec. 5.2.4) elaborates compositional changes upon electrochemical cycling, which is not only relevant for magnetic tuning experiments, but also links to the presented methods for compositional tuning in nanoporous Pd in Sec. 4.3.

5.2.1 Tuning magnetism in the double-layer

Capacitive charging experiments on npPd(Co) electrodes have been conducted in different electrolytes (Na-based, Li-based and aqueous), which are presented in Sec. 4.4.1. While voltage application in the Na-based electrolyte yielded no observable changes in the magnetic moment upon charging besides a drifting baseline (Fig. 4.23), interesting results were obtained in the Li-based and aqueous electrolytes.

A direct effect of voltage on the magnetic properties has been observed for all annealing treatments of npPd(Co) (Fig. 4.24), with a negative magneto-electric charge coefficient $\Delta M/Q < 0$ as apparent from Fig. 4.25. The negative sign for $\Delta M/Q$ immediately rules out classical electronic band filling in the rigid band model as a possible explanation for the magnetisation variation: Adding electrons to the nearly filled Pd d-band would increase the density of states at the Fermi energy $D(E_\mathrm{F})$, which decreases the Stoner-enhanced paramagnetic susceptibility and thus magnetisation[76]. The magneto-electric charge coefficient for the band filling mechanism must be positive for such a scenario ($\Delta M/Q > 0$), contradicting the charge coefficient observed in the present experiment. Even when alloying with Co is considered in the band structures[47], at all alloy compositions band filling strives to level

the spin difference and retains a positive charge coefficient. Therefore, three alternative mechanisms are considered:

- **Changes in surface anisotropy:** Surface-charging can change the surface anisotropy on crystalline surfaces. This option has been pointed out for nanoporous systems in a theoretical study by Subkow and Fähnle[212].

- **Magneto-elastic effects:** The modification of surface stress and strain upon double-layer charging in porous systems[10,11,49,213] induces a compensating stress and strain in the bulk of the material. Concomitant magneto-elastic effects are a conceivable explanation for changes observed here, as contemplated in earlier works on the magnetisation tuning in porous materials[10,11,76,214].

- **Pseudocapacitve reactions:** The possibility of (pseudocapacitive) chemical reactions has already been pointed out in Sec. 4.4.1. Reversible redox reactions were found to be responsible for the tuning of magnetic moment in the same Li-based electrolyte for FePt thin films[8].

While all three mechanisms can have either sign in magneto-electric charge coefficient, it is impossible to discern those mechanisms on the basis of the present measurements alone. Generally, the magnetisation response always results from the interplay of several different mechanisms, although often a dominant contributor can be determined. The hysteresis in magnetisation as a function of charge does point at pseudocapacitive reactions as this dominant mechanism in the Li-based electrolyte. Both changes in surface anisotropy and magneto-elastic effects are expected to be reversible as a function of surface charge. Pseudocapacitive reactions related to the reversible oxidation and reduction of the transition metals in CoPt[215] and FePt[216] films have previously been found to be responsible for changes in magnetic properties upon cycling in a LiClO$_4$-based electrolyte. A similar reaction, involving the reversible oxidation/reduction of Co on the surface of PCD+T npPd(Co) in the present Li-based electrolyte, could be responsible for the changes in magnetisation here. Such a pseudocapacitive reaction as the underlying mechanism would also support a negative magneto-electric charge coefficient. Larger absolute values for magneto-electric charge coefficients for higher annealing temperatures T_A could be rationalised in terms of a

smaller charge transfer in the double-layer regime due to the reduced surface area (i.e. current in Fig. 4.24(b)) as well as a higher Co-content on the surface upon with higher annealing temperature. The absence of any noticeable effect on the magnetic properties in the Na-based electrolyte in Fig. 4.23, on the other hand, might be connected to the lack of available ions in the electrolyte and the absence of Co atoms on the surface for PCD npPd(Co), which prevents chemical reactions.

The situation is similar for double-layer tuning experiments in aqueous electrolyte as presented in Fig. 4.26 and Fig. 4.27, where the magneto-electric charge coefficient is again negative ($\Delta M/Q < 0$). With band filling being excluded for the same argument as above, the three mechanisms listed, remain certainly plausible. In contrast to the Li-based system, the influence of pseudo-capacitive charging is considered lower in the KOH electrolyte. This is deduced from the absence of hysteresis in the magnetisation as a function of charge in Fig. 4.27 for all annealing temperatures. On the other hand, the increased Co content on the surface for higher annealing temperatures T_A has hardly any influence on the relative changes in magnetisation in Fig. 4.26, which supports the reduced importance of surface reactions.

The small drift in magnetisation during the measurements, which has been corrected from the plots, might be an indication for changes in surface composition in npPd(Co) upon voltammetric cycling. This effect is addressed specifically in Sec. 5.2.4.

Effects of pure electrochemical double-layer charging, i.e. the filling/depletion of the surface Pd d-bands with electrons due to ion attraction, have only been observed for few magnetic systems. First publications as proof of concept included studies on nanocrystalline Pd by Drings et al.[76] and FePt (FePd) thins films by Weisheit et al.[191]. For a thorough investigation of the microscopic origins of tuneable magnetism, a charge induced-variation of surface stress, as shown for nanoporous Pt by Weissmüller in 2003[49], has to be taken into account. In follow up studies on nanoporous PdCo[10] and PdNi (prepared by compaction of nanoparticles), changes in surface stress have been assigned the dominant role for the magneto-electric effect, rather than the electronic band filling model.

Here, it is concluded that direct double-layer charging in nanoporous Pd(Co) has only a minuscule effect on its magnetic properties. Surface excess charge is more likely to influence magnetic properties indirectly via a changing surface stress and a concomitant magnetoelastic

coupling, a changing surface anisotropy, or pseudocapacitive chemical reactions. The simple concept of charge-induced ferromagnetism in high-surface/high-susceptibility paramagnets by means of purely electronic band filling proves elusive in experimental practice, also for the npPd(Co) system. Over the years, inspiring alternative concepts for switchable ferromagnetism have been devised on the basis of more complex magnetic mechanisms, which includes the whole field of magneto-ionics.

5.2.2 Tuning magnetism in the hydrogen regime

5.2.2.1 Mechanism of hydrogen-induced magnetism

Hydrogen-sorption in PdCo alloys and its influence on the magnetic properties has been extensively studied in the scientific literature[91,99,100]. Important findings comprise a reduced hydrogen storage capacity for higher Co concentrations and a decreasing magnetic susceptibility upon hydrogen-charging (negative charge transfer), i.e. a positive magneto-electric charge coefficient $\Delta M/Q$. The decreasing susceptibility is typically interpreted as a filling of Pd d-band holes with hydrogen electrons, which decreases the density of states at the Fermi level in analogy to classical band filling[76]. Interestingly, this simple and acknowledged model fails for the majority of measurements presented in this thesis. One exception to this generic assessment is homogenised npPd(Co) in Fig. 4.30, which shows a positive magneto-electric charge coefficient in agreement with the above-mentioned literature references for PdCoH[91,99,100]. The sustained temperature-treatment for homogenised npPd(Co) is expected to convert the inhomogeneous Co distribution in the as-dealloyed state into a homogeneous alloy, which explains the agreement with literature findings.

However, magnetisation increases reversibly upon hydrogen-charging for npPd(Co) and npPd$_{(1-x)}$Co$_x$, which has not been observed in previous studies concerned with hydrogen in PdCo alloys[91,99,100]. The hydrogen band filling notion discussed in these studies is also not compatible with an increasing magnetisation upon hydrogen-charging $\Delta M/Q < 0$. In order to rationalise the large magnetisation changes in the hydrogen regime, a novel magneto-ionic mechanism has been proposed by our group which makes superparamagnetic Co-rich clusters in npPd(Co) the key component for magnetisation tuning in Ref. 41. A magnetic coupling of

these clusters via a RKKY-type (Ruderman-Kittel-Kasuya-Yosida) interaction upon hydrogen-charging enlarges the effective cluster size and leads to larger observable magnetic moments in line with experimental findings presented here. The full tuning mechanism is elaborated in the following.

The spin polarisation in Pd is mediated by a RKKY-type interaction between ferromagnetic atoms in a metallic matrix. As manifested by the well-known and remarkable magnetic interlayer coupling in FM/metal/FM multilayer systems,[217] the exchange constant oscillates with distance from the ferromagnetic region due to RKKY coupling. For high-susceptibility paramagnets as Pd, this interaction distance is in the order of several nanometers[218–220]. The RKKY interaction is mediated by the conduction electrons and thus highly sensitive to the electronic structure of the transmitting metal, which is Pd in the present case. When hydrogen bonds to Pd, it partly transfers its charge to the Pd d-band, effectively changing the electronic structure of the metal and thus the interaction distance of the RKKY function. Hydrogen-induced changes of RKKY periodicity were reported earlier in studies of magnetic interlayer coupling in Fe/V[221] and Fe/Nb[222] multilayers and were proposed to account for the ordering in PdCo alloy films[98].

Superparamagnetic Co clusters embedded in non-magnetic matrices were found to form correlated magnetic 'dimers', i.e. physically separated but magnetically coupled entities[223], as a result of indirect exchanges forces in the matrix as the RKKY interaction. The notion in the present case is that such magnetic dimers (or units of more than two coupled clusters) are forming reversibly upon hydrogen loading due to the H-induced increase of the RKKY interaction length (see schematic picture, Fig. 5.1).

In contrast to the static dimers previously proposed,[223] cluster dimerisation can be tuned by interstitial hydrogen in the present case. The dimer formed after hydrogen-charging behaves as a magnetic particle with a larger volume compared to each of the uncoupled Co-rich clusters (see Fig. 5.1). As argued below this dramatically changes the magnetic behaviour because the blocking temperature T_B as well as the magnetic moments of the particles both above and below the blocking temperature increase with the particle volume V.
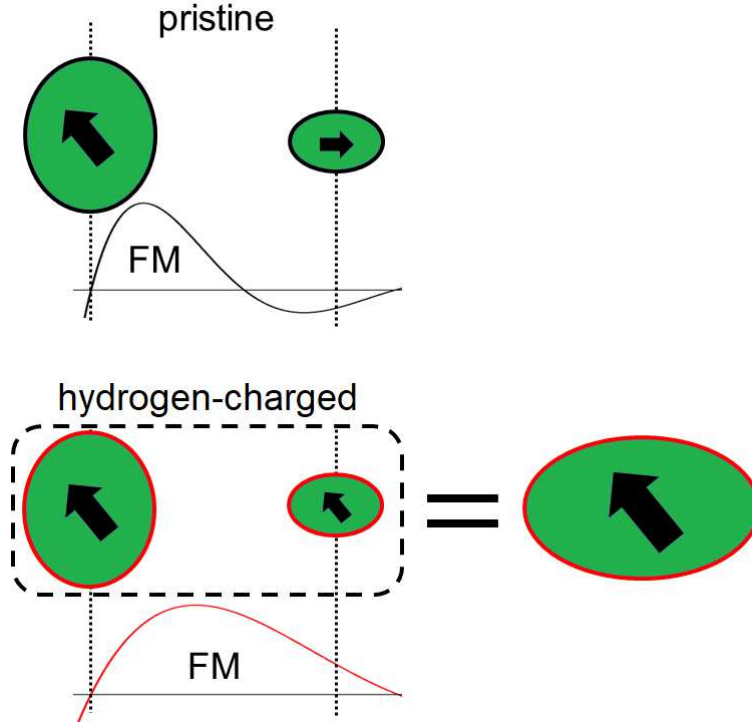
Figure 5.1: Schematic representation of the effective cluster growth mechanism upon hydrogen-charging: The extended reach of the RKKY function upon hydrogen-charging couples adjacent clusters ferromagnetically. Coupled magnetic switching of smaller clusters can be interpreted as an average cluster growth. Adapted from Ref. 41.

For superparamagnetic particles in the blocked state, the average magnetic moment according to the Stoner-Wohlfarth model reads[224]

$$m_{\text{blocked}} = \frac{\mu_0 M_{\text{S}}^2 V H}{3 K_{\text{eff}}},$$
(5.2)

assuming a random orientation of anisotropy axes. Here, M_{S} is the saturation magnetisation, H the magnetic field, K_{eff} the effective anisotropy constant, and μ_0 is the usual physical constant. An analogous equation holds for the average magnetic moment of a particle in the superparamagnetic state above the blocking temperature:[224]

$$m_{\text{SPM}} = \frac{\mu_0 M_{\text{S}}^2 V^2 H}{3 k_b T},$$
(5.3)

where T denotes the temperature and k_b is the Boltzmann constant. Both equations are valid for particles without an average preferred orientation with respect to the external field direction.

The observed change of the magnetisation of npPd(Co) can therefore be understood by the following sequence of arguments: When the magnetic volume V increases upon hydrogen-charging, a larger fraction of the superparamagnetic clusters can no longer flip their moment by thermal excitations within the timescale of the experiment, leading to additional moments pointing in the external field direction. Magnetic moments of the clusters, which are randomly aligned without hydrogen, are being 'blocked' in the external field direction by the increasing V. As a result, the average blocking temperature T_B also shifts to a higher value upon hydrogen-charging. Moments, which were previously statistically oriented due to thermal switching now align in the field direction and contribute to the total magnetic moment following Eq. 5.2. Additionally, growing clusters still below the critical size for blocking also show an enhanced moment in the superparamagnetic state following Eq. 5.3. The sum of both blocked and superparamagnetic moments, which both grow with particle volume V, is measured as an increased magnetisation upon hydrogen-charging (Fig. 4.34a and Fig. 4.38a-f). Upon hydrogen removal from the Pd lattice, magnetic size and T_B decrease, which again enables statistical alignment of the (smaller) cobalt clusters with respect to the field direction and decreases the magnetisation back to the initial values.

The increase of blocking temperatures upon hydrogen-charging as predicted by the mechanism was experimentally confirmed for npPd$_{1-x}$Co$_x$ in Fig. 4.39, where significantly higher values for T_B are observed in the hydrogen-charged state. The proposed cluster growth mechanism upon hydrogen-charging was further put to the test in Fig. 4.31, where magnetisation curves before and after hydrogen-charging are depicted. Both curves are characteristic for superparamagnetic units. Adequate modelling of such superparamagnetic magnetisation curves allows extracting information about the mean superparamagnetic size and the size distribution[225]. Based on a normal (Gaussian) distribution of particle sizes, the Langevin function for superparamagnetic magnetic moment $m(H, T)$ as a function of magnetic field H and temperature T can be written as:

$$m(H, T) = N \int_0^\infty \frac{M_s \pi D^3}{6} \left[\coth(x) - \frac{1}{x} \right] \mathrm{PDF}(D) dD + \chi H, \qquad (5.4)$$

where N is the number of magnetic clusters per unit mass, M_s is the saturation magnetisation

(for Co:1420 emu/cm^3), D is the particle diameter, and χ is a paramagnetic contribution to the magnetisation curve. The argument x of the Langevin function reads

$$x = \frac{\mu_0 M_s \pi D^3 H}{6 k_b T}, \tag{5.5}$$

with μ_0 and k_b being the usual physical constants. The particle distribution function (PDF) was assumed to be a normal (gaussian) distribution centred around $\bar{D}$ with a standard deviation σ:

$$\text{PDF}(D) = \frac{1}{\sqrt{2\pi\sigma^2}} \exp\left(-\frac{(D-\bar{D})^2}{2\sigma^2}\right). \tag{5.6}$$

Experimental data for hydrogen-charging and uncharged npPd(Co) were fitted using a least squares parameter fit following Eq. 5.4, with the resulting parameters N, $\bar{D}$, σ and χ being displayed directly in Fig. 4.31. Fits for both curves are in excellent agreement with the data. While parameters N and χ account for the high field magnetisation, the steeper slope around zero field is modelled by a larger average cluster size $\bar{D}$. This increase in magnetic clusters size upon hydrogen-charging is in perfect agreement with the predictions from the proposed tuning mechanism for npPd(Co).

Both relative and absolute changes in magnetisation for the different cluster sizes in GCD npPd$_{1-x}$Co$_x$ in Fig. 4.38 and Fig 4.39 can also be understood in accordance with the mechanism proposed here: With increasing concentration and size, superparamagnetic clusters tend closer to the ferromagnetic threshold and get easier 'blocked' by the hydrogen-induced cluster coupling in a simple picture. Therefore, absolute changes in magnetisation increase with increasing size of superparamagnetic clusters up to ΔM=1.5 emu g^{-1} for $x_{\text{Co,nom}}$=15% (Tab. 5.1). Existing larger ferromagnetic clusters are no longer relevant for the hydrogen-induced switching mechanism. As a certain fraction of already ferromagnetic clusters exists in npPd$_{(1-x)}$Co$_x$ for $x_{\text{Co,nom}} \geq$12%, the relative tuning amplitude of magnetisation is lower compared to concentrations <12% (Fig. 4.38 and Tab. 5.1).

A hydrogen-mediated coupling between micrometer-domains in Co$_{30}$Pd$_{70}$ alloy films has been experimentally observed by Chang et al.[101] using magneto-optical Kerr effect (MOKE) microscopy. They reported an effective domain growth upon hydrogen-charging, which can be fully explained by the new RKKY-mechanism established above. In contrast to our findings, they observed a decreasing magnetisation upon hydrogenation, which can be

understood in terms of the different magnetic sizes: The key for magnetic switching in our work are the nanometer-sized, superparamagnetic clusters, which are subject to thermal randomisation at room temperature. Micrometer-domains, as studied by Chang et al.,[101] are mostly unaffected by temperature and contribute to the measured magnetisation at room temperature. Enhanced coupling manifests itself in larger magnetic entities in both cases, but enables alignment of magnetic moments and thus an increase of magnetisation only for superparamagnetic clusters. Band filling upon hydrogen-charging decreases the magnetic moment in microscopic CoPd alloy domains, but is not relevant compared to the strong superparamagnetic switching effect in npPd(Co).

Magnetisation changes upon hydrogen adsorption as presented in Sec. 4.4.2.1 naturally yielded smaller magnetisation changes compared to the measurements in the hydrogen absorption regime, where hydrogen is intercalated in the Pd lattice. Adsorption-induced magnetic changes can be rationalised using an interplay of double-layer charging and hydrogen magneto-ionic mechanisms previously outlined. As apparent from Fig. 4.29, a part of the transferred charge ($\Delta Q >$-0.1 V) produces the same loop as for the analogous experiment in the electrochemical double-layer in Fig. 4.27, indicating one of the proposed double-layer mechanisms is responsible for the magnetisation changes. For more negative charge values the slope of the curves gets steeper, indicating a distinctively different magneto-electric mechanism gaining the upper hand. Although hydrogen is not present in the lattice upon hydrogen-adsorption, the proposed intercluster-coupling mechanism might still be a valid explanation: The large interaction distance of the RKKY function in the nm-range might be responsible for a coupling of subsurface Co-rich clusters induced by changes in the electronic structure near the surface due to hydrogen adsorption. Furthermore, a sharp distinction between hydrogen ad- and absorption on the basis of potential values only is often difficult, which might allow a minor contribution of hydrogen absorption already in the nominal adsorption regime. The stimulus of hydrogen adsorption has not been investigated for magneto-ionics to the same extent as the more effective hydrogen absorption process in this thesis, but could prove an interesting option to explore in future experiments. The related PtCo system, where only hydrogen adsorption (but no interstitial absorption) is possible, could be a candidate for such prospective studies.

Tuning magnetisation curves

The magneto-ionic switching mechanism based on the coupling of superparamagnetic Co-rich clusters upon hydrogen-charging coherently explains increasing magnetisation values upon hydrogen-charging for PCD npPd(Co) and GCD $npPd_{1-x}Co_x$ presented in Sec. 4.4.2.3. The mechanism affords a full (reversible) transition from superparamagnetic to ferromagnetic behaviour, which has been attempted experimentally in Sec. 4.4.2.2. For npPd(Co) (U_D=0.7 V; I_R=0.1 mA) in Fig. 4.31 hydrogen-charging lead to steeper superparamagnetic magnetisation curves, which were interpreted in terms of the cluster-growth mechanism above. A similar effect was observed for partly ferromagnetic npPd(Co) in Fig. 4.32, which was only biased to a voltage of U=-0.6 V in the hydrogen adsorption regime. The ferromagnetic part, likely arising from a small piece of alloy covered during dealloying, does not change upon hydrogen-adsorption. Interestingly, hydrogen adsorption as a stimulus increases the paramagnetic slope of the magnetisation curve and allows a reversible tuning of magnetisation curves as evidenced in Fig. 4.32. Although the mechanism behind that change remains not exactly clear, one could surmise a change in RKKY-coupling in surface-near layers due to adsorbed hydrogen species, as outlined above. In any case, a transition to a fully ferromagnetic state could not be achieved upon hydrogen-charging of npPd(Co).

Homogenised npPd(Co) in Fig. 4.33, on the other hand, enabled a transition to ferromagnetism upon stepwise hydrogen-charging. It has to be noted that the obtained effect was not reversible, i.e. magnetisation curves did not return to the pristine state after hydrogen-discharging. Not only coercivity, but also magnetisation increased upon hydrogen-charging. An increasing coercivity has been already observed for CoPd alloy films[93,98] upon hydrogen-charging, although always in combination with a decreasing magnetic moment. Here, a combination of effects might be present in the homogenised PdCo sample. The homogenisation temperature-treatment levels the Co distribution in npPd(Co), transforming it into a single-phase alloy, which explains the increase in coercivity. The superparamagnetic cluster growth mechanism, however, does not fit with the transformation of embedded Co-rich clusters into a homogeneous alloy. A conceivable reason for the increasing magnetisation is the formation of hydrogen-induced defects in the homogenised npPd(Co)sample, which has been reported to increase magnetisation in Pd nanoparticles[200]. The prolonged hydrogen-charging over the full timespan of a magnetisation curve in the order of hours might favour such a scenario.

5.2.2.2 Kinetic aspects of hydrogen-induced magnetism

Switching speed

Although time-dependent magnetisation upon electrochemical cycling allowed a reversible tuning of magnetisation with voltage (see Fig. 4.34 and Fig. 4.38), the goal of tuning from fully superparamagnetic state to pure ferromagnetism has not been reached for npPd(Co) in this thesis. As already mentioned in Sec. 4.4.2.2 a faster acquisition of magnetisation curves for tailor-made npPd(Co) might allow the eventual observation of the full switching between superparamagnetism and ferromagnetism.

Another limitation of the measurement method of SQUID magnetometry became apparent when the magneto-ionic switching speed was tested, which is shown in Fig. 4.35. A cyclic switching in the order of 1% was observed within 20 s, while a faster switching was limited by the sampling frequency of the magnetometer. The reduced magnitude of the magneto-ionic effect is rationalised in terms of the limited diffusion time for hydrogen atoms in the Pd lattice.

Volatility

The volatility test in Fig. 4.36 will be discussed next. In the proposed superparamagnetic coupling mechanism two distinct processes show a time-dependence. On the one hand, hydrogen-charging in npPd(Co) is limited by hydrogen diffusion in the electrolyte and the Pd ligaments, while, on the other hand, superparamagnetic relaxation times affect the net magnetisation. While hydrogen diffusion in nanoporous Pd is expected to be a fast process, superparamagnetic relaxation times crucially depend on the effective magnetic cluster sizes, which change during hydrogen-charging. Though this effect is not fully understood yet, a possible explanation for the volatility and the surprising increase of magnetic moment which persists after charging is presented in the following:

Diffusion of H in Pd is known to be a fast process with a diffusion constant of $D = 3.8 \cdot 10^{-11}$ m^{2}s^{-1} at room temperature[226]. Hydrogen diffusion in PdCo alloys is still comparably fast, with a diffusion constant of $D = 3 \cdot 10^{-12}$ m^{2}s^{-1} for $Pd_{75}Co_{25}$ at room temperature[227]. A brief estimation of the diffusion length L, following $L \sim \sqrt{2D\tau}$, with $\tau \sim 0.5$ h being the time for hydrogen charging and $D = 3 \cdot 10^{-12}$ m^{2}s^{-1} the value cited for $Pd_{75}Co_{25}$, yields a diffusion length in the range of 100 μm, well above the expected ligament

size in the order of 5 nm (see Sec. 4.2.4). Hydrogen atoms within the PdCo matrix can therefore be considered as evenly distributed, with no concentration gradient from surface to core. A direct influence of hydrogen diffusion on the observed latency of magnetisation reversal on larger timescales is therefore considered unlikely.

Superparamagnetic relaxation time τ is determined largely by the volume V of superparamagnetic units following[228]:

$$\frac{1}{\tau} = \frac{1}{\tau_0} \cdot \exp\left(-\frac{K_{\text{eff}}V}{k_{\text{b}}T}\right), \tag{5.7}$$

where τ is the relaxation time, $\frac{1}{\tau_0}$ is the attempt frequency for magnetisation reversal (10^{-9} s), K_{eff} the effective anisotropy constant, k_{b} the Boltzmann factor, and T the temperature. Setting $\tau=100$ s as the typical timescale for a single point measurement of magnetisation, Eq. 5.7 becomes the well-known blocking criterion in Eq. 2.3.

When an applied magnetic field is removed from an assembly of superparamagnetic particles at a time $t = 0$, magnetisation $M(t)$ follows an exponential decay with the time constant τ as[228]:

$$M(t) = M_0 \cdot \exp\left(-\frac{t}{\tau}\right), \tag{5.8}$$

where M_0 is the initial magnetisation.

The period of increasing magnetic moment already at OCP, where hydrogen-charging is stopped (Fig. 4.36), might be interpreted in terms of a similar superparamagnetic equilibration process. Cluster growth upon hydrogen-charging makes superparamagnetic units more stable against thermal fluctuation, while the alignment process in a magnetic field still follows an analogous rate equation as in Eq. 5.7.[e] The alignment of larger clusters in a magnetic field does therefore not occur immediately, but successively with a characteristic relaxation time τ. After hydrogen-charging, once the electrochemical cell is held at OCP, cluster sizes decrease again. However, clusters might still be large enough to align in the magnetic field via thermal relaxation. This latent increase therefore arises from a period where cluster alignment in the field and cluster shrinkage compete with each other.

---

[e]In a simple picture only the energy barrier for magnetisation reversal is altered asymmetrically in an external field H by a Zeeman energy term to $K_{\text{eff}}V \pm \mu H$, where μ is the moment of the superparamagnetic particle[229].

Once desorption becomes the dominant process upon holding at OCP in Fig. 4.36, the magnetic moment begins to decay exponentially. Such an exponential decay would also be typical for hydrogen diffusion in Pd[230]. As already argued above, the time constant, however, is far too large for hydrogen diffusion in the present case ($\tau \sim 7$ h). It is more likely that again superparamagnetic cluster relaxation influences the magnetisation upon desorption: Cluster-coupling induced by hydrogen-charging is weakened upon desorption, which reduces the effective cluster size. Thermal effects start to randomise the magnetisation directions of now smaller magnetic clusters, which leads to an exponential decay as described by Eq. 5.8. An average cluster diameter can be estimated from the observed relaxation time using the blocking criterion in Eq.5.7 and the anisotropy constant for bulk hcp Co of $4.1\ 10^5\,\mathrm{J/m^3}$[231], which yields $\bar{d}$=8.4 nm. This value is larger than the magnetic cluster size for npPd(Co) (U_D=0.7 V; I_R=0.1 mA) prior to the hydrogen treatment, which is $\bar{d}$=5.2 nm estimated from the blocking temperature (Tab. 4.2) using the same formula. Magnetisation after holding at OCP does also not return to the value prior hydrogen-charging, but remains $\sim 10\%$ higher even after 8 h. This might be an indication for residual hydrogen in the lattice and a fraction of clusters still coupled magnetically. Excellent reversibility in the cyclic hydrogen charging tests in Fig. 4.34 nonetheless suggest that the cluster coupling can be fully reversed after complete hydrogen desorption.

5.2.2.3 Alternative tuning mechanisms

Both PCD npPd(Co) in Fig. 4.34 and GCD npPd$_{(1-x)}$Co$_x$ in Fig. 4.38 yielded remarkable magnetic responses upon voltammetric cycling, which has been ascribed to a hydrogen-induced change in the coupling of Co-rich clusters in the previous section. Several other plausible effects, which have been considered as an explanation for the magnetic response upon voltammetric cycling, will be briefly addressed here.

A contribution of magneto-elastic effects, i.e., changes in magnetisation via a strain coupling from the Pd matrix to the Co clusters, is considered first. Although strain-coupling can be efficiently used to alter the magnetic properties of embedded superparamagnetic particles,[106,107] such a scenario is considered unlikely in our case. On the one hand, most of the hydrogen-induced strain is supposed to be relieved in the Pd/PdH matrix considering the larger Young's modulus for Co (Co: 206 GPa, Pd: 115-125 GPa[232]). On the other hand,

compressively strained Co is expected to show a smaller magnetisation in both fcc and hcp lattices compared to the equilibrium configuration, [233] which does not reflect the result of an increasing magnetisation upon hydrogen-charging.

In contrast to the mentioned strain-coupling between Co and Pd, hydrogen-induced strain and anisotropy changes in the Pd matrix alone are also considered. Metallic Pd is known to become ferromagnetic under the application of a small ($\sim 5\%$) tensile strain[81]. Internal hydrogen-induced strain, on the other hand, is unlikely to evoke a ferromagnetic response in Pd or PdCo, due to the much stronger competing electronic effect of donating electrons into the d-band upon hydrogen-charging, which decreases the susceptibility[91,99,100]. A modulation of perpendicular magnetic anisotropy has been reported in Pd/Co multilayer and alloy films upon hydrogen-charging[93,96,97]. As no directional anisotropy axis is expected for arbitrary nanoporous structures, anisotropy effects on the surface cannot account for a large magnetisation increase upon hydrogen-charging as observed in this thesis. An anisotropy modification in the internal Co-rich clusters due to hydrogen, however, could promote a blocking of superparamagnetic clusters and be a part of the overall switching mechanism.

While the aforementioned arguments are only theoretical considerations, the relation of strain and magnetisation has also been checked experimentally. An *in situ* dilatometry experiment upon hydrogen charging has been performed to directly compare changes in hydrogen-induced strain with hydrogen-induced magnetisation changes. Strain and magnetic moment measured using *in situ* measurement setups for PCD npPd(Co) (U_D=0.7 V; I_R=0.1 mA) during a single CV cycle are presented in Fig. 5.2.

External strain $\Delta L/L_0$ measured in the dilatometry experiment (red in Fig. 5.2) increases in both chemical regimes associated with oxygen ad- and desorption on the Pd surface ($U >$-0.5 V) and hydrogen-charging ($U <$-0.6 V). Although strains in the oxide regime are much larger, magnetisation changes (blue in Fig. 5.2) in that region are only a minor fraction of the total change. Accordingly, smaller changes in strain and larger variations in magnetic moment occur in the hydrogen regime. Upon close inspection one notices that the maxima of both strain and magnetic moment curves do not coincide, and magnetic moment decreases only at higher potentials (i.e. the hysteresis loop is larger compared to strain). Both of these are additional experimental indications that a coupling of strain and magnetic moment via
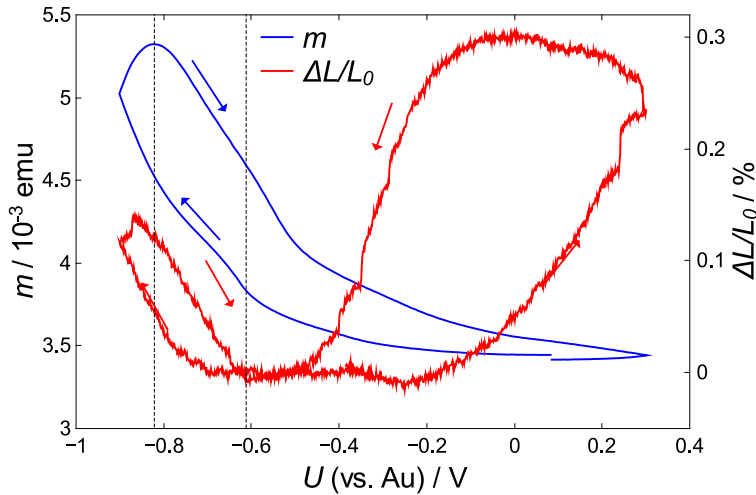
Figure 5.2: Strain $\Delta L/L_0$ and magnetic moment Δm as a function of voltage U between -0.9 V and 0.3 V for npPd(Co) in the hydrogen-charging regime. One out of 10 voltammetric cycles with a scan rate of 0.5 mVs^{-1} is shown. Changes in magnetic moment have been presented already in Fig. 4.34. For the calculation of relative length changes $\Delta L/L_0$, sample length L_0 after dealloying was used. Arrows indicate the cycling direction.

magnetoelastic effects is not the main cause for the variations in magnetic moment in the hydrogen-charging regime, supporting the theoretical considerations above.

Pure surface charging as a significant contribution for the large magnetisation changes in the present work might also be discarded for the following reasons: Surface-charging effects are generally much faster processes compared to ion diffusion, while the magnitude of the effects are typically smaller in comparable voltage windows.[10,12,33] The long switching times in the order of hours for the full switching amplitude and large relative changes in magnetisation support a magneto-ionic mechanism. Most convincingly, the fact that the magnetisation relaxes to its original value on a timescale of hours upon opening the circuit (Fig. 4.36) clearly indicates a chemical, rather than an electrostatic origin of the observed magnetisation changes.

Another possible contribution to the magneto-ionic changes is the direct hydrogen-charging of the Co-rich clusters. Hydrogen-charging has been reported in CoPd alloys of various compositions, although the hydrogen storage capacity drops significantly below 0.1 H per Pd/Co atom, when the Co fraction is larger than 15%[234]. As clusters in the dealloying process can be considered as relics of the original alloy, the composition of those clusters is also close to the initial alloy composition[69], which is $Co_{75}Pd_{25}$ in this work. For such Co-rich Pd alloys, it has been shown that magnetic properties remain unaffected upon

hydrogen-charging[93], likely due to the vanishing hydrogen storage capacity at higher Co concentrations.

As already touched briefly in Sec. 4.4.2.3, Co oxidation/reduction on the surface is considered as another possible mechanism. The reversible oxidation of Co to CoO has already been utilised in tunable magnetic systems[17,235]. A reversible shrinkage of Co(Pt) metallic regions in nanoporous Co-Pt microdisks due to Co oxidation upon voltage application was proposed as a mechanism by Navarro-Senent et al.[17]. The option of such a mechanism for npPd(Co) deserves thorough examination, as it could even account for changing superparamagnetic sizes in our case.

Although as a result of the dealloying process only a minor fraction of the Co atoms is expected on the surface of npPd(Co) (as seen in KMC simulations in e.g. Fig. 4.6), there is still a chance that Co atoms may cause magnetisation changes upon oxidation/reduction. Indeed, oxygen was found on the surface of npPd(Co) in EDS images, which has been generally attributed to Pd oxide. It is challenging to rule out Co oxidation on the basis of electrochemical measurements solely, due to the large magnitude of the hydrogen-associated currents, which would superimpose the weaker Co currents in a similar voltage range. However, one indication against the Co oxidation-reduction mechanism is the voltage position of the magnetisation peak in the CV representation, as shown above in Fig. 4.37. Magnetisation in blue clearly follows the hydrogen desorption peak A' of the current curve (black), indicating a correlation of hydrogen and magnetisation. More importantly, as the onset of Co oxidation is expected at a constant potential, the decrease of magnetisation should always start at the same potential value regardless of the scan limits in the Co oxidation/reduction mechanism.

Further experimental tests have been conducted supporting this indirect electrochemical argument. The sample with the highest overall Co content used for tuning tests (GCD npPd$_{1-x}$Co$_x$ with $x_{Co,nom}$=0.15), where possible Co oxidation and reduction effects are considered most likely, has been investigated using *in situ* Raman spectroscopy and *ex situ* XPS, with the key results displayed in Fig. 5.3. Raman spectroscopy was selected as the method of choice as it is highly sensitive to metal oxides and hydroxides of any kind with detection limits in the order of 1%, whereas pure metals cannot be detected. XPS is an ideal complementary method, as it gives information about the oxidation states of elements. XPS measurements have been performed in cooperation with Prof. Martin Sterrer (Institute of
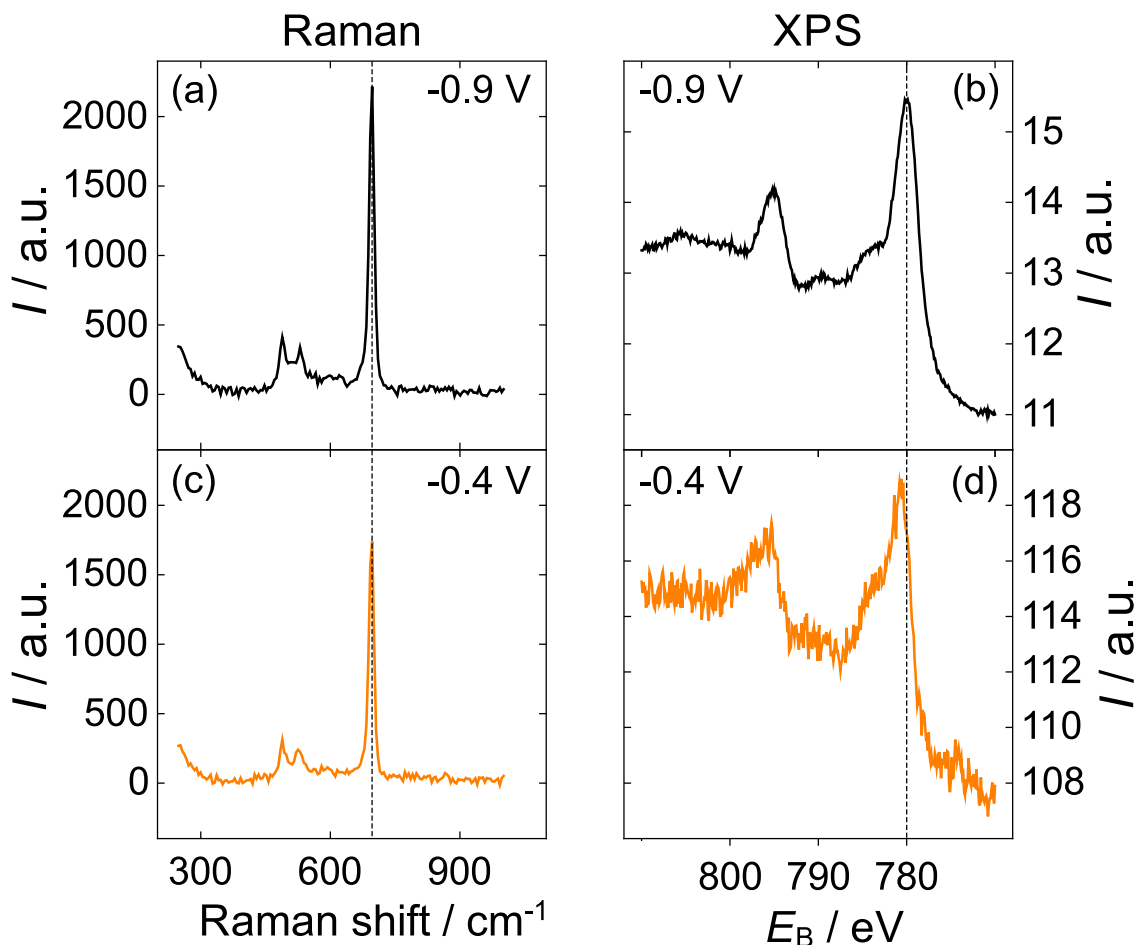
Figure 5.3: *In situ* Raman spectra and *ex situ* XPS spectra of GCD npPd$_{1-x}$Co$_x$ with $x_{Co,nom}$=0.15 upon electrochemical treatment: Spectra recorded at the lower (-0.9 V – a and b) and higher potential limit (-0.4 V – c and d) used for voltammetric cycling in Fig. 4.38. XPS samples have not been in contact with ambient atmosphere after preparation. Vertical lines mark the positions of the most prominent Co oxide peaks, which are unchanged with potential in both Raman and XPS.

Physics, University of Graz), while Raman spectra have been measured in cooperation with Dr. Harald Fitzek (Institute of Electron Microscopy and Nanoanalysis, TU Graz). Details on the experimental setups can be found in Sec. 3.5.

Surprisingly, Co-oxide was indeed found on the surface of some as-prepared samples, as shown for an exemplary sample in Fig. 5.3(a) and (c). Raman peaks can be either associated with CoO (fcc or hcp) or spinel Co$_3$O$_4$[150,152]. The oxide variant detected is also affected by the power intake from the Raman laser beam. However, regardless of the form of Co-oxide on the surface, we could not find any signs for a reduction of this oxide in the voltage range used for magnetometry (-0.9 V< U <-0.4 V) for three different investigated samples. This finding is also confirmed by *ex situ* XPS measurements, which detected Co in the oxidised state

for samples prepared at both potential limits as shown in Fig. 5.3(b) and (d). Even during tests at lower cathodic voltages, well in the range of hydrogen evolution, oxides proved to be remarkably stable during *in situ* Raman spectroscopy (not shown). These findings clearly exclude oxidation effects as an explanation for the magnetisation variation. For all the listed arguments above, a hydrogen-induced change in the RKKY periodicity and a concomitant intercluster coupling as presented in Sec. 5.2.2 is still considered the most likely mechanism for the hydrogen-induced magnetisation changes.

5.2.3 Magneto-electric classification

The performance of magneto-electric materials is generally evaluated using the (converse) magneto-electric coupling coefficient α. The conventional definition of α reads $\Delta M/\Delta E$, where magnetisation changes ΔM (in emu/cm^3) are related to changes in the electric field ΔE (in V/cm). This definition is somewhat impractical for magneto-ionic material systems for different reasons: Inhomogeneities of the electric field within the magnetic material and potential problems with the determination of the electric field E are two main issues using the conventional definition. Furthermore, as magneto-ionic systems often comprise a nanoporous or thin-film electrode, a precise determination of electrode volume can be challenging[5]. Another important point arises for the assessment of magneto-electric systems consisting of a liquid-solid interface. Extremely large electric fields in the order of MV/cm can be obtained at such interfaces thanks to the nanometer-thick electrical double-layer forming upon application of small voltages in the order of 1V. A variation of magnetisation comparable to all solid devices, typically attained using smaller voltages in solid-liquid devices, would paradoxically lead to smaller magnetoelectric coupling coefficients using the conventional definition[4].

For the above-mentioned reasons the magnetoelectric coupling coefficient $\alpha_{C,V}$ was redefined in the review of Molinari et al.[4] as:

$$\alpha_{C,V} = \frac{4\pi\Delta M}{|\Delta U|},$$

(5.9)

with ΔM being the absolute magnetisation changes and $|\Delta U|$ the change in applied voltage.

An alternative definition of a relative magneto-electric voltage coefficient α_{rel} uses the relative variation of magnetisation ΔM_{rel} as the characteristic magnetic quantity[5]:

$$\alpha_{\mathrm{rel}} = \frac{\Delta M_{\mathrm{rel}}}{|\Delta U|}, \tag{5.10}$$

While the first definition in Eq. 5.9 formally converts changes in magnetisation into units of magnetic field, enabling usage for both magneto-ionic field and magnetisation switching, the relative magneto-electric voltage coefficient in Eq. 5.10 enable comparability of magnetic changes obtained via different experimental techniques (Magneto-optical Kerr effect, anomalous Hall effect, vibrating sample magnetometry, SQUID magnetometry)[4,5], as the determination of absolute magnetic moment is no longer necessary. Both definitions share the voltage change in the divisor, which avoids the rather precarious determination of electric field.

Here, magneto-electric performance is evaluated using both absolute and relative magneto-electric voltage coefficients. A summary of all attained magneto-electric effects for npPd(Co) by means of double-layer charging as well as via magneto-ionic hydrogen-charging is presented in Tab. 5.1, where charging and dealloying method, electrolyte, magnetisation changes, voltage range, and magneto-electric voltage coefficient are given.

Table 5.1: Magnetic tuning parameters for npPd(Co) in the present thesis: Charging type, dealloying method and relevant dealloying parameters are stated in the first two columns. The electrolyte for charging is given in the third column. Further, the used voltage window $|\Delta U|$, the absolute changes in magnetisation upon charging ΔM, the relative changes in magnetisation upon charging ΔM_{rel} and two different definitions of magneto-electric voltage coefficients $\alpha_{\mathrm{rel}}=\Delta M_{\mathrm{rel}}/|\Delta U|$ [5] and $\alpha_{\mathrm{C,V}} = 4\pi\Delta M/|\Delta U|$ [4]. The measurement field and temperature were $\mu_0 H$=0.5 T and T=300 K for all measurements. If not stated otherwise, the residual dealloying current for PCD experiments was I_{R}=0.01 mA.

charging type	parameters	electrolyte	$|\Delta U|$ / V	ΔM / emu g^{-1}	ΔM_{rel} / %	α_{rel} / % V^{-1}	$\alpha_{\mathrm{C,V}}$ / Oe V^{-1}	figure
DL-charging	PCD, U_{D}=0.55 V	1 M LiPF$_6$	1.1	0.0036	0.14	0.13	0.49	4.24
DL-charging	PCD+T, T_{A}=373 K, U_{D}=0.55 V	1 M LiPF$_6$	1.1	0.0027	0.24	0.22	0.36	4.24
DL-charging	PCD+T, T_{A}=573 K, U_{D}=0.55 V	1 M LiPF$_6$	1.1	0.0033	0.64	0.58	0.44	4.24
DL-charging	PCD+T, T_{A}=773 K, U_{D}=0.55 V	1 M LiPF$_6$	1.1	0.0018	0.65	0.59	0.24	4.24
DL-charging	PCD, U_{D}=0.55 V	1 M KOH	0.1	0.0041	0.6	6.0	6.1	4.26
DL-charging	PCD+T, T_{A}=373 K, U_{D}=0.55 V	1 M KOH	0.1	0.0042	0.6	6.0	6.2	4.26
DL-charging	PCD+T, T_{A}=573 K, U_{D}=0.55 V	1 M KOH	0.1	0.0029	0.5	5.0	4.3	4.26
DL-charging	PCD+T, T_{A}=773 K, U_{D}=0.55 V	1 M KOH	0.1	0.0031	0.4	4.0	4.6	4.26
H-adsorption	PCD, U_{D}=0.55 V,	1 M KOH	0.3	0.0140	2.8	9.3	6.9	4.28
H-adsorption	PCD+T, T_{A}=373 K, U_{D}=0.55 V	1 M KOH	0.3	0.0269	4.0	13.3	13.3	4.28
H-adsorption	PCD+T, T_{A}=573 K, U_{D}=0.55 V	1 M KOH	0.3	0.0175	2.8	9.3	8.7	4.28
H-adsorption	PCD+T, T_{A}=773 K, U_{D}=0.55 V	1 M KOH	0.3	0.0315	4.6	15.3	15.6	4.28
H-charging	PCD, U_{D}=0.70 V, I_{R}=0.1 mA	1 M KOH	1.2	0.15	100	83	18	4.34(a)
H-charging	PCD, U_{D}=0.70 V, I_{R}=0.1 mA	1 M KOH	1.2	0.25	170	142	31	4.34(c)
H-charging	PCD, U_{D}=0.70 V, I_{R}=0.1 mA	1 M KOH	1.2	0.95	730	608	118	4.34(c)
H-charging	GCD, $x_{\mathrm{Co,nom}}$=0%	1 M KOH	0.5	0.02	1.3	2.6	5	4.38(a)
H-charging	GCD, $x_{\mathrm{Co,nom}}$=3%	1 M KOH	0.5	0.07	3.8	7.6	19	4.38(b)
H-charging	GCD, $x_{\mathrm{Co,nom}}$=6%	1 M KOH	0.5	0.22	8.4	16.8	65	4.38(c)
H-charging	GCD, $x_{\mathrm{Co,nom}}$=9%	1 M KOH	0.5	0.88	24.2	48.4	255	4.38(d)
H-charging	GCD, $x_{\mathrm{Co,nom}}$=12%	1 M KOH	0.5	0.61	7.4	14.8	177	4.38(e)
H-charging	GCD, $x_{\mathrm{Co,nom}}$=15%	1 M KOH	0.5	1.50	11.8	23.6	422	4.38(f)

For experiments using double-layer charging (DL-charging), magnetisation changes remained small, not exceeding ΔM_{rel}=1%. Consequently, magneto-electric charging coefficients were comparably small despite the limited voltage windows $|\Delta U|$ in the electrochemical double-layer. Values for $\alpha_{C,V}$ between 0.24 and 6.2 Oe V^{-1} are in the lower range of literature data of other magneto-electric solid/liquid composite systems using charge-carrier or strain doping, where values vary between 1 and 250 Oe V^{-1} depending on the actual system[4]. Interestingly, for a literature reference for nanoporous PdCo alloy[10] where charging was conducted in LiClO$_4$-based electrolyte, a similar magneto-electric charge coefficient of 1 Oe V^{-1} was obtained[4] in a larger voltage window of $|\Delta U|$=2 V. Relative magneto-electric voltage coefficient α_{rel}=1.5% V^{-1} for the same reference[10] are also comparable. The general conclusion is that double-layer charging of nanoporous Pd(Co) is not suitable to obtain large magneto-electric effects, even when the Co distribution is adjusted via thermal treatment. This is attributed to magneto-elastic effects and pseudocapacitive reactions during charging, while electronic band filling cannot be observed.

Shifting the voltage window towards hydrogen adsorption improves the magneto-electric performance. Absolute and relative magneto-electric charge coefficients increase to 15.6 Oe V^{-1} and 15% V^{-1}, respectively. As from a mechanistic standpoint adsorption can neither be considered as charge carrier doping nor as bulk magneto-ionic mechanism, it is difficult to find adequate references for pure hydrogen adsorption in the literature for comparison. However, it should be noted that already hydrogen adsorption compares quite favourably to numerous bulk magneto-ionic systems in terms of magneto-electric voltage coefficients[4,5].

The highest values for relative magnetisation changes were attained for PCD npPd(Co) upon hydrogen-charging, which reached ΔM_{rel}=100% and even higher values of ΔM_{rel}=730% at lower sorption potentials, although no longer fully reversible. As a result, large values were also attained for magneto-electric voltage coefficients $\alpha_{C,V}$=18 Oe V^{-1} (118 Oe V^{-1} for the lower sorption potential) and α_{rel}=83% V^{-1} (601 % V^{-1} for the lower sorption potential). In a comparison of relative magneto-electric voltage coefficients from recent publications by Nichterwitz et al.[5], the present PCD npPd(Co) as published in Ref. 41, reached the second largest value for α_{rel} out of 20 publications, although it suffers from the limitation of a comparably low switching speed. The large relative change in magnetisation for npPd(Co), however, does not reflect itself in magneto-electric voltage coefficient $\alpha_{C,V}$, where a value

over 4000 Oe V^{-1} has been reported in another liquid/solid magneto-electric composite based on the Li-induced reduction of iron oxides to metallic iron[4,23]. The remarkable feature in the npPd(Co) system clearly is the large relative variation of magnetisation upon hydrogen-charging, which stands out compared to other magneto-ionic systems.

Comparing magnetisation changes in Tab. 5.1 for GCD $npPd_{1-x}Co_x$ and PCD npPd(Co), one realises that a higher relative change of $\Delta M/M_{min} \sim 100\%$ has been obtained for PCD npPd(Co). These higher relative changes (and consequently higher values for α_{rel}) might be explained by more negative lower potential limits down to $U=$-1.05 V, thus stronger hydrogen-charging for PCD npPd(Co), and the different cluster size distributions. Absolute values $\Delta M=0.15$ emu g^{-1} for PCD npPd(Co) reside between values for Co concentrations of $x_{Co,nom}=3\%$ and $x_{Co,nom}=6\%$ for GCD $npPd_{1-x}Co_x$. Considering the Co concentration of $x_{Co,XRF}=7.2\%$, measured for PCD npPd(Co) ($U_D=0.70$ V, $I_R=0.1$ mA) in Tab. 4.2, absolute changes in ΔM roughly follow the trend with Co concentration for GCD. Values of magneto-electric voltage coefficients $\alpha_{C,V}$ and α_{rel} underline that the magneto-ionic tuning effect upon hydrogen charging can be strongly influenced by the superparamagnetic cluster size distribution in $npPd_{1-x}Co_x$.

5.2.4 Compositional changes in npPd(Co) upon voltammetric cycling

Lastly, indications for compositional changes in npPd(Co) electrodes during electrochemical voltage cycling are addressed in this section. While for magneto-ionic applications changes in surface structure and composition upon electrochemical treatment might present an obstacle regarding cycling stability and might even be a reason for drifting magnetisation baselines, such effects have been used in a positive sense to adjust the final composition and pore size in nanoporous electrodes. Electrochemical post-treatments in the form of voltammetric cycles after dealloying have been utilised to reduce the final Ag content[78,236] and coarsen the as-dealloyed structure of nanoporous Au(Ag)[168,169,237,238].

Coarsening upon electrochemical cycling has been ascribed to a changing surface diffusion constant of Au-atoms in the presence of surface adsorbates[168,169]. In particular, cyclic oxygen ad- and desorption on the gold surface has been suspected a stimulus for the electrochemical

coarsening mechanism. A theoretical study by Li et al.[239] corroborates that superficial oxygen is a substantial driving force for Ag segregation and coarsening in npAu(Ag). The dynamic surface restructuring in npAu(Ag) and a concomitant surface segregation of Ag have also been reported as a result of other reactions on the surface[240–242].

Regardless of the specific reaction, surface restructuring typically follows a mechanism as follows: The alloy component with the stronger adsorbate interaction preferentially migrates towards the surface, while an enhanced surface diffusivity for one or both alloy components promotes the coarsening of the nanoporous network via surface diffusion. In the process, a faceting of the porous surfaces is also observed[240,241]. A similar faceting has also been reported without a simultaneous structural coarsening step upon voltage cycling[170].

Here, coarsening and segregation effects for the npPd(Co) material of interest are investigated. For that purpose STEM/EELS elemental maps were recorded for npPd(Co) (U_D=0.7 V; I_R=0.1 mA) in Fig. 5.4 in the as-dealloyed state (a) and after electrochemical cycling in 1 M KOH solution for 2 (b) and 12 cycles (c), respectively. The elemental maps for Co, Pd and the overlay of both are depicted for all electrochemical treatments of npPd(Co). The EELS signature for oxygen on the surface was found on any position on the surface and is omitted in the depiction in Fig. 5.4.

In the as-dealloyed state in Fig. 5.4(a) one observes a typical distribution of Co in Co-rich clusters with sizes in the order of 1.5-3 nm in accordance with the STEM/EELS elemental maps for npPd(Co) and the prediction from the KMC simulation in Fig. 4.6. Interestingly, after the first two voltammetric cycles in KOH in Fig. 5.4(b) a finer dispersion of Co was observed, with cluster sizes well below 1 nm (note the different scale bars). These first two voltammetric cycles (also referred to as reduction treatment) operated at a comparably low scan rate of 0.1 mVs^{-1} in a lower voltage range from -1.0 V to 0.2 V, with the elemental map displayed in Fig. 5.4(b). In the elemental map after ten successive cycles for npPd(Co) at a faster scan rate of 0.5 mVs^{-1} in a higher voltage range from -0.95 V to 0.25 V one observes the opposite effect (Fig. 5.4(c)): Co-rich clusters are larger (up to 5 nm in size) compared to the as-dealloyed state, while Co was also partially detected in pore space in the STEM images. A first conclusion from the elemental maps in Fig. 4.6 is that electrochemical cycling definitely affects the distribution of Co also in npPd(Co). As EELS elemental maps
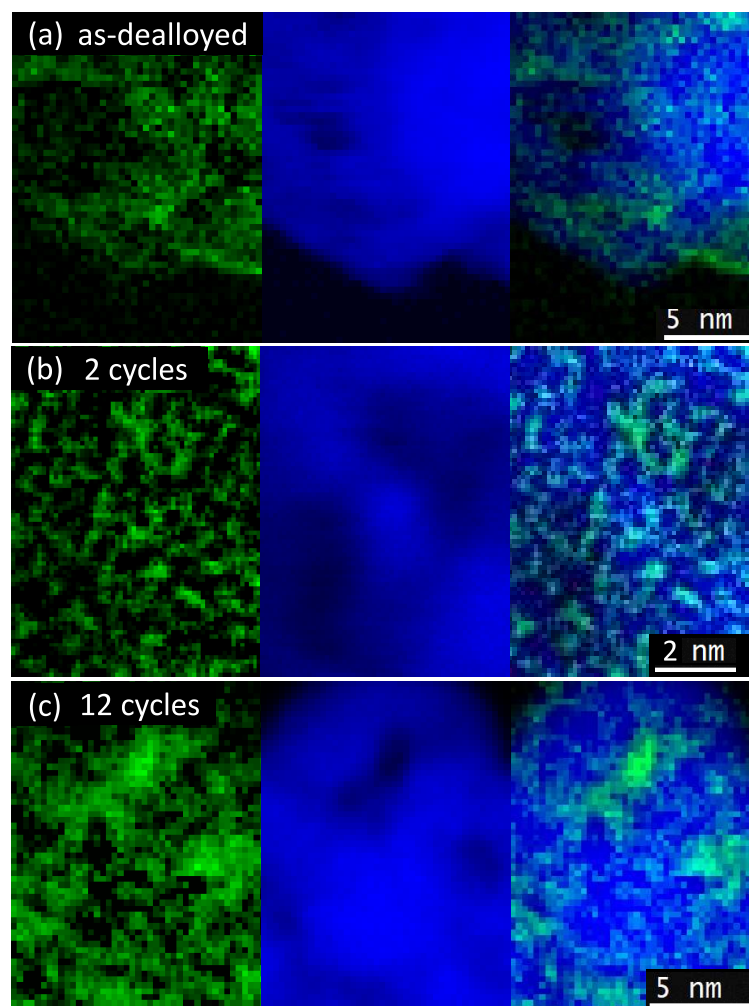
Figure 5.4: Changes in surface composition upon electrochemical treatment of npPd(Co) (U_D=0.7 V; I_R=0.1 mA): STEM/EELS elemental maps for Co (green) on the left, Pd (blue) in the middle, as well as an overlay of both Co and Pd maps on the right for as-dealloyed npPd(Co), npPd(Co) after reduction treatment (2 cycles) and after prolonged cycling (2+10 cycles). Electrochemical treatment for reduction involved two cycles at 0.1 mVs^{-1} in 1 M KOH between -1.0 V and 0.2 V, while the prolonged cycling involved 10 cycles at 0.5 mVs^{-1} between -0.95 V and 0.25 V in the same electrolyte. Note the different scale bars for the images in (b).

are mostly sensitive to surface-near layers, changes in the Co distribution are attributed to compositional changes in surface-near layers in the following.

No specific studies for electrochemically-induced Co segregation and coarsening exist for nanoporous Pd(Co) so far. However, segregation effects have been studied in the PdCo alloy system and related alloys. Co segregation has been predicted by DFT calculations in PtCo nanoparticles in the presence of adsorbed oxygen[243]. Analogously, the PdCo subsurface structure in Pd$_{100-x}$Co$_x$ nanoalloys was also proposed to be unstable in the presence of oxygen due to a Co segregation to the surface[244]. A potential effect, which does not exist for

the AuAg system, is the surface restructuring upon hydrogen ad- and absorption. Ma et al. observed a H_2-induced segregation of Pd to the surface in Pd-Co/Al_2O_3 catalyst material[245]. Moreover, for a PdCo alloy, calculations again predict the migration of Pd to the surface in a hydrogen-atmosphere at elevated temperature[246].

While upon hydrogen-adsorption Pd shows a tendency to be drawn to the surface, oxygen-adsorption tends to move Co atoms towards the sample exterior following the simple rule that the alloy component with the higher adsorbate affinity (Pd-H, Co-O) segregates upon adsorption.

In view of the just mentioned effects, compositional changes in npPd(Co) in Fig.5.4 might be understood as a consequence of an adsorbate-induced surface segregation process: The observed Co enrichment and the segregation of Co into large clusters of up to 5 nm in size upon prolonged cycling in Fig.5.4(c) is attributed to the oxygen-induced Co surface segregation at the upper potential limit in analogy to Ag-segregation to the surface predicted for npAu(Ag) upon oxygen-adsorption[239]. The finer dispersion of Co after only two voltammetric scans might be related to an enhanced surface diffusivity upon voltage cycling for both components, which evens their distribution near the surface.

Co segregation in the hydrogen-regime of the CV, on the other hand, is considered unlikely here as references predict a Pd rather than a Co segregation for similar PdCo materials. The effect of adsorbates on the coarsening behaviour of npPd(Co) was not investigated in this thesis and deserves future attention in both hydrogen- and oxygen-adsorption regimes. The interconnection of Ag segregation and coarsening in npAu(Ag)[239–242] can be expected for npPd(Co) as well, as both effects are governed by the same underlying mechanism of surface diffusion.

Partially irreversible drifts in magnetisation in Sec. 4.4.2 could be related to the presented changing surface composition and Co segregation in this section, although further studies are required to clarify the interconnection of both phenomena. Regardless, one could envisage electrochemical post-treatments as a future playground for the tailoring of surface Co composition and distribution in Pd-based materials for targeted magneto-ionic functionalisation.

CHAPTER 6

Summary and Conclusion

Within the scope of this thesis, both the dealloying process for nanoporous palladium and its applicability for magnetic property tuning have been investigated. Specialised electrochemical cells for the use in a SQUID magnetometer were constructed for both dealloying and tuning, based on preceding work at the Institute of Materials Physics. The influence of dealloying process parameters on the magnetic properties of nanoporous Pd was studied, along with a comprehensive physical and chemical characterisation of nanoporous Pd structures. Core results can be summarised as follows:

In situ dealloying

Co-rich clusters with typical superparamagnetic behaviour were found to emerge buried under the nanoporous Pd surface upon dealloying from a CoPd alloy. A transition from collective ferromagnetism of the alloy to individual cluster superparamagnetism was deduced from coercivity, which can be interpreted as an inverse magnetic percolation mechanism. The magnetic moment allowed the identification of contributions from two dealloying stages (primary and secondary dealloying), which was supported by *in situ* resistometry and *in situ* dilatometry measurements. Differences and similarities in comparison to the parade dealloying example of nanoporous Au were emphasised.

In situ charging

Electrochemical double-layer charging and hydrogen-charging were studied as stimuli for the tuning of the magnetic properties of nanoporous Pd(Co). Double-layer charging in non-aqueous and aqueous electrolyte yielded only small effects ($\Delta M_{\mathrm{rel}} < 1\%$) on the magnetisation, which are ascribed to changes in surface anisotropy, magneto-elastic effects or pseudocapacitive reactions, while it was concluded that classical electronic band filling mechanism upon double-layer charging can be ruled out as a source of magnetism changes in npPd(Co). Upon hydrogen surface adsorption, relative changes in magnetisation could be increased to several percent. Upon hydrogen-charging into the bulk, magnetic moment was found to increase strongly for npPd(Co) which contained superparamagnetic Co-rich clusters, whereas for alloy-like npPd(Co) obtained by thermal homogenisation, hydrogen-charging decreased the magnetic moment. While a decreasing magnetic moment upon hydrogen-charging could be rationalised by the well-known picture of hydrogen donating its electron into the Pd d-bands, the increasing magnetisation upon hydrogen-charging for PdCo samples was new to the literature. After careful examination of all contributions to magnetisation in the hydrogen regime, a mechanism based on the hydrogen-induced coupling of superparamagnetic clusters was presented. The mechanism was put to test in further experiments, investigating different total concentrations of Co, superparamagnetic cluster sizes and hydrogen-charging treatments. A predicted increase of magnetic anisotropy from the proposed tuning mechanism was verified by *in situ* temperature-dependent magnetisation curves upon hydrogen-charging. The magneto-electric performance of the new magneto-ionic system comprising npPd(Co) electrodes is compared to other electrochemical approaches for magnetic property tuning. It was concluded that the superior relative tuning amplitude up to $\Delta M_{\mathrm{rel}} = 600\%$ in a small voltage window makes the combination of magneto-ionics and superparamagnetism a highly attractive tuning scheme.

Outlook

Dealloyed materials are a promising future playground for magneto-ionics. Building on the foundation of this thesis, in a next step the superparamagnetic switching mechanism, which yielded promising results for the npPd(Co) system here, could be expanded to nanoporous Pd alloys with the other ferromagnetic elements Fe and Ni. Due to lower anisotropy constants for both compared to Co, the critical size for stable ferromagnetism is increased, which should greatly affect the tuning response upon hydrogen-charging.

Furthermore, dealloyed materials from ternary precursor alloys are well worth exploring for magnetic property tuning. Upon dealloying of ternary alloys the least noble component is selectively removed, with the ensuing nanoporous structure being composed of a homogeneous binary alloy of the remaining two components. Although the residual Co concentration can be controlled when dealloying from binary alloys, as demonstrated in this thesis, dealloying from ternary dealloying offers greater versatility. For example, the final Co concentration, and thus Curie temperature of the nanoporous alloys, could be engineered by the relative ratios of Pd and Co in a PdCoAl precursor, where Al is dissolved upon dealloying. Such materials with transition temperatures close to room temperature are considered particularly sensitive to external stimuli.

Superparamagnetic switching is by no means limited to dealloyed materials and might become a more general concept finding a permanent home in magneto-ionics. Superparamagnetic particles, clusters or films can be prepared by various methods such as electrodeposition, sputtering or ion-beam deposition techniques. Embedded superparamagnetic units in host materials for ions or atoms could be prepared by sandwiching them between a base and a capping layer. Annealing precipitation from supersaturated alloys is another option to produce embedded superparamagnets in a single step. Simplistically the interaction between superparamagnetic units in a matrix can be adjusted by interparticle distance or by the expansion and contraction of the host lattice upon ion intercalation. More complex interaction schemes can be conceptualised based on alterable dipolar coupling, superexchange (transmitted through oxygen bonds) or RKKY-interactions. The precise control of particle size and distance is crucial for a successful implementation, which remains challenging even with present-day techniques. Besides interparticle coupling, the increase of single particle anisotropy for individual superparamagnets and a transition to single-domain ferromagnetism could also be facilitated by ion intercalation.

Bibliography

[1] J. WEISSMÜLLER. `https://intranet.tuhh.de/aktuell/pressemitteilung_einzeln.php?Lang=de&id=7702`, 2011. Accessed: 2021-05-14

[2] R. L. STAMPS, S. BREITKREUTZ, J. ÅKERMAN, A. V. CHUMAK, Y. OTANI, G. E. W. BAUER, J.-U. THIELE, M. BOWEN, S. A. MAJETICH, M. KLÄUI, I. L. PREJBEANU, B. DIENY, N. M. DEMPSEY, B. HILLEBRANDS. The 2014 Magnetism Roadmap. *J. Phys. D: Appl. Phys.*, **47** (2014) 333001.
DOI: 10.1088/0022-3727/47/33/333001

[3] C. NAVARRO-SENENT, A. QUINTANA, E. MENÉNDEZ, E. PELLICER, J. SORT. Electrolyte-gated magnetoelectric actuation: Phenomenology, materials, mechanisms, and prospective applications. *APL Mater.*, **7** (2019) 030701.
DOI: 10.1063/1.5080284

[4] A. MOLINARI, H. HAHN, R. KRUK. Voltage-Control of Magnetism in All-Solid-State and Solid/Liquid Magnetoelectric Composites. *Adv. Mater.*, **31** (2019) 1806662.
DOI: 10.1002/adma.201806662

[5] M. NICHTERWITZ, S. HONNALI, M. KUTUZAU, S. GUO, J. ZEHNER, K. NIELSCH, K. LEISTNER. Advances in magneto-ionic materials and perspectives for their application. *APL Mater.*, **9** (2021) 030903.
DOI: 10.1063/5.0042544

[6] N. A. SPALDIN, R. RAMESH. Advances in magnetoelectric multiferroics. *Nat. Mater.*, **18** (2019) 203.
DOI: 10.1038/s41563-018-0275-2

[7] H. Ohno, D. Chiba, F. Matsukura, T. Omiya, E. Abe, T. Dietl, Y. Ohno, K. Ohtani. Electric-field control of ferromagnetism. *Nature*, **408** (2000) 944. DOI: 10.1038/35050040

[8] K. Leistner, N. Lange, J. Hänisch, S. Oswald, F. Scheiba, S. Fähler, H. Schlörb, L. Schultz. Electrode processes and in situ magnetic measurements of FePt films in a LiPF6 based electrolyte. *Electrochim. Acta*, **81** (2012) 330. DOI: 10.1016/j.electacta.2012.07.055

[9] A. Molinari, H. Hahn, R. Kruk. Voltage-Controlled On/Off Switching of Ferromagnetism in Manganite Supercapacitors. *Adv. Mater.*, **30** (2018) 1703908. DOI: 10.1002/adma.201703908

[10] S. Ghosh, C. Lemier, J. Weissmüller. Charge-Dependent Magnetization in Nanoporous Pd-Co Alloys. *IEEE INTERMAG*, **42** (2006) 3617. DOI: 10.1109/TMAG.2006.880922

[11] S. Ghosh. Charge-response of magnetization in nanoporous Pd-Ni alloys. *J. Magn. Magn. Mater.*, **323** (2011) 552. DOI: 10.1016/j.jmmm.2010.10.008

[12] A. Quintana, J. Zhang, E. Isarain-Chávez, E. Menéndez, R. Cuadrado, R. Robles, M. D. Baró, M. Guerrero, S. Pané, B. J. Nelson, C. M. Müller, P. Ordejón, J. Nogués, E. Pellicer, J. Sort. Voltage-Induced Coercivity Reduction in Nanoporous Alloy Films: A Boost toward Energy-Efficient Magnetic Actuation. *Adv. Funct. Mater.*, **27** (2017) 1701904. DOI: 10.1002/adfm.201701904

[13] K. Leistner, J. Wunderwald, N. Lange, S. Oswald, M. Richter, H. Zhang, L. Schultz, S. Fähler. Electric-field control of magnetism by reversible surface reduction and oxidation reactions. *Phys. Rev. B*, **87** (2013) 224411. DOI: 10.1103/PhysRevB.87.224411

[14] K. Duschek, M. Uhlemann, H. Schlörb, K. Nielsch, K. Leistner. Electrochemical and in situ magnetic study of iron/iron oxide films oxidized and reduced in KOH solution for magneto-ionic switching. *Electrochem. Commun.*, **72** (2016) 153. DOI: 10.1016/j.elecom.2016.09.018

[15] K. Duschek, A. Petr, J. Zehner, K. Nielsch, K. Leistner. All-electrochemical voltage-control of magnetization in metal oxide/metal nanoislands. *J. Mater. Chem. C*, **6** (2018) 8411. DOI: 10.1039/C8TC01994K

[16] A. Quintana, E. Menéndez, E. Isarain-Chávez, J. Fornell, P. Solsona, F. Fauth, M. D. Baró, J. Nogués, E. Pellicer, J. Sort. Tunable Magnetism in Nanoporous CuNi Alloys by Reversible Voltage-Driven Element-Selective Redox Processes. *Small*, **14** (2018) 1704396. DOI: 10.1002/smll.201704396

[17] C. Navarro-Senent, J. Fornell, E. Isarain-Chávez, A. Quintana, E. Menéndez, M. Foerster, L. Aballe, E. Weschke, J. Nogués, E. Pellicer, J. Sort. Large Magnetoelectric Effects in Electrodeposited Nanoporous Microdisks Driven by Effective Surface Charging and Magneto-Ionics. *ACS Appl. Mater. Interfaces*, **10** (2018) 44897. DOI: 10.1021/acsami.8b17442

[18] S. Topolovec, P. Jerabek, D. V. Szabó, H. Krenn, R. Würschum. SQUID magnetometry combined with in situ cyclic voltammetry: A case study of tunable magnetism of γ-Fe2O3 nanoparticles. *J. Magn. Magn. Mater.*, **329** (2013) 43. DOI: 10.1016/j.jmmm.2012.09.071

[19] T. Traussnig, S. Topolovec, K. Nadeem, D. Vinga Szabó, H. Krenn, R. Würschum. Magnetization of Fe-oxide based nanocomposite tuned by surface charging. *Phys. Status Solidi Rapid Res. Lett.*, **5** (2011) 150. DOI: 10.1002/pssr.201004483

[20] A. J. TAN, M. HUANG, C. O. AVCI, F. BÜTTNER, M. MANN, W. HU, C. MAZZOLI, S. WILKINS, H. L. TULLER, G. S. D. BEACH. Magneto-ionic control of magnetism using a solid-state proton pump. *Nat. Mater.*, **18** (2019) 35. DOI: 10.1038/s41563-018-0211-5

[21] S. DASGUPTA, B. DAS, Q. LI, D. WANG, T. T. BABY, S. INDRIS, M. KNAPP, H. EHRENBERG, K. FINK, R. KRUK, H. HAHN. Toward On-and-Off Magnetism: Reversible Electrochemistry to Control Magnetic Phase Transitions in Spinel Ferrites. *Adv. Funct. Mater.*, **26** (2016) 7507. DOI: 10.1002/adfm.201603411

[22] D. A. GILBERT, J. OLAMIT, R. K. DUMAS, B. J. KIRBY, A. J. GRUTTER, B. B. MARANVILLE, E. ARENHOLZ, J. A. BORCHERS, K. LIU. Controllable positive exchange bias via redox-driven oxygen migration. *Nat. Commun.*, **7** (2016) 11050. DOI: 10.1038/ncomms11050

[23] Q. ZHANG, X. LUO, L. WANG, L. ZHANG, B. KHALID, J. GONG, H. WU. Lithium-Ion Battery Cycling for Magnetism Control. *Nano Lett.*, **16** (2016) 583. DOI: 10.1021/acs.nanolett.5b04276

[24] A. QUINTANA, E. MENÉNDEZ, M. O. LIEDKE, M. BUTTERLING, A. WAGNER, V. SIREUS, P. TORRUELLA, S. ESTRADÉ, F. PEIRÓ, J. DENDOOVEN, C. DETAVERNIER, P. D. MURRAY, D. A. GILBERT, K. LIU, E. PELLICER, J. NOGUES, J. SORT. Voltage-Controlled ON-OFF Ferromagnetism at Room Temperature in a Single Metal Oxide Film. *ACS Nano*, **12** (2018) 10291. DOI: 10.1021/acsnano.8b05407

[25] S. VASALA, A. JAKOB, K. WISSEL, A. I. WAIDHA, L. ALFF, O. CLEMENS. Reversible Tuning of Magnetization in a Ferromagnetic Ruddlesden-Popper-Type Manganite by Electrochemical Fluoride-Ion Intercalation. *Adv. Electron. Mater.*, **6** (2020) 1900974. DOI: 10.1002/aelm.201900974

[26] X. YE, H. K. SINGH, H. ZHANG, H. GESSWEIN, M. R. CHELLALI, R. WITTE, A. MOLINARI, K. SKOKOV, O. GUTFLEISCH, H. HAHN, R. KRUK. Giant voltage-induced modification of magnetism in micron-scale ferromagnetic metals by hydrogen charging. *Nat. Commun.*, **11** (2020) 4849.
DOI: 10.1038/s41467-020-18552-z

[27] X. YE, F. YAN, L. SCHÄFER, D. WANG, H. GESSWEIN, W. WANG, M. R. CHELLALI, L. T. STEPHENSON, K. SKOKOV, O. GUTFLEISCH, *et al.* Magnetoelectric Tuning of Pinning-Type Permanent Magnets through Atomic-Scale Engineering of Grain Boundaries. *Adv. Mater.*, **33** (2021) 2006853.
DOI: 10.1002/adma.202006853

[28] K. LEISTNER. Electrochemical approaches to room temperature magnetoelectric materials. *Curr. Opin. Electrochem.*, **25** (2021) 100636.
DOI: 10.1016/j.coelec.2020.09.003

[29] J. ZEHNER, I. SOLDATOV, S. SCHNEIDER, R. HELLER, N. B. KHOJASTEH, S. SCHIEMENZ, S. FÄHLER, K. NIELSCH, R. SCHÄFER, K. LEISTNER. Voltage-Controlled Deblocking of Magnetization Reversal in Thin Films by Tunable Domain Wall Interactions and Pinning Sites.
Adv. Electron. Mater., **6** (2020) 2000406.
DOI: 10.1002/aelm.202000406

[30] M. NICHTERWITZ, S. HONNALI, J. ZEHNER, S. SCHNEIDER, D. POHL, S. SCHIEMENZ, S. T. B. GOENNENWEIN, K. NIELSCH, K. LEISTNER. Control of Positive and Negative Magnetoresistance in Iron Oxide-Iron Nanocomposite Thin Films for Tunable Magnetoelectric Nanodevices.
ACS Appl. Electron. Mater., **2** (2020) 2543.
DOI: 10.1021/acsaelm.0c00448

[31] J. DE ROJAS, A. QUINTANA, A. LOPEANDÍA, J. SALGUERO, J. L. COSTA-KRÄMER, L. ABAD, M. O. LIEDKE, M. BUTTERLING, A. WAGNER, L. HENDERICK, *et al.* Boosting Room-Temperature Magneto-Ionics in a Non-Magnetic Oxide Semiconductor. *Adv. Funct. Mater.*, **30** (2020) 2003704.
DOI: 10.1002/adfm.202003704

[32] F. Maroun, F. Reikowski, N. Di, T. Wiegmann, J. Stettner, O. M. Magnussen, P. Allongue. Potential dependence of the structure and magnetism of electrodeposited Pd/Co/Au(111) layers. *J. Electroanal. Chem.*, **819** (2018) 322.
DOI: 10.1016/j.jelechem.2017.11.002

[33] S. Ghosh. Switching magnetic order in nanoporous Pd-Ni by electrochemical charging. *J. Mater. Res.*, **28** (2013) 3010.
DOI: 10.1557/jmr.2013.291

[34] A. Nicolenco, C. Navarro-Senent, J. Sort. Nanoporous Composites With Converse Magnetoelectric Effects for Energy-Efficient Applications. *Reference Module in Materials Science and Materials Engineering*. Elsevier, 2021.
DOI: 10.1016/B978-0-12-803581-8.11870-3

[35] S. Robbennolt, P. Yu, A. Nicolenco, P. Mercier Fernandez, M. Coll, J. Sort. Magneto-ionic control of magnetism in two-oxide nanocomposite thin films comprising mesoporous cobalt ferrite conformally nanocoated with HfO_2.
Nanoscale, **12** (2020) 5987.
DOI: 10.1039/C9NR10868H

[36] C. Navarro-Senent, A. Quintana, E. Isarain-Chávez, E. Weschke, P. Yu, M. Coll, E. Pellicer, E. Menéndez, J. Sort. Enhancing Magneto-Ionic Effects in Magnetic Nanostructured Films via Conformal Deposition of Nanolayers with Oxygen Acceptor/Donor Capabilities. *ACS Appl. Mater. Interfaces*, **12** (2020) 14484.
DOI: 10.1021/acsami.9b19363

[37] M. Nichterwitz, S. Neitsch, S. Röher, D. Wolf, K. Nielsch, K. Leistner. Voltage-controlled ON switching and manipulation of magnetization via the redox transformation of β-FeOOH nanoplatelets.
J. Phys. D: Appl. Phys., **53** (2019) 084001.
DOI: 10.1088/1361-6463/ab5bca

[38] G. Klinser, S. Topolovec, H. Krenn, R. Würschum. Process Monitoring of Charging/Discharging of Lithium Ion Battery Cathodes by Operando SQUID Magnetometry. *Encyclopedia of Interfacial Chemistry* (edited by K. Wandelt), pp. 849 – 855. Elsevier, Oxford, 2018.
DOI: 10.1016/B978-0-12-409547-2.14200-3

[39] K. Taniguchi, K. Narushima, H. Sagayama, W. Kosaka, N. Shito, H. Miyasaka. In Situ Reversible Ionic Control for Nonvolatile Magnetic Phases in a Donor/Acceptor Metal-Organic Framework. *Adv. Funct. Mater.*, **27** (2017) 1604990.
DOI: 10.1002/adfm.201604990

[40] G. Klinser, R. Zettl, M. Wilkening, H. Krenn, I. Hanzu, R. Würschum. Redox processes in sodium vanadium phosphate cathodes - insights from operando magnetometry. *Phys. Chem. Chem. Phys.*, **21** (2019) 20151.
DOI: 10.1039/C9CP04045E

[41] M. Gößler, M. Albu, G. Klinser, E.-M. Steyskal, H. Krenn, R. Würschum. Magneto-Ionic Switching of Superparamagnetism. *Small*, **15** (2019) 1904523.
DOI: 10.1002/smll.201904523

[42] M. Gößler, S. Topolovec, H. Krenn, R. Würschum. Nanoporous $Pd_{1-x}Co_x$ for hydrogen-intercalation magneto-ionics. *APL Mater.*, **9** (2021) 041101.
DOI: 10.1063/5.0039136

[43] R. Dittmann, J. Strachan. Redox-based memristive devices for new computing paradigm. *APL Mater.*, **7** (2019) 110903.
DOI: 10.1063/1.5129101

[44] S. Menzel, M. von Witzleben, V. Havel, U. Böttger. The ultimate switching speed limit of redox-based resistive switching devices. *Faraday Discuss.*, **213** (2019) 197.
DOI: 10.1039/c8fd00117k

[45] K.-Y. Lee, S. Jo, A. J. Tan, M. Huang, D. Choi, J. H. Park, H.-I. Ji, J.-W. Son, J. Chang, G. S. Beach, *et al.* Fast magneto-ionic switching of interface anisotropy using yttria-stabilized zirconia gate oxide. *Nano. Lett.*, **20** (2020) 3435.
DOI: 10.1021/acs.nanolett.0c00340

[46] M. Gößler, M. Nachtnebel, H. Schröttner, H. Krenn, E.-M. Steyskal, R. Würschum. Evolution of superparamagnetism in the electrochemical dealloying process. *J. Appl. Phys.*, **128** (2020) 093904.
DOI: 10.1063/5.0015397

[47] A. Steiner. *Magnetic Tuning of Nanoporous Palladium by Surface Charging: Influence of Electrolyte and of Coarsening.* Master thesis, TU Graz, 2020

[48] M. Gößler, E.-M. Steyskal, M. Stütz, N. Enzinger, R. Würschum. Hydrogen-induced plasticity in nanoporous palladium.
Beilstein J. Nanotechnol., **9** (2018) 3013.
DOI: 10.3762/bjnano.9.280

[49] J. Weissmüller, R. Viswanath, D. Kramer, P. Zimmer, R. Würschum, H. Gleiter. Charge-induced reversible strain in a metal. *Science*, **300** (2003) 312.
DOI: 10.1126/science.1081024

[50] J. Erlebacher, M. J. Aziz, A. Karma, N. Dimitrov, K. Sieradzki. Evolution of nanoporosity in dealloying. *Nature*, **410** (2001) 450.
DOI: 10.1038/35068529

[51] M. Stratmann, M. Rohwerder. A pore view of corrosion.
Nature, **410** (2001) 421.
DOI: 10.1038/35068652

[52] T. Wada, K. Yubuta, A. Inoue, H. Kato. Dealloying by metallic melt.
Mater. Lett., **65** (2011) 1076.
DOI: 10.1016/j.matlet.2011.01.054

[53] I. McCue, B. Gaskey, P.-A. Geslin, A. Karma, J. Erlebacher. Kinetics and morphological evolution of liquid metal dealloying. *Acta Mater.*, **115** (2016) 10.
DOI: 10.1016/j.matlet.2011.01.054

[54] Z. Lu, C. Li, J. Han, F. Zhang, P. Liu, H. Wang, Z. Wang, C. Cheng, L. Chen, A. Hirata, *et al.* Three-dimensional bicontinuous nanoporous materials by vapor phase dealloying. *Nat. Commun.*, **9** (2018) 1.
DOI: 10.1038/s41467-017-02167-y

[55] J. Han, C. Li, Z. Lu, H. Wang, Z. Wang, K. Watanabe, M. Chen. Vapor phase dealloying: A versatile approach for fabricating 3D porous materials. *Acta Mater.*, **163** (2019) 161.
DOI: 10.1016/j.actamat.2018.10.012

[56] J. Erlebacher. An Atomistic Description of Dealloying: Porosity Evolution, the Critical Potential, and Rate-Limiting Behavior. *J. Electrochem. Soc.*, **151** (2004) C614.
DOI: 10.1149/1.1784820

[57] Y. Ding, Y.-J. Kim, J. Erlebacher. Nanoporous Gold Leaf: Ancient Technology/Advanced Material. *Adv. Mater.*, **16** (2004) 1897.
DOI: 10.1002/adma.200400792

[58] Q. Chen, K. Sieradzki. Spontaneous evolution of bicontinuous nanostructures in dealloyed Li-based systems. *Nat. Mater.*, **12** (2013) 1102.
DOI: 10.1038/nmat3741

[59] I. McCue, A. Karma, J. Erlebacher. Pattern formation during electrochemical and liquid metal dealloying. *MRS Bull.*, **43** (2018) 27.
DOI: 10.1557/mrs.2017.301

[60] D. Artymowicz, J. Erlebacher, R. Newman. Relationship between the parting limit for de-alloying and a particular geometric high-density site percolation threshold. *Philos. Mag.*, **89** (2009) 1663.
DOI: 10.1080/14786430903025708

[61] J. Weissmüller, K. Sieradzki. Dealloyed nanoporous materials with interface-controlled behavior. *MRS Bull.*, **43** (2018) 14.
DOI: 10.1557/mrs.2017.299

[62] I. McCue, E. Benn, B. Gaskey, J. Erlebacher. Dealloying and Dealloyed Materials. *Ann. Rev. Mater. Res.*, **46** (2016) 263.
DOI: 10.1146/annurev-matsci-070115-031739

[63] F. Liu, H.-J. Jin. Extrinsic Parting Limit for Dealloying of Cu-Rh. *J. Electrochem. Soc.*, **165** (2018) C999.
DOI: 10.1149/2.0631816jes

[64] J. R. Hayes, A. M. Hodge, J. Biener, A. V. Hamza, K. Sieradzki. Monolithic nanoporous copper by dealloying Mn-Cu. *J. Mater. Res.*, **21** (2006) 2611.
DOI: 10.1557/jmr.2006.0322

[65] M. Hakamada, M. Takahashi, T. Furukawa, M. Mabuchi. Coercivity of nanoporous Ni produced by dealloying. *Appl. Phys. Lett.*, **94** (2009) 153105.
DOI: 10.1063/1.3119663

[66] C. Mahr, M. Schowalter, C. Mitterbauer, A. Lackmann, L. Fitzek, T. Mehrtens, A. Wittstock, A. Rosenauer. Nanoporous gold dealloyed from AuAg and AuCu: Comparison of structure and chemical composition. *Materialia*, **2** (2018) 131.
DOI: 10.1016/j.mtla.2018.07.014

[67] M. Hakamada, M. Mabuchi. Fabrication of nanoporous palladium by dealloying and its thermal coarsening. *J. Alloys*, **479** (2009) 326.
DOI: 10.1016/j.jallcom.2008.12.078

[68] Q. Kong, L. Lian, Y. Liu, J. Zhang, L. Wang, W. Feng. Bulk hierarchical nanoporous palladium prepared by dealloying PdAl alloys and its electrochemical properties. *Microporous Mesoporous Mater.*, **208** (2015) 152.
DOI: 10.1016/j.micromeso.2015.01.017

[69] T. Krekeler, A. V. Strasser, M. Graf, K. Wang, C. Hartig, M. Ritter, J. Weissmüller. Silver-rich clusters in nanoporous gold. *Mater. Res. Lett.*, **5** (2017) 314.
DOI: 10.1080/21663831.2016.1276485

[70] S. Shi, J. Markmann, J. Weissmüller. Synthesis of uniform bulk nanoporous palladium with tunable structure. *Electrochim. Acta*, **285** (2018) 60.
DOI: 10.1016/j.electacta.2018.07.081

[71] Y. Z. Chen, X. Y. Ma, W. X. Zhang, H. Dong, G. B. Shan, Y. B. Cong, C. Li, C. L. Yang, F. Liu. Effects of dealloying and heat treatment parameters on microstructures of nanoporous Pd. *J. Mater. Sci. Technol.*, **48** (2020) 123.
DOI: 10.1016/j.jmst.2020.03.012

[72] K. Sieradzki, N. Dimitrov, D. Movrin, C. McCall, N. Vasiljevic, J. Erlebacher. The dealloying critical potential.
J. Electrochem. Soc., **149** (2002) B370.
DOI: 10.1149/1.1492288

[73] X.-L. Ye, N. Lu, X.-J. Li, K. Du, J. Tan, H.-J. Jin. Primary and Secondary Dealloying of Au(Pt)-Ag: Structural and Compositional Evolutions, and Volume Shrinkage. *J. Electrochem. Soc.*, **161** (2014) C517.
DOI: 10.1149/2.0131412jes

[74] E.-M. Steyskal, M. Seidl, M. Graf, R. Würschum. Dealloying progress during nanoporous structure evolution analyzed by in situ resistometry. *Phys. Chem. Chem. Phys.*, **19** (2017) 29880.
DOI: 10.1039/C7CP05706G

[75] H. Gleiter, J. Weissmüller, O. Wollersheim, R. Würschum. Nanocrystalline materials: a way to solids with tunable electronic structures and properties? *Acta Mater.*, **49** (2001) 737.
DOI: 10.1016/s1359-6454(00)00221-4

[76] H. Drings, R. N. Viswanath, D. Kramer, C. Lemier, J. Weissmüller, R. Würschum. Tuneable magnetic susceptibility of nanocrystalline palladium.
Appl. Phys. Lett., **88** (2006) 253103.
DOI: 10.1063/1.2216897

[77] H.-J. JIN, J. WEISSMÜLLER. A Material with Electrically Tunable Strength and Flow Stress. *Science*, **332** (2011) 1179.
DOI: 10.1126/science.1202190

[78] N. MAMEKA, J. MARKMANN, H.-J. JIN, J. WEISSMÜLLER. Electrical stiffness modulation–confirming the impact of surface excess elasticity on the mechanics of nanomaterials. *Acta Mater.*, **76** (2014) 272.
DOI: 10.1016/j.actamat.2014.04.067

[79] S. SUN, X. CHEN, N. BADWE, K. SIERADZKI. Potential-dependent dynamic fracture of nanoporous gold. *Nat. Mater.*, **14** (2015) 894.
DOI: 10.1038/nmat4335

[80] E.-M. STEYSKAL, Z. QI, P. PÖLT, M. ALBU, J. WEISSMÜLLER, R. WÜRSCHUM. Electrochemically Tunable Resistance of Nanoporous Platinum Produced by Dealloying. *Langmuir*, **32** (2016) 7757.
DOI: 10.1021/acs.langmuir.6b01734

[81] V. L. MORUZZI, P. M. MARCUS. Magnetism in fcc rhodium and palladium. *Phys. Rev. B*, **39** (1989) 471.
DOI: 10.1103/PhysRevB.39.471

[82] R. M. BOZORTH, P. A. WOLFF, D. D. DAVIS, V. B. COMPTON, J. H. WERNICK. Ferromagnetism in Dilute Solutions of Cobalt in Palladium.
Phys. Rev., **122** (1961) 1157.
DOI: 10.1103/PhysRev.122.1157

[83] M. B. STEARNS. 1.1.2.4 Spontaneous magnetisation: Datasheet from Landolt-Börnstein - Group III Condensed Matter · Volume 19A: "3d, 4d and 5d Elements, Alloys and Compounds" in SpringerMaterials.
DOI: 10.1007/10135124_8

[84] M. A. RUDERMAN, C. KITTEL. Indirect Exchange Coupling of Nuclear Magnetic Moments by Conduction Electrons. *Phys. Rev.*, **96** (1954) 99.
DOI: 10.1103/PhysRev.96.99

[85] T. Kasuya. A theory of metallic ferro-and antiferromagnetism on Zener's model. *Prog. Theor. Phys.*, **16** (1956) 45.
DOI: 10.1143/PTP.16.45

[86] K. Yosida. Magnetic Properties of Cu-Mn Alloys. *Phys. Rev.*, **106** (1957) 893.
DOI: 10.1103/PhysRev.106.893

[87] B. Verbeek, G. Nieuwenhuys, J. Mydosh, C. Van Dijk, B. Rainford. Inhomogeneous ferromagnetic ordering in Pd Fe and Pd Mn alloys studied via small-angle neutron scattering. *Phys. Rev. B*, **22** (1980) 5426.
DOI: 10.1103/PhysRevB.22.5426

[88] Y. Takahashi. Interlayer exchange coupling mediated by a nonmagnetic spacer layer with a large electron-electron exchange interaction.
Phys. Rev. B, **56** (1997) 8175.
DOI: 10.1103/PhysRevB.56.8175

[89] T. Graham. On the relation of hydrogen to palladium.
Proc. Roy. Soc. London, **17** (1869) 212.
DOI: 10.1098/rspl.1868.0030

[90] G. Jerkiewicz, A. Zolfaghari. Comparison of Hydrogen Electroadsorption from the Electrolyte with Hydrogen Adsorption from the Gas Phase.
J. Electrochem. Soc., **143** (1996) 1240.
DOI: 10.1149/1.1836623

[91] S. Akamaru, T. Matsumoto, M. Hara, K. Nishimura, N. Nunomura, M. Matsuyama. Magnetic susceptibility of the Pd-Co-H system.
J. Alloys, **580** (2013) S102.
DOI: 10.1016/j.jallcom.2013.03.097

[92] S. Akamaru, A. Kimura, M. Hara, K. Nishimura, T. Abe. Hydrogenation effect on magnetic properties of Pd-Co alloys. *J. Magn. Magn. Mater.*, **484** (2019) 8.
DOI: 10.1016/j.jmmm.2019.03.121

[93] W.-C. Lin, B.-Y. Wang, H.-Y. Huang, C.-J. Tsai, V. R. Mudinepalli. Hydrogen absorption-induced reversible change in magnetic properties of Co–Pd alloy films. *J. Alloys*, **661** (2016) 20.
DOI: 10.1016/j.jallcom.2015.11.144

[94] D. Chiba. Electric field effect on magnetism in metallic ultra-thin films. *AIP Conf. Proc.*, **3** (2015) 83.
DOI: 10.3389/fphy.2015.00083

[95] A. Obinata, Y. Hibino, D. Hayakawa, T. Koyama, K. Miwa, S. Ono, D. Chiba. Electric-field control of magnetic moment in Pd. *Sci. Rep.*, **5** (2015) 14303.
DOI: 10.1038/srep14303

[96] W.-C. Lin, C.-J. Tsai, B.-Y. Wang, C.-H. Kao, W.-F. Pong. Hydrogenation induced reversible modulation of perpendicular magnetic coercivity in Pd/Co/Pd films.
Appl. Phys. Lett., **102** (2013) 252404.
DOI: 10.1063/1.4812664

[97] W.-C. Lin, C.-J. Tsai, X.-M. Liu, A. O. Adeyeye. Critical hydrogenation effect on magnetic coercivity of perpendicularly magnetized Co/Pd multilayer nanostructures.
J. Appl. Phys., **116** (2014) 073904.
DOI: 10.1063/1.4893588

[98] W.-C. Lin, C.-J. Tsai, H.-Y. Huang, B.-Y. Wang, V. R. Mudinepalli, H.-C. Chiu. Hydrogen-mediated long-range magnetic ordering in Pd-rich alloy film. *Appl. Phys. Lett.*, **106** (2015) 012404.
DOI: 10.1063/1.4905463

[99] K. Munbodh, F. A. Perez, D. Lederman. Changes in magnetic properties of Co/Pd multilayers induced by hydrogen absorption. *J. Appl. Phys.*, **111** (2012) 123919.
DOI: 10.1063/1.4729797

[100] K. MUNBODH, F. A. PEREZ, C. KEENAN, D. LEDERMAN, M. ZHERNENKOV, M. R. FITZSIMMONS. Effects of hydrogen/deuterium absorption on the magnetic properties of Co/Pd multilayers. *Phys. Rev. B*, **83** (2011) 094432.
DOI: 10.1103/PhysRevB.83.094432

[101] P.-C. CHANG, C.-M. LIU, C.-C. HSU, W.-C. LIN. Hydrogen-mediated magnetic domain formation and domain wall motion in Co30Pd70 alloy films.
Sci. Rep., **8** (2018) 6656.
DOI: 10.1038/s41598-018-25114-3

[102] C. LUENG, P. J. METAXAS, M. SUSHRUTH, M. KOSTYLEV. Adjustable sensitivity for hydrogen gas sensing using perpendicular-to-plane ferromagnetic resonance in Pd/Co Bi-layer films. *Int. J. Hydrog. Energy*, **42** (2017) 3407.
DOI: 10.1016/j.ijhydene.2016.09.204

[103] J.-Y. LIANG, Y.-C. PAI, T.-N. LAM, W.-C. LIN, T.-S. CHAN, C.-H. LAI, Y.-C. TSENG. Using magnetic structure of Co40Pd60/Cu for the sensing of hydrogen.
Appl. Phys. Lett., **111** (2017) 023503.
DOI: 10.1063/1.4993158

[104] H. KRONMÜLLER, M. FÄHNLE. *Micromagnetism and the Microstructure of Ferromagnetic Solids.* Cambridge University Press, 2013

[105] S. BEDANTA, W. KLEEMANN. Supermagnetism. *J. Phys. D*, **42** (2009) 013001.
DOI: 10.1088/0022-3727/42/1/013001

[106] H. K. KIM, L. T. SCHELHAS, S. KELLER, J. L. HOCKEL, S. H. TOLBERT, G. P. CARMAN. Magnetoelectric control of superparamagnetism.
Nano Lett., **13** (2013) 884.
DOI: 10.1021/nl3034637

[107] A. ARORA, L. C. PHILLIPS, P. NUKALA, M. BEN HASSINE, A. A. ÜNAL, B. DKHIL, L. BALCELLS, O. IGLESIAS, A. BARTHÉLÉMY, F. KRONAST, M. BIBES, S. VALENCIA. Switching on superferromagnetism.
Phys. Rev. Mater., **3** (2019) 024403.
DOI: 10.1103/PhysRevMaterials.3.024403

[108] T. Traussnig. *Charge-induced property tuning of nanoscaled metals and metal oxides*. PhD thesis, TU Graz, 2011

[109] S. Topolovec, H. Krenn, R. Würschum. Electrochemical cell for in situ electrodeposition of magnetic thin films in a superconducting quantum interference device magnetometer. *Rev. Sci. Instrum.*, **86** (2015) 063903.
DOI: 10.1063/1.4922462

[110] S. Topolovec, H. Krenn, R. Würschum. Enhanced magnetic moment of ultrathin Co films measured by in situ electrodeposition in a SQUID.
J. Magn. Magn. Mater., **397** (2016) 96.
DOI: 10.1016/j.jmmm.2015.08.088

[111] S. Topolovec, H. Kren, G. Klinser, S. Koller, H. Krenn, R. Würschum. Operando magnetometry on LixCoO2 during charging/discharging.
J. Solid State Electrochem., **20** (2016) 1491.
DOI: 10.1007/s10008-015-3110-6

[112] G. Klinser, M. Stückler, H. Kren, S. Koller, W. Goessler, H. Krenn, R. Würschum. Charging processes in the cathode $LiNi_{0.6}Mn_{0.2}Co_{0.2}O_2$ as revealed by operando magnetometry. *J. Power Sources*, **396** (2018) 791.
DOI: 10.1016/j.jpowsour.2018.06.090

[113] G. Klinser. *Operando Studies of Charging Processes in Battery Cathodes by Magnetometry and Positron Annihilation*. PhD thesis, TU Graz, 2019

[114] S. Topolovec. *In-situ studies of the correlations between electrochemical processes and magnetic properties*. PhD thesis, TU Graz, 2015

[115] R. G. Compton, C. E. Banks. *Understanding Voltammetry Second Edition*. Imperial College Press, 2010.
DOI: 10.1142/p726

[116] A. Molinari, P. M. Leufke, C. Reitz, S. Dasgupta, R. Witte, R. Kruk, H. Hahn. Hybrid supercapacitors for reversible control of magnetism.
Nat. Commun., **8** (2017) 15339.
DOI: 10.1038/ncomms15339

[117] L. A. Dubraja, C. Reitz, L. Velasco, R. Witte, R. Kruk, H. Hahn, T. Brezesinski. Electrochemical Tuning of Magnetism in Ordered Mesoporous Transition-Metal Ferrite Films for Micromagnetic Actuation. *ACS Appl. Nano Mater.*, **1** (2018) 65. DOI: 10.1021/acsanm.7b00037

[118] IUPAC. Recommendations for sign conventions and plotting of electrochemical data. *Pure Appl. Chem.*, **45** (01 Jan. 1976) 131. DOI: 10.1351/pac197645020131

[119] G. Denuault, C. Milhano, D. Pletcher. Mesoporous palladium-the surface electrochemistry of palladium in aqueous sodium hydroxide and the cathodic reduction of nitrite. *Phys. Chem. Chem. Phys.*, **7** (2005) 3545. DOI: 10.1039/b508835f

[120] W. Schmickler, E. Santos. *Interfacial Electrochemistry Second Edition.* Springer, 2010. DOI: 10.1007/978-3-642-04937-8

[121] A. Lackmann, M. Bäumer, G. Wittstock, A. Wittstock. Independent control over residual silver content of nanoporous gold by galvanodynamically controlled dealloying. *Nanoscale*, **10** (2018) 17166. DOI: 10.1039/c8nr03699c

[122] K. Ishida, T. Nishizawa. The Co-Pd (Cobalt-Palladium) System. *J. Phase Equilibria*, **12** (1991) 83. DOI: 10.1007/BF02663680

[123] M. McElfresh. Fundamentals of Magnetism and Magnetic Measurements Featuring Quantum Design's Magnetic Property Measurement System. Rech. Rep., Purdue University, 1994

[124] Quantum Design Inc. *MPMS Application Note 1014-213*, 2002

[125] E. MANIOS, D. STAMOPOULOS, N. MOUTIS, M. PISSAS, D. NIARCHOS. Magnetic measurements in thin film specimens: Rejecting the contribution of the substrate. *J. Magn. Magn. Mater.*, **320** (2008) 3264.
DOI: 10.1016/j.jmmm.2008.06.020

[126] D. DROUIN, A. R. COUTURE, D. JOLY, X. TASTET, V. AIMEZ, R. GAUVIN. CASINO V2.42–A Fast and Easy-to-use Modeling Tool for Scanning Electron Microscopy and Microanalysis Users. *Scanning*, **29** (2007) 92.
DOI: 10.1002/sca.20000

[127] P. SCHLOSSMACHER, D. KLENOV, B. FREITAG, H. VON HARRACH. Enhanced Detection Sensitivity with a New Windowless XEDS System for AEM Based on Silicon Drift Detector Technology. *Micros. Today*, **18** (2010) 14.
DOI: 10.1017/S1551929510000404

[128] A. GUBBENS, M. BARFELS, C. TREVOR, R. TWESTEN, P. MOONEY, P. THOMAS, N. MENON, B. KRAUS, C. MAO, B. MCGINN. The GIF Quantum, a next generation post-column imaging energy filter. *Ultramicroscopy*, **110** (2010) 962.
DOI: 10.1016/j.ultramic.2010.01.009

[129] J. I. GOLDSTEIN, D. B. WILLIAMS, G. CLIFF. *Quantitative X-Ray Analysis*, pp. 155–217. Springer US, Boston, MA, 1986.
DOI: 10.1007/978-1-4899-2037-9_5

[130] M. ANDERSEN, C. PANOSETTI, K. REUTER. A Practical Guide to Surface Kinetic Monte Carlo Simulations. *Front. Chem.*, **7** (2019) 202.
DOI: 10.3389/fchem.2019.00202

[131] T. DE LA RUBIA, N. SONEDA, M. CATURLA, E. ALONSO. Defect production and annealing kinetics in elemental metals and semiconductors. *J. Nucl. Mater.*, **251** (1997) 13.
DOI: 10.1016/S0022-3115(97)00265-1

[132] W. Cai, V. V. Bulatov, J. ao F Justo, A. S. Argon, S. Yip. Kinetic Monte Carlo approach to modeling dislocation mobility. *Comput. Mater. Sci.*, **23** (2002) 124.
DOI: 10.1016/S0927-0256(01)00223-3

[133] B. Temel, H. Meskine, K. Reuter, M. Scheffler, H. Metiu. Does phenomenological kinetics provide an adequate description of heterogeneous catalytic reactions? *J. Chem. Phys.*, **126** (2007) 204711.
DOI: 10.1063/1.2741556

[134] J. Erlebacher. Mechanism of Coarsening and Bubble Formation in High-Genus Nanoporous Metals. *Phys. Rev. Lett.*, **106** (2011) 225504.
DOI: 10.1103/PhysRevLett.106.225504

[135] J. Erlebacher, I. McCue. Geometric characterization of nanoporous metals. *Acta Mater.*, **60** (2012) 6164.
DOI: 10.1016/j.actamat.2012.07.059

[136] I. McCue, J. Snyder, X. Li, Q. Chen, K. Sieradzki, J. Erlebacher. Apparent Inverse Gibbs-Thomson Effect in Dealloyed Nanoporous Nanoparticles. *Phys. Rev. Lett.*, **108** (2012) 225503.
DOI: 10.1103/PhysRevLett.108.225503

[137] R. Callejas-Tovar, C. A. Diaz, J. M. M. de la Hoz, P. B. Balbuena. Dealloying of platinum-based alloy catalysts: Kinetic Monte Carlo simulations. *Electrochim. Acta*, **101** (2013) 326.
DOI: 10.1016/j.electacta.2013.01.053

[138] Y. Li, B.-N. Dinh Ngô, J. Markmann, J. Weissmüller. Topology evolution during coarsening of nanoscale metal network structures. *Phys. Rev. Mater.*, **3** (2019) 076001.
DOI: 10.1103/PhysRevMaterials.3.076001

[139] Y. Lı, B.-N. D. Ngô, J. Markmann, J. Weissmüller. Datasets for the microstructure of nanoscale metal network structures and for its evolution during coarsening. *Data in Brief*, **29** (2020) 105030.
DOI: 10.1016/j.dib.2019.105030

[140] A. Stukowski. Visualization and analysis of atomistic simulation data with OVITO-the Open Visualization Tool. *Model. Simul. Mater. Sci. Eng.*, **18** (2010).
DOI: 10.1088/0965-0393/18/1/015012

[141] M. Hakamada, M. Takahashi, T. Furukawa, M. Mabuchi. Surface effects on saturation magnetization in nanoporous Ni. *Philos. Mag.*, **90** (2010) 1915.
DOI: 10.1080/14786430903571461

[142] L. Sun, C.-L. Chien, P. C. Searson. Fabrication of Nanoporous Nickel by Electrochemical Dealloying. *Chem. Mater.*, **16** (2004) 3125.
DOI: 10.1021/cm0497881

[143] H. Zhang, Z. Wang, M. Yang, Q. Deng. The effect of an external magnetic field on the dealloying process of the Ni-Al alloy in alkaline solution.
Phys. Chem. Chem. Phys., **19** (2017) 18167.
DOI: 10.1039/C7CP03363J

[144] H. Xu, K. Shen, S. Liu, L.-C. Zhang, X. Wang, J. Qin, W. Wang. Micromorphology and Phase Composition Manipulation of Nanoporous Gold with High Methanol Electro-oxidation Catalytic Activity through Adding a Magnetic Field in the Dealloying Process. *J. Phys. Chem. C*, **122** (2018) 3371.
DOI: 10.1021/acs.jpcc.7b10475

[145] R. Sueptitz, K. Tschulik, M. Uhlemann, L. Schultz, A. Gebert. Magnetic field effects on the active dissolution of iron. *Electrochim. Acta*, **56** (2011) 5866.
DOI: 10.1016/j.electacta.2011.04.126

[146] L. Brant. Magnetic Susceptibility of Nickel and Cobalt Chloride Solutions.
Phys. Rev., **17** (1921) 678.
DOI: 10.1103/PhysRev.17.678

[147] S. Parida, D. Kramer, C. A. Volkert, H. Rösner, J. Erlebacher, J. Weissmüller. Volume Change during the Formation of Nanoporous Gold by Dealloying. *Phys. Rev. Lett.*, **97** (2006) 035504.
DOI: 10.1103/PhysRevLett.97.035504

[148] C. Mahr, P. Kundu, A. Lackmann, D. Zanaga, K. Thiel, M. Schowalter, M. Schwan, S. Bals, A. Wittstock, A. Rosenauer. Quantitative determination of residual silver distribution in nanoporous gold and its influence on structure and catalytic performance. *J. Catal.*, **352** (2017) 52.
DOI: 10.1016/j.jcat.2017.05.002

[149] P. Brunner. *Nanoporous Structure of Dealloyed Metals Investigated by Electrochemical Impedance Spectroscopy.* Master thesis, TU Graz, 2018

[150] A. V. Ravindra, B. C. Behera, P. Padhan. Laser Induced Structural Phase Transformation of Cobalt Oxides Nanostructures.
J. Nanosci. Nanotechnol., **14** (2014) 5591.
DOI: 10.1166/jnn.2014.9023

[151] C. Brolly, J. Parnell, S. Bowden. Raman spectroscopy: Caution when interpreting organic carbon from oxidising environments.
Planet. Space Sci., **121** (2016) 53.
DOI: 10.1016/j.pss.2015.12.008

[152] B. Rivas-Murias, V. Salgueiriño. Thermodynamic CoO-Co3O4 crossover using Raman spectroscopy in magnetic octahedron-shaped nanocrystals.
J. Raman Spectrosc., **48** (2017) 837.
DOI: 10.1002/jrs.5129

[153] P. Durkin, A. J. Forty. Oxide formation during the selective dissolution of silver from silver-gold alloys in nitric acid. *Philos. Mag. A*, **45** (1982) 95.
DOI: 10.1080/01418618208243905

[154] A. Baylet, P. Marécot, D. Duprez, P. Castellazzi, G. Groppi, P. Forzatti. In situ Raman and in situ XRD analysis of PdO reduction and Pd° oxidation supported on γ-Al2O3 catalyst under different atmospheres. *Phys. Chem. Chem. Phys.*, **13** (2011) 4607. DOI: 10.1039/C0CP01331E

[155] E. M. Garcia, J. S. Santos, E. C. Pereira, M. B. J. G. Freitas. Electrodeposition of cobalt from spent Li-ion battery cathodes by the electrochemistry quartz crystal microbalance technique. *J. Power Sources*, **185** (2008) 549. DOI: 10.1016/j.jpowsour.2008.07.011

[156] L. Fang, Q. Tao, M.-F. Li, L. wen Liao, D. Chen, Y. xia Chen. Determination of the Real Surface Area of Palladium Electrode. *Chin. J. Chem. Phys.*, **23** (2010) 543. DOI: 10.1088/1674-0068/23/05/543-548

[157] M. Gössler. *Hydrogen Storage and Actuation Properties of Nanoporous Palladium Prepared by Dealloying.* Master thesis, TU Graz, 2017

[158] E. Detsi, M. van de Schootbrugge, S. Punzhin, P. R. Onck, J. T. M. D. Hosson. On tuning the morphology of nanoporous gold. *Scr. Mater.*, **64** (2011) 319. DOI: 10.1016/j.scriptamat.2010.10.023

[159] K. S. W. Sing. Reporting physisorption data for gas/solid systems with special reference to the determination of surface area and porosity (Recommendations 1984). *Pure Appl. Chem.*, **57** (01 Jan. 1985) 603. DOI: 10.1351/pac198557040603

[160] M. Thommes, K. Kaneko, A. V. Neimark, J. P. Olivier, F. Rodriguez-Reinoso, J. Rouquerol, K. S. Sing. Physisorption of gases, with special reference to the evaluation of surface area and pore size distribution (IUPAC Technical Report). *Pure Appl. Chem.*, **87** (01 Oct. 2015) 1051. DOI: 10.1515/pac-2014-1117

[161] E. P. Barrett, L. G. Joyner, P. P. Halenda. The Determination of Pore Volume and Area Distributions in Porous Substances. I. Computations from Nitrogen Isotherms. *J. Am. Chem. Soc.*, **73** (1951) 373.
DOI: 10.1021/ja01145a126

[162] H. Keiser, K. D. Beccu, M. A. Gutjahr. Abschätzung der Porenstruktur poröser Elektroden aus Impedanzmessungen. *Electrochim. Acta*, **21** (1976) 539.
DOI: 10.1016/0013-4686(76)85147-x

[163] K. Eloot, F. Debuyck, M. Moors, A. P. V. Peteghem. Calculation of the impedance of noncylindrical pores Part I: Introduction of a matrix calculation method. *J. Appl. Electrochem.*, **25** (1995) 326.
DOI: 10.1007/bf00249650

[164] J. Landesfeind, D. Pritzl, H. A. Gasteiger. An Analysis Protocol for Three-Electrode Li-Ion Battery Impedance Spectra: Part I. Analysis of a High-Voltage Positive Electrode. *J. Electrochem. Soc.*, **164** (2017) A1773.
DOI: 10.1149/2.0131709jes

[165] Y. Xue, J. Markmann, H. Duan, J. Weissmüller, P. Huber. Switchable imbibition in nanoporous gold. *Nat. Commun.*, **5** (2014) 1.
DOI: 10.1038/ncomms5237

[166] L. H. Qian, M. W. Chen. Ultrafine nanoporous gold by low-temperature dealloying and kinetics of nanopore formation. *Appl. Phys. Lett.*, **91** (2007) 083105.
DOI: 10.1063/1.2773757

[167] M. Graf, B. Roschning, J. Weissmüller. Nanoporous Gold by Alloy Corrosion: Method-Structure-Property Relationships. *J. Electrochem. Soc.*, **164** (2017) C194.
DOI: 10.1149/2.1681704jes

[168] A. Sharma, J. K. Bhattarai, A. J. Alla, A. V. Demchenko, K. J. Stine. Electrochemical annealing of nanoporous gold by application of cyclic potential sweeps. *Nanotechnology*, **26** (2015) 085602.
DOI: 10.1088/0957-4484/26/8/085602

[169] Z. Matharu, P. Daggumati, L. Wang, T. S. Dorofeeva, Z. Li, E. Seker. Nanoporous-Gold-Based Electrode Morphology Libraries for Investigating Structure-Property Relationships in Nucleic Acid Based Electrochemical Biosensors. *ACS Appl. Mater. Interfaces*, **9** (2017) 12959.
DOI: 10.1021/acsami.6b15212

[170] A. R. S. Olaya, B. Zandersons, G. Wittstock. Restructuring of Nanoporous Gold Surfaces During Electrochemical Cycling in Acidic and Alkaline Media. *ChemElectroChem*, **7** (2020) 3670.
DOI: 10.1002/celc.202000923

[171] F. D. Manchester, A. San-Martin, J. M. Pitre. The H-Pd (Hydrogen-Palladium) System. *J. Phase Equilibria*, **15** (1994) 62.
DOI: 10.1007/bf02667685

[172] E.-M. Steyskal, C. Wiednig, N. Enzinger, R. Würschum. In situ characterization of hydrogen absorption in nanoporous palladium produced by dealloying. *Beilstein J. Nanotechnol.*, **7** (2016) 1197.
DOI: 10.3762/bjnano.7.110

[173] M. Hakamada, H. Nakano, T. Furukawa, M. Takahashi, M. Mabuchi. Hydrogen Storage Properties of Nanoporous Palladium Fabricated by Dealloying. *J. Phys. Chem. C*, **114** (2010) 868.
DOI: 10.1021/jp909479m

[174] R. Kirchheim, A. Pundt. 25 - Hydrogen in Metals. *Physical Metallurgy* (edited by D. E. Laughlin, K. Hono), pp. 2597–2705. Elsevier, Oxford, fifth edition, 2014.
DOI: https://doi.org/10.1016/B978-0-444-53770-6.00025-3

[175] S. Shi, J. Markmann, J. Weissmüller. Actuation by hydrogen electrosorption in hierarchical nanoporous palladium. *Philos. Mag.*, **97** (2017) 1571.
DOI: 10.1080/14786435.2017.1311428

[176] Z. YANG, X. DU, X. YE, X. QU, H. DUAN, Y. XING, L.-H. SHAO, C. CHEN. The free-standing nanoporous palladium for hydrogen isotope storage.
J. Alloys, **854** (2021) 157062.
DOI: 10.1016/j.jallcom.2020.157062

[177] Y. LIU, S. BLIZNAKOV, N. DIMITROV. Factors Controlling the Less Noble Metal Retention in Nanoporous Structures Processed by Electrochemical Dealloying.
J. Electrochem. Soc., **157** (2010) K168.
DOI: 10.1149/1.3454753

[178] Z. ZHANG, C. ZHANG, Y. GAO, J. FRENZEL, J. SUN, G. EGGELER. Dealloying strategy to fabricate ultrafine nanoporous gold-based alloys with high structural stability and tunable magnetic properties. *CrystEngComm*, **14** (2012) 8292.
DOI: 10.1039/C2CE26187A

[179] F. FABRIS, K.-H. TU, C. A. ROSS, W. C. NUNES. Influence of dipolar interactions on the magnetic properties of superparamagnetic particle systems.
J. Appl. Phys, **126** (2019) 173905.
DOI: 10.1063/1.5125595

[180] H.-J. JIN, D. KRAMER, Y. IVANISENKO, J. WEISSMÜLLER. Macroscopically strong nanoporous Pt prepared by dealloying. *Adv. Eng. Mater.*, **9** (2007) 849.
DOI: 10.1002/adem.200700177

[181] M. HAKAMADA, M. MABUCHI. Thermal coarsening of nanoporous gold: Melting or recrystallization. *J. Mater. Res.*, **24** (2009) 301.
DOI: 10.1557/jmr.2009.0037

[182] F. KERTIS, J. SNYDER, L. GOVADA, S. KHURSHID, N. CHAYEN, J. ERLEBACHER. Structure/processing relationships in the fabrication of nanoporous gold.
JOM, **62** (2010) 50.
DOI: 10.1007/s11837-010-0087-6

[183] M. E. COX, D. C. DUNAND. Bulk gold with hierarchical macro-, micro-and nano-porosity. *Mater. Sci. Eng. A*, **528** (2011) 2401.
DOI: 10.1016/j.msea.2010.11.072

[184] Y.-C. K. CHEN-WIEGART, S. WANG, Y. S. CHU, W. LIU, I. MCNULTY, P. W. VOORHEES, D. C. DUNAND. Structural evolution of nanoporous gold during thermal coarsening. *Acta Mater.*, **60** (2012) 4972.
DOI: 10.1016/j.actamat.2012.05.012

[185] A. HAMZIĆ, I. CAMPBELL. The ferromagnetic to spin glass transition.
J. Physique Lett., **42** (1981) 17.
DOI: 10.1051/jphyslet:0198100420101700

[186] L. ZHANG, L. CHEN, H. LIU, Y. HOU, A. HIRATA, T. FUJITA, M. CHEN. Effect of residual silver on surface-enhanced raman scattering of dealloyed nanoporous gold.
J. Phys. Chem. C, **115** (2011) 19583.
DOI: 10.1021/jp205892n

[187] M. GRAF, M. HAENSCH, J. CARSTENS, G. WITTSTOCK, J. WEISSMÜLLER. Electrocatalytic methanol oxidation with nanoporous gold: microstructure and selectivity. *Nanoscale*, **9** (2017) 17839.
DOI: 10.1039/c7nr05124g

[188] M. GRAF, B.-N. D. NGÔ, J. WEISSMÜLLER, J. MARKMANN. X-ray studies of nanoporous gold: Powder diffraction by large crystals with small holes.
Phys. Rev. Mater., **1** (2017) 076003.
DOI: 10.1103/physrevmaterials.1.076003

[189] M. HAENSCH, M. GRAF, W. WANG, A. NEFEDOV, C. WÖLL, J. WEISSMÜLLER, G. WITTSTOCK. Thermally Driven Ag–Au Compositional Changes at the Ligament Surface in Nanoporous Gold: Implications for Electrocatalytic Applications.
ACS Appl. Nano Mater., **3** (2020) 2197.
DOI: 10.1021/acsanm.9b02279

[190] S. S. WELBORN, S. VAN DER MEER, J. S. CORSI, J. T. M. DE HOSSON, E. DETSI. Using X-Ray Scattering to Elucidate the Microstructural Instability of 3D Bicontinuous Nanoporous Metal Scaffolds for Use in an Aperiodic 3D Tricontinuous Conductor–Insulator–Conductor Nanocapacitor.
ACS Appl. Mater. Interfaces, (2021).
DOI: 10.1021/acsami.0c16869

[191] M. Weisheit, S. Fähler, A. Marty, Y. Souche, C. Poinsignon, D. Givord. Electric field-induced modification of magnetism in thin-film ferromagnets. *Science*, **315** (2007) 349.
DOI: 10.1126/science.1136629

[192] E. Dislaki, S. Robbennolt, M. Campoy-Quiles, J. Nogués, E. Pellicer, J. Sort. Coercivity Modulation in Fe-Cu Pseudo-Ordered Porous Thin Films Controlled by an Applied Voltage: A Sustainable, Energy-Efficient Approach to Magnetoelectrically Driven Materials. *Adv. Sci.*, **5** (2018) 1800499.
DOI: 10.1002/advs.201800499

[193] S. Robbennolt, A. Quintana, E. Pellicer, J. Sort. Large magnetoelectric effects mediated by electric-field-driven nanoscale phase transformations in sputtered (nanoparticulate) and electrochemically dealloyed (nanoporous) Fe-Cu films. *Nanoscale*, **10** (2018) 14570.
DOI: 10.1039/C8NR03924K

[194] K. Christmann. Interaction of hydrogen with solid surfaces. *Surf. Sci. Rep.*, **9** (1988) 1.
DOI: 10.1016/0167-5729(88)90009-x

[195] T. Tanaka, M. Keita, D. E. Azofeifa. Theory of hydrogen absorption in metal hydrides. *Phys. Rev. B*, **24** (1981) 1771.
DOI: 10.1103/physrevb.24.1771

[196] R. Dietz, P. Selwood. Effect of Chemisorbed Hydrogen on the Magnetization of Nickel. *J. Chem. Phys.*, **35** (1961) 270.
DOI: 10.1063/1.1731899

[197] G. Mankey, M. Kief, F. Huang, R. Willis. Hydrogen chemisorption on ferromagnetic thin film surfaces. *J. Vac. Sci. Technol.*, **11** (1993) 2034.
DOI: 10.1116/1.578405

[198] P. Amann, M. Cordin, J. Redinger, S. D. Stolwijk, K. Zumbrägel, M. Donath, E. Bertel, A. Menzel. Circumstantial evidence for hydrogen-induced surface magnetism on Pd (110). *Phys. Rev. B*, **85** (2012) 094428.
DOI: 10.1103/physrevb.85.094428

[199] J. Park, C. Park, M. Yoon, A.-P. Li. Surface magnetism of cobalt nanoislands controlled by atomic hydrogen. *Nano Lett.*, **17** (2017) 292.
DOI: 10.1021/acs.nanolett.6b04062

[200] P. K. Kulriya, B. R. Mehta, D. C. Agarwal, P. Kumar, S. M. Shivaprasad, J. C. Pivin, D. K. Avasthi. Giant enhancement in ferromagnetic properties of Pd nanoparticle induced by intentionally created defects. *J. Appl. Phys.*, **112** (2012) 014318.
DOI: 10.1063/1.4733950

[201] M. Grdeń, A. Piaścik, Z. Koczorowski, A. Czerwiński. Hydrogen electrosorption in Pd-Pt alloys. *J. Electroanal. Chem.*, **532** (2002) 35.
DOI: 10.1016/s0022-0728(02)00750-7

[202] E. F. Kneller, F. E. Luborsky. Particle Size Dependence of Coercivity and Remanence of Single-Domain Particles. *J. Appl. Phys.*, **34** (1963) 656.
DOI: 10.1063/1.1729324

[203] G. Xiao, C. L. Chien. Giant magnetic coercivity and percolation effects in granular Fe-(SiO$_2$) solids. *Appl. Phys. Lett.*, **51** (1987) 1280.
DOI: 10.1063/1.98705

[204] C. Verdes, B. Ruiz-Diaz, S. M. Thompson, R. W. Chantrell, A. Stancu. Computational model of the magnetic and transport properties of interacting fine particles. *Phys. Rev. B*, **65** (2002) 174417.
DOI: 10.1103/PhysRevB.65.174417

[205] S. Komogortsev, V. Felk, O. Li. The magnetic dipole-dipole interaction effect on the magnetic hysteresis at zero temperature in nanoparticles randomly dispersed within a plane. *J. Magn. Magn. Mater.*, **473** (2019) 410.
DOI: 10.1016/j.jmmm.2018.10.091

[206] V. Franco, X. Batlle, A. Labarta. CoFe-Cu granular alloys: From noninteracting particles to magnetic percolation. *J. Appl. Phys.*, **85** (1999) 7328. DOI: 10.1063/1.369357

[207] M. Cialone, F. Celegato, F. Scaglione, G. Barrera, D. Raj, M. Coïsson, P. Tiberto, P. Rizzi. Nanoporous FePd alloy as multifunctional ferromagnetic SERS-active substrate. *Appl. Surf. Sci.*, **543** (2021) 148759. DOI: 10.1016/j.apsusc.2020.148759

[208] G. Barrera, F. Celegato, M. Cialone, M. Coïsson, P. Rizzi, P. Tiberto. Structural, Wetting and Magnetic Properties of Sputtered Fe70Pd30 Thin Film with Nanostructured Surface Induced by Dealloying Process. *Nanomaterials*, **11** (2021). DOI: 10.3390/nano11020282

[209] G. Herzer. Grain size dependence of coercivity and permeability in nanocrystalline ferromagnets. *IEEE Trans. Magn.*, **26** (1990) 1397. DOI: 10.1109/intmag.1990.733930

[210] I. M. L. Billas, A. Chatelain, W. A. de Heer. Magnetism from the Atom to the Bulk in Iron, Cobalt, and Nickel Clusters. *Science*, **265** (1994) 1682. DOI: 10.1126/science.265.5179.1682

[211] S. U. Jen, T. P. Chen, S. A. Chang. Electrical resistivity of Co-Ni-Pd and Co-Pd alloys. *J. Appl. Phys.*, **70** (1991) 5831. DOI: 10.1063/1.350125

[212] S. Subkow, M. Fähnle. Potential explanation of charge response of magnetization in nanoporous systems. *Phys. Rev. B*, **84** (2011) 220409. DOI: 10.1103/PhysRevB.84.220409

[213] D. Kramer, R. N. Viswanath, J. Weissmüller. Surface-Stress Induced Macroscopic Bending of Nanoporous Gold Cantilevers. *Nano Lett.*, **4** (2004) 793. DOI: 10.1021/nl049927d

[214] A. MISHRA, C. BANSAL, M. GHAFARI, R. KRUK, H. HAHN. Tuning properties of nanoporous Au-Fe alloys by electrochemically induced surface charge variations. *Phys. Rev. B*, **81** (2010) 155452.
DOI: 10.1103/physrevb.81.155452

[215] L. REICHEL, S. OSWALD, S. FÄHLER, L. SCHULTZ, K. LEISTNER. Electrochemically driven variation of magnetic properties in ultrathin CoPt films. *J. Appl. Phys.*, **113** (2013) 143904.
DOI: 10.1063/1.4799413

[216] K. LEISTNER, N. LANGE, S. OSWALD, L. SCHULTZ. (Invited) Reversible Change of Magnetism in FePt Films by Electrochemical Charging in a LiClO$_4$ Based Electrolyte. *ECS Trans.*, **50** (2013) 49.
DOI: 10.1149/05010.0049ecst

[217] P. BRUNO, C. CHAPPERT. Oscillatory coupling between ferromagnetic layers separated by a nonmagnetic metal spacer. *Phys. Rev. Lett.*, **67** (1991) 1602.
DOI: 10.1103/PhysRevLett.67.1602

[218] R. J. HICKEN, A. J. R. IVES, D. E. P. ELEY, C. DABOO, J. A. C. BLAND, J. R. CHILDRESS, A. SCHUHL. Interlayer exchange coupling and weakened surface exchange in ultrathin epitaxial Fe(100)/Pd(100)/MgO(100) structures. *Phys. Rev. B*, **50** (1994) 6143.
DOI: 10.1103/PhysRevB.50.6143

[219] Z. CELINSKI, B. HEINRICH, J. F. COCHRAN, W. B. MUIR, A. S. ARROTT, J. KIRSCHNER. Growth and magnetic studies of lattice expanded Pd in ultrathin Fe(001)/Pd(001)/Fe(001) structures. *Phys. Rev. Lett.*, **65** (1990) 1156.
DOI: 10.1103/PhysRevLett.65.1156

[220] Z. CELINSKI, B. HEINRICH. Exchange coupling in Fe/Cu, Pd, Ag, Au/Fe trilayers. *J. Magn. Magn. Mater.*, **99** (1991) L25.
DOI: 10.1016/0304-8853(91)90043-A

[221] B. Hjörvarsson, J. A. Dura, P. Isberg, T. Watanabe, T. J. Udovic, G. Andersson, C. F. Majkrzak. Reversible Tuning of the Magnetic Exchange Coupling in Fe/V (001) Superlattices Using Hydrogen. *Phys. Rev. Lett.*, **79** (1997) 901. DOI: 10.1103/PhysRevLett.79.901

[222] F. Klose, C. Rehm, D. Nagengast, H. Maletta, A. Weidinger. Continuous and Reversible Change of the Magnetic Coupling in an Fe/Nb Multilayer Induced by Hydrogen Charging. *Phys. Rev. Lett.*, **78** (1997) 1150. DOI: 10.1103/PhysRevLett.78.1150

[223] A. Hillion, A. Tamion, F. Tournus, C. Albin, V. Dupuis. From vanishing interaction to superferromagnetic dimerization: experimental determination of interaction lengths for embedded Co clusters. *Phys. Rev. B*, **95** (2017) 134446. DOI: 10.1103/PhysRevB.95.134446

[224] F. Tournus, A. Tamion. Magnetic susceptibility curves of a nanoparticle assembly II. Simulation and analysis of ZFC/FC curves in the case of a magnetic anisotropy energy distribution. *J. Magn. Magn. Mater.*, **323** (2011) 1118. DOI: 10.1016/j.jmmm.2010.11.057

[225] A. Tamion, M. Hillenkamp, F. Tournus, E. Bonet, V. Dupuis. Accurate determination of the magnetic anisotropy in cluster-assembled nanostructures. *Appl. Phys. Lett.*, **95** (2009) 062503. DOI: 10.1063/1.3200950

[226] J. Völkl, G. Wollenweber, K.-H. Klatt, G. Alefeld. Notizen: Reversed Isotope Dependence for Hydrogen Diffusion in Palladium. *Z. Naturforsch. A*, **26** (1971) 922. DOI: 10.1515/zna-1971-0522

[227] P.-C. Chang, Y.-Y. Chang, W.-H. Wang, F.-Y. Lo, W.-C. Lin. Visualizing hydrogen diffusion in magnetic film through magneto-optical Kerr effect. *Commun. Chem.*, **2** (2019) 89. DOI: 10.1038/s42004-019-0189-1

[228] B. D. CULLITY, C. D. GRAHAM. *Introduction to magnetic materials.*
John Wiley & Sons, 2011.
DOI: 10.1002/9780470386323

[229] Y. ZHANG, J. BUDNICK, W. HINES, C. CHIEN, J. XIAO. Effect of magnetic field
on the superparamagnetic relaxation in granular Co-Ag samples.
Appl. Phys. Lett., **72** (1998) 2053.
DOI: 10.1063/1.121262

[230] M. A. V. DEVANATHAN, Z. STACHURSKI. The Adsorption and Diffusion of
Electrolytic Hydrogen in Palladium. *Proc. Roy. Soc. London*, **270** (1962) 90.
DOI: 10.1098/rspa.1962.0205

[231] J. M. D. COEY. *Magnetism and Magnetic Materials.*
Cambridge University Press, 2010.
DOI: 10.1017/CBO9780511845000.009

[232] I. S. GRIGORIEV, E. Z. MEILIKHOV. *Handbook of Physical Quantities.*
CRC Press, 1997

[233] M. HAKAMADA, F. HIRASHIMA, M. TAKAHASHI, T. NAKAZAWA, M. MABUCHI.
Large-strain-induced magnetic properties of Co electrodeposited on nanoporous Au.
J. Appl. Phys., **109** (2011) 084315.
DOI: 10.1063/1.3575327

[234] D. WANG, K.-Y. LEE, S. LUO, T. B. FLANAGAN. The thermodynamics of
hydrogen absorption/desorption by Pd–Co alloys. *J. Alloys*, **252** (1997) 209.
DOI: 10.1016/S0925-8388(96)02715-6

[235] U. BAUER, L. YAO, A. J. TAN, P. AGRAWAL, S. EMORI, H. L. TULLER, S. VAN
DIJKEN, G. S. D. BEACH. Magneto-ionic control of interfacial magnetism.
Nat. Mater., **14** (2014) 174.
DOI: 10.1038/nmat4134

[236] L. Lührs, B. Zandersons, N. Huber, J. Weissmüller. Plastic Poisson's ratio of nanoporous metals: A macroscopic signature of tension–compression asymmetry at the nanoscale. *Nano Lett.*, **17** (2017) 6258.
DOI: 10.1021/acs.nanolett.7b02950

[237] H.-J. Jin, S. Parida, D. Kramer, J. Weissmüller. Sign-inverted surface stress-charge response in nanoporous gold. *Surf. Sci.*, **602** (2008) 3588.
DOI: 10.1016/j.susc.2008.09.038

[238] N. Mameka, J. Markmann, J. Weissmüller. On the impact of capillarity for strength at the nanoscale. *Nat. Commun.*, **8** (2017) 1976.
DOI: 10.1038/s41467-017-01434-2

[239] Y. Li, W. Dononelli, R. Moreira, T. Risse, M. Bäumer, T. Klüner, L. V. Moskaleva. Oxygen-driven surface evolution of nanoporous gold: insights from Ab initio molecular dynamics and auger electron spectroscopy.
J. Phys. Chem. C, **122** (2017) 5349.
DOI: 10.1021/acs.jpcc.7b08873

[240] T. Fujita, T. Tokunaga, L. Zhang, D. Li, L. Chen, S. Arai, Y. Yamamoto, A. Hirata, N. Tanaka, Y. Ding, *et al.* Atomic observation of catalysis-induced nanopore coarsening of nanoporous gold. *Nano Lett.*, **14** (2014) 1172.
DOI: 10.1021/nl403895s

[241] B. Zugic, L. Wang, C. Heine, D. N. Zakharov, B. A. Lechner, E. A. Stach, J. Biener, M. Salmeron, R. J. Madix, C. M. Friend. Dynamic restructuring drives catalytic activity on nanoporous gold–silver alloy catalysts.
Nat. Mater., **16** (2017) 558.
DOI: 10.1038/nmat4824

[242] G. Pia, E. Sogne, A. Falqui, F. Delogu. Ag surface segregation in nanoporous Au catalysts during CO oxidation. *Sci. Rep.*, **8** (2018) 1.
DOI: 10.1038/s41598-018-33631-4

[243] B. Farkaš, C. B. Perry, G. Jones, N. H. de Leeuw. Adsorbate-Induced Segregation of Cobalt from PtCo Nanoparticles: Modeling Au Doping and Core AuCo Alloying for the Improvement of Fuel Cell Cathode Catalysts.
J. Phys. Chem. C, **124** (2020) 18321.
DOI: 10.1021/acs.jpcc.0c04460

[244] H. Liu, W. Li, A. Manthiram. Factors influencing the electrocatalytic activity of $Pd_{100-x}Co_x$ ($0 \leq x \leq 50$) nanoalloys for oxygen reduction reaction in fuel cells.
Appl. Catal., B, **90** (2009) 184.
DOI: 10.1016/j.apcatb.2009.03.008

[245] R. Ma, T. Yang, J. Sun, Y. He, J. Feng, J. T. Miller, D. Li. Nanoscale surface engineering of $PdCo/Al_2O_3$ catalyst via segregation for efficient purification of ethene feedstock. *Chem. Eng. Sci.*, **210** (2019) 115216.
DOI: 10.1016/j.ces.2019.115216

[246] M. Zhao, W. G. Sloof, A. J. Böttger. Modelling of surface segregation for palladium alloys in vacuum and gas environments.
Int. J. Hydrog. Energy, **43** (2018) 2212.
DOI: 10.1016/j.ijhydene.2017.12.039

Acknowledgements

Here I would like to express my gratitude to a number of people who contributed to this thesis.

Univ.-Prof. Dr. Roland Würschum, Institute of Materials Physics, Graz University of Technology

For giving me the opportunity to work on an exciting PhD project at the Institute of Materials Physics and supervising my thesis. I benefited greatly from his professional attitude and expertise.

Univ.-Prof. Dr. Heinz Krenn, Institute of Physics, University of Graz

For his invaluable help with SQUID magnetometry and the many discussions about magnetism.

Univ.-Prof. Dr. Karin Leistner, Institute of Chemistry, Chemnitz University of Technology and IFW Dresden

For gratefully accepting to act as an external reviewer for this thesis. As a pioneer in the field of magneto-ionics, her comments in the preliminary evaluation stage greatly improved this thesis in its final from.

Dr. Stefan Topolovec, Institute of Materials Physics, Graz University of Technology

For his valuable suggestions and the exchange of ideas regarding magneto-ionics.

Dr. Gregor Klinser, formerly Institute of Materials Physics, Graz University of Technology

For the introduction to practical SQUID magnetometry at the start of my thesis and technical discussions at later stages.

My colleagues at the Institute of Materials Physics, Graz University of Technology

For the great working environment and everybody's help with smaller issues in the lab.

My fellow PhD students and friends

For countless lunch and coffee breaks spend together, chatting casually or discussing science.

My family

For their continuous support and encouragement.